The Numerical Simulation of Wavepackets in a Transitional Boundary Layer

Claire Heaney

May 2007

ProQuest LLC
789 East Eisenhower Parkway
P.O. Box 1346
Ann Arbor, MI 48106-1346

For a very thin plate in a stream,
The laminar flow is your dream,
Not turbulent meanie;
In fact, says Claire Heaney,
It's somewhere between, it would seem.

(Professor Huxley 6th June 2003)

Contents

List of Figures

Acknowledgements

In writing this thesis I have benefited greatly from the guidance of my supervisor Dr Christopher Davies whose scholarship, patience and kindness ensured its completion. I also acknowledge the receipt of financial assistance from the School of Mathematics at Cardiff University.

I would also like to thank Dr Jonathan Healey (Keele University) for giving so generously of his time and for his many insightful comments.

Thanks also go to Jonathan Giddy (Grid Technologies Co-ordinator for the Welsh e-Science Centre) and Dr James Osborne (High End Computing Support Officer) who have both helped me to run computing jobs with Condor on the SGI-Origin machines, and also to Dr Peter Bollada and Mike Kennard for their help with various software programmes.

Both Karen Kudar and Christian Thomas have kindly supplied me with numerical results: Karen with results generated from two versions of a Poisson Solver (see section 3.3), and Tom with results from an eigenvalue solver (see section 4.2). Thanks to Michael Togneri who proof-read this thesis with his customary eye for detail.

Somewhat belatedly, I would like to extend special thanks to Prof Russell Davies, Prof Tim Phillips, Dr Rob Douglas, Dr Spencer Jones and others involved with the MSc course in Complex Fluids at Aberystwyth, as it was their enthusiasm together with a fantastic course which ignited my interest in fluids.

For fond memories, thanks must go to Tim, Janis, Ani, Steve ... and of course all those at the Embassy Café. Finally, for his many words of wisdom and his indefatigable interest it remains for me to thank Marc. Diolch o galon i chi i gyd.

Presentations & Publications

In preparation for submission to the Journal of Fluid Mechanics:
C Heaney, S Houten, J J Healey & C Davies, *'Direct numerical simulation of a wave-envelope steepening effect in Blasius and Falkner–Skan Boundary Layers'*

University of Wales Mathematics Colloquium (Gregynnog, May 2006)

'A Wave-Envelope Steepening Effect in transitional flow over a flat plate'

British Applied Mathematics Colloquium (Keele University, April 2006)

'A Wave-Envelope Steepening Effect in transitional flow over a flat plate: modelling with a higher-order Ginzburg–Landau equation'

Graduate School of Physical Sciences & Engineering (Cardiff, 2006)

A poster presentation given at the inauguration, currently available at:
www.cardiff.ac.uk/maths/people/postgraduate/heaney.html

British Applied Mathematics Colloquium (Liverpool University, April 2005)

'A Wave-Envelope Steepening Effect in transitional flow over a flat plate: the effect of streamwise pressure gradients'

Speaking of Science (Cardiff University, 2004)

'Wavepackets in a Transitional Boundary Layer'

Abstract

Results from two-dimensional direct numerical simulations of the governing equations that model incompressible fluid flow over a flat plate are presented. The Navier–Stokes equations are cast in a novel velocity-vorticity formulation (see Davies and Carpenter (2001)) and discretized with a mixed pseudospectral and compact finite-difference scheme in space, and a three-level backward-difference scheme in time.

A method to determine the envelope of a wavepacket (from numerical data) was developed. Based on the usual Hilbert Transform, new stages were incorporated to ensure a smooth envelope was found when the wavepacket was asymmetric.

The early transitional stages of the Blasius flow (flow over a flat plate with zero streamwise pressure gradient) are investigated with particular regard to a weakly nonlinear effect called wave-envelope steepening. Blasius flow is linearly unstable and so-called Tollmien–Schlichting modes develop. As nonlinearities become significant, the envelope of the wavepacket starts to develop differently at its leading and trailing edges. Numerical results presented here show that the envelope becomes steeper at the leading edge than it is at the trailing edge.

The effect of a non-zero streamwise pressure gradient on wave-envelope steepening is investigated by using Falkner–Skan profiles in place of the Blasius profile.

Natural transition is triggered by randomly-modulated waves. A disturbance with a randomly-modulated envelope was modelled and its effect on wave-envelope steepening was studied.

The higher-order Ginzburg–Landau equation was used to model the evolution of an envelope of a wavepacket disturbance. These results gave good qualitative comparison with the direct numerical simulations.

Finally, in preparation for developing a three-dimensional nonlinear version of the code, the discretization of one of the governing equations (the Poisson equation) was extended to three dimensions. Results from this new three-dimensional version of the Poisson solver show good agreement with those from an iterative solver, and also demonstrate the robustness of the numerical scheme.

Chapter 1

Introduction

This thesis investigates a weakly nonlinear phenomenon known as wave-envelope steepening that occurs in transitional boundary-layer flow over a flat plate.

Introduced below are the concepts of the boundary layer and transitional flow. Results from experiments which have identified dominant characteristics of transitional flow are discussed. Section 1.2 discusses results from experiments using wavepackets to disturb boundary layer flow, including that work which has identified this wave-envelope steepening effect. Numerical work carried out by scientists investigating transition that is relevant to this work is identified in section 1.3, before the layout of the thesis is described in the final section of this chapter.

1.1 The Boundary Layer and Transitional Flow

There has been a keen interest in this field ever since Prandtl introduced the notion of the boundary layer in 1904, reconciling a uniform velocity profile with the no-slip condition on the surface. The boundary layer height may be defined to be the height at which the velocity has the value $0.99U_\infty$ where U_∞ is the freestream velocity. It can be thought of as an imaginary line dividing the flow into two regions: one extremely narrow region immediately above the surface (the boundary layer), and the other region above this (the freestream or external flow). In the case of a stationary plate, within the boundary layer the velocity profile is reduced from $0.99U_\infty$ to zero on the surface, thereby satisfying the no-slip condition. As this region is narrow, the velocity gradient is large.

Vorticity is created at the surface, it diffuses and is convected throughout the flow. In the three dimensions vortex bending and stretching occurs. Above the boundary layer, the velocity is almost constant so the velocity gradient is negligible and the flow can be approximated by an inviscid flow. See figure 1.1 for an illustration of the boundary layer.

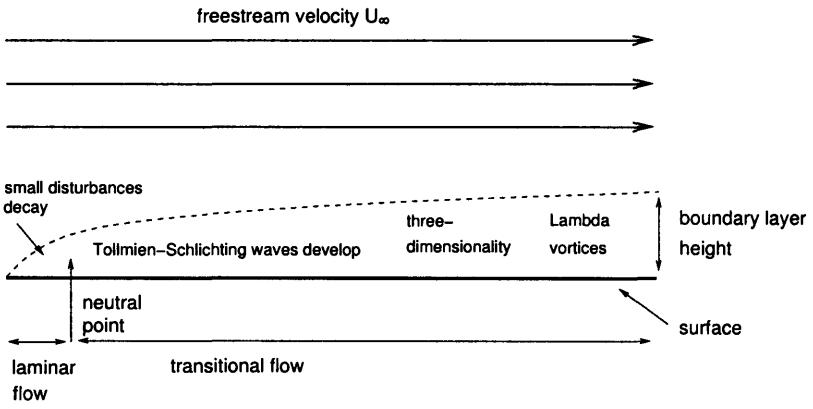

Figure 1.1: A schematic view of the boundary layer.

There are three types of flow observed over a surface: laminar flow, transitional flow and turbulent flow. In general a flow does not remain laminar for long; transition to a turbulent flow usually occurs. For the case of flow over a flat plate, today's scientists still endeavour to answer the questions of where and why transition occurs. As well as being a fascinating mathematical nonlinear stability problem in its own right, transitional flow has practical application to aerodynamics. If we know where and why transition occurs we can attempt either to delay the onset of transition or to promote transition depending on the particular context. For example, in flight, if the flow over an aeroplane wing could be made mostly laminar this would bring about a large saving on fuel. Conversely, in combustion we would wish to promote efficient mixing of air and fuel, and would therefore look to encourage transition.

Two-dimensional flow over a flat plate in the absence of a pressure gradient (Blasius flow) has been shown to be linearly unstable for Reynolds numbers greater than 520. For boundary layer flow, the usual definition of the Reynolds number has a characteristic length scale based on the displacement thickness (approximately one third of the boundary

layer height for Blasius flow), which is proportional to the square root of streamwise distance. So the Reynolds number of 520 (which is the critical Reynolds number for this flow), translates to a streamwise distance sometimes referred to as the neutral point. Upstream of this point the flow is laminar and all small disturbances decay. However, downstream of this point small disturbances with certain wavenumbers and frequencies will grow according to linear theory and the flow becomes transitional. At their simplest, these disturbances take the form of two-dimensional travelling waves known as Tollmien–Schlichting waves. These slow-developing long-wavelength disturbances are the starting point for transition. The features which develop further downstream have shorter length- and time-scales and these processes ultimately lead to the transition to turbulence.

Many experimental studies on transitional flow have been carried out in wind tunnels. The high background disturbances that are present, can preclude certain stages of transition from occurring. It was only when wind tunnels were improved by reducing the levels of background disturbances present, that Schubauer and Skramstad (1948) and later Klebanoff, Tidstrom and Sargent (1962) were able to witness the theoretically predicted Tollmien–Schlichting modes. Stuart (1965) gave one of the first reviews of the transition process of flow over a flat plate, including the ground-breaking results of Schubauer and Skramstad (1948), and Klebanoff et al. (1962). According to Stuart, and others who have written on the subject, the process of transition can be split into several stages

- receptivity: the means by which a disturbance enters the boundary layer. This disturbance might arise from surface roughness, acoustic waves, or vorticity in the freestream.

- the linear regime: here disturbances are small enough that the nonlinear terms are insignificant. The flow develops according to linear theory, which predicts the development of Tollmien–Schlichting waves.

- secondary instabilities: the Tollmien–Schlichting waves create regions of high shear which leads to the warping of the vortex lines resulting in a three-dimensional flow. For theoretical analysis, the basic flow and Tollmien–Schlichting waves are taken together as a new basic state which is unstable to three-dimensional instabilities.

At this stage the instabilities that develop depend to some extent on the initial disturbance. Commonly seen are three-dimensional structures known as lambda vortices (Λ vortices), as they resemble the Greek letter Λ.

- breakdown: following the appearance of the Λ vortices there is a rapid breakdown to short-scale structures known as spikes. Simultaneously, areas of turbulence develop (known as 'turbulent spots') which mark the onset of turbulence.

- turbulence: unsteady and disorderly flow characterized by structures with very short temporal and spatial scales.

As wind tunnels have been further improved, a more detailed picture of transition has emerged. Since Stuart's review (1965), authors have classified several types of transition (Kachanov, 1994; Herbert, 1988; Bowles, 2000), according to differences in the secondary instabilities which have been observed. The secondary instabilities can take three forms, known as K-type transition (after Klebanoff), N-type transition (after Novosibirsk where experiments investigating this were carried out by Kachanov (1994) and others) or H-type transition (after Herbert), and O-type transition (oblique). As described in a review article by Kachanov (1994), the latter stages of all three of these types of transition are similar; Λ vortices develop, soon followed by a breakdown of the flow into turbulence. However there are also differences. Characteristic of N-type transition is a staggered arrangement of Λ vortices. This type of transition would be expected to occur for flow over a flat plate in a low background disturbance environment, as the spanwise mode which leads to N-type transition has the highest growth rate. However Klebanoff, in 1962, observed aligned Λ vortices (see figure 1.2). Known as K-type transition, this phenomenon can be triggered by streamwise vorticity in the background environment. Another feature of K-type transition is the appearance of large spikes in the streamwise velocity variable. These were thought to be peculiar to K-type transition until recent experiments by Bake et al. (2000) who have seen spikes in N-type transition as well. O-type transition occurs when two three-dimensional modes develop with spanwise wavenumbers of $\pm\ \beta$. A special case of this occurs when these two oblique modes resonate with the most unstable mode according to linear theory. These three modes are known together as Craik's resonant triad (Craik, 1971). In experiments, methods of introducing disturbances to boundary layers are often carefully chosen in order to excite one particular type of transition. Illustrations of these

three types of transition can be seen in Schmid and Henningson (2001, page 441). In natural transition any combination of the features described above might be seen.

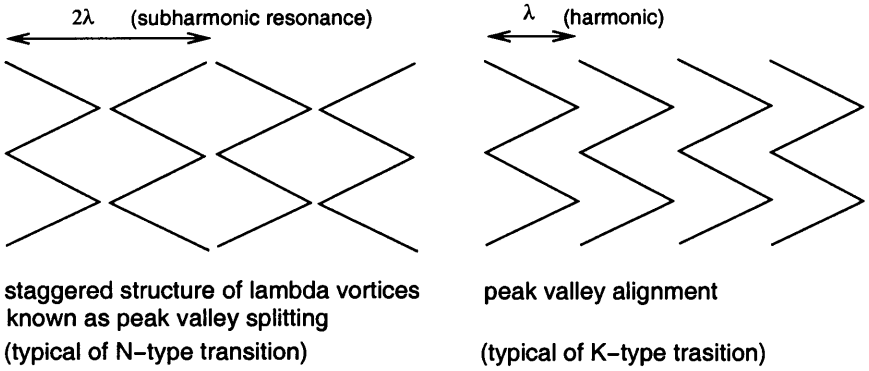

Figure 1.2: Two patterns of Λ vortices.

There are other mechanisms which cause transition to turbulence, often collectively called 'bypass transition'. Here the initial stages of transition are circumvented. Either, the initial disturbances are amplified by processes other than the linear Tollmien–Schlichting mechanism, or the initial disturbances or large enough to pass by the early stages of transition. The flow may show some of the stages described above, or may become turbulent straight away. Central to this study of flow over a flat plate presented in this thesis is the development of disturbances that are small enough so that bypass mechanisms need not be considered.

1.2 Results from Experiments

After having discussed transitional flow, we now review some experimental results relevant to this thesis. We therefore focus upon experiments which used localised disturbances (ie wavepackets), rather than monochromatic wavetrains to perturb the boundary layer.

Schubauer and Skramstad (1948) were the first to see in their experiments waves of the form predicted by Tollmien and Schlichting. Since this success, there has been much work done in studying the linear theory of two-dimensional flow over a flat surface. The linear theory is used as a standard test against which to validate the results of numerical codes. Shaikh and Gaster (1994) point out that Schubauer and Skramstad's

work was two-pronged. First they used freestream fluctuations to disturb the boundary layer. This excited a broad range of modes which formed a wavepacket that grew whilst propagating downstream, culminating in the formation of turbulent spots. Second they used a vibrating ribbon to excite wavetrains so their results could be compared directly with linear theory. Many experimentalists have been influenced by the second part of the work, but Shaikh and Gaster believe that the first part of their work is informative when investigating nonlinear effects.

Gaster and co-workers (Gaster and Grant, 1975; Gaster, 1979; Shaikh and Gaster, 1994) have suggested that the modulation of these wave disturbances should be taken into account. Gaster and Grant (1975) discovered from their experiments, that modulated waves behave differently from purely sinusoidal waves. They used an acoustic pulse to disturb a boundary layer. They compared their results with three-dimensional theory and found that the experimental results followed the theory closely initially. Further downstream however, the wave crests deformed in a way not predicted by the theory. Two oblique waves developed either side of the centreline. High frequency bursts were also seen at surprisingly low disturbance amplitudes; amplitudes which would not excite nonlinear terms for monochromatic disturbances. Their work shows that nonlinear breakdown is seen to occur at much lower amplitudes for modulated waves than for periodic wave trains. Shaikh and Gaster (1994) investigate this using white noise to disturb the boundary layer. This generated a wavepacket composed of modes of random phase. The development followed linear theory initially, however, once again high frequency bursts, so typical of nonlinear breakdown, occurred at much lower amplitudes than would be expected for periodic wavetrains.

Cohen et al. (1991) and Breuer et al. (1997) were also carrying out experiments with wavepacket disturbances. They investigated transition caused by a small-amplitude wavepacket and followed its development through to the formation of a turbulent spot, finding oblique modes were present when the disturbance velocity was between $0.005U_\infty$ and $0.05U_\infty$. The oblique modes had a frequency of half that of the frequency of the most unstable mode according to linear theory. Once the disturbance velocity exceeded $0.05U_\infty$ streaky structures were observed before turbulent spots formed.

Medeiros and Gaster (1999a,b) have extended this work and investigated the influence of phase of the disturbance relative to the envelope of the disturbance. They have shown that the phase plays a significant part in determining where (or how far) downstream, the nonlinearities develop. Certain phases result in nonlinearities occurring much sooner (at much lower amplitudes) than for other phases. They have shown that this is not because of the way in which the disturbances were excited, and state that the reason is linked to the phase difference between the wave and its envelope. They have also identified a subharmonic resonance. The subharmonic frequency is excited and sustained by the disturbance as it evolves. Medeiros and Gaster even filter out the subharmonic frequency from the forcing, and find that this frequency will still emerge downstream. It is not part of the band of artificially-excited Tollmien–Schlichting modes.

Medeiros (2004a,b) has extended this work further to look at three-dimensional disturbances as a model for investigating natural transition. His first paper concentrates on natural transition as triggered by a wavetrain. Two stages of nonlinear behaviour were identified: first, that streamwise vortices led to algebraic growth, and second, that a secondary instability leads to a pattern of aligned Λ vortices. This was apparently triggered by the proximity of the disturbance to the second (or upper) branch of the neutral curve. These results also reveal that for three dimensions, the mean-flow distortion[1] is negative in the early stages of nonlinear development. The second paper discusses a similar investigation, only the streamwise modulation of the disturbance is varied, so the flow is disturbed by a wavepacket. This disturbance produces three stages of nonlinear development: first, streamwise vortices once again led to algebraic growth, second the aligned Λ vortices of K-type transition were observed, and finally, a staggered array of Λ vortices were seen, from N-type transition. As Medeiros and Gaster (1999a,b) observed, the subharmonic modes seem to be excited as part of the nonlinear development of the wavepacket, and in fact Medeiros proposes that the large mean-flow distortion which occurs in three dimensional flows when modulated disturbances are present, is responsible for seeding the subharmonic frequencies.

[1]The term 'mean-flow distortion' refers to a distortion of the basic or mean flow which comes about as a result of the interactions of nonlinear modes.

Their experiments revealed that modulated waves are susceptible to nonlinear effects at much lower amplitudes than unmodulated waves. As natural transition is triggered by randomly modulated waves, it is necessary to use wavepackets rather than wavetrains as disturbances, in order to gain a deeper insight into natural transition.

Jonathan Healey and co-workers (Healey, 1995a, 2000; Houton et al., 2001; Houten et al., 2000; Houten, 2004; Walker, 2005) have carried out similar investigations into transitional flow, continuing to study the effect of wavepacket disturbances to the boundary layer. Healey (2000) identifies one particular effect seen in transition and describes it as a wave-envelope steepening effect. In his experiments, Healey found that the envelope of the wavepacket disturbance became steeper at the trailing edge than it was at the leading edge. When he used randomly-modulated disturbances he found a skew in the gradient towards negative values, showing that the larger the amplitude of the disturbance, the steeper the decaying parts of the wavepacket would become in comparison to the growing parts. In two-dimensional nonlinear simulations, however, Healey and Houten found that the envelope became steeper at the leading edge than at the trailing edge. In other words, the gradient at the leading edge was larger than the absolute value of the gradient at the trailing edge.

This result contradicts their experimental data however, which showed the steepest part of the envelope developed at the trailing edge. Two possible reasons for this disagreement are given here. First, in wind tunnels it is notoriously difficult to obtain a zero pressure gradient. If there had been a non-zero pressure gradient this may have affected whether the steepest part of the envelope was to develop at the leading or trailing edge. In the computer simulations there is no such difficulty as the Blasius flow, which is prescribed at the inflow, has a zero pressure gradient. Second, the simulation is based on a two-dimensional nonlinear model. If wave-envelope steepening is essentially a three-dimensional effect, then it will not be accurately represented in two dimensions and the experimental and computational results will differ.

The aim of this thesis is to investigate why the two-dimensional model shows steepening occurring at the leading edge rather than the trailing edge. The two ideas above are used

as starting points. Whilst developing a method for calculating the envelope of a wave, it became evident that the mean flow of the disturbance (or mean flow distortion) plays an important role in its nonlinear development. Before the layout of the thesis is given, some time is spent describing important numerical work carried out in the area of transitional flow over a flat plate.

1.3 Numerical Work

Having already noted that Gaster, Medeiros and Healey have all made significant contributions to numerical work in the area of wavepackets disturbing boundary-layer flows as well as other areas, it remains necessary to indicate the contribution of Hermann Fasel. His work in the simulation of boundary-layer flows has been pioneering. Alongside those of his co-workers, Fasel's investigations provide a detailed picture of the numerical solution of boundary-layer flow (see for example Fasel, 1976, 1980, 1984; Fasel and Konzelmann, 1990; Fasel et al., 1990; Fasel, 2002; Kloker et al., 1993; Rist and Fasel, 1995). Fasel (1976) presented results using a code based on a vorticity-velocity formulation, overcoming the difficulties of finding a suitable boundary condition for the vorticity and implementing the no-slip condition. Other researchers at this time were still favouring the primitive-variable formulation. Later he championed the spatial model over the much-used temporal model (Rist and Fasel, 1995). The spatial model is very similar to the set-up used by experimentalists, and similar to the physical problems being modelled. Results are therefore more easily comparable. Fasel also developed a direct method to solve the Poisson equation(s) for velocity that arise in the velocity-vorticity formulation. A similar method is implemented in the code devised by Davies (see Bowles et al., 2003) and described here in chapter 3.

We return now to the particular numerical code used to generate the results presented in this thesis. The formulation and the numerical scheme are described in chapters 2 and 3. The code has been widely used by its author, Dr Christopher Davies, and his co-workers and PhD students. A variety of boundary-layer flows have been investigated, and both small and large disturbances have been utilized. Davies and Carpenter (2003), and Davies et al. (2007) use the code to simulate linear disturbances to flow over a rotating disc. The simulations show the effect of the non-parallelism in the base flow on

the development of disturbances. The usual stability analysis simplifies the basic flow, assuming it to be parallel (independent of the radial co-ordinate), and therefore cannot predict the effect of non-parallel behaviour. The code has been used to simulate flow over a compliant panel (Davies and Carpenter, 1997b) with biological applications. The effect of disturbance-control devices has been investigated (Davies et al., 2001; Carpenter et al., 2002) with applications to the aircraft industry. Lockerby et al. (2002) have used a three-dimensional linear version of the code to investigate the interaction between microelectromechanical systems (MEMS) and mesoscale actuators in a boundary layer. Kudar (2004) has used a three-dimensional linear version of the code to investigate flow control using pulsed jets for Falkner–Skan–Cooke basic flows. Receptivity has been investigated by Ali (2003). Nonlinear work includes an investigation of the spiking that occurs in the final stages of transition (Bowles et al., 2003). Other nonlinear studies include work investigating wave-envelope steepening, which have been undertaken by Houten (2004); Houten et al. (2000) and the current author. As part of his study, Houten (2004) carefully validated the code comparing its results against that of linear theory for a parallel Blasius flow. He also generated results investigating the effects of finite-amplitude disturbances, and a non-parallel Blasius flow. Both these sets of results agreed well with theory and experiment and are discussed further in chapter 4.

1.4 Layout of the thesis

At the outset of this period of research, we were looking to resolve contradictory experimental and numerical results describing wave-envelope steepening. As well as resolving this conflict, the work is of interest as the growth in perturbation variables found at the trailing edge of a wavepacket is a precursor of spikes. Healey (2000) reports that the asymmetries seen in these weakly nonlinear stages are the precursor to the spikes which have been observed to form at the back of turbulent spots.

In an attempt to explain the wave-envelope steepening mechanism, the complex picture of natural (three-dimensional) transition has been simplified here, by using throughout both two-dimensional simulations and the parallel Blasius flow as a basic state. These simplifications allow us to build up a clearer picture of wave-envelope steepening and

model the phenomenon well, as will be demonstrated.

Chapter 2 sets out the particular formulation of the governing equations used in this investigation. It explains the discretization of the equations which have been implemented in a computer program by Dr Christopher Davies.

Chapter 3 presents a three-dimensional discretization of one of the governing equations and presents some results. This work was done in preparation for the larger task of three-dimensionalizing the whole code. The chapter presents the first full documentation of a direct Poisson Solver included in current versions of Davies' code.

After introducing Blasius flow and linear theory, chapter 4 presents a review of weakly nonlinear theory. Authors mentioned in this chapter have derived the higher-order complex Ginzburg–Landau equation as that which governs the evolution of the amplitude of the disturbance in a weakly nonlinear parallel flows. It is shown to model the wave-envelope steepening effect with success.

Chapter 5 shows results of direct numerical simulations using the formulation and discretization explained in chapter 2. The results illustrate weakly nonlinear behaviour in a transitional boundary layer, and in particular demonstrate the wave-envelope steepening effect.

Chapter 6 investigates the effect of a streamwise pressure gradient on wave-envelope steepening.

Chapter 7 investigates the effect on wave-envelope steepening of adding a random modulation to the disturbance.

This thesis concludes with chapter 8, by offering thoughts on further work that might be undertaken to follow up the research described here.

Much of the work presented here stems from the computational code written by Dr Christo-

pher Davies, which is based on the velocity-vorticity formulation and numerical scheme presented in Davies and Carpenter (2001). The code solves the Navier–Stokes equations for boundary-layer flow. Minor modifications have been made to the code by Davies since this paper, such as the use of compact difference schemes for the first order streamwise derivatives, and a direct Poisson Solver replacing the iterative scheme (documented in chapter 2 and 3). Post-processing routines have been devised by the current author in order to quantitatively assess the wave-envelope steepening effect (presented in chapter 5). Throughout this thesis, unless otherwise specified, this computational code will be referred to as 'the code' or 'Davies' code'. Developments in computer speed and memory means that the simulations documented in chapters 5 and 6 run successfully on a PC in a matter of hours.

Chapter 2

Formulation of governing equations and their discretization

In this chapter the novel velocity-vorticity formulation of Davies and Carpenter (2001) is described. This formulation lies at the heart of Davies' computer code which has been used to generate the results presented in this thesis. The formulation provides a set of governing equations which are then discretized using a mixed pseudo-spectral compact-difference method. The features of the discretization process are outlined here for the two-dimensional case. Chapter 3 indicates how to adapt one of the governing equations (the Poisson equation) for a three-dimensional system.

2.1 Velocity-vorticity formulation

2.1.1 Advantages of velocity-vorticity formulations

The absence of the pressure variable is a key advantage that velocity-vorticity formulations have over primitive-variable formulations. In the latter, pressure is represented only through its spatial derivatives. Lacking an evolution equation therefore, the pressure can only be determined up to a constant in primitive-variable formulations.

For certain flows, vorticity is central to the behaviour of the fluid and therefore a natural choice of variable. For example, for flow over a surface the no-slip condition causes the generation of vorticity at the surface. This vorticity is then diffused and convected

throughout the flow and its behaviour determines the flow profile.

Having mentioned two advantages of velocity-vorticity formulations, two drawbacks are now highlighted. First, finding a boundary condition for the vorticity is difficult. Second, there are more variables to solve for in three-dimensional problems. In two dimensions, both velocity-vorticity formulations and primitive variable formulations have three variables (two velocity components and either a vorticity component or pressure respectively). However, in three dimensions there is an imbalance: velocity-vorticity formulations have six variables (three velocity components and three vorticity components), whereas the primitive variables formulation has only four variables (three velocity components and pressure).

Despite the extra variables (and extra computational work therefore) velocity-vorticity formulations have been implemented with success (Fasel et al. (1990); Fasel and Konzelmann (1990); Fasel (2002); Rist and Fasel (1995); Kloker et al. (1993)). Fasel was in fact the first person to publish results based on direct numerical simulations of solutions of the Navier–Stokes equations for flow over a flat plate.

Those who opt to use a velocity-vorticity formulation have to address both the previously-highlighted drawbacks. Davies and Carpenter observe that only three of the six variables need be considered, because three variables (the 'secondary variables') can be written entirely in terms of the other three variables (the 'primary variables'). Therefore, Davies' code solves for the three primary variables, stores them for an appropriate number of time steps, and calculates the secondary variables wherever necessary. Second, Davies and Carpenter impose a constraint on the vorticity that is naturally linked to the no-slip condition (see section 2.1.4).

2.1.2 The Formulation

The novel velocity-vorticity formulation of Davies and Carpenter is set out in detail in Davies and Carpenter (2001). A summary of the main features is given here.

We look to model an incompressible fluid in the domain $z \in [0, \infty)$ with a flat plate

located at $z = 0$. A steady solution of the Navier–Stokes equations is denoted by $\mathbf{U^B}$, $\mathbf{\Omega^B}$; for this thesis the two-dimensional Blasius profile is taken as the base flow. Throughout this thesis we use the 'parallel flow' approximation: this assumes the growth of the boundary layer to be negligible over the streamwise distances that are considered. As a consequence the stability properties at all locations are identical which makes the interpretation of the results more straightforward. Therefore, the Reynolds number[1] R remains constant and the base velocity varies only with respect to the wall-normal direction. The Blasius profile is then $\mathbf{U^B} = (U^B(z), 0, 0)$ and $\mathbf{\Omega^B} = (0, \frac{dU^B}{dz}, 0)$.

We aim to model the development of small disturbances to the base flow, so we introduce the perturbation variables $\mathbf{u} = (u, v, w)$ and $\boldsymbol{\omega} = (\omega_x, \omega_y, \omega_z)$. All these variables have been made non-dimensional. The x-coordinate is aligned in the streamwise direction, the y-coordinate refers to the spanwise direction and the z-coordinate is the wall-normal coordinate, see figure 2.1.

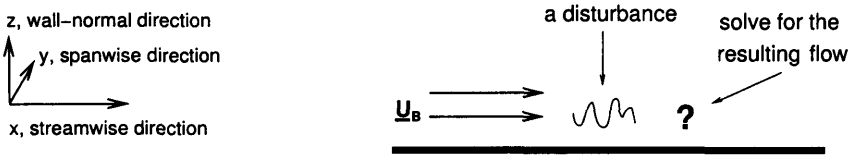

Figure 2.1: An arbitrary disturbance to a flow over a surface.

The Navier–Stokes equations for the primary perturbation variables can be written as

$$\frac{\partial \omega_x}{\partial t} + \frac{\partial N_z}{\partial y} - \frac{\partial N_y}{\partial z} = \frac{1}{R}\nabla^2 \omega_x \tag{2.1a}$$

$$\frac{\partial \omega_y}{\partial t} + \frac{\partial N_x}{\partial z} - \frac{\partial N_z}{\partial x} = \frac{1}{R}\nabla^2 \omega_y \tag{2.1b}$$

$$\nabla^2 w = \frac{\partial \omega_x}{\partial y} - \frac{\partial \omega_y}{\partial x}, \tag{2.1c}$$

where $\mathbf{N} := \mathbf{\Omega^B} \times \mathbf{u} + \boldsymbol{\omega} \times \mathbf{U^B} + \boldsymbol{\omega} \times \mathbf{u}$. The primary variables we look to solve for are $\{\omega_x, \omega_y, w\}$. The secondary variables $\{u, v, \omega_z\}$ can be calculated explicitly in terms of the

[1]The Reynolds number is defined in terms of the displacement thickness (δ^*), the freestream velocity (U^*) and the kinematic viscosity of the fluid (ν) through the relationship $R = U^*\delta^*/\nu$.

primary variables as follows:

$$u(z) = -\int_z^\infty \left(\omega_y + \frac{\partial w}{\partial x}\right) dz \tag{2.2a}$$

$$v(z) = \int_z^\infty \left(\omega_x - \frac{\partial w}{\partial y}\right) dz \tag{2.2b}$$

$$\omega_z(z) = \int_z^\infty \left(\frac{\partial \omega_x}{\partial x} + \frac{\partial \omega_y}{\partial y}\right) dz\,. \tag{2.2c}$$

These expressions are derived by integrating the definition of vorticity (for ω_x and ω_y) and integrating $\nabla \cdot \boldsymbol{\omega} = 0$. This relationship is known as the solenoidal property of vorticity and arises from the fact that the divergence of the curl of a vector is always zero. In these definitions we have assumed that $u(\infty) = v(\infty) = \omega_z(\infty) = 0$.

This formulation is equivalent to the primitive-variable formulation of the Navier–Stokes equations if the perturbations satisfy certain conditions in the limit $z \to \infty$. Davies and Carpenter show that these conditions are easily satisfied for boundary-layer flows. At the end of section 2.1.3 (page 17) these conditions will be mentioned.

With the exception of chapter 3, throughout this thesis the two-dimensional case is studied, so we now present the two-dimensional system with streamwise co-ordinate x and wall-normal co-ordinate z, total velocity field $(U^B(z) + u(x,z,t), w(x,z,t))$ and spanwise vorticity $\Omega^B(z) + \omega_y(x,z,t) \equiv dU^B/dz + \omega_y(x,z,t)$. From (2.1) we can deduce the two-dimensional governing equations by setting $v = \omega_x = \omega_z = 0$ and $\partial/\partial y \equiv 0$, which gives

$$\frac{\partial \omega_y}{\partial t} + \frac{\partial N_x}{\partial z} - \frac{\partial N_z}{\partial x} = \frac{1}{R}\nabla^2 \omega_y\,, \tag{2.3a}$$

$$\nabla^2 w = -\frac{\partial \omega_y}{\partial x}\,, \tag{2.3b}$$

or, expanding the convective terms N_x and N_z,

$$\frac{\partial \omega_y}{\partial t} + U^B \frac{\partial \omega_y}{\partial x} + \frac{d^2 U^B}{dz^2} w + u \frac{\partial \omega_y}{\partial x} + w \frac{\partial \omega_y}{\partial z} = \frac{1}{R} \nabla^2 \omega_y , \tag{2.4a}$$

$$\nabla^2 w = -\frac{\partial \omega_y}{\partial x} . \tag{2.4b}$$

The streamwise velocity u is the only secondary variable here, and it can be calculated from ω_y and w using

$$u(z) = -\int_z^\infty \left(\omega_y + \frac{\partial w}{\partial x} \right) dz , \tag{2.5}$$

assuming that the streamwise velocity vanishes at $z = \infty$.

The equations are solved for the perturbation variables (u, w and ω_y) rather than for the 'total variables' ($U^B + u$, w and $\Omega_y + \omega_y$) as the formulation for the perturbation variables is more convenient. The total variables can be easily calculated if desired.

2.1.3 Wall-normal mapping

In order to use a Chebyshev spectral expansion for the variables in the wall-normal direction, the domain must be finite. To map the semi-infinite domain $z \in [0, \infty)$ onto a finite domain $\zeta \in [1, 0)$ the following diffeomorphism is employed:

$$\begin{aligned} \zeta &= \frac{l^*}{l^* + z^*} \\ &= \frac{l}{l + z} , \end{aligned} \tag{2.6}$$

where, for Blasius flow, $z = \frac{z^*}{\delta^*} = \frac{\eta}{1.21678}$, η represents the Blasius variable and l is a dimensionless stretching parameter $l = \frac{l^*}{\delta^*}$. Derivatives with respect to z now take the form

$$\frac{\partial f}{\partial z} = \frac{-\zeta^2}{l} \frac{\partial f}{\partial \zeta} . \tag{2.7}$$

For this velocity-vorticity formulation to be equivalent to the Navier–Stokes equations we require that the following two conditions be satisfied:

$$(i) \lim_{z \to \infty} \frac{\partial w}{\partial z} \to 0 \qquad \text{and} \qquad (ii) \lim_{z \to \infty} \frac{1}{R} \frac{\partial}{\partial z} \left(\frac{\partial \omega_x}{\partial x} + \frac{\partial \omega_y}{\partial y} \right) \to 0 . \tag{2.8}$$

The second condition is automatically satisfied in two dimensions. The first condition is equivalent to saying that $\frac{\partial w}{\partial \zeta}$ is bounded as $\zeta \to 0$. This criterion will be satisfied if w is a smooth function of ζ, meaning that the Navier–Stokes equations are also satisfied. In practice the stricter condition that $w = 0$ as $\zeta \to 0$ is applied. The solutions are then inspected to ascertain that nothing untoward happens in this limit.

2.1.4 Boundary Conditions and Inflow Outflow settings

Boundary Conditions At the wall we wish to impose two conditions

- no slip, $u(x, 0, t) = 0$, as the wall is stationary with respect to the streamwise coordinate;
- and no penetration, $w(x, 0, t) = w_{wall}$ (the velocity at the wall) .

A long way from the wall we assume the perturbations will be insignificant:

$$u(x, \infty, t) = w(x, \infty, t) = \omega_y(x, \infty, t) = 0 \; . \tag{2.9}$$

When solving the vorticity transport equation a constraint is imposed on the vorticity which makes use of the no-slip condition:

$$\begin{aligned} \int_0^\infty \omega_y dz &= -\int_0^\infty \frac{\partial w}{\partial x} dz - u(x, 0, t) \\ &= -\int_0^\infty \frac{\partial w}{\partial x} dz \; . \end{aligned} \tag{2.10}$$

Many numerical methods have to introduce artificial constraints for the vorticity. This constraint has been derived naturally by linking the no-slip condition to the definition of vorticity. The result is an integral constraint for vorticity which is a direct consequence of the no-slip condition on the streamwise velocity.

When solving the Poisson equation for w we make use of the no-penetration condition. The wall is taken as stationary so $w_{wall} = 0$. However, this condition can be made non-zero as a means of introducing a disturbance to the flow. For instance, in order to generate a disturbance with a modulated amplitude and an underlying time periodicity, a suction

and blowing strip can be modelled in the following way

$$w_{wall} = A\, f(x)\, g(t)\, \sin(\omega_0 t)\ , \tag{2.11}$$

$$\text{where} \quad f(x) = \tanh\left(\frac{x - x_f}{L_{slot}}\right) \exp\left(-\left(\frac{x - x_f}{L_{slot}}\right)^2\right) \tag{2.12}$$

$$g(t) = 0.5\left(\tanh\left(\frac{\omega_0(t - t_a)}{t_0}\right) + \tanh\left(\frac{\omega_0(t_b - t)}{t_0}\right)\right)\ , \tag{2.13}$$

and where A is the initial amplitude, ω_0 is the frequency of the most unstable Tollmien–Schlichting wave at the chosen Reynolds number, t_a and t_b are constants which determine the duration of the wavepacket, t_0 determines the slope of the wavepacket in time, x_f is the point about which the forcing is centered and L_{slot} is the streamwise length over which the forcing is imposed. The frequency ω_0 is chosen to ensure that the most unstable Tollmien–Schlichting mode is most strongly excited by this forcing: section 5.2.1 discusses this further. For R=2240, typical values used for these parameters are for $A = 10^{-5}$, $\omega_0 = 0.065$, $x_f = 100$, $L_{slot} = 8$, $t_a = 400$, $t_b = 1400$ and $t_0 = 5$. Results obtained using these parameters are shown in chapter 5.

In time, the forcing is an even function about the centre of the wavepacket, $(t_a + t_b)/2$. Although the wave mode with frequency ω_0 is most strongly exited, other modes will also be present in the disturbance. In the streamwise direction the forcing is an odd function about x_f. The negative forcing corresponds to suction and the positive forcing to blowing. There is no net mass flux in or out of the domain due to this forcing. See figure 2.2 for a plot of these functions. Figure 2.3 displays the spectrum of the temporal part of the forcing function, that is $g(t)\sin(\omega_0 t)$. The value of ω_0 is 0.065 and, as can be seen, this mode is most strongly excited by the forcing. However, this forcing does also excite a band of modes either side of ω_0, but this band does not extend to the second harmonic $2\omega_0$. As will be seen later, the harmonics of ω_0 will be seen in a power spectrum of a disturbance, and this is not due to the forcing, but instead due to the nonlinear interactions of the Tollmien–Schlichting wave.

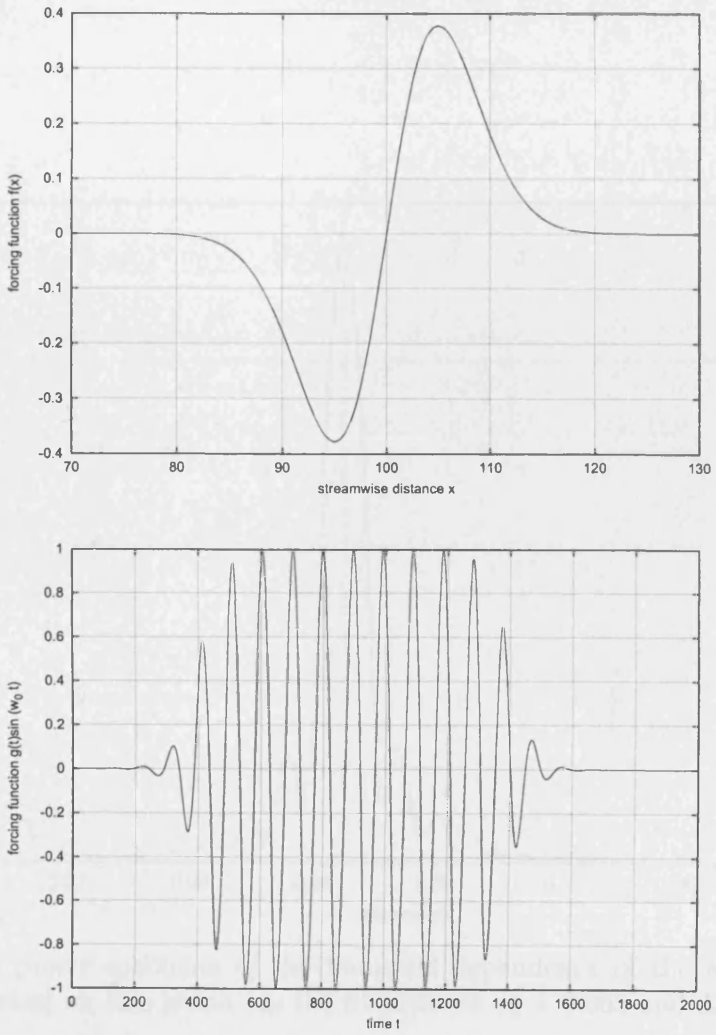

Figure 2.2: Above is $f(x)$, the spatial variation of the forcing, and below is $g(t)\ \sin(\omega_0 t)$ the temporal variation of the forcing. Together, these functions determine the forcing (see equation (2.11)). The parameters used are $\omega_0 = 0.065$, $x_f = 100$, $L_{slot} = 8$, $t_a = 400$, $t_b = 1400$ and $t_0 = 5$.

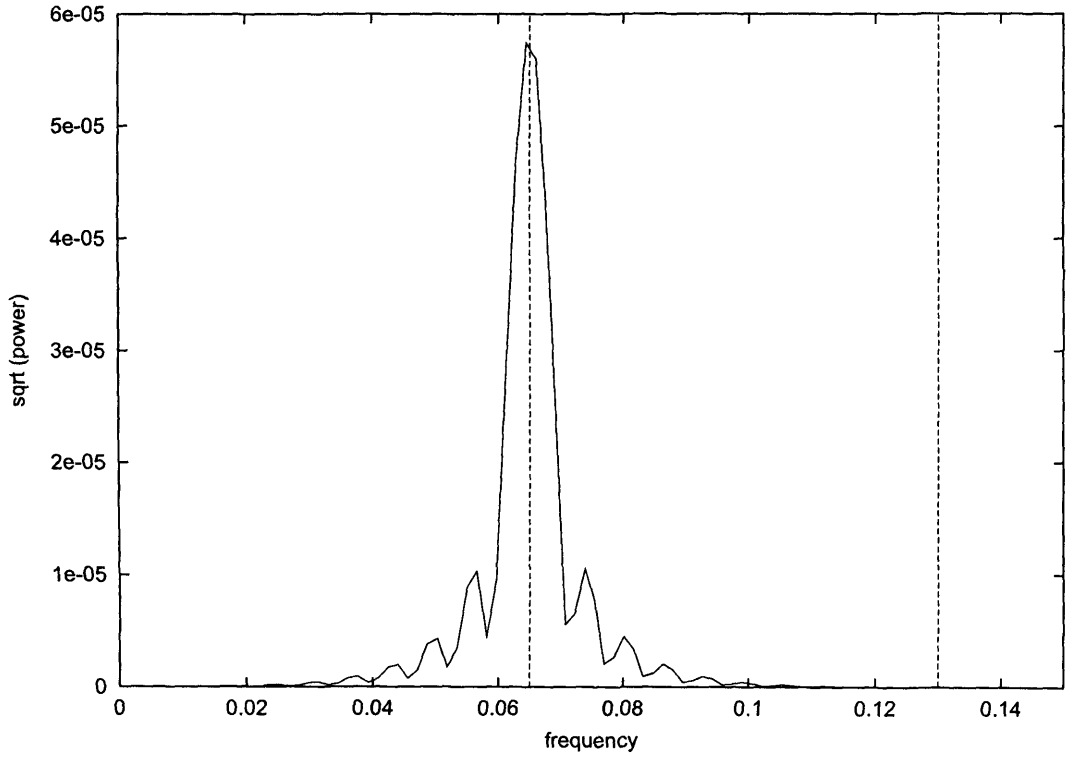

Figure 2.3: The power spectrum of the temporal dependence of the forcing (see equation (2.11)). Marked on this graph are the frequencies $\omega_0 = 0.065$ and $2\omega_0$.

Inflow and Outflow conditions The inflow condition is simply the Blasius profile (the perturbations are set to zero).

The outflow condition presents a problem that is peculiar to the computational domain. We model a disturbance which is convected downstream. Although physically, this disturbance may not reach the outflow, the numerical scheme requires both an outflow and an appropriate boundary condition there. As it is introduced purely to make numerical solution of the equations possible, rather than to model the physical behaviour, the outflow boundary must not interfere with the flow.

To ensure that the outflow does not affect the flow, one possibility is to set the boundary to be so far downstream that the disturbance never reaches it. This would create a large domain in which the Navier–Stokes equations were solved, but the solution would be of interest only in a small part of this domain. To reduce the waste of computational effort, the wave is allowed to reach the boundary where we impose the condition $\frac{\partial^2 w}{\partial x^2} = -\alpha^2 w$. This is designed to allow waves with wavenumber close to α to pass out of the domain without reflection. This constant α is chosen to be the wavenumber of the most unstable Tollmien–Schlichting wave at whichever Reynolds number has been selected. Experience shows that the success of the code is not strongly dependent on the value of α. This condition may not be sufficient to prevent reflection if the wave has become susceptible to nonlinearities by the time it reaches the outflow. In which case a buffer domain can be used in conjunction with this outflow condition, as is now described.

Inside our particular buffer domain, the solution is multiplied by a function which varies with streamwise direction decreasing from the value one to zero. This means that there will be no disturbance at the outflow and therefore no reflection. As a result, however, the solution inside the buffer domain is not a solution of the Navier–Stokes equations and should therefore be disregarded. There is still a waste of computational effort, however, this method seems to be less wasteful than the alternatives. Kloker et al. (1993) have tested a variety of methods and found that a buffer domain of the type that we shall deploy is the most effective at reducing the possibility of reflection at the outflow whilst minimizing the extra numerical work. For strongly nonlinear simulations, the same buffer

domain technique has been favoured by Fasel and co-workers (see Fasel (2002); Meitz and Fasel (2000); Rist and Fasel (1995)), and also by Joslin et al. (1991, 1993).

For our implementation, the function used to ramp down the solution in the buffer domain is

$$f(x_b) = 1 - \tanh\left(\sinh\left(\frac{x_b - 0.5\ell_b}{S}\right)\right) , \tag{2.14}$$

where ℓ_b is the length of the buffer domain, x_b is the streamwise co-ordinate in the buffer domain ($x_b \in [0, \ell_b]$) which is related to the streamwise co-ordinate x by $x = x_b + X_{end} - \ell_b$, S controls how rapidly the solution is ramped down, and X_{end} is the total length of the streamwise domain. For each streamwise location x_b which is inside the buffer domain, the following is applied to the vorticity in the time-stepping algorithm after the predictor stage

$$\omega_y(\zeta_k, X_{end} - \ell_b + x_b) \longrightarrow f(x_b)\, \omega_y(\zeta_k, X_{end} - \ell_b + x_b) \qquad \text{for } k = 1 \text{ to } N . \tag{2.15}$$

For the typical values of $X_{end} = 1023$, $\ell_b = 100$, $S = 20$ the damping function is shown in figure 2.4:

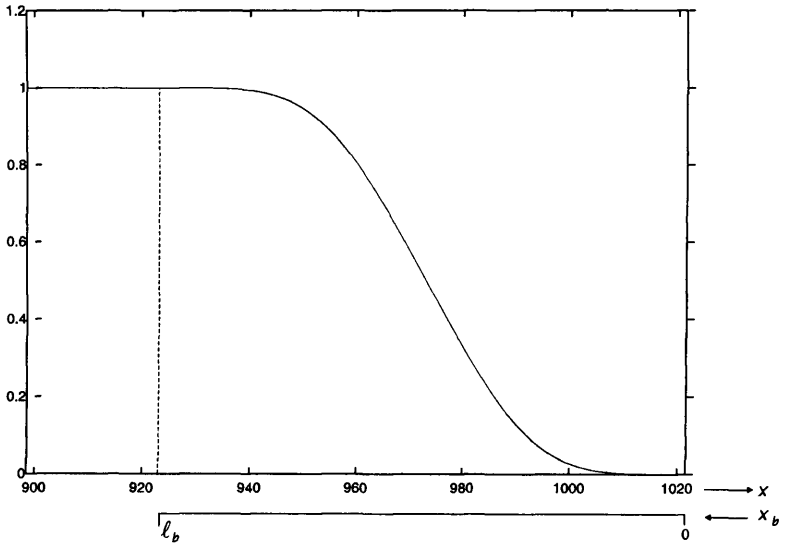

Figure 2.4: The ramping function used in the buffer domain $x \in [923, 1023]$. Solutions to the left of the dotted line are unaffected, solutions to the right of the line are ramped down.

Employing both an outflow condition and a buffer domain allows for a certain amount of flexibility. The buffer domain can be 'switched off' if the disturbances are known to be linear when reaching the downstream boundary. This will mean that the numerical solution is valid throughout the entire domain. If, by the time they reach the downstream boundary, the disturbances are nonlinear, then the buffer domain can be 'switched on' to prevent spurious reflection.

2.2 Discretization

2.2.1 Temporal discretization

2.2.1.1 The general scheme

A three-level backward-difference scheme was adopted for the time derivative.

$$\left(\frac{\partial \omega_y}{\partial t}\right)^l = \frac{3\omega_y^l - 4\omega_y^{l-1} + \omega_y^{l-2}}{2\Delta t}, \tag{2.16}$$

where the time at the lth time-step, t^l, is given by $t^l = l\Delta t$ and $\omega_y^l = \omega_y(t = l\Delta t)$. Three-level schemes are renowned for their stability, which is often more important than the extra memory that such a scheme needs in comparison with two-level schemes. This particular scheme has an error of the order $(\Delta t)^2$. Convective terms and the viscous term involving the second streamwise derivative are treated explicitly with a predictor-corrector scheme. If all such terms are represented by M, then, the value of M at the predictor stage is calculated by

$$2M^{l-1} - M^{l-2} \qquad \text{or} \qquad 2M(\omega_y^{l-1}, w^{l-1}) - M(\omega_y^{l-2}, w^{l-2}). \tag{2.17}$$

From the vorticity transport equation (2.4a) the predictor stage calculates ω_y^{lp}. This value is then fed into the Poisson equation (2.4b) which is solved directly for w^l. These values are then used in a corrector stage to recalculate the vorticity:

$$M^{lp} \qquad \text{or} \qquad M(\omega_y^{lp}, w^l).$$

The viscous term, which involves a second derivative in the wall-normal direction is treated implicitly. This is to avoid a restrictive limit on the time-step that would occur if

this term were treated explicitly.[2]

To combine the explicit and implicit terms, we first write the vorticity transport equation as

$$\frac{\partial \omega_y}{\partial t} + N = \frac{1}{R}\left(\frac{\partial^2 \omega_y}{\partial x^2} + \frac{\partial^2 \omega_y}{\partial z^2}\right) , \tag{2.18}$$

where N represents the convective terms. Applying the numerical scheme outlined above,

[2]To illustrate this, albeit heuristically, we shall compare the two viscous terms and their discretizations. First consider the streamwise derivative

$$\frac{\partial \omega}{\partial t} \sim \frac{1}{R}\frac{\partial^2 \omega}{\partial x^2} .$$

In general, with finite difference schemes in x and t, we expect that for stability, the time-step, Δt be less than $\mathcal{O}(R\ (\Delta x)^2)$. As $R \sim \mathcal{O}(1000)$ this can easily be satisfied without requiring an overly small value for Δt. Say $\Delta x = 0.5$, then the restriction on the time-step is $\Delta t < R\ (\Delta x)^2 \sim 250$. Consider the other viscous term,

$$\frac{\partial \omega}{\partial t} \sim \frac{1}{R}\frac{\partial^2 \omega}{\partial z^2} .$$

In the wall-normal direction we have unequal step lengths. In terms of the mapped variable, the effective step lengths are given by

$$\zeta_k - \zeta_{k+1} = \cos\left(\frac{\pi(k-1)}{2N_k}\right) - \cos\left(\frac{\pi k}{2N_k}\right) , \quad \text{for} \quad k = 1, 2, \ldots, N_k - 1 .$$

The smallest step-length will be given by $\zeta_1 - \zeta_2$:

$$\zeta_1 - \zeta_2 \;=\; 1 - \cos\left(\frac{\pi}{2N_k}\right) \;\approx\; \frac{1}{2}\left(\frac{\pi}{2N_k}\right)^2 \sim \mathcal{O}\left(\frac{1}{N_k}\right)^2 .$$

In terms of z this is

$$z_1 - z_2 \;=\; l\left(\frac{1}{\zeta_1} - \frac{1}{\zeta_2}\right) \;=\; l\left(\frac{\zeta_2 - \zeta_1}{\zeta_1\,\zeta_2}\right) \;\sim\; \mathcal{O}\left(\frac{1}{N_k}\right)^2 .$$

If, somewhat naïvely, we apply the result for finite difference schemes, that the time step (Δt) be less than $\mathcal{O}(R\ (\Delta z)^2)$, then

$$\Delta t < R(\Delta z)^2 \;\sim\; \mathcal{O}\left(\frac{R}{N_k^4}\right)$$

For typical values of $R \sim 1000$ and $N_k^2 \sim 1000$ this requires a time-step $\Delta t < \mathcal{O}\left(10^{-3}\right)$! This heuristic argument suggests that it will be necessary to treat the viscous term implicitly in order to avoid excessively small time-steps. A more rigorous method to demonstrate that the viscous second derivative term in z requires an implicit scheme, would involve calculating eigenvalues of the appropriate matrix operator due to the Chebyshev discretization rather than extrapolating typical results for finite difference schemes to Chebyshev spectral schemes.

we have for the predictor stage,

$$\left(\frac{3}{2\Delta t}-\frac{1}{R}\frac{\partial}{\partial z^2}\right)\omega_y^{lp}=2\left(\frac{1}{R}\frac{\partial^2\omega_y^{l-1}}{\partial x^2}-N^{l-1}+\frac{\omega_y^{l-1}}{\Delta t}\right) - \left(\frac{1}{R}\frac{\partial^2\omega_y^{l-2}}{\partial x^2}-N^{l-2}+\frac{\omega_y^{l-2}}{2\Delta t}\right) \tag{2.19}$$

This is solved for ω_y^{lp} by inverting what becomes a matrix on the left-hand side with the Thomas algorithm (see page 43). The Poisson equation is then solved directly for w^l:

$$\nabla^2 w^l=-\frac{\partial\omega_y^{lp}}{\partial x}\ . \tag{2.20}$$

This value of velocity alongside the predicted vorticity are then used to re-evaluate convective terms in a corrector stage:

$$\left(\frac{3}{2\Delta t}-\frac{1}{R}\frac{\partial^2}{\partial z^2}\right)\omega_y^{l}=\frac{1}{R}\frac{\partial^2\omega_y^{lp}}{\partial x^2}-N^{lp}+\frac{4\omega^{l-1}-\omega^{l-2}}{2\Delta t}\ . \tag{2.21}$$

2.2.1.2 The first time-step

With all three-level schemes, the initial condition (at $l=0$) alone cannot provide enough information to start the scheme. The solution at $l=1$ is determined by a Crank-Nicolson step. Then we have the solution at two time levels and can use this information with the scheme outlined above to determine the solution at the next time level. In general the Crank-Nicolson scheme takes the following form:

$$\frac{\partial\omega}{\partial t}=rhs \qquad \text{is approximated by} \qquad \frac{\omega^l-\omega^{l-1}}{\Delta t}=\frac{1}{2}\left(rhs^l+rhs^{l-1}\right)\ . \tag{2.22}$$

This scheme is accurate to second-order. Applying it to our case gives:

$$\left(\frac{1}{\Delta t}-\frac{1}{2R}\frac{\partial^2}{\partial z^2}\right)\omega^{1,i}=\frac{1}{2}\left(N^{1,i-1}+N^0\right)+\frac{1}{2R}\left(\frac{\partial^2\omega^{1,i-1}}{\partial x^2}+\frac{\partial^2\omega^0}{\partial x^2}\right)+\frac{1}{2R}\frac{\partial^2\omega^0}{\partial z^2}+\frac{\omega^0}{\Delta t}\ , \tag{2.23}$$

where i indicates an iteration loop. Here the initial condition provides the values at $l=0$. The these values are fed in the Poisson equation giving w^0. Then the values ω_y^0 and w^0 are

used in (2.23) to determine $\omega_y^{1,1}$. This first iteration step was typically carried out 5 times.

2.2.2 Streamwise discretization

The streamwise derivatives are discretized with compact difference schemes as described comprehensively by Lele (1990). Compact schemes have two advantages over the standard finite difference schemes:

- they have a smaller truncation error (for schemes involving the same number of grid-points in the stencil),
- they are better at preserving wave properties.

Souza et al. (2005) have shown that compact difference schemes are superior to finite difference schemes, especially in regard to their ability of preserving wave properties. For several numerical schemes, the ability to capture the evolution of small-amplitude Tollmien–Schlichting waves in a plane Poiseuille flow was tested.

Compact schemes take the following general forms:
first derivatives:

$$\begin{aligned}\gamma f'_{i+2} + \beta f'_{i+1} + f'_i + \beta f'_{i-1} + \gamma f'_{i-2} &= \frac{a}{2\Delta x}(f_{i+1} - f_{i-1}) + \frac{b}{4\Delta x}(f_{i+2} - f_{i-2}) \\ &\quad + \frac{c}{6\Delta x}(f_{i+3} - f_{i-3}) \,, \end{aligned} \tag{2.24}$$

and second derivatives:

$$\begin{aligned}\gamma f''_{i+2} + \beta f''_{i+1} + f''_i + \beta f''_{i-1} + \gamma f''_{i-2} &= \frac{a\,(f_{i+1} - 2f_i + f_{i-1})}{(\Delta x)^2} + \frac{b\,(f_{i+2} - 2f_i + f_{i-2})}{4(\Delta x)^2} \\ &\quad + \frac{c\,(f_{i+3} - 2f_i + f_{i-3})}{9(\Delta x)^2} \,. \end{aligned} \tag{2.25}$$

The streamwise step-length is represented by Δx. The choice of the constants β, γ, a, b and c will determine the truncation error. To illustrate the two afore-mentioned advantages we will consider some special cases. The scheme used in Davies' code for the first derivative

can be obtained from (2.24) by setting $\gamma = c = 0$, $\beta = \frac{1}{3}$, $a = \frac{14}{9}$ and $b = \frac{1}{9}$:

$$\frac{1}{3}f'_{i+1} + f'_i + \frac{1}{3}f'_{i-1} = \frac{14}{18\Delta x}(f_{i+1} - f_{i-1}) + \frac{1}{36\Delta x}(f_{i+2} - f_{i-2}) + \mathcal{O}(\Delta x)^6 \ . \tag{2.26}$$

We shall compare this with a standard sixth-order finite difference scheme, a fourth-order compact difference scheme, a fourth-order finite difference scheme and a second-order finite difference scheme. All these schemes are described by substituting the values of a, b, c, β and γ, given in the table below, into the general formula (2.24).

	a	b	c	β	γ
second-order finite difference (fd_2)	1	0	0	0	0
fourth-order finite difference (fd_4)	4/3	-1/3	0	0	0
fourth-order compact difference (cd_4)	3/2	0	0	1/4	0
sixth-order finite difference (fd_6)	3/2	-3/5	1/10	0	0
sixth-order compact difference (cd_6)	14/9	1/9	0	1/3	0

Table 2.1: Coefficients for various finite and compact difference schemes

Notice that for a finite difference method to have the same order of truncation error as a compact difference scheme, a larger number of grid points are required. For example, the sixth-order finite difference scheme uses function values at the gridpoints $i \pm 1$, $i \pm 2$ and $i \pm 3$, whereas the sixth-order compact difference scheme uses function values at the points $i \pm 1$ and $i \pm 2$. However, a disadvantage of compact schemes is that a matrix system has to be solved.

Following Lele's approach (1990), in order to analyse the resolution characteristics of numerical schemes we study the effect a scheme has on a wave mode. Consider a wave of the form $f(x) = \hat{f}_k \exp(i\alpha_k x)$ where $\alpha_k = \frac{2\pi k}{N\Delta x}$ and $x = m\Delta x$. This represents N wave modes with wavenumber $\{\alpha_k\}_{k=1}^{N}$ over a length $N\Delta x$. Substituting this f into the general compact difference scheme (2.24) we have

$$i\alpha_k f = i\left(\frac{\frac{a}{\Delta x}\sin(\alpha_k\Delta x) + \frac{b}{2\Delta x}\sin(2\alpha_k\Delta x) + \frac{c}{3\Delta x}\sin(3\alpha_k\Delta x)}{1 + 2\beta\cos(\alpha_k\Delta x) + 2\gamma\cos(\alpha_k\Delta x)}\right) f \ . \tag{2.27}$$

The expression in brackets represents the wavenumber that is generated by the numerical scheme and the exact wavenumber is α_k. For convenience we rescale the wavenumber, so that $\tilde{\alpha}_k = \alpha_k \Delta x$. We can write down the numerical wavenumber for a particular scheme by substituting in the values of a, b, c, β and γ into the general expression (2.27). For the second order finite difference scheme we have

$$\tilde{\alpha}_k^{fd_2} = \sin(\tilde{\alpha}_k) \ , \tag{2.28}$$

for the fourth-order finite difference scheme we have

$$\tilde{\alpha}_k^{fd_4} = \frac{1}{6}\left(8\sin(\tilde{\alpha}_k) - \sin(2\tilde{\alpha}_k)\right) \ , \tag{2.29}$$

for the fourth-order compact difference scheme we have

$$\tilde{\alpha}_k^{cd_4} = \frac{\frac{3}{2}\sin(\tilde{\alpha}_k)}{1 + \frac{1}{2}\cos(\tilde{\alpha}_k)} \ , \tag{2.30}$$

for the sixth-order finite difference scheme we have

$$\tilde{\alpha}_k^{fd_6} = \frac{1}{10}\left(15\sin(\tilde{\alpha}_k) - 3\sin(2\tilde{\alpha}_k) + \sin(3\tilde{\alpha}_k)\right) \ , \tag{2.31}$$

and finally, for the sixth-order compact scheme (shown in (2.26)) we have

$$\tilde{\alpha}_k^{cd_6} = \frac{\frac{14}{9}\sin(\tilde{\alpha}_k) + \frac{1}{18}\sin(2\tilde{\alpha}_k)}{1 + \frac{2}{3}\cos(\tilde{\alpha}_k)} \ . \tag{2.32}$$

The graph in figure 2.5 compares the rescaled wavenumber of the numerical schemes with the exact rescaled wavenumber. All the schemes are capable of resolving rescaled wavenumbers of up to $\pi/10$. This corresponds to the rule-of-thumb that for any finite difference scheme to accurately resolve a wave, there should be a minimum of about 20 points per wavelength.[3] As can be seen from figure 2.5, the higher-order schemes do better than this, requiring fewer than 20 points per wavelength to accurately representing the wave. The graph can be interpreted in two ways. If the step length, Δx is kept

[3]For 21 points per wavelength we have $\lambda_{min} = 20\Delta x$. This corresponds to a maximum wavenumber of $\alpha_{max} = 2\pi/(20\Delta x) = \pi/(10\Delta x)$ or $\tilde{\alpha}_{max} = \pi/10$.

constant, then moving along the x-axis in the positive direction corresponds to increasing the wavenumber. If the wavenumber is kept constant, then moving along the x-axis in the positive direction corresponds to an increasing step length.

The Tollmien–Schlichting waves that develop in a boundary layer have a typical wavenumber of $\alpha_{ts} = 0.2$ and therefore a typical rescaled wavenumber of $\alpha_{ts} = 0.1$ (for $\Delta x = 0.5$). All the schemes shown in figure 2.5 are capable of resolving wavenumbers of this order. However, the nonlinear interactions which occur in boundary layers excite higher harmonics of the Tollmien–Schlichting wave, such as $2\alpha_{ts}$, $3\alpha_{ts}$, $4\alpha_{ts}$, and so on. Not all the schemes will be able to resolve these harmonics. Figure 2.5 demonstrates that the compact difference schemes can resolve larger wavenumbers than finite difference schemes (with the same order truncation error).

For the second derivatives, the code implements the scheme derived from (2.25) by setting $b = c = \gamma = 0$, $\beta = 0.1$ and $a = 1.2$:

$$\frac{1}{12}(f''(x_{i+1}) + f''(x_{i-1})) + \frac{10}{12}f''(x_i) = \frac{(f_{i+1} - 2f_i + f_{i-1})}{(\Delta x)^2} + \mathcal{O}(\Delta x)^4 \,. \tag{2.33}$$

Again we shall compare this scheme with the fourth- and second-order finite difference schemes given below.

$$f''(x_i) = \frac{4(f_{i+1} - 2f_i + f_{i-1})}{3(\Delta x)^2} - \frac{f_{i+1} - 2f_i + f_{i-1}}{12(\Delta x)^2} + \mathcal{O}(\Delta x)^4 \,, \tag{2.34}$$

$$f''(x_i) = \frac{f_{i+1} - 2f_i + f_{i-1}}{(\Delta x)^2} + \mathcal{O}(\Delta x)^2 \,. \tag{2.35}$$

The coefficients used to derive these schemes are shown in table 2.2.

	a	b	c	β	γ
second-order finite difference (fd_2)	1	0	0	0	0
fourth-order finite difference (fd_4)	4/3	-1/3	0	0	0
fourth-order compact difference (cd_4)	6/5	0	0	1/10	0

Table 2.2: Coefficients for various finite and compact difference schemes for calculating the second derivative.

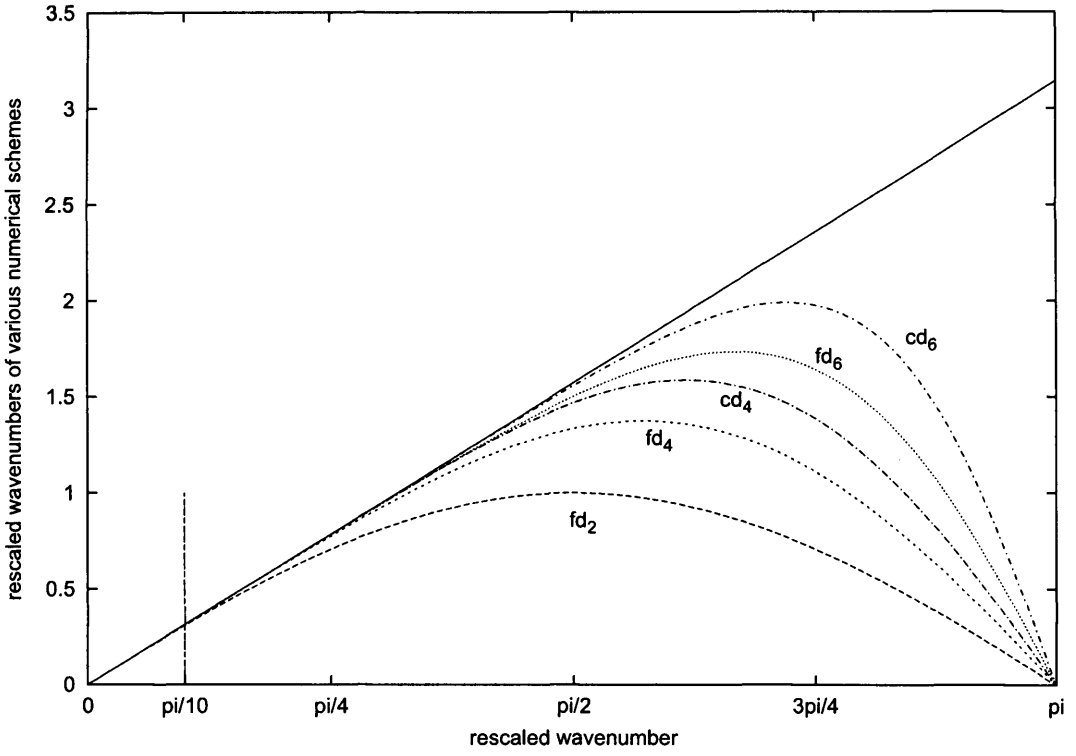

Figure 2.5: Rescaled wavenumbers of the numerical schemes (the coefficients of which are given in table 2.1) for calculating the first derivative, against $\widetilde{\alpha}_k = \frac{2\pi k}{N}$. The value $\frac{\pi}{10}$ corresponds to the maximum scaled wavenumber according to the rule-of-thumb, that finite difference schemes require about 20 points per wavelength to resolve a wave accurately.

For the second derivative schemes we can also calculate the general form of the square of the numerical wavenumber

$$\widetilde{\alpha}_k^2 = \frac{2a(1-\cos(\widetilde{\alpha}_k)) + \frac{b}{2}(1-\cos(2\widetilde{\alpha}_k)) + \frac{2c}{9}(1-\cos(3\widetilde{\alpha}_k))}{1 + 2\alpha\cos(\widetilde{\alpha}_k) + 2\beta\cos(\widetilde{\alpha}_k)} \tag{2.36}$$

The second-order finite difference scheme has a square wavenumber of

$$(\widetilde{\alpha}_k^{fd})^2 = 2(1-\cos(\widetilde{\alpha}_k)) \ , \tag{2.37}$$

the fourth-order finite difference scheme has a square wavenumber of

$$(\widetilde{\alpha}_k^{cd})^2 = \frac{8}{3}(1 - \cos(\widetilde{\alpha}_k)) - \frac{1}{6}(1 - \cos(2\widetilde{\alpha}_k)) \ , \tag{2.38}$$

and the fourth-order compact scheme has a square wavenumber of

$$(\widetilde{\alpha}_k^{cd})^2 = \frac{2.4(1 - \cos(\widetilde{\alpha}_k))}{1 + 0.2\cos(\widetilde{\alpha}_k)} \ . \tag{2.39}$$

These re-scaled wavenumbers are compared in the graph shown in figure 2.6. Again it is clear that the compact scheme resolves a larger range of wavenumbers than the other schemes, although the difference between compact and standard finite difference schemes is less marked than in the case of the first derivative.

As nonlinearities become significant the waves which develop have larger and larger wavenumbers. It is clear that the compact difference schemes will cope better with such nonlinearities than the 'standard' finite difference schemes.

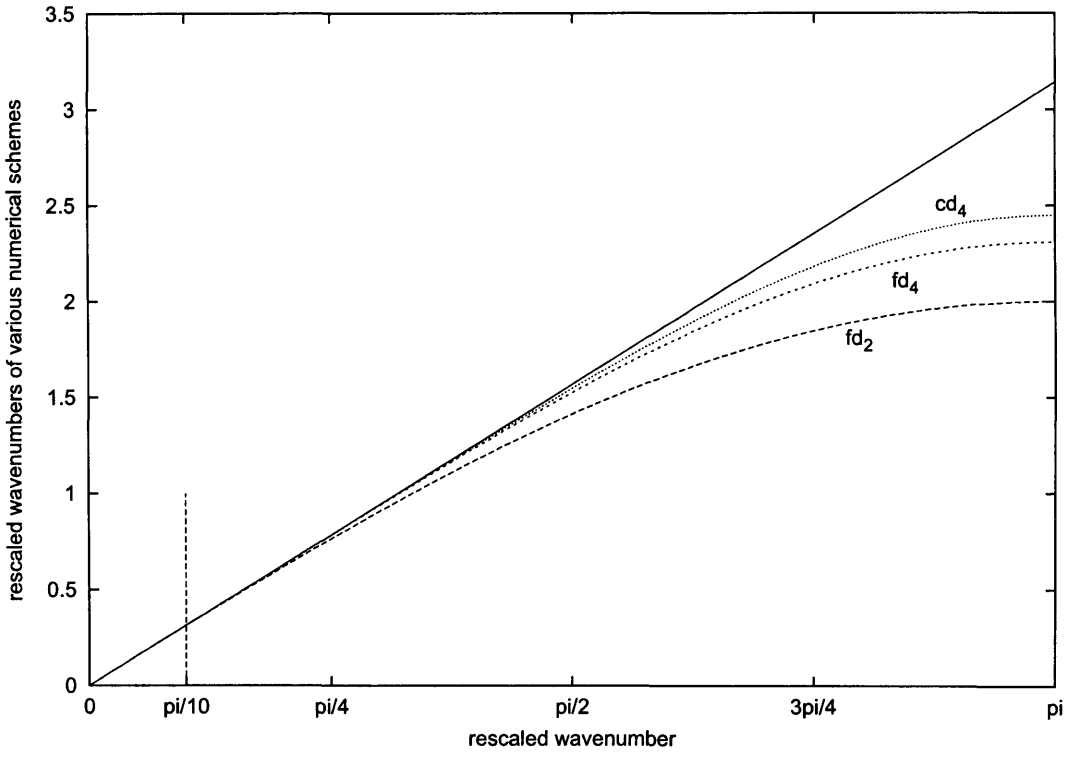

Figure 2.6: Rescaled wavenumbers of three numerical schemes (the coefficients of which are given in table 2.2) for calculating the second derivative, against $\widetilde{\alpha}_k = \frac{2\pi k}{N}$. The value $\frac{\pi}{10}$ corresponds to the maximum scaled wavenumber according to the rule-of-thumb, that finite difference schemes require about 20 points per wavelength to resolve a wave accurately.

Boundary Schemes The sixth-order scheme set out in (2.26) is used for the inner points. Near the boundaries, however, slight adjustments must be made. Lele (1990) gives the general form these can take. In Davies' code, for the first derivative, the 1st and Nth points have 3rd order schemes and their neighbours have 5th order schemes:

$$f'_1 + 2f'_2 = \frac{1}{\Delta x}\left(\frac{-5}{2}f_1 + 2f_2 + \frac{1}{2}f_3\right), \tag{2.40a}$$

$$\frac{1}{3}f'_1 + f'_2 + \frac{1}{3}f'_3 = \frac{1}{\Delta x}\left(\frac{-5}{9}f_1 - \frac{1}{2}f_2 + f_3 + \frac{1}{18}f_4\right), \tag{2.40b}$$

$$\frac{1}{3}f'_{N-2} + f'_{N-1} + \frac{1}{3}f'_{N-1} = \frac{1}{\Delta x}\left(\frac{1}{18}f_{N-3} + f_{N-2} - \frac{1}{2}f_{N-1} - \frac{5}{9}f_N\right), \tag{2.40c}$$

$$2f'_{N-1} + f'_N = \frac{1}{\Delta x}\left(\frac{1}{2}f_{N-2} + 2f_{N-1} - \frac{5}{2}f_N\right). \tag{2.40d}$$

The first derivative f'_i of a set of values f_i is calculated from:

$$\begin{bmatrix} 1 & 2 & 0 & 0 & 0 & \dots & \\ \frac{1}{3} & 1 & \frac{1}{3} & 0 & 0 & & \\ 0 & \frac{1}{3} & 1 & \frac{1}{3} & 0 & & \\ \vdots & & \ddots & \ddots & \ddots & & \\ & & & \frac{1}{3} & 1 & \frac{1}{3} & 0 \\ & & & 0 & \frac{1}{3} & 1 & \frac{1}{3} \\ & & & 0 & 0 & 2 & 1 \end{bmatrix} \begin{bmatrix} f'_1 \\ f'_2 \\ \\ \vdots \\ \\ f'_{N-1} \\ f'_N \end{bmatrix} = \frac{1}{\Delta x} \begin{bmatrix} \frac{-5}{2} & 2 & \frac{1}{2} & 0 & 0 & 0 & \dots & \\ \frac{-5}{9} & \frac{-1}{2} & 1 & \frac{1}{18} & 0 & 0 & & \\ \frac{-1}{36} & \frac{-7}{9} & 0 & \frac{7}{9} & \frac{1}{36} & 0 & & \\ 0 & \frac{-1}{36} & \frac{-7}{9} & 0 & \frac{7}{9} & \frac{1}{36} & & \\ \vdots & & \ddots & \ddots & \ddots & \ddots & & \\ & & & \frac{-1}{36} & \frac{-7}{9} & 0 & \frac{7}{9} & \frac{1}{36} \\ & & & 0 & \frac{1}{18} & 1 & \frac{-1}{2} & \frac{-5}{9} \\ & & & 0 & 0 & \frac{1}{2} & 2 & \frac{-5}{2} \end{bmatrix} \begin{bmatrix} f_1 \\ f_2 \\ \\ \vdots \\ \\ f_{N-1} \\ f_N \end{bmatrix}$$

The Thomas Algorithm is used to solve this problem and find the values f'_i.

Similarly for the second derivative, the following boundary scheme is employed:

$$f''_1 + \frac{1}{10}f''_2 = \frac{1.2}{(\Delta x)^2}\left(\frac{65}{6}f_1 - \frac{145}{24}f_2 + \frac{25}{2}f_3 + \frac{5}{6}f_4\right), \tag{2.41}$$

$$\frac{1}{10}f''_{N-1} + f''_N = \frac{1.2}{(\Delta x)^2}\left(\frac{5}{6}f_{N-3} + \frac{25}{2}f_{N-2} - \frac{145}{24}f_{N-1}\frac{65}{6}f_N\right). \tag{2.42}$$

The following matrix problem is solved in order to calculate the second derivative, $\frac{\partial^2 f}{\partial x^2}\big|_{x_i}$

from a set of values f_i:

$$\begin{bmatrix} 1 & \frac{1}{10} & 0 & 0 & 0 & \dots & \\ \frac{1}{10} & 1 & \frac{1}{10} & 0 & 0 & & \\ 0 & \frac{1}{10} & 1 & \frac{1}{10} & 0 & & \\ \vdots & & \ddots & \ddots & \ddots & & \\ & & & \frac{1}{10} & 1 & \frac{1}{10} & 0 \\ & & & 0 & \frac{1}{10} & 1 & \frac{1}{10} \\ & & & 0 & 0 & \frac{1}{10} & 1 \end{bmatrix} \begin{bmatrix} f_1'' \\ f_2'' \\ \\ \vdots \\ \\ f_{N-1}'' \\ f_N'' \end{bmatrix} = \frac{1.2}{(\Delta x)^2} \begin{bmatrix} \frac{65}{6} & \frac{-145}{24} & \frac{25}{2} & \frac{10}{12} & 0 & \dots & \\ 1 & -2 & 1 & 0 & 0 & & \\ 0 & 1 & -2 & 1 & 0 & & \\ \vdots & & \ddots & \ddots & \ddots & \ddots & \\ & & 0 & 1 & -2 & 1 & 0 \\ & & 0 & 0 & 1 & -2 & 1 \\ & & 0 & \frac{10}{12} & \frac{25}{2} & \frac{-145}{24} & \frac{65}{6} \end{bmatrix} \begin{bmatrix} f_1 \\ f_2 \\ \\ \vdots \\ \\ f_{N-1} \\ f_N \end{bmatrix}.$$

2.2.3 Wall normal discretization

2.2.3.1 Properties of Chebyshev polynomials

The Chebyshev polynomials may be defined as follows. The kth Chebyshev polynomial is given by

$$T_k(\cos\theta) = \cos(k\theta). \tag{2.43}$$

They can also be written explicitly as polynomials by making the substitution $x = \cos\theta$. In this form, the Chebyshev polynomials satisfy the following recurrence relation

$$T_{k+1}(x) = 2xT_k(x) - T_{k-1}(x) \qquad \text{for } k \geqslant 1\,, \text{ with } T_0\,,\ T_1 \text{ given.}$$

Therefore the first few Chebyshev polynomials are given by

$$\begin{aligned} T_0(x) &= 1 \\ T_1(x) &= x \\ T_2(x) &= 2x^2 - 1 \\ T_3(x) &= 4x^3 - 3x \\ T_4(x) &= 8x^4 - 8x^2 + 1 \\ T_5(x) &= 16x^5 - 20x^3 + 5x\ . \end{aligned}$$

These polynomials have many useful properties. Some of these, pertinent to this thesis, are laid out below.

- they are orthogonal polynomials with respect to the weighting $\sqrt{1-x^2}$:

$$\int_{-1}^{1} \frac{T_m T_n}{\sqrt{1-x^2}}\, dx = \begin{cases} 0 & m \neq n \\ \frac{\pi}{2} & m = n \neq 0 \\ \pi & m = n = 0 \end{cases}$$

- they satisfy $T_k(\pm 1) = (\pm 1)^k$
- they satisfy

$$x^2 T_k = \frac{1}{4}\left(T_{k+2} + 2T_k + T_{k-2}\right) \qquad \text{for } k > 1$$

- $$\int^{x} T_k(y)\, dy = \frac{T_{k+1}(x)}{2(k+1)} - \frac{T_{k-1}(x)}{2(k-1)} \qquad \text{for } k > 1$$

- the extrema of the Nth-order Chebyshev polynomial occur at the points x_k,

$$x_k = \cos\left(\frac{k\pi}{N}\right) \qquad \text{for } k = 0, \ldots, N$$

and are also referred to as the Gauss-Lobatto points or the Chebyshev points.

2.2.3.2 Cheybshev representation of variables

The solution varies extremely rapidly in the wall-normal direction, so a spectral Chebyshev scheme is used as such schemes are renowned for their accuracy. See the general texts by Canuto et al. (1988) or Peyret (2002) for further information. The primary variables ω_y and w are represented by an expansion of odd Chebyshev polynomials, since the semi-infinite domain maps onto half of the usual Chebyshev interval:

$$z\,[0, \infty) \longrightarrow \zeta\,[1, 0)\ , \tag{2.44}$$

where the mapping is given in (2.6). The expansion for the primary variable ω_y, is

$$\omega_y(\zeta) = \sum_{k=1}^{N} \hat{\omega}_k T_{2k-1}(\zeta)\ . \tag{2.45}$$

The collocation points for the wall normal direction are taken from the extrema of the highest-order Chebyshev polynomial. This choice converts the summation in (2.45) into a Fourier cosine transform, which has the advantage of ensuring exponential decay of the coefficients (for large enough N), and also means that fast Fourier transform methods allow efficient transform between the Chebyshev coefficients $\{\hat{\omega}_k\}_{k=1}^N$ and the collocation values $\{\omega_y(\zeta_j)\}_{j=1}^N$. Furthermore, the collocation points are closest together at the wall and furthest apart a long way from the wall. This is opportune as, in boundary layers, the flow changes most close to the wall, and changes least a long way from the wall. The collocation points are given by

$$\zeta_j = \cos\left(\frac{(j-1)\pi}{2N}\right) \qquad \text{for} \quad k = 1, \ldots, N \; . \tag{2.46}$$

These points make up half of the extrema points. As we expand with just the odd Chebyshev polynomials we have half of the unknowns that we would have were we using a full Chebyshev expansion which means that we need only half the number of collocation points. Our primary variables are expanded as follows

$$\omega_y(\zeta_j) = \sum_{k=1}^{N} \hat{\omega}_k \, T_{2k-1}(\zeta_j) \tag{2.47}$$

$$= \sum_{k=1}^{N} \hat{\omega}_k \cos\left(\frac{(2k-1)(j-1)\pi}{2N}\right) , \tag{2.48}$$

and

$$w(\zeta_j) = \sum_{k=1}^{N} \hat{w}_k \cos\left(\frac{(2k-1)(j-1)\pi}{2N}\right) . \tag{2.49}$$

The secondary variable is represented by an even expansion

$$u(\zeta_j) = \sum_{k=1}^{N} \hat{u}_k \, \left(T_{2k}(\zeta_j) - T_{2k}(0)\right) \; . \tag{2.50}$$

Including the constant term $\sum_{k=1}^{N} -\hat{u}_k T_{2k}(0)$ ensures that for $\zeta = 0$ (infinitely far above the plate) the streamwise perturbation velocity is zero.

2.2.3.3 Wall-normal spectral scheme

A Tau method (to be described shortly) is used in this particular formulation, therefore the code solves for the Chebyshev coefficients of the above expansions, that is $\hat{\omega}_k$ and $\hat{w}_k$. (A collocation method would solve for the values of the variables ω_y and w at the collocation points ζ_j.) The numerical method is called pseudo-spectral, however, because terms involving products of variables are calculated not in terms of Chebyshev coefficients but in terms of the collocation values, as this is more efficient and can be implemented to avoid aliasing problems. So, to evaluate a product, the variables are temporarily transformed back to physical space where the product is evaluated. The result is then transformed back to Chebyshev space. These transformations are carried out efficiently using Fast Fourier Transforms from the Numerical Library of the Numerical Algorithms Group, Oxford (known as the NAG library, see www.nag.co.uk for further details). For example, to evaluate the product of w and $\partial\omega_y/\partial z$ which occurs in the N_x term,

- evaluate $w(\zeta_j)$ from the coefficients $\hat{w}_k$ by means of a Fast Fourier transform (FFT),
- similarly evaluate $\frac{\partial\omega}{\partial z}(\zeta_j)$ from $\frac{\partial\hat{\omega}_k}{\partial z}$ with an FFT,
- evaluate the product $p(\zeta_j) = \frac{\partial\omega}{\partial z}(\zeta_j)w(\zeta_j)$ for $j = 1, \ldots, N$ (requires N multiplications),
- transform back to Chebyshev space by finding $\hat{p}_k$ from $p(\zeta_j)$,

Having indicated how the product terms are evaluated we now proceed to show how the formulation's wall-normal discretization works in general.

The governing equations (2.3) are integrated twice with respect to the mapped variable ζ; hence the differential operators involving wall-normal derivatives become integral operators (step 1). These operators act on Chebyshev series in an expeditious manner (step 2) because the result can be represented by at most pentadiagonal matrices (step 3). The matrices can then be inverted using a modified form of the highly-efficient Thomas algorithm (step 4). These four steps are illustrated below.

Step 1 Integrating the two-dimensional system of governing equations twice with respect to ζ we have

$$\iint \left(\frac{\partial \omega_y}{\partial t} + \frac{\partial N_x}{\partial z} - \frac{\partial N_z}{\partial x} \right) d\zeta d\zeta = \frac{1}{R} \iint \nabla^2 \omega_y \, d\zeta d\zeta \,, \tag{2.51a}$$

$$\iint \nabla^2 w \, d\zeta d\zeta = - \iint \frac{\partial \omega_y}{\partial x} \, d\zeta d\zeta \,. \tag{2.51b}$$

Express the z derivatives in terms of ζ:

$$\iint \left(\frac{\partial \omega_y}{\partial t} - \frac{\partial N_z}{\partial x} \right) d\zeta d\zeta - \iint \frac{\zeta^2}{l} \frac{\partial N_x}{\partial \zeta} \, d\zeta d\zeta = \frac{1}{R} \iint \left(\frac{\partial^2 \omega_y}{\partial x^2} + \frac{2\zeta^3}{l^2} \frac{\partial \omega_y}{\partial \zeta} + \frac{\zeta^4}{l^2} \frac{\partial^2 \omega_y}{\partial \zeta^2} \right) d\zeta d\zeta \,,$$

$$\iint \left(\frac{\partial^2 w}{\partial x^2} + \frac{2\zeta^3}{l^2} \frac{\partial w}{\partial \zeta} + \frac{\zeta^4}{l^2} \frac{\partial^2 w}{\partial \zeta^2} \right) d\zeta d\zeta = - \iint \frac{\partial \omega_y}{\partial x} \, d\zeta d\zeta \,.$$

Terms involving products of ζ and derivatives with respect to ζ can by simplified by integrating by parts:

$$\iint \zeta^2 \frac{\partial N_x}{\partial \zeta} \, d\zeta d\zeta = \int \zeta^2 N_x \, d\zeta - 2 \iint \zeta N_x \, d\zeta d\zeta \,,$$

$$\iint \zeta^3 \frac{\partial \omega_y}{\partial \zeta} \, d\zeta d\zeta = \int \zeta^3 \omega_y \, d\zeta - 3 \iint \zeta^2 \omega_y \, d\zeta d\zeta \,,$$

$$\iint \zeta^4 \frac{\partial^2 \omega_y}{\partial \zeta^2} \, d\zeta d\zeta = \zeta^4 \omega_y - 8 \int \zeta^3 \omega_y \, d\zeta + 12 \iint \zeta^2 \omega_y \, d\zeta d\zeta \,.$$

Substituting this into the governing equations gives

$$\iint \left(\frac{\partial \omega_y}{\partial t} - \frac{\partial N_z}{\partial x} \right) d\zeta d\zeta - \int \frac{\zeta^2}{l} N_x \, d\zeta + \frac{2}{l} \iint \zeta N_x \, d\zeta d\zeta$$
$$= \frac{1}{R} \left(\iint \frac{\partial^2 \omega_y}{\partial x^2} \, d\zeta d\zeta + \frac{\zeta^4 \omega_y}{l^2} - \frac{6}{l^2} \int \zeta^3 \omega_y \, d\zeta + \frac{6}{l^2} \iint \zeta^2 \omega_y \, d\zeta d\zeta \right) \,,$$

$$\iint \frac{\partial^2 w}{\partial x^2} \, d\zeta d\zeta + \frac{\zeta^4 \omega_y}{l^2} - \frac{6}{l^2} \int \zeta^3 \omega_y \, d\zeta + \frac{6}{l^2} \iint \zeta^2 \omega_y \, d\zeta d\zeta = - \iint \frac{\partial \omega_y}{\partial x} \, d\zeta d\zeta \,.$$

If we define the following integral operators

$$\begin{aligned}
\mathbf{I}[f] &:= \iint f \, d\zeta d\zeta \,, \\
\mathbf{J}[f] &:= \int \zeta^2 f \, d\zeta - 2 \iint \zeta f \, d\zeta d\zeta \,, \\
\mathbf{K}[f] &:= \zeta^4 f - 6 \int \zeta^3 f \, d\zeta + 6 \iint \zeta^2 f \, d\zeta d\zeta \,,
\end{aligned}$$

then the integral form of the governing equations in (2.51) can be written more compactly as

$$\mathbf{I}\left[\frac{\partial \omega_y}{\partial t} - \frac{\partial N_z}{\partial x}\right] - \frac{\mathbf{J}[N_x]}{l} = \mathbf{I}\left[\frac{1}{R}\frac{\partial^2 \omega_y}{\partial x^2}\right] + \frac{\mathbf{K}[\omega_y]}{R l^2} \,, \tag{2.52a}$$

$$\mathbf{I}\left[\frac{\partial^2 w}{\partial x^2}\right] + \frac{\mathbf{K}[w]}{l^2} = \mathbf{I}\left[-\frac{\partial \omega_y}{\partial x}\right] \,. \tag{2.52b}$$

Step 2 We will show how these integral operators act on Chebyshev polynomials. To calculate the effect of the operator $\mathbf{I}$ on a function f which is expanded as a series of odd Chebyshev polynomials we have

$$\mathbf{I}[f(\zeta)] = \int^{\zeta}\int^{\zeta} \sum_{k=1}^{\infty} \hat{f}_k T_{2k-1}(\zeta) d\zeta d\zeta \,. \tag{2.53}$$

As the integrand converges we can swap the order of summation and integration, leaving a double integral of Chebyshev polynomials.

$$\mathbf{I}[f(\zeta)] = \sum_{k=1}^{\infty} \hat{f}_k \int^{\zeta}\int^{\zeta} T_{2k-1}(\zeta) d\zeta d\zeta \,. \tag{2.54}$$

This can be calculated by applying the general formula twice given earlier in section 2.2.3.1 (page 35):

$$\begin{aligned}
\mathbf{I}[f(\zeta)] &= \int^{\zeta} a\hat{f}_1 T_0(\zeta) d\zeta + \sum_{k=2}^{\infty} \hat{f}_k \int^{\zeta} \left(\frac{T_{2k}(\zeta)}{4k} - \frac{T_{2(k-1)}(\zeta)}{4(k-1)}\right) d\zeta \\
&= a\hat{f}_1 T_1(\zeta) + b\hat{f}_1 T_0(\zeta) + \sum_{k=2}^{\infty} \left(\frac{T_{2k+1}(\zeta)}{8k(2k+1)} - \frac{T_{2k-1}(\zeta)}{8k(k-1)} + \frac{T_{2k-3}(\zeta)}{8(k-1)(2k-3)}\right) \hat{f}_k \,.
\end{aligned}$$

This can be re-arranged and truncated to give

$$\mathbf{I}[f(\zeta)] = b\hat{f}_1 T_0(\zeta) + a\hat{f}_1 T_1(\zeta) + \sum_{k=2}^{N} \frac{1}{8}\left(\frac{\hat{f}_{k-1}}{(2k-1)(k-1)} - \frac{\hat{f}_k}{k(k-1)} + \frac{\hat{f}_{k+1}}{k(2k-1)}\right) T_{2k-1}(\zeta)\,. \tag{2.55}$$

Similar calculations show that

$$\begin{aligned}\mathbf{J}[f(\zeta)] = \sum_{k=2}^{N} \frac{T_{2k-1}(\zeta)}{8(2k-1)}\left(\frac{(k-2)}{(k-1)}\hat{f}_{k-2} + \frac{(k+1)}{k}\hat{f}_{k-1} - \frac{(k-2)}{(k-1)}\hat{f}_k - \frac{(k+1)}{k}\hat{f}_{k+1}\right) \\ + b\hat{f}_1 T_0(\zeta) + a\hat{f}_1 T_1(\zeta)\,,\end{aligned} \tag{2.56}$$

$$\begin{aligned}\mathbf{K}[f(\zeta)] = b\hat{f}_1 T_0(\zeta) + a\hat{f}_1 T_1(\zeta) + \sum_{k=2}^{N}\Bigg(&\left[\frac{1}{16} - \frac{3}{8(2k-1)} + \frac{3}{16(k-1)(2k-1)}\right]\hat{f}_{k-2} \\ &+ \left[\frac{1}{4} - \frac{3}{4(2k-1)} + \frac{3}{16k(k-1)(2k-1)}\right]\hat{f}_{k-1} + \left[\frac{1}{16} - \frac{3}{16k(k-1)}\right]\hat{f}_k \\ &+ \left[\frac{1}{4} + \frac{3}{4(2k-1)} - \frac{3}{16k(k-1)(2k-1)}\right]\hat{f}_{k+1} \\ &+ \left[\frac{1}{16} + \frac{3}{8(2k-1)} + \frac{3}{16k(2k-1)}\right]\hat{f}_{k+2}\Bigg) T_{2k-1}(\zeta)\,.\end{aligned} \tag{2.57}$$

Step 3 Combining the time discretization (2.16) at the predictor stage (2.17) with the vorticity transport equation (2.52a), we get

$$\begin{aligned}\left[\frac{3}{2\Delta t}\mathbf{I} - \frac{1}{Rl^2}\mathbf{K}\right]\omega_y^{lp} = 2\Bigg[&\mathbf{I}\frac{\partial N_z}{\partial x} + \frac{\mathbf{J}N_x}{l} + \frac{\omega_y}{\Delta t} + \frac{1}{R}\mathbf{I}\frac{\partial^2 \omega_y}{\partial x^2}\Bigg]^{l-1} \\ &- \Bigg[\mathbf{I}\frac{\partial N_z}{\partial x} + \frac{\mathbf{J}N_x}{l} + \frac{\omega_y}{2\Delta t} + \frac{1}{R}\mathbf{I}\frac{\partial^2 \omega_y}{\partial x^2}\Bigg]^{l-2}\,.\end{aligned} \tag{2.58}$$

On the left-hand side of (2.58) the integral operators $\mathbf{I}$ and $\mathbf{K}$ will act on ω_y in the manner described by (2.55), (2.56) and (2.57). Their actions combine to give a pentadiagonal matrix acting on the Chebyshev coefficients of ω_y. The value of vorticity calculated by the

predictor step, ω_y^{lp}, is used to calculate the normal velocity with

$$\left[\mathbf{I}\frac{\partial^2}{\partial x^2} + \frac{\mathbf{K}}{l^2}\right] w^l = \mathbf{I}\left[-\frac{\partial \omega_y^{lp}}{\partial x}\right] . \tag{2.59}$$

With the exception of the first rows, the left-hand sides of both (2.58) and (2.59) form pentadiagonal matrices and can be written as

$$\begin{bmatrix} \cdot & \cdot & \cdot & \cdot & \cdot & \cdot & \cdot & \cdot \\ b_2 & c_2 & d_2 & e_2 & & & & \\ a_3 & b_3 & c_3 & d_3 & e_3 & & & \\ & \ddots & & \ddots & & \ddots & & \\ & & & a_{N-2} & b_{N-2} & c_{N-2} & d_{N-2} & d_{N-2} \\ & & & & a_{N-1} & b_{N-1} & c_{N-1} & d_{N-1} \\ & & & & & a_N & b_N & c_N \end{bmatrix} \begin{bmatrix} \hat{\omega}_1^l \\ \hat{\omega}_2^l \\ \hat{\omega}_3^l \\ \vdots \\ \hat{\omega}_{N-2}^l \\ \hat{\omega}_{N-1}^l \\ \hat{\omega}_N^l \end{bmatrix} .$$

For the vorticity transport equation, (2.58), the matrix elements are given by

$$\begin{aligned}
a_k &= \frac{-1}{Rl^2}\left(\frac{1}{16} - \frac{3}{8(2k-1)} + \frac{3}{16(k-1)(2k-1)}\right) \\
b_k &= \frac{3}{16\Delta t(2k-1)(k-1)} - \frac{1}{Rl^2}\left(\frac{1}{4} - \frac{3}{4(2k-1)} + \frac{3}{16k(k-1)(2k-1)}\right) \\
c_k &= \frac{-3}{16\Delta t(k-1)k} - \frac{1}{Rl^2}\left(\frac{1}{16} - \frac{3}{16k(k-1)}\right) \\
d_k &= \frac{3}{16\Delta t(2k-1)k} - \frac{1}{Rl^2}\left(\frac{1}{4} + \frac{3}{4(2k-1)} - \frac{3}{16k(k-1)(2k-1)}\right) \\
e_k &= \frac{-1}{Rl^2}\left(\frac{1}{16} + \frac{3}{8(2k-1)} + \frac{3}{16k(2k-1)}\right) .
\end{aligned}$$

In this case the matrix elements depend on the Reynolds number and the time step. The elements of the matrix operating on the normal velocity w depend on the streamwise step length. These quantities are fixed, and so once the matrix elements have been calculated they are stored and used when required.

The Chebyshev series for both primary variables are substituted into the integrated governing equations. Matching the coefficients of T_{2k-1} for $k = 2, N$ yields a system of $2(N-1)$ partial differential equations for the $2N$ unknowns. The coefficient of T_0 is discarded as the primary variables have been taken to be odd functions. The coefficients of T_1 are not solved for. Instead these are replaced by the integral constraint when solving for the vorticity (see (2.10) on page 18), or by the boundary condition on the wall when solving for the wall-normal velocity (see (2.11) on page 19). This gives a total of $2N$ equations for the $2N$ unknowns. There are some higher-order coefficients in the sum above which, according to the Tau method, are not matched. They give an estimate of the truncation error.

Step 4 The Thomas Algorithm is an efficient method for inverting tridiagonal matrices. The method consists of a 'forward' sweep (which eliminates the a_i elements and normalizes the b_i elements, see (2.60)) and a 'backward' sweep (which eliminates the c_i elements), leaving the identity matrix on the left. When inverting an $N \times N$ matrix it makes only $5N - 4$ operations. For this algorithm to work the matrix must be strictly diagonally dominant (that is $|b_i| > |a_i| + |c_i|$), however it is recognised that the algorithm is much more robust than this in practice (Press et al., 1989, see pages 40-41). The Thomas Algorithm can be easily extended to cope with pentadiagonal matrices, either by making four 'sweeps' instead of two, or by rewriting the pentadiagonal matrix as a block tridiagonal matrix, where each entry consists of a 2×2 submatrix. According to Fletcher (2003), for $M \times M$ submatrices the operation count is $\mathcal{O}(5NM^3/3)$, and for the other method (four 'sweeps'), $\mathcal{O}(5NM)$. Both are superior to full Gaussian elimination ($\mathcal{O}((NM)^3/3)$ operations). As $M = 2$ there is little difference between the efficiency of the methods. Fletcher (2003, pages 183-189) describes the Thomas algorithm for inverting tridiagonal and pentadiagonal matrices, but does not give describe the modification required when using tridiagonal block matrices. It is this particular method which is implemented in Davies' code. For our purposes, one further adaption of the Thomas Algorithm has to be made due to the fact that the top row of the matrix is a full row. Once again, the algorithm is easily adapted, by eliminating the elements on the top row one-by-one whilst performing the first sweep.

To illustrate how a matrix with a full first row is dealt with, the following tridiagonal matrix is used as an example.

$$\begin{pmatrix} d_1 & d_2 & d_3 & d_4 & \dots & d_N \\ a_2 & b_2 & c_2 & & & \\ & a_3 & b_3 & c_3 & & \\ & & \ddots & & \ddots & \\ & & & a_{N-1} & b_{N-1} & c_{N-1} \\ & & & & a_N & b_N \end{pmatrix} \begin{pmatrix} \hat{\omega}_1 \\ \hat{\omega}_2 \\ \hat{\omega}_3 \\ \vdots \\ \hat{\omega}_{N-1} \\ \hat{\omega}_N \end{pmatrix} = \begin{pmatrix} r_1 \\ r_2 \\ r_3 \\ \vdots \\ r_{N-1} \\ r_N \end{pmatrix} \tag{2.60}$$

A backward sweep is carried out first: using the Nth equation, the dependence on ω_N is eliminated from the $(N-1)$th equation and the 1st equation. The modified $(N-1)$th equation is used to remove the dependence on ω_{N-1} from the $(N-2)$th equation and the first equation, etc. This results in a matrix of the following form:

$$\begin{pmatrix} \widetilde{d}_1 & & & & & \\ a_2 & \beta_2 & & & & \\ & a_3 & \beta_3 & & & \\ & & \ddots & \ddots & & \\ & & & a_{N-1} & \beta_{N-1} & \\ & & & & a_N & \beta_N \end{pmatrix} \begin{pmatrix} \hat{\omega}_1 \\ \hat{\omega}_2 \\ \hat{\omega}_3 \\ \vdots \\ \hat{\omega}_{N-1} \\ \hat{\omega}_N \end{pmatrix} = \begin{pmatrix} s_1 \\ \widetilde{r}_2 \\ \widetilde{r}_3 \\ \vdots \\ \widetilde{r}_{N-1} \\ \widetilde{r}_N \end{pmatrix}, \tag{2.61}$$

where $\beta_N = b_N$, $\widetilde{r}_N = r_N$, $\widetilde{d}_N = d_N$, $s_N = \widetilde{r}_1$

$$\beta_i = b_i - \frac{c_i}{\beta_{i+1}} a_{i+1}, \qquad \text{for} \quad i = N-1, \dots, 2$$

$$\widetilde{d}_i = d_i - \frac{\widetilde{d}_{i+1}}{\beta_{i+1}} a_{i+1}, \qquad \text{and} \quad s_i = s_{i+1} - \frac{\widetilde{d}_{i+1}}{\beta_{i+1}} \widetilde{r}_{i+1} \quad \text{for} \quad i = N-1, \dots, 1 \ .$$

The usual forward sweep will then solve this matrix system.

2.2.4 Summary

This chapter has presented the novel velocity-vorticity formulation of Davies and Carpenter (2001), as this system provides the foundation for the computer code which has

generated the results shown in this thesis. Davies and Carpenter (2001) have described many of the details of the discretization given in this chapter. However, novel aspects of the current implementation are the higher-order compact-difference scheme used for the streamwise derivative, and the direct solver for the Poisson equation. This thesis has presented the first full documentation of the former, although the scheme had already been utilized in the work of Bowles et al. (2003) where only an outline of the numerical method was given. The direct Poisson solver will be described in the following chapter. This has also been utilized in the same, earlier study (Bowles et al., 2003), but again, no full description was given.

Given that the two-dimensional governing equations and their discretization have thus been explained, it is sufficient to comment briefly on the three-dimensional case.

In this thesis, we impose two-dimensional disturbances on a number of two-dimensional mean-flow profiles. The disturbances will develop in two dimensions initially, however, due to a secondary instability, three-dimensional behaviour will develop. The extension from this two-dimensional code to a three-dimensional linear code could be achieved by using the routines already in the code, and has already been done. Lockerby et al. (2002) have used a three-dimensional linear version of the code to investigate the interaction between microelectromechanical systems (MEMS) and mesoscale actuators in a boundary layer. Kudar (2004) has used a three-dimensional linear version of the code to investigate flow control using pulsed jets for Falkner–Skan–Cooke basic flows. By assuming that the spanwise dependence is wave-like, the code could be run in parallel for several spanwise wavenumbers. The inclusion of nonlinear terms would require some attention, but as the number of spanwise wave modes can be low, nonlinear products could be evaluated explicity, avoiding aliasing errors.

The following chapter indicates how to adapt the numerical discretization of the Poisson equation for three-dimensional disturbances.

Chapter 3

Poisson Solver

This chapter explains the discretization of the Poisson equation. First the two-dimensional case is considered, then alterations resulting from the introduction of the spanwise direction are explained as the three-dimensional case is considered. This direct Poisson solver has been utilized in previous two-dimensional studies (Bowles et al., 2003) however no comprehensive description of the method has been presented.

3.1 The two-dimensional case

In two dimensions the wall-normal velocity $w(x,z)$ is related to the vorticity ω_y through the following relationship:

$$\nabla^2 w = -\frac{\partial \omega_y}{\partial x} \,. \tag{3.1}$$

The vorticity, ω_y is calculated by the predictor step (see equation (2.18) on page 25). It can then be substituted into equation (3.1), from which the wall normal velocity can be calculated. A direct method for doing this is described in this chapter.

3.1.1 At the inflow and outflow

The value of the wall-normal velocity at the inflow is taken to be zero. This is reasonable, for Blasius flow disturbances are not expected to propagate strongly upstream towards the inflow. The disturbance is placed far enough downstream of the inflow boundary so that the disturbances will not affect the inflow.

At the outflow we impose the boundary condition $\dfrac{\partial^2 w}{\partial x^2} = -\alpha^2 w$. Substituting this

into (3.1) results in

$$-\alpha^2 w + \frac{\partial^2 w}{\partial z^2} = -\frac{\partial \omega_y}{\partial x} .$$

The right hand-side can be calculated from the known value for ω_y and there is no longer any dependence on x on the left-hand side, so all that remains to be done is to integrate the equation twice with respect to the mapped wall-normal coordinate (ζ). From (2.52b) (see page 40) we have

$$\left[-\alpha^2 \mathbf{I} + \frac{\mathbf{K}}{l^2}\right][w] = -\mathbf{I}\left[\frac{\partial \omega_y}{\partial x}\right] . \tag{3.2}$$

The integral operators $\mathbf{I}$ and $\mathbf{K}$ act on w in the manner described by (2.55) and (2.57) so this problem is reduced to a matrix problem of the form $A\hat{w}_k = B$ where A and B are known matrices. The modified Thomas Algorithm is used to invert A in order to find the Chebyshev coefficients of the wall-normal velocity $\hat{w}_k$, where $w = \sum_{k=1}^{N} \hat{w}_k T_{2k-1}$.

3.1.2 The interior points

We use the 4th-order compact difference scheme presented in (2.33) on page 30 for the second derivative in the streamwise direction at the interior points. The Poisson equation takes the form

$$\frac{\partial^2 w}{\partial x^2} = -\frac{\partial \omega_y}{\partial x} - \frac{\partial^2 w}{\partial z^2} ,$$

which leads to the following discretization:

$$\frac{w_{i-1} - 2w_i + w_{i+1}}{(\Delta x)^2} = \frac{1}{12}\left[\left(\frac{\partial \omega_y}{\partial x} - \frac{\partial^2 w}{\partial z^2}\right)_{i-1} + 10\left(\frac{\partial \omega_y}{\partial x} - \frac{\partial^2 w}{\partial z^2}\right)_{i} + \left(\frac{\partial \omega_y}{\partial x} - \frac{\partial^2 w}{\partial z^2}\right)_{i+1}\right] .$$

Rearranging this so that the known values of ω_y are on the right-hand side we have

$$\left(\frac{1}{(\Delta x)^2} + \frac{1}{12}\frac{\partial^2}{\partial z^2}\right)(w_{i-1} + w_{i+1}) + \left(\frac{-2}{(\Delta x)^2} + \frac{5}{6}\frac{\partial^2}{\partial z^2}\right) w_i = \frac{-1}{12}\left(\frac{\partial \omega_y}{\partial x}\Big|_{i-1} + 10\frac{\partial \omega_y}{\partial x}\Big|_{i} + \frac{\partial \omega_y}{\partial x}\Big|_{i+1}\right) .$$

For ease of notation we define

$$r_i := \frac{-1}{12}\left(\frac{\partial \omega_y}{\partial x}\Big|_{i-1} + 10\frac{\partial \omega_y}{\partial x}\Big|_{i} + \frac{\partial \omega_y}{\partial x}\Big|_{i+1}\right)$$

so the scheme can be written as

$$\left(\frac{1}{(\Delta x)^2}+\frac{1}{12}\frac{\partial^2}{\partial z^2}\right)(w_{i-1}+w_{i+1})+\left(\frac{-2}{(\Delta x)^2}+\frac{5}{6}\frac{\partial^2}{\partial z^2}\right)w_i \;=\; r_i\,. \tag{3.3}$$

Consider the two extreme interior points $i=2$ and $i=N_x-1$.

$$\left(\frac{1}{(\Delta x)^2}+\frac{1}{12}\frac{\partial^2}{\partial z^2}\right)(w_1+w_3)+\left(\frac{-2}{(\Delta x)^2}+\frac{5}{6}\frac{\partial^2}{\partial z^2}\right)w_2 \;=\; r_2 \qquad (i=2)$$

$$\left(\frac{1}{(\Delta x)^2}+\frac{1}{12}\frac{\partial^2}{\partial z^2}\right)(w_{N_x-2}+w_{N_x})+\left(\frac{-2}{(\Delta x)^2}+\frac{5}{6}\frac{\partial^2}{\partial z^2}\right)w_{N_x-1} \;=\; r_{N_x-1} \qquad (i=N_x-1)$$

We have previously calculated the solution w at the inflow (w_1) and the outflow (w_{N_x}). We move these known values over to the right-hand side and define new variables $\widetilde{w}_i$ and $\widetilde{r}_i$ as follows:

$$\left(\frac{1}{(\Delta x)^2}+\frac{1}{12}\frac{\partial^2}{\partial z^2}\right)(\widetilde{w}_{i-1}+\widetilde{w}_{i+1})+\left(\frac{-2}{(\Delta x)^2}+\frac{5}{6}\frac{\partial^2}{\partial z^2}\right)\widetilde{w}_i=\widetilde{r}_i \quad (i=2,\ldots,N_x-1) \tag{3.4}$$

where

$$\begin{aligned}
&\widetilde{w}_i = w_i && \widetilde{r}_i = r_i \qquad \text{for } i=3,\cdots N_x-2\\
&\widetilde{w}_1 = 0 && \widetilde{r}_2 = r_2-\left(\frac{1}{(\Delta x)^2}+\frac{1}{12}\frac{\partial^2}{\partial z^2}\right)w_1\\
&\widetilde{w}_{N_x} = 0 && \widetilde{r}_{N_x-1} = r_{N_x-1}-\left(\frac{1}{(\Delta x)^2}+\frac{1}{12}\frac{\partial^2}{\partial z^2}\right)w_{N_x}.
\end{aligned}$$

The problem at the interior points has thus been reduced to solving for $\{\widetilde{w}_i\}_{i=2}^{N_x-1}$. Whilst the equation is in this form, an iterative scheme would seem appropriate, and in fact one has been implemented in the code previously (Davies and Carpenter, 2001). The value of $\widetilde{w}_{i+1}$ is taken from the previous time-step, $\widetilde{w}_{i-1}$ has been calculated for the present time step. These values are used to estimate w_i. Iteration is then carried out (using an over-relaxation technique) until the w_i converges. This procedure is then repeated at the next streamwise point, and is known as a line-iteration procedure.

An alternative to such an iterative scheme is the following direct method, which works

due to a sine transform that is able to 'uncouple' the solution w_i from the solution at neighbouring grid-points $w_{i\pm1}$. We define a sine transform as follows:

$$\widetilde{w}_i = \sqrt{\frac{2}{N_x - 1}} \sum_{j=1}^{N_x-1} \check{w}_j \sin\left(\frac{(i-1)(j-1)\pi}{N_x - 1}\right) , \qquad i = 1, N_x - 1 . \tag{3.5}$$

Applying this sine transform to (3.4) gives

$$\left(\frac{1}{(\Delta x)^2} + \frac{1}{12}\frac{\partial^2}{\partial z^2}\right) \sum_{j=1}^{N_x-1} \check{w}_j \left\{\sin\left(\frac{(i-2)(j-1)\pi}{N_x - 1}\right) + \sin\left(\frac{i(j-1)\pi}{N_x - 1}\right)\right\}$$
$$+\left(\frac{-2}{(\Delta x)^2} + \frac{5}{6}\frac{\partial^2}{\partial z^2}\right) \sum_{j=1}^{N_x-1} \check{w}_j \sin\left(\frac{(i-1)(j-1)\pi}{N_x - 1}\right) = \sum_{j=1}^{N_x-1} \check{r}_j \sin\left(\frac{(i-1)(j-1)\pi}{N_x - 1}\right) .$$

Employing the relationship $\sin(k-1)\theta + \sin(k+1)\theta = 2\sin(k\theta)\cos\theta$ gives

$$\left(\frac{1}{(\Delta x)^2} + \frac{1}{12}\frac{\partial^2}{\partial z^2}\right) \sum_{j=1}^{N_x-1} \check{w}_j \left(2\sin\left(\frac{(i-1)(j-1)\pi}{N_x - 1}\right) \cos\left(\frac{(j-1)\pi}{N_x - 1}\right)\right)$$
$$+\left(\frac{-2}{(\Delta x)^2} + \frac{5}{6}\frac{\partial^2}{\partial z^2}\right) \sum_{j=1}^{N_x-1} \check{w}_j \sin\left(\frac{(i-1)(j-1)\pi}{N_x - 1}\right) = \sum_{j=1}^{N_x-1} \check{r}_j \sin\left(\frac{(i-1)(j-1)\pi}{N_x - 1}\right) .$$

This expression can now be simplified

$$\sum_{j=1}^{N_x-1} \left\{2\left[\cos\left(\frac{(j-1)\pi}{N_x - 1}\right)\right]\left(\frac{1}{(\Delta x)^2} + \frac{1}{12}\frac{\partial^2}{\partial z^2}\right) + \left(\frac{-2}{(\Delta x)^2} + \frac{5}{6}\frac{\partial^2}{\partial z^2}\right)\right\} \check{w}_j \sin\left(\frac{(i-1)(j-1)\pi}{N_x - 1}\right)$$
$$= \sum_{j=1}^{N_x-1} \check{r}_j \sin\left(\frac{(i-1)(j-1)\pi}{N_x - 1}\right) .$$

Therefore, for each particular j we must have that

$$\left\{2\left[\cos\left(\frac{(j-1)\pi}{N_x - 1}\right)\right]\left(\frac{1}{(\Delta x)^2} + \frac{1}{12}\frac{\partial^2}{\partial z^2}\right) + \left(\frac{-2}{(\Delta x)^2} + \frac{5}{6}\frac{\partial^2}{\partial z^2}\right)\right\} \check{w}_j = \check{r}_j . \tag{3.6}$$

If we define λ_j and μ_j as follows

$$\lambda_j = \frac{6}{5 + \cos\left(\frac{j-1}{N_x-1}\right)} \tag{3.7}$$

$$\mu_j = \frac{2\lambda_j}{(\Delta x)^2}\left[\cos\left(\frac{j-1}{N_x-1}\right) - 1\right] , \tag{3.8}$$

we can rewrite (3.6) as

$$\mu_j \check{w}_j - \frac{\partial^2 \check{w}_j}{\partial z^2} = \lambda_j \check{r}_j . \tag{3.9}$$

We need to integrate this twice with respect to the mapped wall-normal variable ζ, which results in

$$\iint \left(\mu_j \check{w}_j - \frac{\partial^2 \check{w}_j}{\partial z^2}\right) d\zeta d\zeta = \iint \lambda_j \check{r}_j \, d\zeta d\zeta . \tag{3.10}$$

Solving the Poisson equation at the interior streamwise points has thus been reduced to solving an ordinary differential equation for the coefficients of the sine-transformed wall-normal velocity. The values $\check{r}_j$ are calculated by taking the sine transform of the appropriate values of $-\frac{\partial \omega_y}{\partial x}$. The elements of the pentadiagonal matrix representing $\iint \left(\mu_j - \frac{\partial^2}{\partial z^2}\right) d\zeta d\zeta$ are calculated at the outset. As they depend only on discretization parameters and constants, the elements remain the same throughout the simulation and need only be calculated once. The problem $A\check{w}_j = B$ is then inverted by applying the modified Thomas Algorithm (as indicated on page 43) to solve for $\check{w}_j$. The inverse of the sine transform is then applied to $\check{w}_j$ to give $\hat{w}_k$. These values representing the wall-normal velocity are then used for the corrector stage to update the convective terms (see (2.20) on page 26).

3.2 The three-dimensional case

$$\nabla^2 w = \frac{\partial \omega_x}{\partial y} - \frac{\partial \omega_y}{\partial x} \tag{3.11}$$

When boundary-layer flow is disturbed by a (two-dimensional) Tollmien–Schlichting wave, the disturbance develops initially in two dimensions. Secondary instabilities will occur once the Tollmien–Schlichting wave has become large enough, giving rise to variation in the third dimension. This dependence on the spanwise co-ordinate is known to be sinusoidal. (In

the more general case, the initial disturbances could give rise to oblique three-dimensional Tollmien–Schlichting waves rather than two-dimensional Tollmien–Schlichting waves. The linear development would then be three dimensional.) We can model a sinusoidal variation in the spanwise direction by writing the primary variables as

$$\omega_x^T(x,y,z,t) = \omega_x(x,z,t)\sin\beta y \tag{3.12a}$$
$$\omega_y^T(x,y,z,t) = \omega_y(x,z,t)\cos\beta y \tag{3.12b}$$
$$w^T(x,y,z,t) = w(x,z,t)\cos\beta y\ , \tag{3.12c}$$

and the secondary variables as

$$u^T(x,y,z,t) = u(x,z,t)\cos\beta y \tag{3.13a}$$
$$v^T(x,y,z,t) = v(x,z,t)\sin\beta y \tag{3.13b}$$
$$w_z^T(x,y,z,t) = \omega_z(x,z,t)\sin\beta y\ , \tag{3.13c}$$

where β is the spanwise wavenumber. Note that symmetry requires that the variables used in the two-dimensional case depend on $\cos(\beta y)$ and those that are involved only when three dimensions are considered depend on $\sin(\beta y)$.

3.2.1 At the inflow and the outflow

Again, the value of the wall-normal velocity at the inflow is taken to be zero for the same reasons as in the two-dimensional case.

At the outflow the equation to be solved takes a similar form to that for the two-dimensional case, only now, there is a term involving β and one involving ω_x:

$$\left[-(\alpha^2+\beta^2)\,\mathbf{I}+\frac{\mathbf{K}}{l^2}\right][w] = -\mathbf{I}\left[\omega_x+\frac{\partial\omega_y}{\partial x}\right]\ . \tag{3.14}$$

3.2.2 The interior points

If we substitute the total variables given by (3.12) into (3.11) we can see the y-dependence will be simply factored out:

$$\left(\frac{\partial^2}{\partial x^2} - \beta^2 + \frac{\partial^2}{\partial z^2}\right) w(x,z,t)\ \cos(\beta y) = -\left(\omega_x + \frac{\partial \omega_y}{\partial x}\right)\cos(\beta y)\ . \tag{3.15}$$

Both ω_x and ω_y are known. The y-derivative of the Laplacian term has been replaced by a constant $(-\beta^2)$ so we can apply the techniques used in the previous section to discretize the x and z variables. Applying the fourth-order compact difference scheme for the second streamwise derivative results in

$$\left(\frac{1}{(\Delta x)^2} - \frac{\beta^2}{12} + \frac{1}{12}\frac{\partial^2}{\partial z^2}\right)(w_{i-1} + w_{i+1}) + \left(\frac{-2}{(\Delta x)^2} - \frac{5}{6}\beta^2 + \frac{5}{6}\frac{\partial^2}{\partial z^2}\right) w_i \ = \ r_i\ ,$$

where the two-dimensional expression on the right-hand side now needs modification

$$r_i := \frac{-1}{12}\left(\left[\omega_x + \frac{\partial \omega_y}{\partial x}\right]_{i-1} + 10\left[\omega_x + \frac{\partial \omega_y}{\partial x}\right]_i + \left[\omega_x + \frac{\partial \omega_y}{\partial x}\right]_{i+1}\right)$$

(The equivalent of (3.3).)

Once again, as in (3.4) we transform variables using:

$$\left(\frac{1}{(\Delta x)^2} - \frac{\beta^2}{12} + \frac{1}{12}\frac{\partial^2}{\partial z^2}\right)(\widetilde{w}_{i-1}+\widetilde{w}_{i+1}) + \left(\frac{-2}{(\Delta x)^2} - \frac{5}{6}\beta^2 + \frac{5}{6}\frac{\partial^2}{\partial z^2}\right)\widetilde{w}_i = \widetilde{r}_i \quad (i = 2,\ldots,N_x-1) \tag{3.16}$$

where

$$\begin{aligned}
&\widetilde{w}_i = w_i && \widetilde{r}_i = r_i \qquad \text{for } i = 3,\cdots N_x - 2\\
&\widetilde{w}_1 = 0 && \widetilde{r}_2 = r_2 - \left(\frac{1}{(\Delta x)^2} - \frac{\beta^2}{12} + \frac{1}{12}\frac{\partial^2}{\partial z^2}\right) w_1\\
&\widetilde{w}_{N_x} = 0 && \widetilde{r}_{N_x-1} = r_{N_x-1} - \left(\frac{1}{(\Delta x)^2} - \frac{\beta^2}{12} + \frac{1}{12}\frac{\partial^2}{\partial z^2}\right) w_{N_x}.
\end{aligned}$$

Next we apply the sine transform as defined by (3.5), and we can see that for any partic-

ular j the following equation must be satisfied:

$$\left\{2\left[\cos\left(\frac{(j-1)\pi}{N_x-1}\right)\right]\left(\frac{1}{(\Delta x)^2}-\frac{\beta^2}{12}+\frac{1}{12}\frac{\partial^2}{\partial z^2}\right)+\left(\frac{-2}{(\Delta x)^2}-\frac{5}{6}\beta^2+\frac{5}{6}\frac{\partial^2}{\partial z^2}\right)\right\}\check{w}_j=\check{r}_j\ . \tag{3.17}$$

We integrate this equation twice and get

$$\iint\left(\mu_j^{3D}\,\check{w}_j-\frac{\partial^2\check{w}_j}{\partial z^2}\right)\,d\zeta d\zeta=\iint\lambda_j^{3D}\check{r}_j\,d\zeta d\zeta\ , \tag{3.18}$$

where

$$\lambda_j^{3D} = \frac{6}{5+\cos\left(\frac{j-1}{N_x-1}\right)} \equiv \lambda_j\ , \tag{3.19}$$

$$\mu_j^{3D} = \lambda_j\left[\frac{2}{(\Delta x)^2}\left(\cos\left(\frac{j-1}{N_x-1}\right)-1\right)-\frac{\beta^2}{6}\left(\cos\left(\frac{j-1}{N_x-1}\right)+5\right)\right]\ . \tag{3.20}$$

As can be seen by comparing (3.10) with (3.18), the general form of the integrated, discretized two-dimensional and three-dimensional Poisson equations is the same. All that needs to be altered are the multipliers λ_j and μ_j. In the two-dimensional case, we solve for $\hat{w}_k$, the Chebyshev coefficients of the wall-normal disturbance velocity w. In the three-dimensional case, we solve for $\hat{w}_k$, the Chebyshev coefficients of $w(x,z,t)$. Should the 'total' wall-normal disturbance velocity need to be calculated, $w(x,z,t)$ should be multiplied by $\cos(\beta y)$ (see (3.12)).

3.3 Verification

3.3.1 A Test Case

Let us pose the following problem on the domain given by $x\in[0,L]$, $y\in\mathcal{R}$ and $z\in\mathcal{R}^+$:

$$\nabla^2 w(x,y,z)=(-\alpha^2-\beta^2+\eta^2)\sin(\alpha x)\cos(\beta y)\exp(-\eta z)\ , \tag{3.21}$$

where α and β are real-valued parameters, and η is positive. The solution is subject to the following boundary conditions

$$\begin{array}{lll} x = 0 & w(0,y,z) = & 0 \ , \\ x = L & w''(L,y,z) = & -\alpha^2 w(L,y,z) \ , \\ z = 0 & w(x,y,0) = & \sin(\alpha x)\cos(\beta y) \ , \\ z = \infty & w(x,y,\infty) = & 0 \ . \end{array} \tag{3.22}$$

The analytical solution, w_A, is given by

$$w_A(x,y,z) = \sin(\alpha x)\cos(\beta y)\exp(-\eta z) \ . \tag{3.23}$$

We will now compare this analytical solution with the numerical solution calculated using the method outlined in section 3.2. The parameters chosen are $\alpha = 0.3$, $\beta = 0.1$ and $\eta = 0.05$. Figure 3.1 shows excellent agreement between the numerical and analytical solutions. Figure 3.2 overlays the analytical solution with the numerical solution (only at selected points for clarity), which allows for easier comparison. To analyse the difference between the analytical and numerical solutions, we define the absolute error e as

$$e = | \, w_A - w_{Num} | \ , \tag{3.24}$$

where w_{Num} is the numerical solution. This quantity is plotted in the second graph shown in figure 3.2 and is small (less than 1% for the maximum value of the solution). This is an excellent result since the solution w decays slowly in the z direction.
In order to investigate the discretization errors of the numerical schemes more thoroughly, we define an error using a discrete L^2 norm,

$$E_{\mathsf{L}^2} = \sqrt{\frac{\sum_{i=1}^{N_x}\sum_{j=1}^{N_z}\left(w_A(x_i\,,z_j) - w_{Num}(x_i\,,z_j)\right)^2}{N_x N_z}} \tag{3.25}$$

This measure of error takes into account the error over the whole domain. The simulations were run several times for different values of Δx and also different values of N_z. Figure 3.3 plots the error E_{L^2} against the number of points in the x direction for three different values of N_z. Since the compact difference scheme used for the streamwise direction has a

truncation error $\mathcal{O}(\Delta x)^4$, which depends algebraically on Δx therefore, we would expect that, on a log–log plot, this error would depend linearly on the number of points used in the streamwise direction. For each value of N_z, as the number of streamwise points increases linear dependence is seen at first, but then the error can be seen to reach a constant value. This constant is different for each N_z and would therefore seem to depend on N_z. Using a Chebyshev spectral scheme for the z direction means that we can achieve exponential convergence, and the error from the z discretization should be negligible compared to that from the x discretization. However, the exponential convergence rate is only guaranteed for suitably decaying functions. The value of η used in these simulations is small, $\eta = 0.05$. The exponential decay in the z direction is given by $\exp(-\eta z)$, which represents a relatively slow decay. The fact that the numerical results are so good for such a slowly-decaying function is worthy of note, however, in this case the accuracy of compact difference scheme is compromised by the algebraic accuracy of the spectral method.

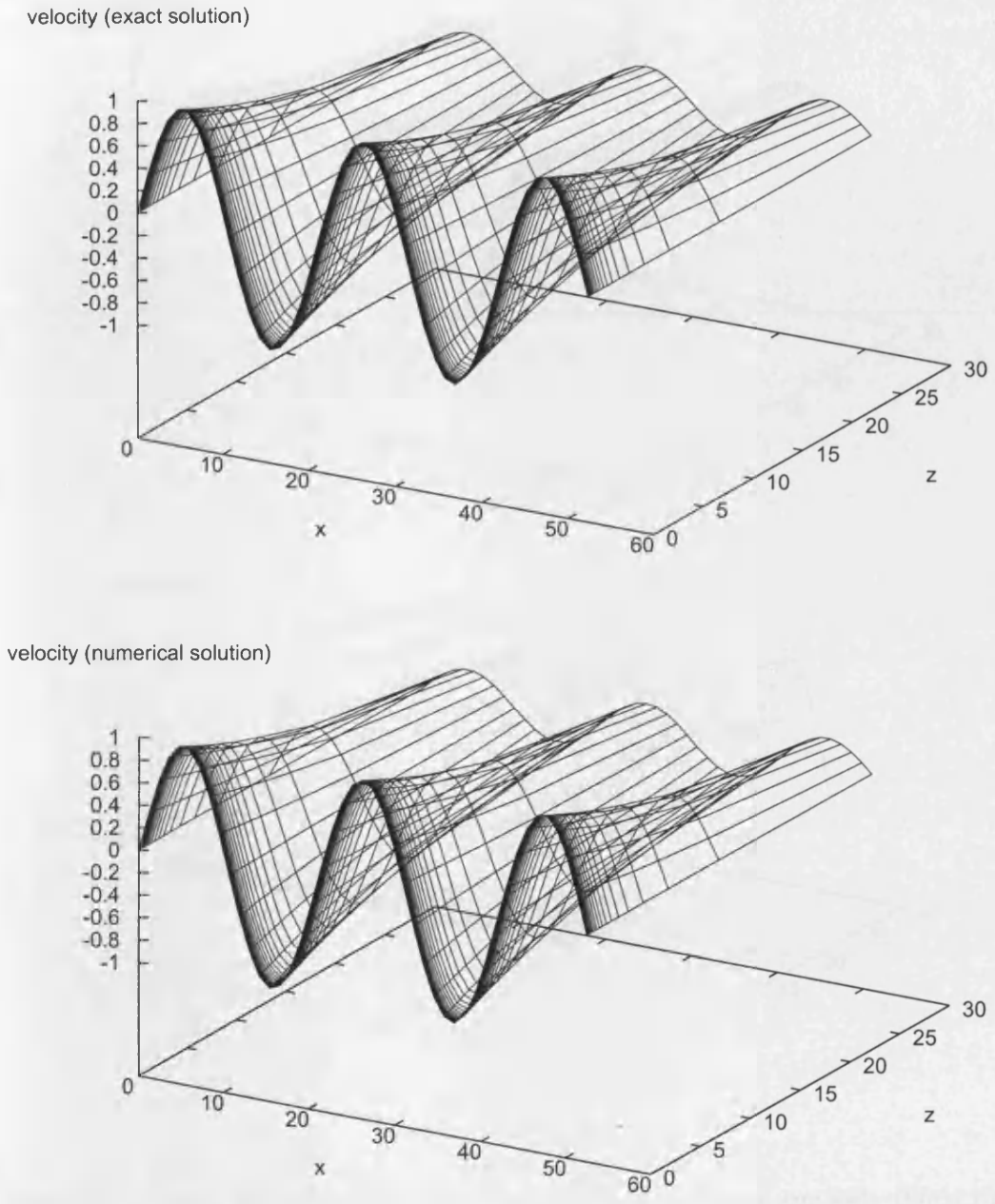

Figure 3.1: Analytical and numerical solutions at $y = 0$ of the test case presented in (3.21) and (3.22), for the parameters $\alpha = 0.3$, $\beta = 0.1$, $\eta = 0.05$, $N_x = 45$ and $N_z = 24$.

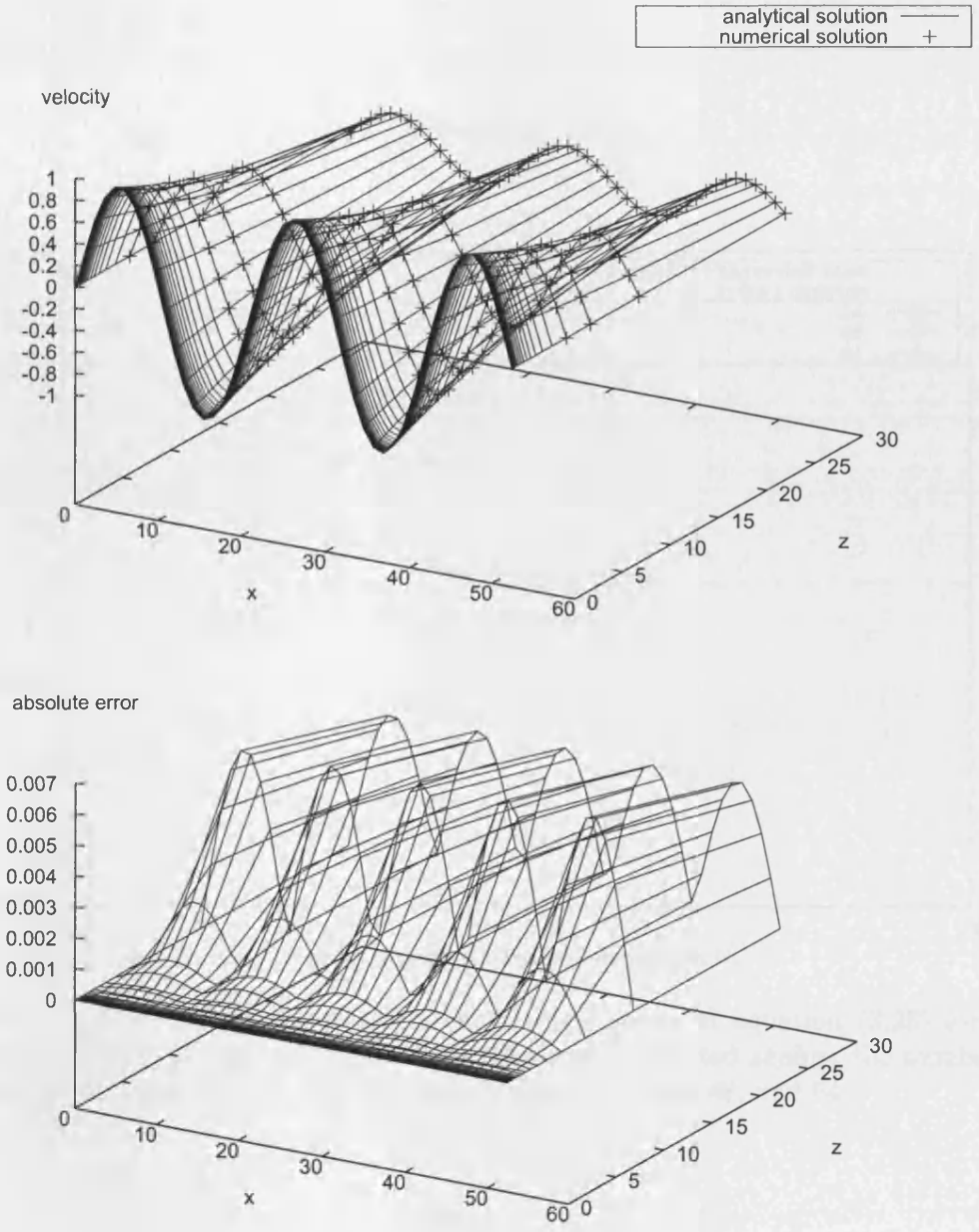

Figure 3.2: Above: analytical and numerical solutions at $y = 0$ overlaid. (Only some of the numerical data points are shown in order to improve the clarity.) Below: the absolute error, e, given in equation (3.24). Parameters used: $\alpha = 0.3$, $\beta = 0.1$, $\eta = 0.05$, $N_x = 45$ and $N_z = 24$.

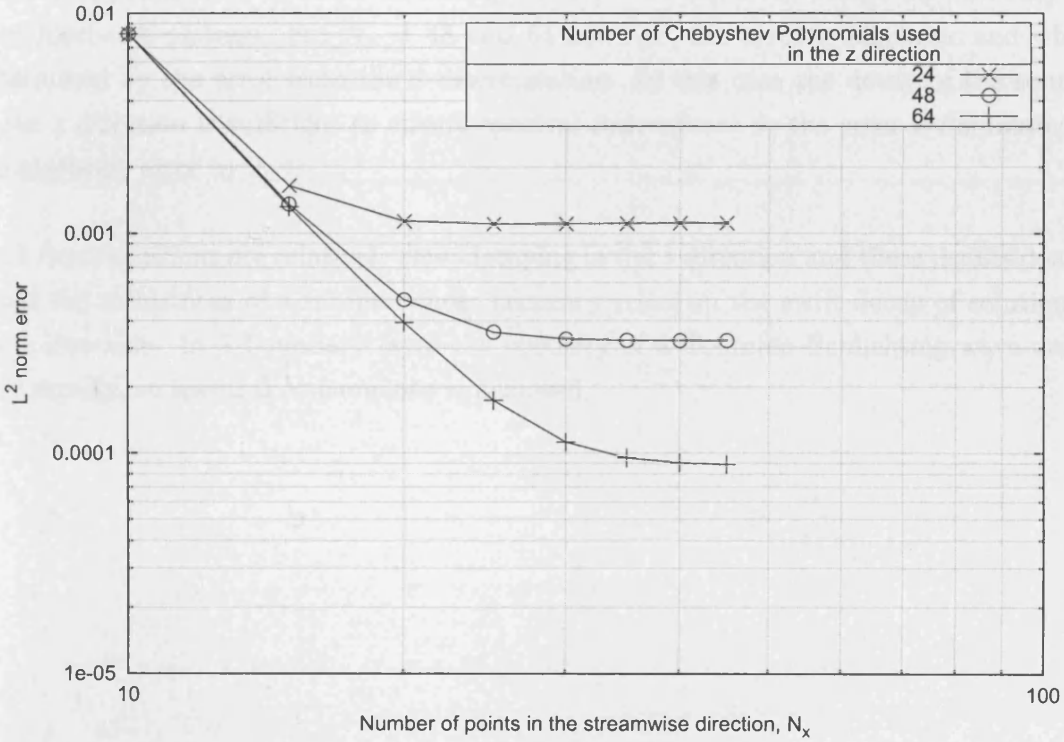

Figure 3.3: Error calculated by the discrete L^2 norm given in equation (3.25) for the parameters $\alpha = 0.3$, $\beta = 0.1$, and $\eta = 0.05$. The error is plotted against the number of streamwise grid points, N_x, for three different values of N_z: 24, 48, and 64.

Presented below are results taken from the same problem, but with a faster exponential decay in the z direction. For this purpose η is increased by a factor of 10, so $\eta = 0.5$. Once again there is good agreement between the analytic and numerical solutions seen in figure 3.4. Analytic and numerical solutions are overlaid as before, and also the absolute error is plotted against x and z in figure 3.5. The same three values of N_z were used, and the error calculated with the L^2 norm is plotted for these three values against the number of points used in the x direction. For $N_z = 24$ the error decays algebraically but then reaches a plateau. For $N_z = 48$ and 64 however, the error is algebraic and wholly determined by the error from the x discretization. In this case the decay of the solution in the z direction is sufficient to ensure spectral convergence so the error is dominated by the algebraic error in x.

Both these solutions are relatively slow-decaying in the z direction and these results demonstrate the robustness of a scheme whose accuracy relies on the swift decay of solutions in the z direction. In a boundary layer the vorticity of a Tollmien–Schlichting wave decays very rapidly, so spectral convergence is achieved.

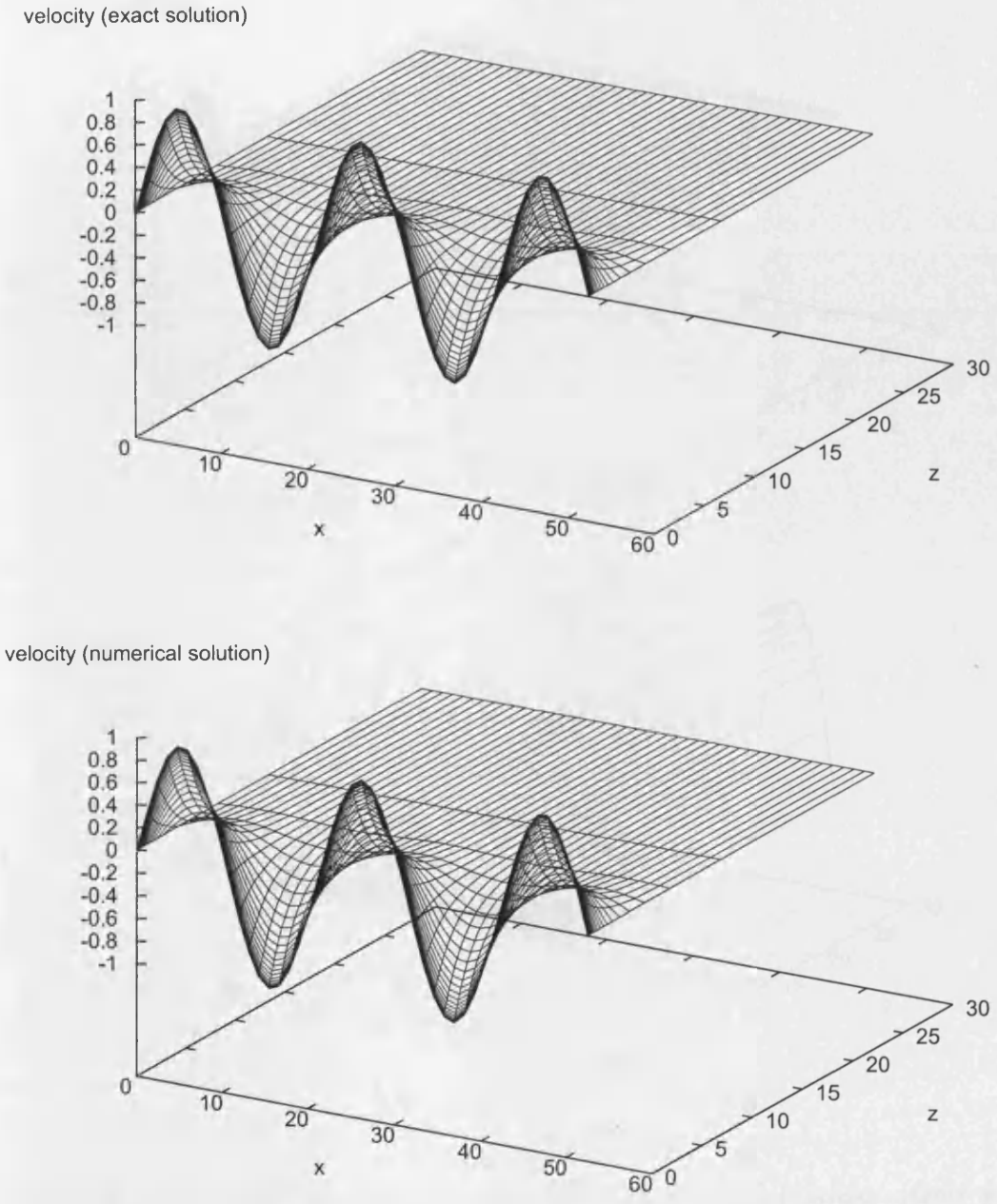

Figure 3.4: Analytical and numerical solutions at $y = 0$ of the test case presented in (3.21) and (3.22), for the parameters $\alpha = 0.3$, $\beta = 0.1$, $\eta = 0.5$, $N_x = 45$ and $N_z = 24$.

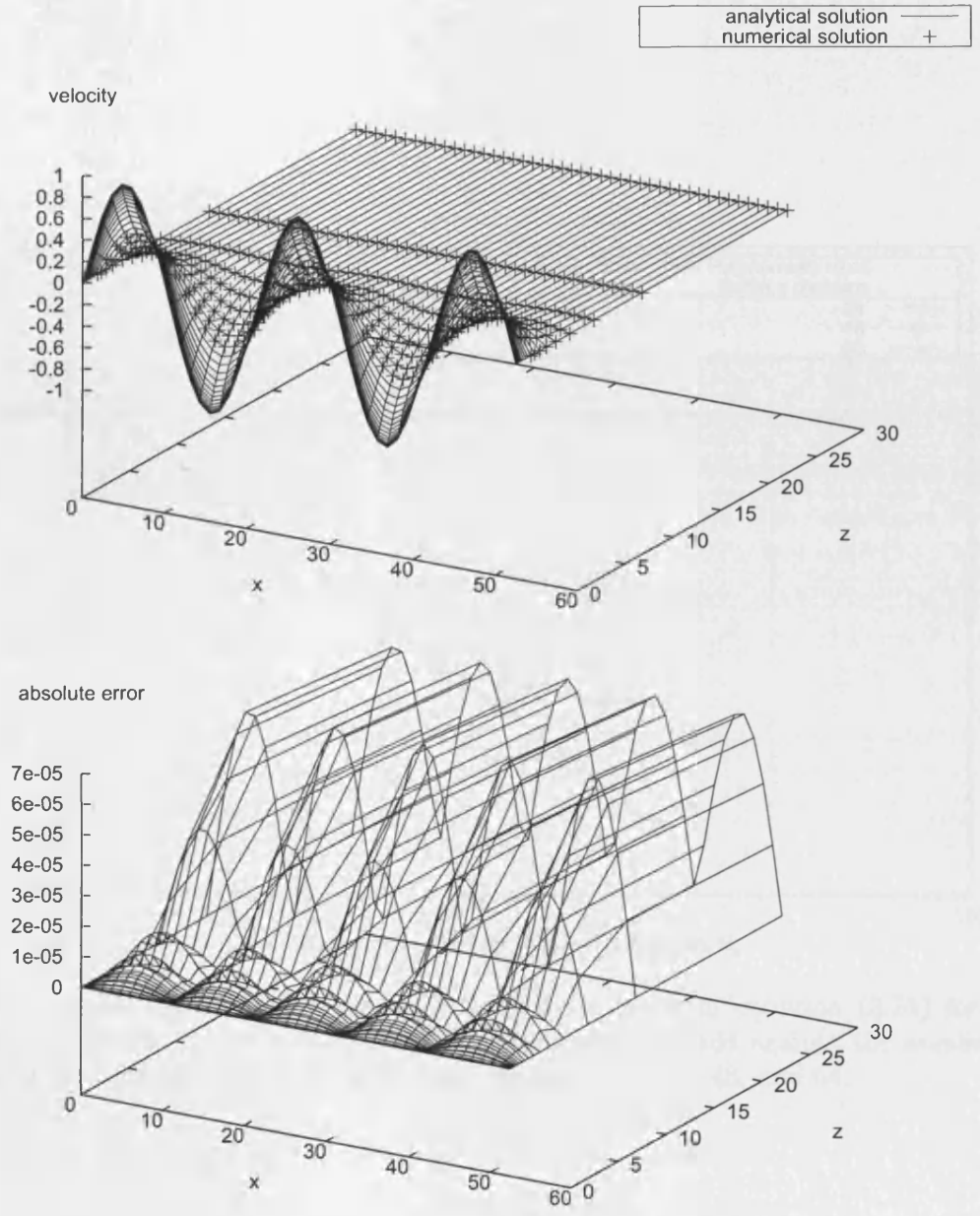

Figure 3.5: Above: analytical and numerical solutions at $y = 0$ overlaid. (Only some of the numerical data points are shown in order to improve the clarity.) Below: the absolute error, e, given in equation (3.24). Parameters used: $\alpha = 0.3$, $\beta = 0.1$, $\eta = 0.5$, $N_x = 45$ and $N_z = 24$.

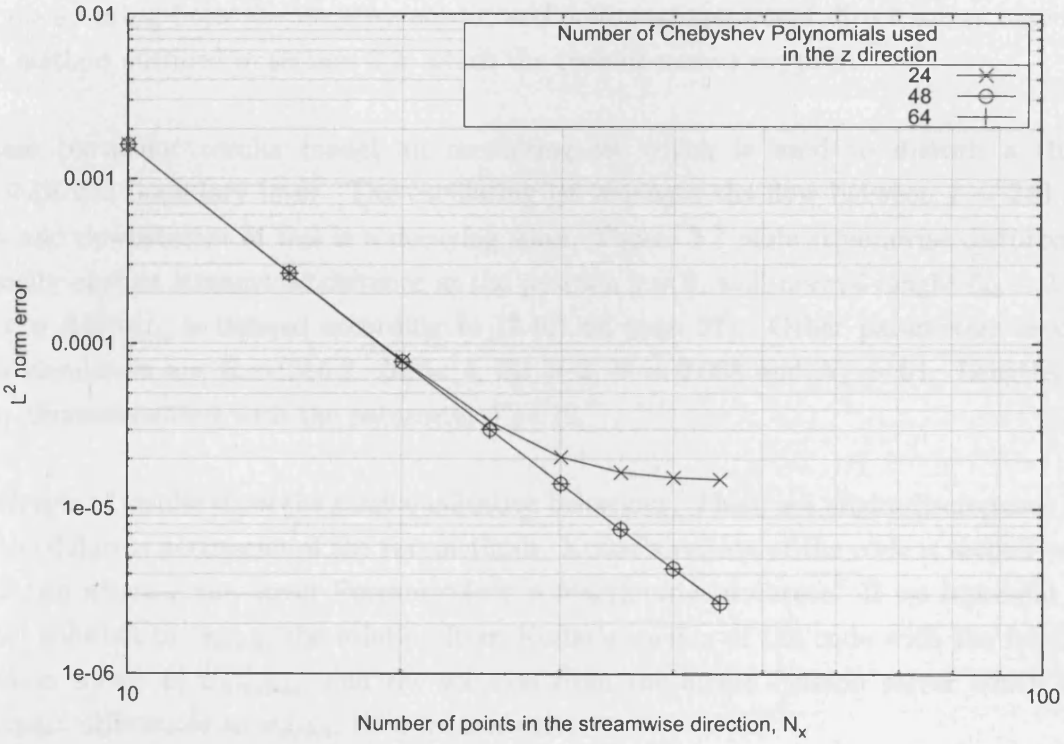

Figure 3.6: Error calculated by the discrete L^2 norm given in equation (3.25) for the parameters $\alpha = 0.3$, $\beta = 0.1$, and $\eta = 0.5$. The error is plotted against the number of streamwise grid points, N_x, for three different values of N_z: 24, 48, and 64.

3.3.2 Comparison with an iterative solver

The previous subsection demonstrates the potential accuracy of this Poisson solver. This section further illustrates that point. Kudar (2004) uses a linear three-dimensional version of Davies' code to investigate the effect of turbulent near-wall structures, such as streaks in three-dimensional boundary layers. The Poisson solver in her version of the code is based on an iterative method. She has supplied the following results of simulations produced using both the iterative solver, and a three-dimensional direct solver based on the method outlined in section 3.2, which the current author supplied.

These particular results model an oscillating jet which is used to disturb a three-dimensional boundary layer. The oscillating jet impinges the flow between $x = 249$ and 264 and downstream of this is a decaying wave. Figure 3.7 plots streamwise disturbance velocity against streamwise distance at the position $y = 0$, wall-normal height $\zeta_{48} \equiv 3.642$ at $t = 6400$ (ζ_j is defined according to (2.46) on page 37). Other parameters used in this simulation are $R = 316.2$, $\Delta x = 4$, $\Delta t = 2$, $\beta = 0.063$ and $N_z = 64$. Lengths are non-dimensionalized with the parameter $\delta^*/1.72$.

Both sets of results show the same qualitative behaviour. There is a slight discrepancy due to the different accuracies of the two methods. Kudar's version of the code is second-order accurate whereas the direct Poisson solver is fourth-order accurate. If we represent the exact solution by w_{exact}, the solution from Kudar's version of the code with the iterative Poisson solver as $w_{iterative}$, and the solution from the direct Poisson solver which uses compact differences as w_{direct}, then we can write

$$\begin{aligned} w_{exact} &= w_{iterative} + \mathcal{O}(\Delta x)^2 \; ; \\ w_{exact} &= w_{direct} + \mathcal{O}(\Delta x)^4 \; . \end{aligned}$$

Therefore, when comparing the two sets of numerical results the difference is

$$\begin{aligned} |\, w_{iterative} - w_{direct}| &= \mathcal{O}(\Delta x)^2 - \mathcal{O}(\Delta x)^4 \\ &= \mathcal{O}(\Delta x)^2 \end{aligned}$$

Therefore, we would expect a discrepancy in the results as they are generated by schemes of different order accuracies. When comparing the two sets of results, as the streamwise distance increases, the phase difference between the two schemes becomes more apparent. As demonstrated in the previous chapter (see section 2.2.2 on page 27) higher-order compact difference schemes are better at preserving wave-like properties such as phase, than second-order finite difference methods are. This difference between the solutions is attributable to the difference between the numerical schemes of the fourth-order direct Poisson solver (with compact differences) and the second-order iterative Poisson solver.

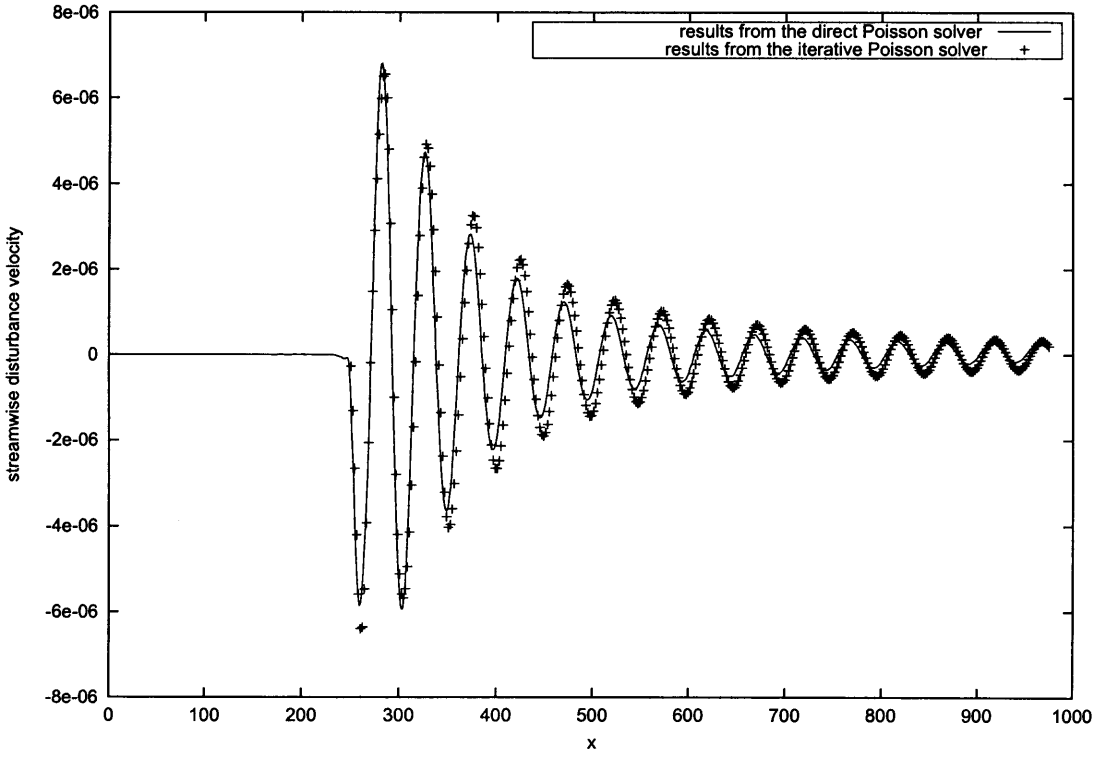

Figure 3.7: Velocity produced by Navier–Stokes Solver with an iterative Poisson solver compared with that produced by the Navier–Stokes solver with a direct Poisson solver.

Chapter 4

Linear and Weakly Nonlinear theories of parallel flows

One aim of fluid dynamics is to develop a greater understanding of transition with the ideal of being able to predict where and why transition occurs. To this end much work has been done to investigate how small disturbances develop. From the early 1900s the linear theory of parallel flows was developed, first in regard to Couette flow, then Poiseuille flow. Later, this was extended to the Blasius flow.

Weakly nonlinear theories can be developed by perturbing a basic state which comprises the undisturbed flow and the linear instability. As will be seen, for parallel flows, the result is an amplitude equation, which governs the evolution of the amplitude of the disturbance.

This chapter describes the basic two-dimensional flow over a flat plate (the Blasius profile) and then considers the linear stability of this flow. Some weakly nonlinear theories and their application to almost parallel flows are reviewed. The derivation of the higher-order Ginzburg–Landau equation is presented in some detail. Finally the merits of modelling wave-envelope steepening by such amplitude equations are considered and results of simulations of the evolution of wave packets according to Ginzburg–Landau equations are presented.

4.1 Blasius Flow

In 1904 Ludwig Prandtl gave a paper called 'On the motion of fluids with very little friction' at the 3rd International Mathematics Congress in Heidelberg. This was to have ground-breaking consequences for fluid dynamics. Prandtl introduced the concept of the 'boundary layer' for problems involving flow over a surface. Previously it was thought that viscosity played no part in such problems for fluids with a low viscosity. However, as a result of this assumption, the predictions made were known to be flawed, for example, indications suggested that there was no drag on objects immersed in a flow, which is clearly counter-intuitive.

Prandtl proposed that the flow field be split into two regions. One narrow region adjacent to the surface where, despite the fluid's low viscosity, viscous effects are retained in the governing equations. This region is known as the boundary layer. The second region is the remainder of the flow field, where viscous effects are assumed to be negligible. Therefore, throughout most of the domain the fluid is unaffected by the flat plate. Only in the boundary layer is its presence felt as the velocity is reduced from that of the freestream, to zero on the plate, thereby satisfying the no-slip condition.

Starting from the steady two-dimensional Navier–Stokes equations, Prandtl's boundary later equations can be derived by an 'order of magnitude analysis' as seen in standard text books such as Tritton (1988, chapter 11), Schlichting (2000, chapter 6) and Acheson (1990, chapter 8). If L^* is a typical lengthscale over which variation in the x-direction occurs and if δ^* is a typical lengthscale over which variation in the z-direction occurs, then the (dimensional) boundary layer equations are valid for $\delta^* \ll L^*$ and take the form

$$\rho\left(u^*\frac{\partial u^*}{\partial x^*} + w^*\frac{\partial u^*}{\partial z^*}\right) = \mu\frac{\partial^2 u^*}{\partial z^{*2}} \tag{4.1}$$

$$\frac{\partial u^*}{\partial x^*} + \frac{\partial w^*}{\partial z^*} = 0\,, \tag{4.2}$$

where ρ is the density and μ is the viscosity. Later we shall use the kinematic viscosity ν

given by $\nu = \mu/\rho$. The appropriate boundary conditions are

$$u^*, w^* = 0 \quad \text{at} \quad z^* = 0 \,, \tag{4.3a}$$

$$u^* = U_\infty^* \quad \text{at} \quad z^* = \infty \,, \tag{4.3b}$$

$$u^* = U_\infty^* \quad \text{at} \quad x^* = 0 \,. \tag{4.3c}$$

A global Reynolds number is defined as $R_L = \frac{U_\infty^* L^*}{\nu}$. For the flat-plate boundary layer, the displacement thickness δ^* can be shown to equal $\delta^* = 1.7208\sqrt{\nu L^*/U_\infty^*}$ at a streamwise distance L^*. It follows that

$$\left(\frac{\delta^*}{L^*}\right)^2 \sim \frac{\nu}{U_\infty^* L^*} = \frac{1}{R_L} \,.$$

So the assertion that $\delta^* \ll L^*$ is equivalent to assuming a large Reynolds number for a non-dimensional formulation.

Shortly after the boundary layer equations (4.1) were derived, Prandtl's student Blasius published their solution in 1908. In order to solve these equations, a so-called similarity solution is sought. In fact, Prandtl had already observed that by making the change of variable $\eta = z^*/\sqrt{x^*}$, the boundary layer equations are reduced to an ordinary differential equation.

Consider the variable $\eta = z^*\sqrt{U_\infty^*/2\nu x^*}$, and the streamfunction $\psi^* = \sqrt{2U_\infty^* \nu x^*} f(\eta)$. This gives a streamwise velocity of $u^* = U_\infty^* f'(\eta)$ and a wall-normal velocity of $v^* = \sqrt{U_\infty^* \nu/2x}\,(\eta f'(\eta) - f(\eta))$. On substituting these expressions into the boundary layer equations (4.1) we obtain an ordinary differential equation entirely in terms of the non-dimensional quantity η:

$$f''' + f f'' = 0 \,.$$

This is known as the Blasius equation and is subject to the conditions $f(0) = 0$, $f'(0) = 0$ and $f'(\infty) = 1$. Blasius solved this by using asymptotic expansions, however, nowadays it is solved numerically.

The displacement thickness, δ^*, is defined as

$$\begin{aligned}\delta^* &= \int_0^\infty (1 - f')\, dz^* \\ &= \sqrt{\frac{2\nu x^*}{U_\infty^*}} \lim_{\eta\to\infty}(\eta - f) \\ &= 1.21678 \sqrt{\frac{2\nu x^*}{U_\infty^*}}\end{aligned}$$

This corresponds physically to the height by which an inviscid flow would be displaced due to loss of speed as a result of viscosity. Conventionally a Reynolds number based on displacement thickness is used for boundary layer flows:

$$R = \frac{U_\infty^* \delta^*}{\nu} . \tag{4.4}$$

It is related to the global Reynolds number R_x by

$$R = \frac{U_\infty^* \delta^*}{\nu} = \frac{U_\infty^*}{\nu} 1.21678 \sqrt{\frac{2\nu x^*}{U_\infty^*}} = 1.7208 \sqrt{\frac{U_\infty^* x^*}{\nu}} = 1.7208 \sqrt{R_x} . \tag{4.5}$$

4.2 Linear theory

Linear stability theory predicts how a flow will react to a small disturbance and describes the evolution of this disturbance for as long as the nonlinear terms are insignificant. Flows for which linear stability theory predicts a growth in the disturbance are said to be linearly unstable. Flows for which the theory predicts decay of the disturbance are linearly stable.

Orr[1] investigated the stability of plane Couette flow in 1907, and Sommerfeld[2] carried out such work independently for plane Poiseuille flow in 1908. These two flows are parallel and

[1] Orr, W. McF. (1907) The stability or instability of the steady motions of a perfect liquid and of a viscous liquid, *Proceedings Royal Irish Academy*, A27, pp9-68,69-138 (cited in Criminale et al. (2003, page 426)).

[2] Sommerfeld, A. (1908) Ein Beitrag zur hydrodynamischen Erklaerung der turbulenten Fluessigkeitsbewegungen, *Proceedings Fourth International Congress of Mathematicians*, Rome, pp116-124 (cited in Criminale et al. (2003, page 431)).

the equations which govern the perturbation variables reduce to a fourth-order eigenvalue problem. In 1929 Tollmien[3] solved the eigenvalue problem for plane Poiseuille flow and in 1933 Schlichting[4] applied this theory to Blasius flow. The predicted instability waves are called Tollmien–Schlichting waves (TS waves) in their honour. The work of these scientists founded the basis of Hydrodynamic Stability Theory in regard to boundary-layer flows.

They predicted a small disturbance to a laminar boundary layer could cause transition. The disturbance can be represented as a linear superposition of waves. If the frequency of a wave and the Reynolds number of the flow are such that the wave is unstable then the disturbance will grow exponentially in the streamwise direction and the flow will undergo transition. If a wave is stable then the disturbance will be damped and the flow is unchanged.

It was not until the 1940s, however, that these theoretical predictions were confirmed by experiment, finally squashing the speculation and disbelief that had surrounded this work. In 1943 Schubauer and Skramstad conducted experiments with extremely low levels of background turbulence and were therefore able to observe the Tollmien–Schlichting waves.

Consider the linear stability of Blasius flow given by $\mathbf{U} = (U(x,z), W(x,z))$ and $\mathrm{P} = 0$. We first stipulate that this flow satisfies the Navier–Stokes equations (4.6). We introduce a small two-dimensional perturbation[5] to this flow given by $\mathbf{u} = (u(x,z,t), w(x,z,t))$ and $p(x,z,t)$ and assume that the total flow, $\mathbf{U}^{\mathrm{T}} = \mathbf{U} + \mathbf{u}$ and $\mathrm{P_T} = p(x,z,t)$, also satisfies the

[3]Tollmien, W. (1929) Über die Entstehung der Turbulenz, *Gesellschaft der Wissenschaften. Göttingen Mathematisch-Naturwissenschaftliche Klasse. Nachrichten*, pp21-44. Translated as The Production of Turbulence. NACA TM-609, 1931 (cited in Criminale et al. (2003, page 432 respectively)).

[4]Schlichting, H. (1933) Zur Entstehung der Turbulenz bei der Plattenströmung, *Gesellschaft der Wissenschaften. Göttingen. Mathematisch-Physikalische Klasse*, pp181-208 (cited in Criminale et al. (2003, page 430)).

[5]Squire's Theorem (1933) states that for incompressible parallel flows, for every three-dimensional linear disturbance there exists a two-dimensional disturbance at a lower Reynolds number. This result has made an important contribution to stability theory, since it means that it is sufficient to study two-dimensional disturbances when searching for the critical Reynolds number of a parallel flow. For large Reynolds numbers Blasius flow can be approximated by a parallel flow.

Navier–Stokes equations (4.7).

$$\begin{aligned} \mathbf{U}\cdot\nabla\mathbf{U} &= \frac{1}{R}\nabla^2\mathbf{U}, \\ \nabla\cdot\mathbf{U} &= 0, \\ \mathbf{U} &= (0,0) \quad \text{on } z=0, \\ \mathbf{U} &= (U_\infty,0) \quad \text{on } z=\infty\ ; \end{aligned} \tag{4.6}$$

$$\begin{aligned} \frac{\partial \mathbf{U}^{\mathrm{T}}}{\partial t} + \mathbf{U}^{\mathrm{T}}\cdot\nabla\mathbf{U}^{\mathrm{T}} &= -\nabla \mathrm{P_T} + \frac{1}{R}\nabla^2\mathbf{U}^{\mathrm{T}}, \\ \nabla\cdot\mathbf{U}^{\mathrm{T}} &= 0, \\ \mathbf{U}^{\mathrm{T}} &= (0,0) \quad \text{at } z=0, \\ \mathbf{U}^{\mathrm{T}} &= (U_\infty,0) \quad \text{at } z=\infty\ . \end{aligned} \tag{4.7}$$

Subtracting the equations in (4.6) from those in (4.7) yields a system of equations that govern the perturbation variables $\mathbf{u}=(u,w)$ and p:

$$\begin{aligned} \frac{\partial \mathbf{u}}{\partial t} + \mathbf{U}\cdot\nabla\mathbf{u} + \mathbf{u}\cdot\nabla\mathbf{U} + \mathbf{u}\cdot\nabla\mathbf{u} &= -\nabla p + \frac{1}{R}\nabla^2\mathbf{u}, \\ \nabla\cdot\mathbf{u} &= 0, \\ \mathbf{u} &= (0,0) \quad \text{at } z=0, \\ \mathbf{u} &= (0,0) \quad \text{at } z=\infty\ . \end{aligned} \tag{4.8}$$

The equations (4.8) are now linearized as the perturbation is necessarily small enough to justify disregarding the nonlinear products of perturbation variables. For large enough Reynolds numbers the growth in boundary layer thickness is small and so we can make the further approximation that the Blasius flow is parallel (that is $\mathbf{U}=(U(z),0)$). The

final system of equations is

$$\begin{aligned}
\frac{\partial u}{\partial t} + U\frac{\partial u}{\partial x} + w\frac{dU}{dz} &= -\frac{\partial p}{\partial x} + \frac{1}{R}\left(\frac{\partial^2 u}{\partial x^2} + \frac{\partial^2 u}{\partial z^2}\right), \\
\frac{\partial w}{\partial t} + U\frac{\partial w}{\partial x} &= -\frac{\partial p}{\partial z} + \frac{1}{R}\left(\frac{\partial^2 w}{\partial x^2} + \frac{\partial^2 w}{\partial z^2}\right), \\
\frac{\partial u}{\partial x} + \frac{\partial w}{\partial z} &= 0, \\
(u, w) &= (0,0) \quad \text{at } z = 0, \\
(u, w) &= (0,0) \quad \text{at } z = \infty .
\end{aligned} \tag{4.9}$$

As the coefficients in the above system of equations are independent of x and t, we look for solutions in the following form:

$$\begin{aligned}
\begin{pmatrix} u \\ w \\ p \end{pmatrix} &= \mathfrak{Re}\left\{ \begin{pmatrix} \hat{u}(z) \\ \hat{w}(z) \\ \hat{p}(z) \end{pmatrix} \exp[i(\alpha x - \omega t)] \right\} \\
&= \mathfrak{Re}\left\{ \begin{pmatrix} \hat{u}(z) \\ \hat{w}(z) \\ \hat{p}(z) \end{pmatrix} \exp[i(\alpha_r x - \omega t)] \exp(-\alpha_i x) \right\},
\end{aligned} \tag{4.10}$$

for $\alpha = \alpha_r + i\alpha_i$, $\hat{u}$, $\hat{v}$, $\hat{p} \in \mathbb{C}$ and $\omega \in \mathbb{R}$. This particular choice of $\alpha \in \mathbb{C}$ and $\omega \in \mathbb{R}$ constitutes a spatial analysis. From (4.10) we can see that this perturbation corresponds to a travelling wave in space (streamwise direction) and time which either grows or decays in the streamwise direction according to the sign of α_i. The z-dependence is contained in the eigenfunction. This spatial analysis relates well to the physical problem and is the natural choice in the case of the boundary layer, rather than a temporal analysis. If (4.10) is substituted into the system of linearized equations (4.9) and the result is expressed in terms of just one variable, say $\hat{w}$, then we find that $\hat{w}(z)$ satisfies the fourth-order linear eigenvalue problem

$$\left(U - \frac{\omega}{\alpha}\right)\left(\mathcal{D}^2 - \alpha^2\right)\hat{w} - U''\hat{w} = \frac{1}{i\,\alpha R}\left(\mathcal{D}^2 - \alpha^2\right)^2 \hat{w}, \qquad \left(\mathcal{D} \equiv \frac{d}{dz}\right) \tag{4.11}$$

which is known as the Orr–Sommerfeld equation. The eigenfunction satisfies homogeneous boundary conditions at $z = 0$ and $z = \infty$.

For a given parallel base flow $U(z)$ (here the Blasius flow), a given Reynolds number and a given frequency, the eigenvalues (α_r, α_i) and eigenfunctions $\hat{w}$ can be determined numerically. The eigenvalues are often displayed in a stability diagram (see figure 4.1 and figure 4.3 for example). Values of ω and R that correspond to the interior of the curve have a negative imaginary wavenumber, and from (4.10) we can see that these modes will be unstable and will grow exponentially. Values of ω and R lying outside the curve result in stable modes which decay exponentially, and values lying on the curve are said to be neutrally stable.

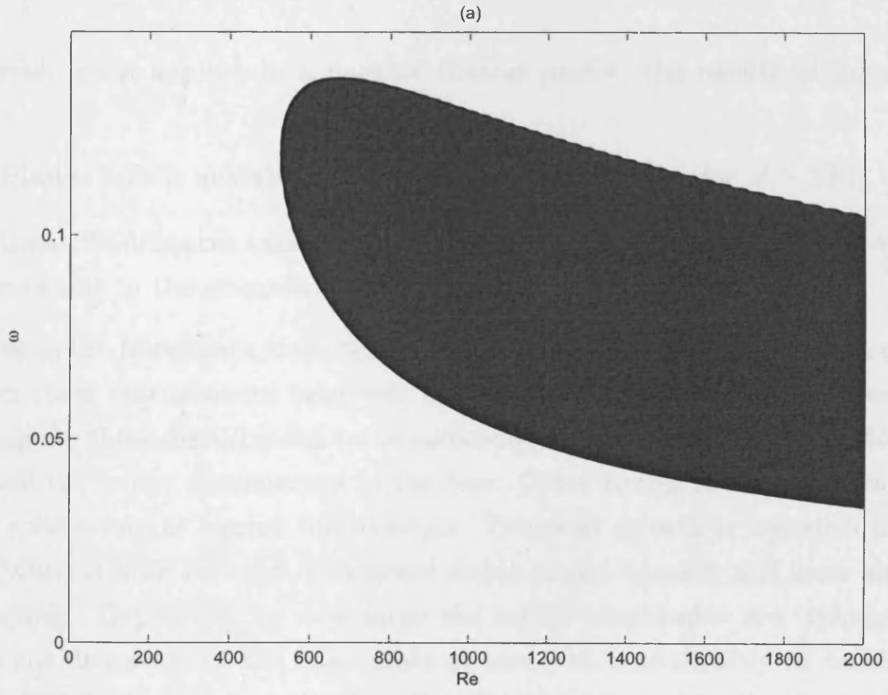

Figure 4.1: A neutral stability curve for the Blasius flow: non-dimensional frequency $\omega = \omega^* \delta^* / U_\infty^*$ against the Reynolds number, Re. The unstable region is shaded.

The stability curve shown in figure 4.1 plots non-dimensional frequency against Reynolds

number. The non-dimensional frequency is derived from the physical frequency ω^* by

$$\omega = \frac{\omega^* \delta^*}{U_\infty^*} ,$$

which means that physical frequency is inversely proportional to the Reynolds number. Therefore on a graph of non-dimensional frequency against Reynolds number, a constant physical frequency will correspond to lines which emanate from the origin:

$$\omega^* = \frac{(U_\infty^*)^2 \omega}{\nu R} .$$

As this can be confusing, plots of the neutral stability curve frequently divide the non-dimensional frequency by the Reynolds number. Constant values of physical frequency will then be represented by lines parallel to the x axis. This can be seen in figure 4.3.

To summarize, when applied to a parallel Blasius profile, the results of linear stability theory are

- that Blasius flow is unstable to infinitesimal disturbances (for $R > 520$),
- that these disturbances take the form of travelling waves which either grow or decay exponentially in the streamwise direction.

Disturbances in the freestream enter the boundary layer by a process known as receptivity. Which form these disturbances take will influence how the flow breaks down. In this thesis we assume these disturbances to be sufficiently small, so that linear stability theory describes well the initial development of the flow. Other routes to transition do exist and are known collectively as bypass mechanisms. Transient growth is one such mechanism, and occurs when at least two non-orthogonal stable modes interact, and grow algebraically before decaying. Depending on how large the initial amplitudes are, transient growth can trigger the distortion of the basic state or can even lead directly to breakdown, see Saric et al. (2002). In this investigation, the disturbances are small enough so that any transient growth will have taken place and then decayed, all within the linear regime. Another route to transition can be caused by high levels of freestream vorticity. The initial disturbance levels used in this study are much lower than those required for this type of bypass transition. Physically, levels of freestream turbulence can be very low for

aircraft when cruising at altitude (Bowles, 2000). (See Schmid and Henningson (2001, chapter 9) and Reshotko (1976) for more details on receptivity and the different routes to transition).

4.3 Weakly Nonlinear Theories

Once disturbances grow to such an extent that linear theory is invalid, we require theories that take into account the nonlinear terms. A common approach is to extend the analysis by considering only the early stages of nonlinearity. Several papers which have done just this with regard to parallel flows are now reviewed.

4.3.1 Results from Triple-deck Theory

The classical linear theory which yields the Orr–Sommerfeld equation is only an approximation when used for almost parallel flows like boundary-layer flow. For non-parallel flows there is a contradiction in the derivation of the Orr–Sommerfeld equation, namely that R is taken as large enough (strictly infinite) to ensure that the flow is parallel, but at the same time, not so large (finite) that the term $\frac{1}{R}\frac{\partial^2 u}{\partial z^2}$ should be neglected. Both conditions for R cannot be satisfied simultaneously. However, the theory has survived as it agrees so well with experiment (aided by the fact that in experiments the dominant disturbances will be those with the highest growth rates, furthest away from the neutral curve).

Smith (1979) makes the point that because of this inherent contradiction in linear theory for boundary-layer flow, the linear theory should not be used as a starting point for a weakly nonlinear theory.

One additional difficulty arises when deriving amplitude equations for boundary layers rather than for parallel flows, namely how to include the non-parallel effects. The slow spatial scale, ξ, should be the slow scale of both the boundary layer growth and the amplitude growth. Close to the critical Reynolds number growth rates are small, and so the scale on which the amplitude develops can be much larger than the scale on which the boundary develop, therefore non-parallel effects will become significant. The experiments of Klingmann et al. (1993) and the numerical work of Fasel and Konzelmann (1990) both show non-parallel effects to be slightly destabilizing. Smith

(1979) and Smith and Burggraf (1985) confirm with asymptotic theory that non-parallel effects are more significant for linear disturbances than for strongly nonlinear disturbances.

By using the triple-deck scalings, Smith (1979) systematically included non-parallel effects. He goes on to show that at first order a Tollmien–Schlichting wave is excited, and at second order various terms are excited, including a mean flow correction term (with no oscillatory part). It is this term that we see in the numerical simulation results wherever $u_{max} \neq |u_{min}|$ (for example see figure 5.15, page 128) where $u_{max} = 0.0265$ and $u_{min} = -0.031$.

Now follows a review of several papers working with exact solutions of the Navier–Stokes equations. Consequently non-parallel effects are not taken into account and the results apply only to parallel flows.

4.3.2 The Landau equation

Stuart (1960) considers the development of a Tollmien–Schlichting wave in plane Poiseuille flow for a temporally evolving disturbance (ie real wavenumber α, and complex frequency ω and phase speed c). The Reynolds number R is close to the critical Reynolds number R_c, in fact $R - R_c := \mathcal{O}(\epsilon^2)$, which ensures that the linear growth rate is small. To determine the growth rate, c_i, for such Reynolds numbers R an expansion is used:

$$\begin{aligned} c_i(R) &= c_i(R_c) + \left.\frac{\mathrm{d}c_i}{\mathrm{d}R}\right|_{R_c} (R - R_c) + \mathcal{O}\left((R - R_c)^2\right) \\ c_i(R) &\propto R - R_c \\ \therefore\ c_i(R) &= \mathcal{O}(\epsilon^2)\ . \end{aligned}$$

Therefore, for a Tollmien–Schlichting wave of the form $\hat{\phi}(z)\exp(i\alpha(x - c_r t))\exp(\alpha c_i t)$, there are two distinct timescales: the slow scale $((\alpha c_i)^{-1})$ related to the growth of the wave, and the relatively fast scale $((\alpha c_r)^{-1})$ related to the oscillation of the wave. This means that the amplitude of the Tollmien–Schlichting wave will change on a slow scale relative to the oscillation.

Stuart then considers the wave interactions that arise due to a streamfunction perturbation

of the form

$$\psi = \epsilon A(t)\hat{\phi}(z)E^1 + \text{cc} \ ,$$

where $E^m = \exp(im\alpha(x - c_r)t)$ and cc is an abbreviation for the complex conjugate. At second order, second harmonics are excited, $E^{\pm 2} = \exp(\pm 2i\alpha(x - c_r)t)$, and also a mean flow term with no oscillatory part, E^0. These second-order terms interact with the original wave in order to produce third order terms, including $\exp(\pm i\alpha(x - c_r)t)$. So it is at third order that the nonlinear terms affect the original wave, which is also the order at which the growth of the Tollmien–Schlichting wave occurs. Stuart shows that the equation satisfied by the wave amplitude $A(t)$ is

$$\frac{\mathrm{d}A}{\mathrm{d}t} = aA + l|A|^2A \ , \tag{4.12}$$

where a is the linear growth rate and l is known as the Landau coefficient.

At this order the nonlinear interactions have given rise to a mode with the same wavenumber as the Tollmien–Schlichting wave, therefore we can derive an equation describing the evolution of the amplitude of the Tollmien–Schlichting wave. The fact that the amplitude equation is cubic is no coincidence. Partial differential equations whose base solution is unstable to wavelike disturbances typically have cubic amplitude equations, since it is at third order that the nonlinear interactions can effect the original disturbance.

Watson (1962) considered the spatial case where the wavenumber is complex and the frequency is real. He showed that the amplitude once again satisfies a Landau equation:

$$\frac{\mathrm{d}A}{\mathrm{d}x} = aA + l|A|^2A \ . \tag{4.13}$$

To see what behaviour the (temporal) Landau equation describes, we first consider two real-valued functions, an amplitude $R(t)$, and a phase, $\theta(t)$ combining to give $A(t) = R(t)\exp(i\theta(t))$. Substituting this into the Landau equation and factoring out an $\exp(i\theta)$ term yields

$$\begin{aligned} \frac{\mathrm{d}R}{\mathrm{d}t} &= a_rR + l_rR^3 \\ \frac{\mathrm{d}\theta}{\mathrm{d}t} &= a_i + l_iR^2 \ . \end{aligned} \tag{4.14}$$

Fixed points R_0 of (4.14) occur for $R_0 = 0$, and $R_0^2 = -a_r/l_r$ provided that $a_r l_r < 0$. (In the case $a_r l_r > 0$ there are two scenarios, neither involving a non-zero fixed point. First, for a_r, $l_r > 0$, there is linear growth for small amplitudes. The nonlinear term then enhances this growth. Second, for a_r, $l_r < 0$ both small and large disturbances will decay so once again there is no non-zero fixed point.) The stability of these fixed points, R_0, can be investigated in the usual manner, by considering the behaviour of $R = R_0 + \varepsilon r$. Substituting this into (4.14) gives

$$\begin{aligned} \frac{\mathrm{d}R}{\mathrm{d}t} &= \varepsilon \frac{\mathrm{d}r}{\mathrm{d}t} = a_r(R_0 + \varepsilon r) + l_r(R_0 + \varepsilon r)^3 \\ \Rightarrow \frac{\mathrm{d}r}{\mathrm{d}t} &= a_r A + 3 l_r R_0^2 r + \mathcal{O}(\varepsilon^2) \, . \end{aligned}$$

For small ε this has the solution $r(t) = r_0 \exp[(a_r + 3 l_r R_0^2)t]$. For $R_0 = 0$ this reduces to $r_0 \exp[a_r t]$ demonstrating that the solution $R_0 = 0$ is stable for $a_r < 0$ and unstable for $a_r > 0$, and furthermore, its stability does not depend on l_r. For $R_0^2 = -a_r/l_r$ the solution reduces to $r_0 \exp[-2a_r t]$, which is stable for $a_r > 0$ and unstable for $a_r < 0$. This information can be displayed on bifurcation diagrams.

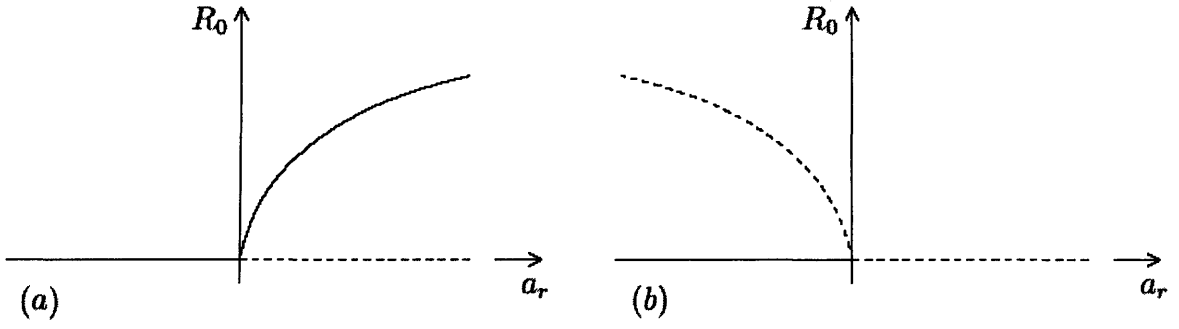

Figure 4.2: Bifurcation diagrams for the solution of (4.14) for (a) $l_r < 0$ and (b) $l_r > 0$. The solid lines correspond to stable branches of the solution and the dashed lines to unstable branches. From Houten (2004).

Referring to figure 4.2, case (a) is known as a supercritical bifurcation, where, for $a_r > 0$, small solutions are unstable, but nonlinearity is stabilizing and so acts to bring about a stable solution. For $a_r < 0$ all solutions are stable. Case (b) is known as a subcritical

bifurcation, where, for $a_r < 0$ small solutions are stable, however large solutions are unstable. For $a_r > 0$ solutions are unstable.

Seen in figure 4.3 are numerical results generated by Houten (2004). Neutral points of disturbances with finite amplitudes of 2% and 4% of the freestream velocity are compared with the neutral curve determined by linear theory for small disturbances. There is a small stabilizing tendency at the lower branch, and at the upper branch the region of instability is extended, which agrees with asymptotic theories. Smith (1979), and Sen and Vashist (1989) predict that waves near the lower branch are stabilized. Goldstein and Durbin (1986) demonstrated that waves of finite amplitude are destabilized close to the upper branch of the neutral curve.

4.3.3 The Ginzburg–Landau equation

Stuart (1960) assumes that the Tollmien–Schlichting wave is periodic in the streamwise direction by choosing an x-dependence of the form $\exp(i\alpha x)$, $\alpha \in \mathcal{R}$. Watson (1962) similarly assumes that the Tollmien–Schlichting wave is periodic, but in time, and chooses a t-dependence of the form $\exp(i\omega t)$, $\omega \in \mathcal{R}$. Stewartson and Stuart (1971) go through a similar process to that laid out in these earlier papers, but allow the wave's amplitude to vary slowly in both space and time. The method is discussed in some detail shortly, in section 4.4. Suffice to say that for a Tollmien–Schlichting wave of the form

$$\psi = \epsilon A(\xi, T)\hat{\phi}(z)E^1 + \text{cc} \ ,$$

where ξ and T vary more slowly than x and t, at third order in ϵ the complex amplitude is shown to satisfy the Ginzburg–Landau equation:

$$\frac{\partial A}{\partial T} - b\frac{\partial^2 A}{\partial \xi^2} = aA + l|A|^2 A \ , \tag{4.15}$$

where a, b, and l are constants.

4.3.4 The Higher-order Ginzburg–Landau Equation

Weinstein (1981) took the multiple-scales approach of Stewartson and Stuart (1971) to higher order and found the following correction terms for the Ginzburg–Landau equa-

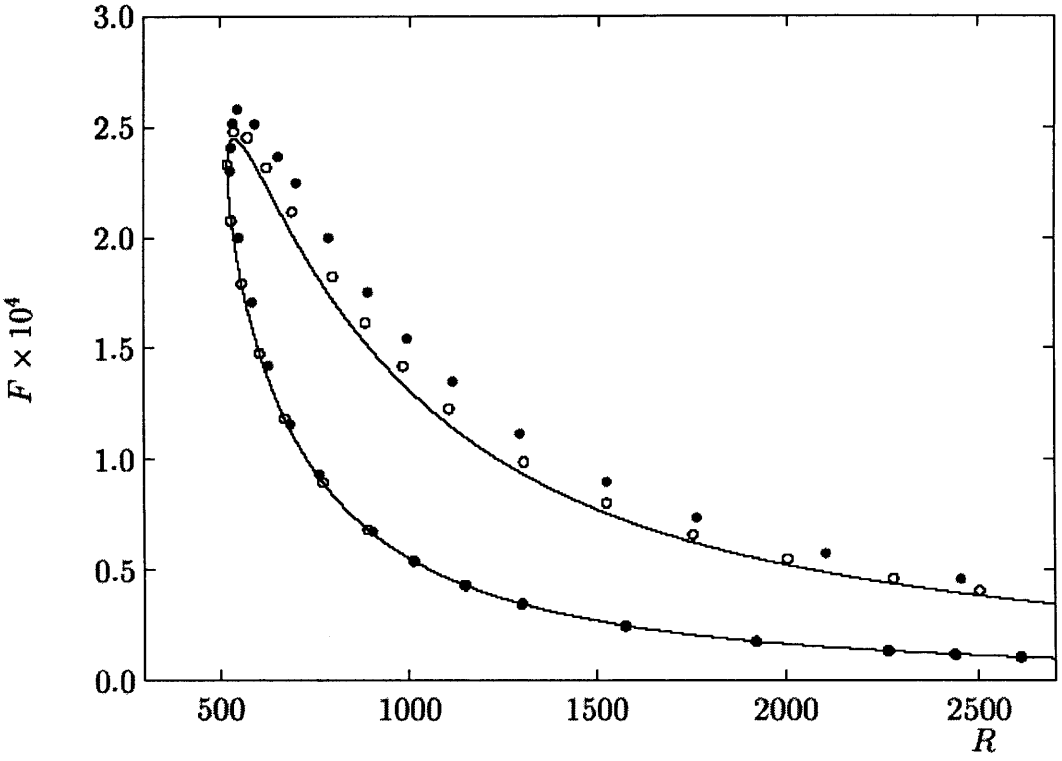

Figure 4.3: Neutral curve from the Orr–Sommerfeld equation (solid curve), with open and filled circles representing numerical results for waves of amplitude of 2% and 4% of the freestream velocity respectively (from Houten, 2004). F is the non-dimensional frequency which is related to the dimensional frequency ω^* (measured in radians/sec) by the following $F = \frac{\omega}{R} = \frac{\omega^* \delta^*}{R U_\infty^*}$.

tion (4.15) at fourth order in ϵ

$$\frac{\partial A}{\partial \xi} + \frac{\partial^3 A}{\partial \xi^3} + A\frac{\partial |A|^2}{\partial \xi} .$$

Ikeda (1977) also found the following fourth-order terms for a wavepacket (symmetric about $\xi = 0$) developing in channel flow using an amplitude expansion method

$$A\frac{\partial |A|^2}{\partial \xi} \qquad \text{or} \qquad A^2\frac{\partial A^*}{\partial \xi} + |A|^2\frac{\partial A}{\partial \xi} . \tag{4.16}$$

Both Weinstein's and Ikeda's terms are spatially varying, and spatially asymmetric. These terms could therefore give rise to wave-envelope steepening. Furthermore, Ikeda argues that the coefficients of the fourth-order terms in (4.16) are large enough that they dominate the third-order term $A|A|^2$ in the case of channel flow, and concludes that, in this case, the evolution of a wavepacket should not be modelled with the Ginzburg–Landau equation, as these correction terms found at 'higher order' are actually significant at the same scale as the cubic term $A|A|^2$.

4.4 Amplitude Equations

Due to their complexity, the Navier–Stokes equations are often treated by methods that aim to simplify them but still capture the essential characteristics of the flow being modelled. This section introduces one such method; the method of multiple scales. For parallel shear flows the multiple scales method reduces the Navier–Stokes equations to much simpler Landau-type equations, which describe the evolution of the amplitude of a disturbance to the base flow. Despite its reduced form, the Landau equation has successfully captured important features of weakly nonlinear fluid flow for parallel flows. This success has led to nearly parallel flows also being modelled by Landau equations.

This section first compares the multiple scales method with its precursor, perturbation theory; then, using the multiple scales theory, an outline of the derivation of the Ginzburg–Landau equation for a parallel flow is presented; the ability of the higher-order Ginzburg–Landau equation to model the wave-envelope steepening effect is then examined, and finally, numerical simulations of the Ginzburg–Landau equation are compared with those

of the full Navier–Stokes equations.

4.4.1 Perturbation Theory and Multiple Scales

This section compares regular perturbation theory with the method of multiple scales by way of example. The problem we look to solve is a second order, ordinary differential equation that describes a linearly-damped oscillator:

$$\begin{aligned} \ddot{y} + y &= -2\epsilon\dot{y}\,, \qquad (0 < \epsilon \ll 1) \\ y(0) &= 1\,, \\ \dot{y}(0) &= 0\,. \end{aligned} \tag{4.17}$$

The dot represents differentiation with respect to t. Regular perturbation theory looks for a solution in the form of an asymptotic approximation

$$y(t) \sim \sum_{n=0}^{N} \epsilon^n y_n(t) \qquad \text{as} \quad \epsilon \to 0. \tag{4.18}$$

For this approximation to be asymptotic, we require that for each $M \leqslant N$

$$\frac{y - \sum_{n=0}^{M} \epsilon^n y_n}{\epsilon^M y_M} \to 0 \qquad \text{as} \quad \epsilon \to 0\,.$$

Following Hinch (1991), in this example we will use a second-order approximation given by

$$y(t) \sim y_0(t) + \epsilon\, y_1(t) + \epsilon^2\, y_2(t)\,. \tag{4.19}$$

According to the definition of an asymptotic approximation, the function ϵy_1 acts as a correction to the leading-order solution y_0, and similarly the function $\epsilon^2 y_2$ acts as a correction to the first-order solution $y_0 + \epsilon y_1$.

On substituting the truncated expansion (4.19) into equation (4.17), collecting terms of the same order and then solving the resulting systems of equations, we have the following second-order approximation to the solution

$$y(t) \sim \cos t + \epsilon\,(\sin t - t\cos t) - \frac{\epsilon^2 t}{2}\,(\sin t - t\cos t)\,. \tag{4.20}$$

For sufficiently large times, that is $t \geqslant \mathcal{O}(1/\epsilon)$, this expansion becomes disordered: successive terms have a similar order of magnitude and no longer act as corrections of decreasing size. Hence, for $t \geqslant \mathcal{O}(1/\epsilon)$, the approximation is no longer asymptotic nor valid.

The breakdown of the asymptotic expansion is associated with the appearance of so-called 'secular' terms[6] in the solution ($\epsilon\, t$ and $(\epsilon\, t)^2$ in (4.20)). These terms arise through a resonance between the forcing term and the homogeneous equation. For example, at first order we wish to solve $\ddot{y}_1 + y_1 = -2\dot{y}_0 = 2\sin t$. The sine term is itself a solution of the homogeneous equation $\ddot{y}_1 + y_1 = 0$, so resonance causes the appearance of a term proportional to ϵt in the solution. This means the solution will grow unbounded in time, which we know to be unphysical. The multiple scales method allows us to eliminate such secular terms.

Upon re-examination of the differential equation (4.17) we can see behaviour on two different time scales. First there is the action of the restoring force that causes the oscillator to overshoot its equilibrium position and oscillate. This occurs on a time scale of $\mathcal{O}(1)$. Second there is a damping effect which occurs on a time scale of $\mathcal{O}(\epsilon^{-1})$. The method of multiple scales allows the leading order solution to depend on both these time scales and therefore to reflect both physical forces.

We will now solve equation (4.17) a second time using the method of multiple scales. Assume the solution takes the form

$$y(\tau, t) \sim y_0(\tau, t) + \epsilon\, y_1(\tau, t) + \epsilon^2\, y_2(\tau, t)\,, \tag{4.21}$$

where $\tau = \epsilon t$ is a slow timescale. The derivatives in (4.17) must be modified because y is now a function of two variables. The multiple scales method is sometimes referred to as

[6]Secular comes from the Latin *saeculum*, literally century, originates as a mathematical term from the field of celestial mechanics. When modelling a planet's orbit it was discovered that, for times of the order of a century (that is long in comparison with the time scale of orbit), the perturbation theory solution would break down. This is directly linked to the fact that a planet's orbit deviates on this long time scale.

the derivative expansion method for this reason.

$$\text{Thus} \quad \frac{d}{dt} \quad \text{is replaced by} \quad \frac{\partial}{\partial t} + \epsilon \frac{\partial}{\partial \tau} \tag{4.22}$$

$$\text{and} \quad \frac{d^2}{dt^2} \quad \text{is replaced by} \quad \frac{\partial^2}{\partial t^2} + 2\epsilon \frac{\partial^2}{\partial \tau \, \partial t} + \epsilon^2 \frac{\partial^2}{\partial^2 \tau} \, . \tag{4.23}$$

Equation (4.17) becomes

$$\begin{aligned} \frac{\partial^2 y}{\partial^2 t} + 2\epsilon \frac{\partial^2 y}{\partial t \partial \tau} + \epsilon^2 \frac{\partial^2 y}{\partial^2 \tau} + y &= -2\epsilon \left(\frac{\partial y}{\partial t} + \epsilon \frac{\partial y}{\partial \tau} \right) \\ y\,(0,0) &= 1 \\ \left. \frac{\partial y}{\partial t} + \epsilon \frac{\partial y}{\partial \tau} \right|_{(0,0)} &= 0 \, . \end{aligned} \tag{4.24}$$

After substituting our expression for y (from (4.21)) into (4.24), at leading order, the partial differential equation and boundary conditions are

$$\begin{aligned} \frac{\partial^2 y_0}{\partial^2 t} + y_0 &= 0 \\ y_0\,(0,0) &= 1 \\ \left. \frac{\partial y_0}{\partial t} \right|_{(0,0)} &= 0 \, . \end{aligned} \tag{4.25}$$

The solution to this equation is

$$y_0 = A(\tau) \cos t + B(\tau) \sin t \, , \qquad \text{with } A(0) = 1 \text{ and } B(0) = 0 \, . \tag{4.26}$$

At first order the partial differential equation to be solved is

$$\begin{aligned} \frac{\partial^2 y_1}{\partial^2 t} + y_1 &= -2 \frac{\partial^2 y_0}{\partial t \partial \tau} - 2 \frac{\partial y_0}{\partial t} \\ &= 2 \left(\frac{dA(\tau)}{d\tau} + A(\tau) \right) \sin t - 2 \left(\frac{dB(\tau)}{d\tau} + B(\tau) \right) \cos t \, . \end{aligned} \tag{4.27}$$

This is an inhomogeneous equation, so for a unique solution to exist the right-hand side

must be orthogonal to solutions of the homogenous equation. In other words

$$2\int_0^{2\pi}\left[\left(\frac{dA(\tau)}{d\tau}+A(\tau)\right)\sin t-\left(\frac{dB(\tau)}{d\tau}+B(\tau)\right)\cos t\right]\sin t\,dt \;=\; 0 \quad (4.28)$$

$$\text{and}\quad 2\int_0^{2\pi}\left[\left(\frac{dA(\tau)}{d\tau}+A(\tau)\right)\sin t-\left(\frac{dB(\tau)}{d\tau}+B(\tau)\right)\cos t\right]\cos t\,dt \;=\; 0 \quad (4.29)$$

In order to satisfy equations (4.28) and (4.29) we require that

$$\frac{dA(\tau)}{d\tau}+A(\tau)=0 \quad \text{and} \quad \frac{dB(\tau)}{d\tau}+B(\tau)=0\,. \quad (4.30)$$

Solving these with the initial conditions $A(0)=1$ and $B(0)=1$ yields $A(\tau)=\exp(-\tau)$ and $B(\tau)=0$. The leading-order approximation to the solution using multiple scales is therefore

$$y(\tau,t)\sim\exp(-\tau)\cos t\,. \quad (4.31)$$

Unlike when using regular perturbation theory, we are now in a position to suppress the resonance that would occur between the inhomogeneous terms and the homogeneous differential equation. The free parameters $A(\tau)$ and $B(\tau)$ that were introduced in (4.26) appear in (4.27) and can be chosen to suppress this resonance. Thus we prevent the appearance of secular terms in the solution.

Note that the first term in the asymptotic approximation is not the solution to the reduced problem, but already an improvement on it. There is no zeroth-order term with this method, the leading-order term is correct to first order.

To proceed further, we return to the first-order equation (4.27) and substitute for A and B, leaving

$$\begin{aligned}\frac{\partial^2 y_1}{\partial t^2}+y_1 &= 0\,,\\ y_1(0,0) &= 0\,,\\ \left.\frac{\partial y_1}{\partial t}\right|_{(0,0)} &= -\left.\frac{\partial y_0}{\partial \tau}\right|_{(0,0)}=1\,.\end{aligned} \quad (4.32)$$

The general solution of this is

$$C(\tau)\cos t + D(\tau)\sin t \qquad \text{where} \quad C(0) = 0 \quad \text{and} \quad D(0) = 1 \ .$$

To fully evaluate C and D we need to look at the second-order equation

$$\begin{aligned} \frac{\partial^2 y_2}{\partial^2 t} + y_2 &= -2\frac{\partial^2 y_1}{\partial t \partial \tau} - 2\frac{\partial y_1}{\partial t} - \frac{\partial^2 y_0}{\partial \tau^2} - 2\frac{\partial y_0}{\partial \tau} \\ &= 2\left(\frac{dC(\tau)}{d\tau} + C(\tau)\right)\sin t - 2\left(\frac{dD(\tau)}{d\tau} + D(\tau) - \frac{1}{2}\exp(-\tau)\right)\cos t \ . \end{aligned} \tag{4.33}$$

Once again, we enforce the condition that C and D must satisfy

$$\frac{dC(\tau)}{d\tau} + C(\tau) = 0 \qquad \text{and} \qquad \frac{dD(\tau)}{d\tau} + D(\tau) - \frac{1}{2}\exp(-\tau) = 0 \ ,$$

hence eliminating terms which would otherwise lead to a resonant forcing and secular terms. Solving for C and D with the initial conditions $C(0) = 0$ and $D(0) = 1$, yields $C(\tau) = 0$ and $D(\tau) = \left(\frac{\tau}{2} + 1\right)\exp(-\tau)$. The second-order approximation to the solution using the multiple scales method is

$$y(\tau, t) = \exp(-\tau)\cos t + \epsilon\left(\frac{\tau}{2} + 1\right)\exp(-\tau)\sin t \ . \tag{4.34}$$

From (4.34) we can see that it is no longer possible to prevent a secular term from appearing in the approximation to the solution. So, when $\tau \geqslant \mathcal{O}(\epsilon^{-1})$ or when $t \geqslant \mathcal{O}(\epsilon^{-2})$ the approximation is no longer valid. In order to increase the range of time for which the solution is valid we could introduce a third time scale to the problem, say $T = \epsilon\tau = \epsilon^2 t$.

There is an exact solution to this problem, given by

$$\exp(-\epsilon t)\left[\cos\left(t\sqrt{1-\epsilon^2}\right) + \frac{\epsilon}{\sqrt{1-\epsilon^2}}\sin\left(t\sqrt{1-\epsilon^2}\right)\right] \ . \tag{4.35}$$

The following plots in figure 4.4 compare the first and second order solutions given by both regular perturbation theory and multiple scales theory with the exact solution. We would expect an accuracy of $\mathcal{O}(\epsilon)$ and $\mathcal{O}(\epsilon^2)$ respectively, however the presence of

the secular terms will restrict the range to $t < \mathcal{O}(1/\epsilon)$. Even in this restricted range the perturbation theory solutions differ substantially from the exact solution. The two multiple scales solutions are almost indistinguishable from one another and also from the exact solution. Only at larger times we can see a (small) difference between the multiple scales solutions and the exact solution (see figure 4.5).

The regular perturbation solutions plotted are

$$y_{p1} \sim \cos t + \epsilon(\sin t - t\cos t) \tag{4.36}$$

$$\text{and} \quad y_{p2} \sim \cos t + \epsilon(\sin t - t\cos t) - \frac{\epsilon^2 t}{2}(\sin t - t\cos t)\ , \tag{4.37}$$

and the multiple scales solutions are

$$y_{m1} \sim \exp(-\tau)\ \cos t \tag{4.38}$$

$$\text{and} \quad y_{m2} \sim \exp(-\tau)\left(\cos t + \epsilon\left(\frac{\tau}{2}+1\right)\sin t\right)\ . \tag{4.39}$$

After having demonstrated the power of the multiple scales method, the next section outlines how this method has been applied to fluid flow.

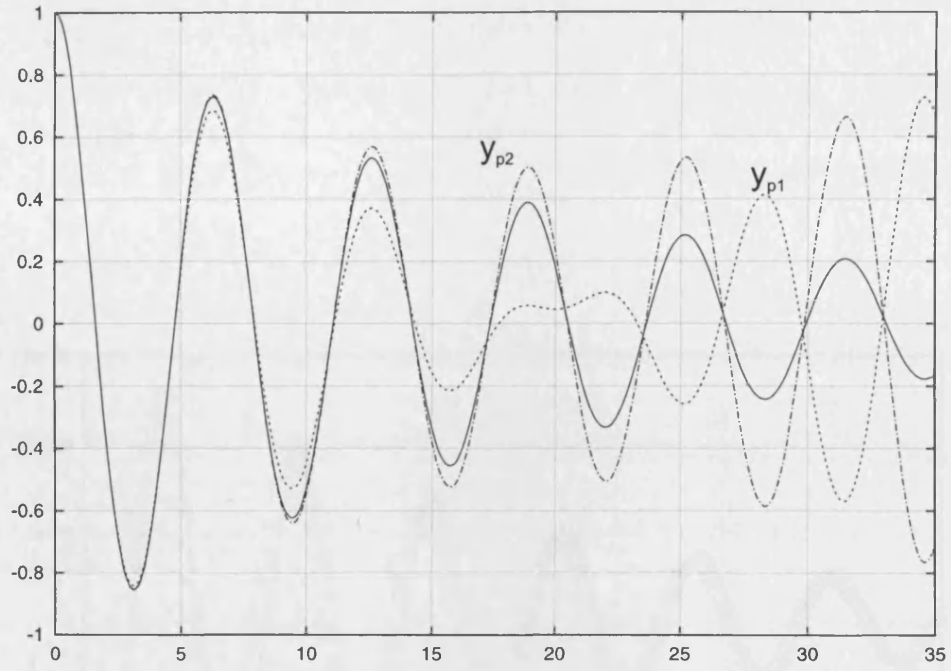

(a) Exact solution (solid curve), and regular perturbation theory solutions; first approximation (y_{p1} dots) and second approximation (y_{p2} dashes and dots)

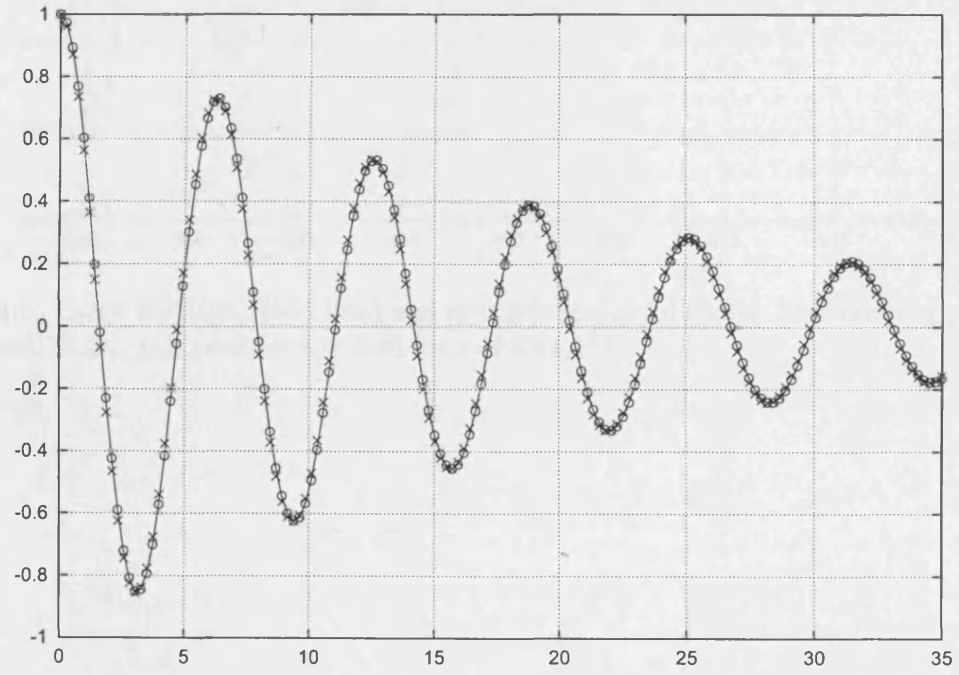

(b) Multiple scales solutions: exact solution (solid curve), first approximation (y_{m1} ($\times\times\times$)) and second approximation (y_{m2} ($\circ\circ\circ$))

Figure 4.4: Solutions of the linearly-damped oscillator for $\epsilon = 0.05$

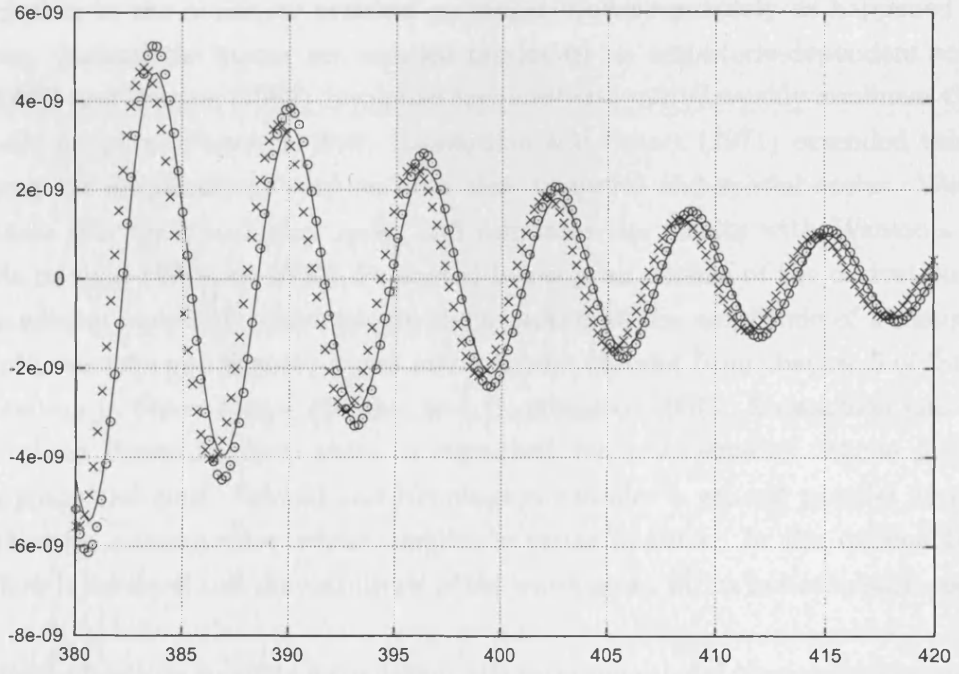

Figure 4.5: Exact solution (solid line) and multiple scales solutions: first order, y_{m1} ($\times\times\times$); and second order, y_{m2} ($\circ\circ\circ$) for $\epsilon = 0.05$ for t of $\mathcal{O}(1/\epsilon^2)$

4.4.2 Derivation of the Ginzburg–Landau equation

The eigenfunctions or solutions arising from linear theory do not depend on the initial amplitude of the disturbance. Therefore, linear theory cannot fully predict how the amplitude of a disturbance will evolve. Once a disturbance grows large enough to invalidate this theory, a new 'theory' is required, which takes into account nonlinearity. A weakly nonlinear theory can be developed using multiple-scales theory when a disturbance has an amplitude that changes slowly in comparison with its wavelength (or frequency). The Fourier modes of the solution to the nonlinear problem no longer evolve separately as happened in the linear case. Instead the modes are coupled producing an amplitude-dependent solution. Stuart (1960) and Watson (1962) developed temporal and spatial weakly nonlinear theories respectively for plane Poiseuille flow. Stewartson and Stuart (1971) extended this work by allowing the amplitude to vary on both slow temporal and spatial scales. Weinstein (1981) takes this work to higher order and compares the results with Watson's earlier amplitude method (Watson, 1960). Presented below is an outline of the derivation of the weakly nonlinear equations which govern the evolution of the amplitude of a disturbance based on Stewartson and Stuart's paper and a similar account from chapter 5 of 'Stability and Transition in Shear Flows' (Schmid and Henningson, 2001). Stewartson and Stuart consider plane Poiseuille flow which is disturbed by a wavepacket whose amplitude varies in space and time. Schmid and Henningson consider a general parallel flow which is disturbed by a wavepacket whose amplitude varies in time. In the outline below a parallel flow is assumed and the amplitude of the wavepacket varies in both space and time.

Using a streamfunction vorticity formulation, the two-dimensional Navier–Stokes equations are

$$\frac{\partial \omega}{\partial t} + U\frac{\partial \omega}{\partial x} + U''\frac{\partial \Psi}{\partial x} - \frac{1}{R}\nabla^2\omega = \frac{\partial \Psi}{\partial x}\frac{\partial \omega}{\partial z} - \frac{\partial \Psi}{\partial z}\frac{\partial \omega}{\partial x}, \tag{4.40}$$

where ω and Ψ are perturbations dependent on x, z, t, and U represents the basic, parallel flow that depends only on z.

We wish to treat this problem using the method of multiple scales and so introduce 'slow' variables in space and time. A linear wavepacket spreads out spatially as the square root

of time, so Stewartson and Stuart chose the following two scales

$$\tau = \epsilon^2 t \qquad \text{and} \qquad \xi = \epsilon(x - c_g t), \tag{4.41}$$

where c_g is the group velocity of the critical Tollmien–Schlichting wave. The perturbations now depend on x, y, t, ξ and τ. The derivatives in (4.40) are expanded as follows:

$$\frac{\partial}{\partial t} \longrightarrow \frac{\partial}{\partial t} - \epsilon c_g \frac{\partial}{\partial \xi} + \epsilon^2 \frac{\partial}{\partial \tau} \tag{4.42a}$$

$$\frac{\partial}{\partial x} \longrightarrow \frac{\partial}{\partial x} + \epsilon \frac{\partial}{\partial \xi} \tag{4.42b}$$

$$\frac{\partial^2}{\partial x^2} \longrightarrow \frac{\partial^2}{\partial x^2} + 2\epsilon \frac{\partial^2}{\partial x \partial \xi} + \epsilon^2 \frac{\partial^2}{\partial \xi^2} \tag{4.42c}$$

In this analysis we expand about a neutral state, in fact, the critical state (α_c, R_c). Being close to the neutral curve means that the growth rates are not too large, and being in the vicinity of the critical point ensures that the range of unstable wavenumbers is not too large. Both these properties ensure that the scale of the oscillation of the wave is well-separated from the scale on which the amplitude of the wavepacket varies. So, we choose $R > R_c$ such that

$$\epsilon^2 = \frac{1}{R_c} - \frac{1}{R} \,. \tag{4.43}$$

Finally an expansion is chosen for the streamfunction

$$\Psi = \sum_{m=-\infty}^{\infty} \sum_{n=0}^{2} \epsilon^{1+|(|m|-1)|+n} \, \phi_{m,1+|(|m|-1)|+n} \, E^m \,, \tag{4.44}$$

where $E^m = \exp(im\alpha(x - ct))$, c is the real phase velocity of the dominant two-dimensional Tollmien–Schlichting wave according to linear theory and $\phi(z, \xi, \tau)$. In fact, to derive an equation governing the amplitude of the disturbance, we need just the following terms:

$$\Psi = \epsilon^2 \phi_{02} E^0 + (\epsilon \phi_{11} + \epsilon^2 \phi_{12} + \epsilon^3 \phi_{13}) E^1 + (\epsilon \phi_{-11} + \epsilon^2 \phi_{-12} + \epsilon^3 \phi_{-13}) E^{-1} + \epsilon^2 \phi_{22} E^2 + \epsilon^2 \phi_{-22} E^{-2} \,. \tag{4.45}$$

(The comma in (4.44) has been dropped from ϕ in (4.45) as here both the indices of ϕ are

single digits.) The expression for ω is

$$\begin{aligned} \omega &= -\nabla^2\Psi \\ &= \left(\frac{\partial^2}{\partial x^2} + \frac{\partial^2}{\partial z^2} + 2\epsilon\frac{\partial^2}{\partial x \partial \xi} + \epsilon^2\frac{\partial^2}{\partial \xi^2}\right)\Psi \ . \end{aligned} \tag{4.46}$$

Substituting for the derivatives using (4.42), the Reynolds number (4.43), for ψ and ω using (4.45) and (4.46), and collecting first order terms we have

$$\underbrace{(U-c)(\mathcal{D}^2-\alpha^2)\phi_{11} - U''\phi_{11} - \frac{1}{i\alpha R_c}(\mathcal{D}^2-\alpha^2)^2\phi_{11}}_{L_{OS(\alpha)}\phi_{11}} = 0 \ , \tag{4.47}$$

where $\mathcal{D} = \frac{d}{dz}$. This is the Orr–Sommerfeld operator acting on ϕ_{11}. As this operator only acts on functions of z we can deduce the following

$$\phi_{11}(\xi,\tau,z) = A_1(\xi,\tau)\,\psi_1(z), \quad \text{where} \quad L_{OS(\alpha)}\psi_1(z) = 0 \ . \tag{4.48}$$

So ϕ_{11} splits into two parts: a slowly-evolving amplitude $A_1(\xi,\tau)$; and a function that depends only on z and which satisfies the Orr–Sommerfeld equation.

At second order we have three equations for three modes:

$$\mathcal{D}^4\phi_{02} = i\alpha|A_1|^2 f_{02}(z) \tag{4.49a}$$

$$L_{OS(\alpha)}\phi_{12} = \frac{i}{\alpha}\frac{\partial A_1}{\partial \xi} f_{12}(z) \tag{4.49b}$$

$$L_{OS(2\alpha)}\phi_{22} = A_1^2 f_{22}(z) \tag{4.49c}$$

With minor modifications due to differences in notation, expressions for $f_{02}(z)$, $f_{12}(z)$ and $f_{22}(z)$ can be found in Stewartson and Stuart (1971, pages 538-539). The important thing is that these functions depend only on z, their particular form does not affect the argument.

Equations (4.49a) and (4.49c) have no complementary function which satisfies the boundary conditions ($\phi_{11} = 0$ at $z = 0$ and $z \to \infty$). This is immediate for (4.49a). In the case

of (4.49c), in general if α and ω satisfy the dispersion relation for Tollmien–Schlichting waves, then 2α and ω do not. The solutions of (4.49a) and (4.49c) take the form

$$\phi_{02} = |A_1|^2 F_{02}(z) \tag{4.50a}$$

$$\phi_{22} = A_1^2 F_{22}(z) \; . \tag{4.50b}$$

The operator on the left-hand side of (4.49b) is the same as that in (4.47). There exists a solution to the inhomogeneous equation (4.49b) if the integral of the right-hand side of (4.49b) multiplied by a solution of the adjoint of the homogeneous operator (4.47) is equal to zero. We assume it exists. It has a particular solution and a complementary function involving a second amplitude function $A_2(\xi, \tau)$:

$$\phi_{12} = \frac{\partial A_1}{\partial \xi} H(z) + A_2 \psi_1 \; .$$

All of this brings us no closer to finding an equation which describes the evolution of the amplitude, so continuing to third order we have

$$L_{OS(\alpha)}\phi_{13} = a_{13}(z)\frac{\partial A_1}{\partial \tau} + b_{13}(z)\frac{\partial^2 A_1}{\partial \xi^2} + c_{13}(z)A_1 + d_{13}(y)A_1|A_1|^2 + \frac{i}{\alpha}\frac{\partial A_2}{\partial \xi} f_{12}(z) \; . \tag{4.51}$$

The functions $a_{13}(z)$, $b_{13}(z)$, $c_{13}(z)$ and $d_{13}(z)$ could be calculated in a similar manner to $f_{02}(z)$, $f_{12}(z)$ and $f_{22}(z)$. This will not be done here: sufficient for this argument is that these functions depend only on z.

At this stage it is useful to observe that at second order there is a term $\frac{i}{\alpha} f_{12}(z)\frac{\partial}{\partial \xi}$ operating on A_1 (see (4.49b)), and here, at third order, the same operator acts on A_2 (see (4.51)). This suggests that the amplitude might take the form $A = A_1 + \epsilon A_2$. Consider the equations involving the wavenumber α at first and second order. If we rewrite these using A instead of A_1 and A_2, we will redistribute the terms in a manner that will allow us to

make progress. Therefore, writing $A = A_1 + \epsilon A_2$ gives

$$\begin{aligned} L_{OS(\alpha)}\phi_{11} &= 0 \\ \phi_{11} &= (A_1 + \epsilon A_2)\psi_1 = A\psi_1 \\ L_{OS(\alpha)}\phi_{12} &= \frac{i}{\alpha}\frac{\partial(A_1 + \epsilon A_2)}{\partial\xi} f_{12}(z) = \frac{i}{\alpha}\frac{\partial A}{\partial\xi} f_{12}(z), \\ \phi_{12} &= \frac{\partial(A_1 + \epsilon A_2)}{\partial\xi} H(z) = \frac{\partial A}{\partial\xi} H(z) \end{aligned}$$

Equation (4.51) can now be rewritten without the term $\frac{i}{\alpha} f_{12}(z)\frac{\partial A_2}{\partial\xi}$, as this has now been taken account of in the equation for $L_{OS(\alpha)}\phi_{12}$. Thus equation (4.51) becomes

$$L_{OS(\alpha)}\phi_{13} = a_{13}(z)\frac{\partial A_1}{\partial\tau} + b_{13}(z)\frac{\partial^2 A_1}{\partial\xi^2} + c_{13}(z)A_1 + d_{13}(z)A_1|A_1|^2 \,. \qquad (4.52)$$

As the operator on the left-hand side of (4.52) already has a homogenous solution, in order that a solution to the problem (4.52) exists, a certain integral condition must be satisfied, namely

$$\int_0^\infty \Phi \left(a_{13}(z)\frac{\partial A_1}{\partial\tau} + b_{13}(z)\frac{\partial^2 A_1}{\partial\xi^2} + c_{13}(z)A_1 + d_{13}(z)A_1|A_1|^2 \right) dz = 0 \,,$$

where Φ is the solution of the adjoint of L_{OS}. As terms involving the amplitude A_1 are not affected by the integral they can be taken outside giving

$$\frac{\partial A_1}{\partial\tau}\int_0^\infty \Phi\, a_{13}(z)dz + \frac{\partial^2 A_1}{\partial\xi^2}\int_0^\infty \Phi\, b_{13}(z)dz + A_1\int_0^\infty \Phi\, c_{13}(z)dz + A_1|A_1|^2\int_0^\infty \Phi\, d_{13}(z)\, dz = 0 \,, \qquad (4.53)$$

or

$$\frac{\partial A_1}{\partial\tau} + b\frac{\partial^2 A_1}{\partial\xi^2} = aA_1 + lA_1|A_1|^2 \,, \qquad \text{(for } b, \text{ } a \text{ and } l \in \mathbb{C}\text{)} \,. \qquad (4.54)$$

where b, a and l are given by

$$b = \frac{\int_0^\infty \Phi\, b_{13}(z)\, dz}{\int_0^\infty \Phi\, a_{13}(z)\, dz} \,, \qquad a = \frac{-\int_0^\infty \Phi\, c_{13}(z)\, dz}{\int_0^\infty \Phi\, a_{13}(z)\, dz} \,; \qquad \text{and} \qquad l = \frac{-\int_0^\infty \Phi\, d_{13}(z)\, dz}{\int_0^\infty \Phi\, a_{13}(z)\, dz} \,.$$

Equation (4.54) is known as the Ginzburg–Landau equation.

Proceeding in a similar manner to fourth-order in ϵ yields the following equation

$$L_{OS(\alpha)}\phi_{14} = a_{13}(z)\frac{\partial A_2}{\partial \tau} + b_{13}(z)\frac{\partial^2 A_2}{\partial \xi^2} + c_{13}(z)A_2 + d_{13}(z)\left(A_1^2 A_2^* + 2|A_1|^2 A_2\right) \quad (4.55a)$$

$$+a_{14}(z)\frac{\partial A_1}{\partial \xi} + b_{14}(z)\frac{\partial^3 A_1}{\partial \xi^3} + c_{14}(z)A_1^2\frac{\partial A_1^*}{\partial \xi} + d_{14}(z)|A_1|^2\frac{\partial A_1}{\partial \xi} + \frac{i}{\alpha}f_{12}(z)\frac{\partial A_3}{\partial \xi}\,. \quad (4.55b)$$

Once again, we recall that $A = A_1 + \epsilon A_2$ and rewrite the third-order equations in terms of A. Consider again the equation for ϕ_{13} given in (4.52). If we write A in place of A_1 here, then the terms on the top row, (4.55a), can be omitted from (4.55) as they will have already been taken account of in equation (4.52). Finally, the last term of (4.55b) will be taken account of in equation (4.49b) if we expand as follows $A = A_1 + \epsilon A_2 + \epsilon^2 A_3$. As previously noted, there is a homogenous solution to the operator $L_{OS(\alpha)}$. Therefore equation (4.55) has a solution if the remaining terms on the right-hand side satisfy an integral constraint:

$$\int_0^\infty \Phi\left(a_{14}(z)\frac{\partial A_1}{\partial \xi} + b_{14}(z)\frac{\partial^3 A_1}{\partial \xi^3} + c_{14}(z)A_1^2\frac{\partial A_1^*}{\partial \xi} + d_{14}(z)|A_1|^2\frac{\partial A_1}{\partial \xi}\right) dz = 0\,. \quad (4.56)$$

Combining the results of the integral conditions (4.53) and (4.56), we have

$$\frac{\partial(A_1+\epsilon A_2)}{\partial \tau} + b\frac{\partial^2(A_1+\epsilon A_2)}{\partial \xi^2} = a(A_1+\epsilon A_2) + lA_1|A_1|^2 + \epsilon\left\{l\left(A_1^2A_2^* + 2|A_1|^2A_2\right)\right.$$
$$\left. + a_{14}(z)\frac{\partial A_1}{\partial \xi} + b_{14}(z)\frac{\partial^3 A_1}{\partial \xi^3} + c_{14}(z)A_1^2\frac{\partial A_1^*}{\partial \xi} + d_{14}(z)|A_1|^2\frac{\partial A_1}{\partial \xi}\right\}.$$

Writing A for $A_1 + \epsilon A_2 + \epsilon^2 A_3 + \cdots$ and including terms of $\mathcal{O}(1)$ and $\mathcal{O}(\epsilon)$ we have the higher-order complex Ginzburg–Landau equation

$$\frac{\partial A}{\partial \tau} + b\frac{\partial^2 A}{\partial \xi^2} = aA + lA|A|^2 + \epsilon\left(a_{14}(z)\frac{\partial A}{\partial \xi} + b_{14}(z)\frac{\partial^3 A}{\partial \xi^3} + c_{14}(z)A^2\frac{\partial A^*}{\partial \xi} + d_{14}(z)|A|^2\frac{\partial A}{\partial \xi}\right).$$

So, in summary,

- by introducing two slow scales τ and ξ, and expanding the derivatives accordingly;

- by expanding the streamfunction according to

$$\Psi = \epsilon^2\phi_{02}E^0+(\epsilon\phi_{11}+\epsilon^2\phi_{12}+\epsilon^3\phi_{13})E^1+(\epsilon\phi_{-11}+\epsilon^2\phi_{-12}+\epsilon^3\phi_{-13})E^{-1}+\epsilon^2\phi_{22}E^2+\epsilon^2\phi_{-22}E^{-2}$$

  where $E = \exp(i\alpha(x-ct))$;

- by expanding about the critical state having chosen R such that $\epsilon^2 = \frac{1}{R_c} - \frac{1}{R}$;

and substituting these expressions into the Navier–Stokes equation, at third order in ϵ we find the evolution of the amplitude of the disturbance is governed by a complex Ginzburg–Landau equation, and at fourth order in ϵ, the amplitude is governed by a higher-order complex Ginzburg–Landau equation. With this description of weakly nonlinear behaviour the following sections go on to investigate whether such Ginzburg–Landau type equations can predict wave-envelope steepening.

4.5 The Ginzburg–Landau equation and Wave-envelope steepening

Healey (2000) comments that the Ginzburg–Landau equation (4.15) cannot explain the wave-envelope steepening effect, as it has no capacity to model spatial asymmetry. This can be demonstrated by considering both positive and negative values of ξ where $\xi > 0$

$$\xi: \qquad \frac{\partial A}{\partial T} - b\frac{\partial^2 A}{\partial \xi^2} = aA + l|A|^2A\,, \tag{4.57a}$$

$$-\xi: \qquad \frac{\partial A}{\partial T} - b\frac{\partial^2 A}{\partial \xi^2} = aA + l|A|^2A\,. \tag{4.57b}$$

The evolution of the amplitude is thus identical for ξ and $-\xi$ according to (4.57). To model wave-envelope steepening we need a model which is not spatially invariant because the growing section of the wavepacket (which occurs for $\xi < 0$), evolves in a different way to the decaying section ($\xi > 0$).

We shall demonstrate that the higher-order terms of the Ginzburg–Landau equation do allow for the possibility of wave-envelope steepening. Taking the higher-order terms of

Ikeda (1977) we have

$$\frac{\partial A}{\partial T} - b\frac{\partial^2 A}{\partial \xi^2} = aA + l|A|^2 A + \epsilon\left(m|A|^2\frac{\partial A}{\partial \xi} + n|A|^2\frac{\partial A^*}{\partial \xi}\right) . \tag{4.58}$$

If we consider positive and negative values of ξ (where $\xi > 0$) then from (4.58) we can see that the evolution of the amplitude differs according to the sign of ξ:

$$\xi : \quad \frac{\partial A}{\partial T} - b\frac{\partial^2 A}{\partial \xi^2} = aA + l|A|^2 A + \epsilon\left(m|A|^2\frac{\partial A}{\partial \xi} + n|A|^2\frac{\partial A^*}{\partial \xi}\right) , \tag{4.59a}$$

$$-\xi : \quad \frac{\partial A}{\partial T} - b\frac{\partial^2 A}{\partial \xi^2} = aA + l|A|^2 A - \epsilon\left(m|A|^2\frac{\partial A}{\partial \xi} + n|A|^2\frac{\partial A^*}{\partial \xi}\right) . \tag{4.59b}$$

From (4.59) we see that the higher-order complex Ginzburg–Landau equation does include terms that depend on the sign of ξ and therefore the higher-order complex Ginzburg–Landau equation could give rise to wave-envelope steepening.

Ikeda (1977) ran some numerical simulations to demonstrate the difference between a wavepacket evolving according to the complex Ginzburg–Landau equation, see (4.54), and one evolving according to the complex Ginzburg–Landau equation with higher-order terms, see (4.58). The results show clearly that a wavepacket governed by (4.54) evolves symmetrically, and one governed by (4.58) evolves asymmetrically. In fact, the wavepacket becomes steeper at the leading edge and less steep at the trailing edge as we have found in our two-dimensional numerical simulations. Ikeda's model is also based on two spatial dimensions.

To gain a better understanding of the behaviour described by the higher-order complex Ginzburg–Landau equation, following Healey (2000), we substitute $A = Re^{i\theta}$ and extract the real terms. Starting from (4.58), making the substitution, and then factoring out $e^{i\theta}$ leaves a real part of

$$\frac{\partial R}{\partial \tau} + C\frac{\partial R}{\partial \xi} - b_r\frac{\partial^2 R}{\partial \xi^2} = DR + LR^3 , \tag{4.60}$$

$$\begin{aligned} \text{where} \quad C &= -\epsilon(m_r + n_r)R^2 + 2b_i\frac{\partial\theta}{\partial\xi}\,, \\ D &= a_r - b_i\frac{\partial^2\theta}{\partial\xi^2} - b_r\left(\frac{\partial\theta}{\partial\xi}\right)^2\,, \\ \text{and} \quad L &= l_r - \epsilon(m_i - n_i)\frac{\partial\theta}{\partial\xi}\,. \end{aligned}$$

These expressions for the coefficients C, D, and L serve as corrections to those given in Healey (2000), where some of the signs are incorrect[7].

The slow spatial scale ξ is in a reference frame moving at the group velocity of the most unstable wave given by two-dimensional linear theory. The coefficient C represents the difference between this and the actual speed of the wavepacket. The crucial result from (4.60) is that the velocity depends on the amplitude (C depends on R). This suggests that the model could give rise to wave-envelope steepening. The following section demonstrates how this real-valued evolution equation behaves using numerical simulation results.

4.6 Numerical Results

To simplify (4.60) further, we will assume that diffusion is negligible and that the coefficient of the convective term is dominated by the R^2 term, so we write $C = \mu R^2$ where $\mu = \pm 1$. If we consider a state very close to the neutral curve then l will be small, and, in fact, at the critical point l changes sign (see Houten, 2004, chapter 5). For the sake of simplicity, we set $L = 0$. So, equation (4.60) reduces to

$$\frac{\partial R}{\partial\tau} + C\frac{\partial R}{\partial\xi} = DR\,. \tag{4.61}$$

This equation can be solved by the method of characteristics to give the behaviour of $R(X(T), T)$ along the characteristic lines $X(T)$. We hope to find these characteristics along which R depends only on time. Restricting the derivative of R to the characteristics gives

$$\frac{dR}{dT}(X(T), T) = \frac{\partial R}{\partial T} + \frac{dX}{dT}\frac{\partial R}{\partial X} \tag{4.62}$$

From equation (4.61), we see that along characteristic lines defined by $\frac{dX}{dT} = \mu R^2$ the

[7] In Healey (2000) the small parameter used, ε, is equivalent to ϵ^2 here.

solution behaves according to $\frac{dR}{dT} = DR$. We solve these two ordinary differential equations:

$$\frac{dR}{dT} = DR \quad \Rightarrow \quad R(X(T),T) = R_{X(0)}\exp(DT)\ , \tag{4.63a}$$

$$\frac{dX}{dT} = \mu R^2 \quad \Rightarrow \quad X(T) = X(0) + \frac{\mu R_{X(0)}^2}{2D}\left(\exp(2DT) - 1\right)\ , \tag{4.63b}$$

where $R_{X(0)} = R(X(0),0))$.

This model requires an initial profile $R(X(0),0)$. We choose an envelope that is even in ξ (that is $R(X(0),0) = R(-X(0),0))$. Although unrealistic for a physically feasible initial condition, this will demonstrate clearly the different evolution of positive and negative ξ. When studying the DNS results, the exponential spatial profile of the wavepacket makes it difficult to compare the gradients of the leading and trailing edges, which is why we have chosen to study time histories. For an even function, the envelope grows, remains constant and then decays allowing for meaningful comparison of leading and trailing edge gradients.

We choose the following initial condition

$$R(X(0),0) = R_{X(0)} = \frac{a_0}{2}\left[\tanh\left(k(\xi+\xi_a)\right) + \tanh\left(k(\xi_a-\xi)\right)\right] \tag{4.64}$$

for real constants ξ_a and k, and a real-valued parameter a_0. The value of μ was chosen to be -1, which will produce steepening at the leading edge, as found in our two-dimensional simulations and the numerical simulations of plane Poiseuille flow by Ikeda (1977). For all the simulation results that follow the following parameters were fixed: $\xi_a = 500$, $k = 0.008125$, $D = 0.005$. The variable ξ is taken over the range $\xi \in [-1000, 1000]$ and time $T \in [0, 80]$. The initial amplitude varies in the range $a_0 = [0.01, 1.0]$.
With the given initial condition stated above (4.64), we evolve the amplitude in time along the characteristic lines, according to the system of (4.63). This process was repeated over the range of values $a_0 = [0.01, 1.0]$.

Figure 4.6 includes three graphs. The first displays the characteristic lines along which

the solution is calculated. At high values of time we can see the bending of these lines so that for negative ξ the characteristics become closer together and for positive ξ they become further apart. The second graph shows the envelope at several values of time. As time increases the amplitude of the envelope increases, and as a result of the spacing of the characteristic lines, the envelope becomes steeper at the trailing edge (for negative values of ξ). The final graph in this figure shows the gradient of this envelope at five different times. It shows the gradient increasing at the trailing edge and staying almost constant at the leading edge.

Figure 4.7 shows the envelope of the wavepacket at a certain value of time for three different initial amplitudes $A_1 < A_2 < A_3$, where $A_1 = 0.46$, $A_2 = 0.66$ and $A_3 = 0.86$. The graphs on the left show the amplitude and gradient of the wavepacket. The graphs on the right show the scaled amplitude and scaled gradient, where the initial value of the wavepacket's amplitude a_0 has been used to scale the results. From the graphs on the left the gradient of the wavepacket clearly becomes steeper at the leading edge of the wavepacket (positive ξ). The graphs on the right demonstrate that the larger the amplitude, the steeper the leading edge becomes compared to the trailing edge.

The graphs on the right have been normalised by dividing the amplitude of the wavepacket by the initial amplitude. This shows the larger the amplitude the more steepening takes place.

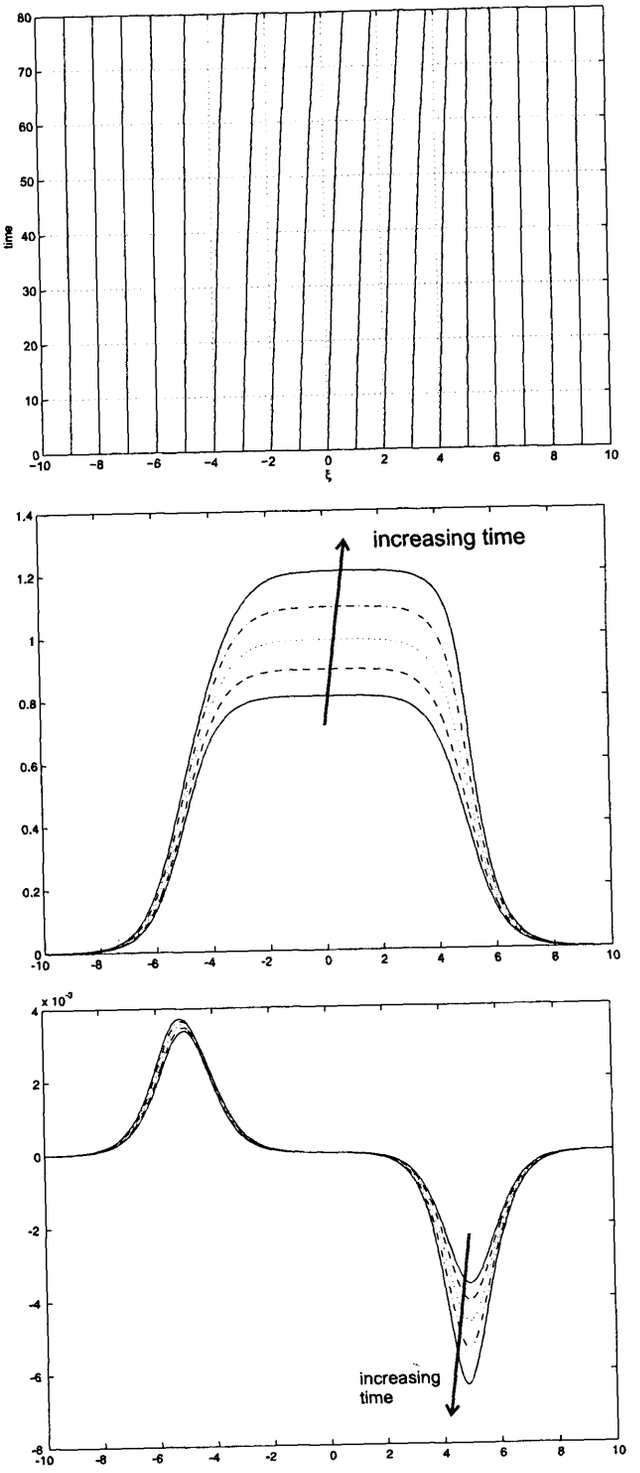

Figure 4.6: For $\mu = -1$. Top: a plot of T against ξ showing the characteristic lines $X(T)$. Middle: the envelope of the wavepacket at $T = 13.3$, 26.7, 40.0, 53.3, and 66.7 against ξ (larger amplitudes correspond to later times). Bottom: the gradient of the wavepacket for the same five different values of time against ξ.

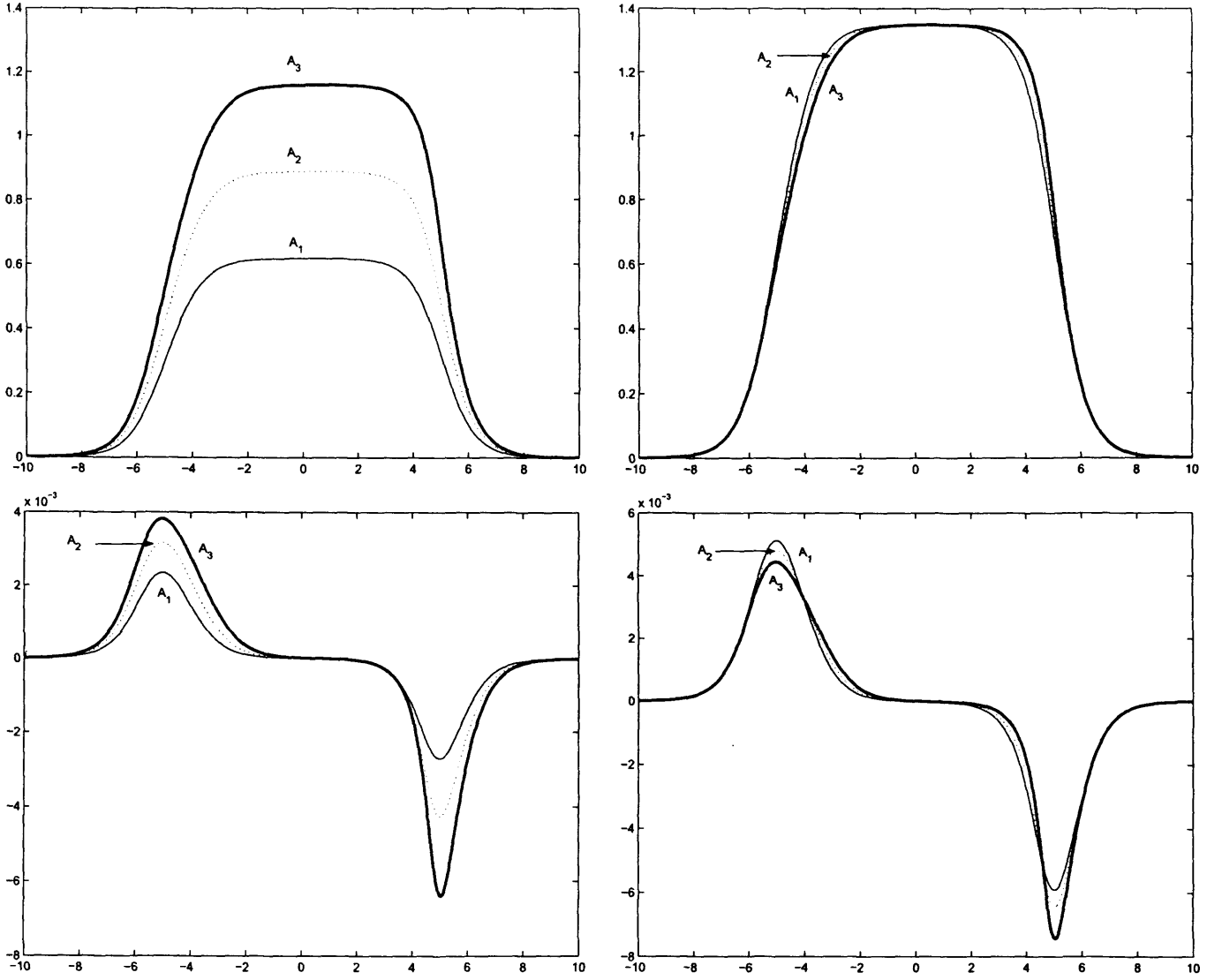

Figure 4.7: For $\mu = -1$. Left: plots of the envelope of the wavepacket (top) and its gradient (bottom) for three different initial amplitudes ($A_1 = 0.46$, $A_2 = 0.66$ and $A_3 = 0.86$) at time $T = 60$. Right: As left, however, the envelope and gradient of the wavepacket have been scaled using the initial amplitude in order to highlight the nonlinearity.

To demonstrate the behaviour of this model for $\mu = +1$ the previous graphs are reproduced with this change made to μ. Figure 4.8 shows characteristics, similar to figure 4.6 but opposite in direction. The other plots in this figure show the envelope of the wavepacket and its gradient at five different times. Once again one edge of the wavepacket becomes steeper than the other; this time, the trailing edge ($\xi < 0$) becomes steeper than the envelope at the leading edge. The behaviour now displayed in figure 4.9 confirms this idea, and show results for the same three amplitudes, A_1, A_2 and A_3. Once again the scaled gradient shows that the larger the amplitude, the steeper the envelope becomes at the trailing edge.

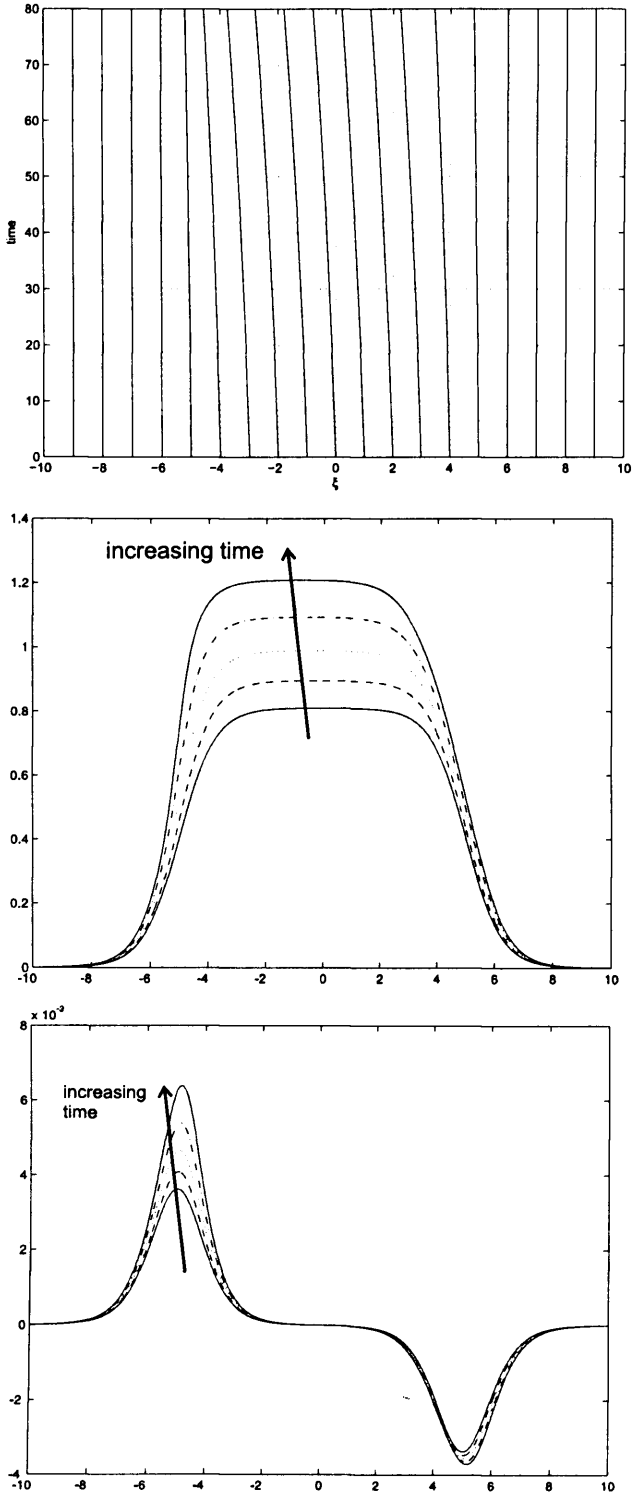

Figure 4.8: For $\mu = 1$. Top: a plot of T against ξ showing the characteristic lines $X(T)$. Middle: the envelope of the wavepacket at $T = 13.3$, 26.7, 40.0, 53.3, and 66.7 against ξ (larger amplitudes correspond to later times). Bottom: the gradient of the wavepacket for the same five different values of time against ξ.

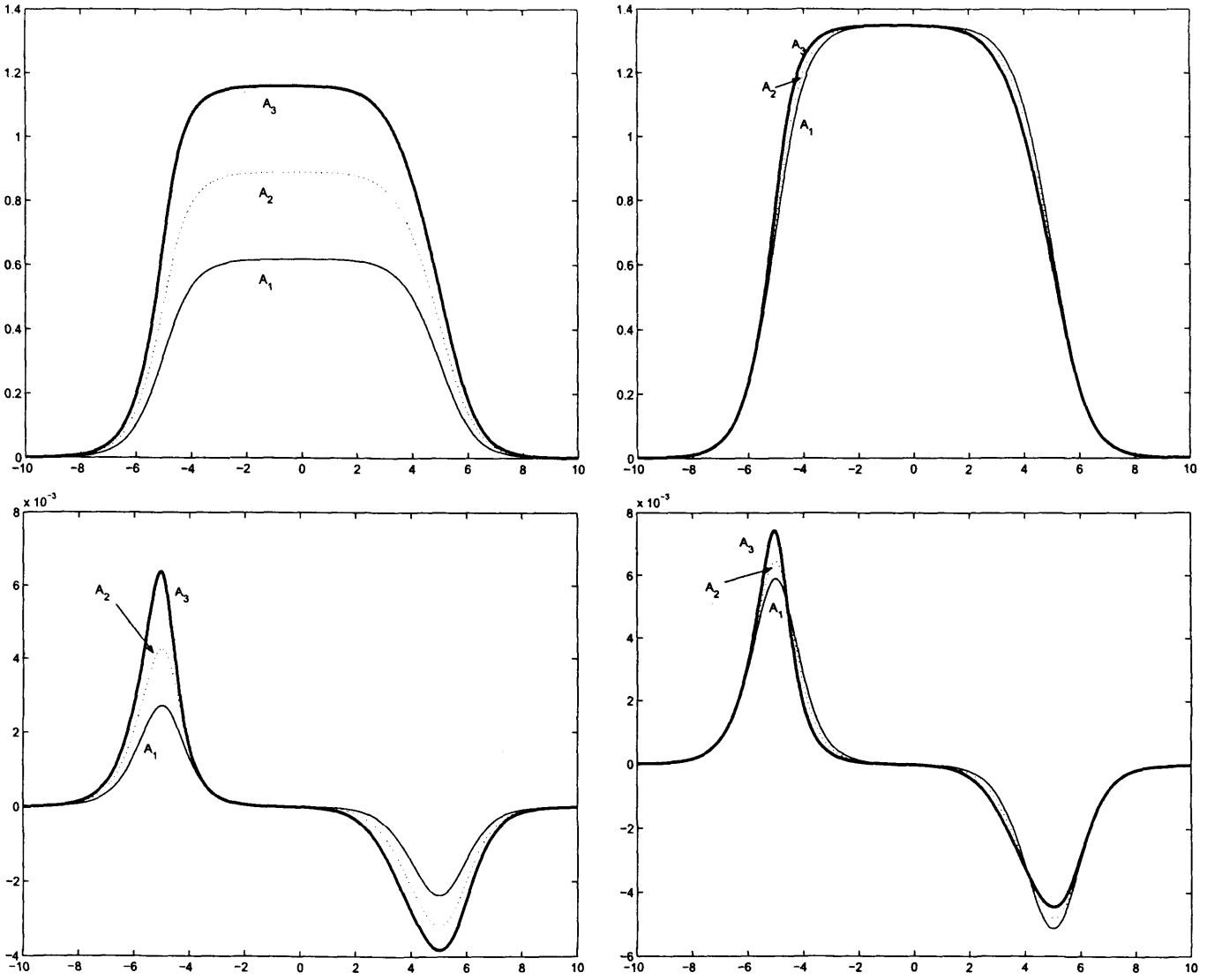

Figure 4.9: For $\mu = 1$. Left: plots of the envelope of the wavepacket (top) and its gradient (bottom) for three different initial amplitudes ($A_1 = 0.46$, $A_2 = 0.66$ and $A_3 = 0.86$) at time $T = 60$. Right: As left, however, the envelope and gradient of the wavepacket have been scaled using the initial amplitude in order to highlight the nonlinearity.

To demonstrate what a Ginzburg–Landau model would predict without higher-order terms, we would have $m = 0 = n$ which means that the coefficient C no longer depends on R (see (4.60)). Assuming C to be a constant we have a new system of equations to solve:

$$\frac{dR}{dT} = DR \quad \Rightarrow \quad R(X(T),T) = R_{X(0)} \exp(DT) \,, \tag{4.65a}$$

$$\frac{dX}{dT} = \mu \quad \Rightarrow \quad X(T) = X(0) + \mu T \,. \tag{4.65b}$$

The same plots are shown as before, for this system. Observe from figure 4.10 that the characteristic lines do not depend on R and depend linearly on T. Therefore the characteristic lines remain equally spaced as time advances, whereas in the previous examples the characteristic lines became squeezed or more spread out in space as time went by. Plots of the scaled amplitude and scaled gradient (see figure 4.11) are telling in this case. The development of the wavepackets is independent of their initial amplitude. These graphs show that a Ginzburg–Landau equation without higher-order terms cannot be used to model wave-envelope steepening.

This chapter has reviewed weakly nonlinear theories for parallel flows. These theories reveal that the slowly-varying envelope of a wavepacket evolves according to a Ginzburg–Landau equation. In order to model wave-envelope steepening higher-order terms must be included. Although the higher-order complex Ginzburg–Landau equation has not been derived by weakly nonlinear theory for the Blasius flow (an 'almost' parallel flow), the numerical results here show that it serves as a promising model.

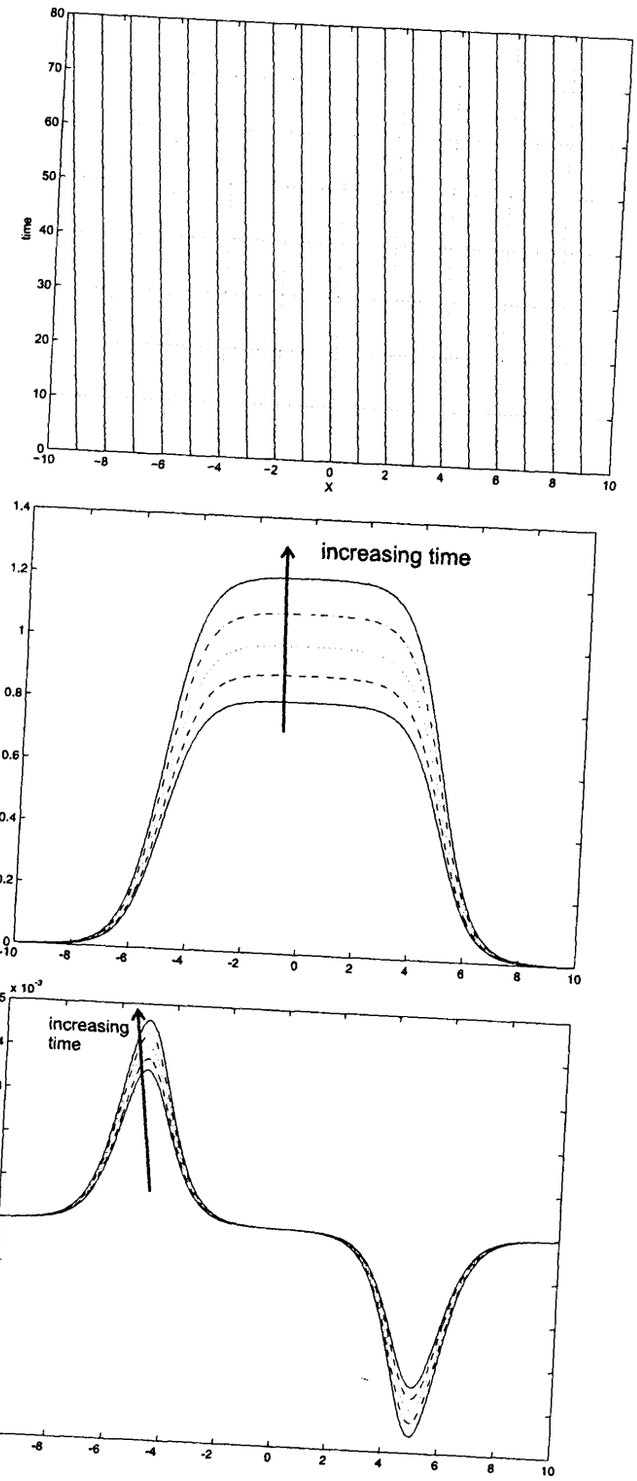

Figure 4.10: For $m = 0 = n$. Top: a plot of T against ξ showing the characteristic lines $X(T)$. Middle: the envelope of the wavepacket at $T = 13.3$, 26.7, 40.0, 53.3, and 66.7 against ξ (larger amplitudes correspond to later times). Bottom: the gradient of the wavepacket for the same five different values of time against ξ.

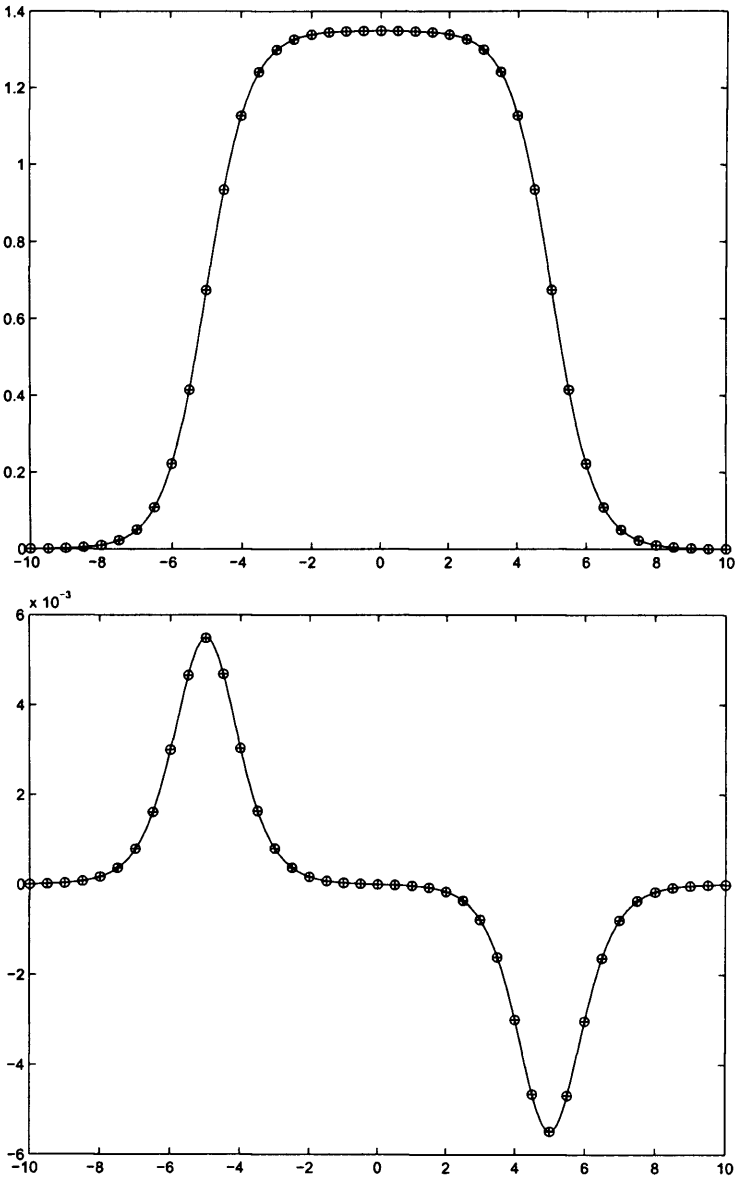

Figure 4.11: The scaled envelope (above) and gradient (below) of the wavepacket for three initial amplitudes $A_1 = 0.46$ (solid curve), $A_2 = 0.66$ (circles) and $A_3 = 0.86$ (crosses) at time $T = 60$.

Chapter 5

The Wave-envelope steepening effect

This chapter presents a method which can be used to calculate the envelope of a wavepacket. This will enable us to form a quantitative measure of wave-envelope steepening. Following this, the second section presents results from direct numerical simulations of Blasius flow which has been disturbed by a wavepacket. These results serve to illustrate the wave-envelope steepening effect.

5.1 Calculating wave envelopes

Wave-type disturbances are known to develop asymmetrically in boundary layers. Figure 5.1 shows an example of such a wave, where its maximum value is not equal to its absolute minimum value. Typically, an asymmetrical wave f has the property $\langle f \rangle \neq 0$, where $\langle \cdot \rangle$ denotes an average taken over a larger timescale than the period of oscillation. This phenomenon has been predicted theoretically to occur in boundary layers by Smith (1979) and has been observed in experiments (for example Healey, 2000). It is useful to be able to calculate the envelope of such asymmetric disturbances as this is the means by which wave-envelope steepening will be detected.

Laid out below is a method, based on the Hilbert Transform, for calculating the envelope of a wave-like function. This function could take the form $A(t)\sin(\omega t - \phi)$ at a particular streamwise location, or $A(x)\sin(\alpha x - \phi)$ at a particular time. There follow explanations of first, how the Hilbert transform of such a function is calculated, and second, how the envelope of this function is calculated. It is demonstrated that this method sometimes

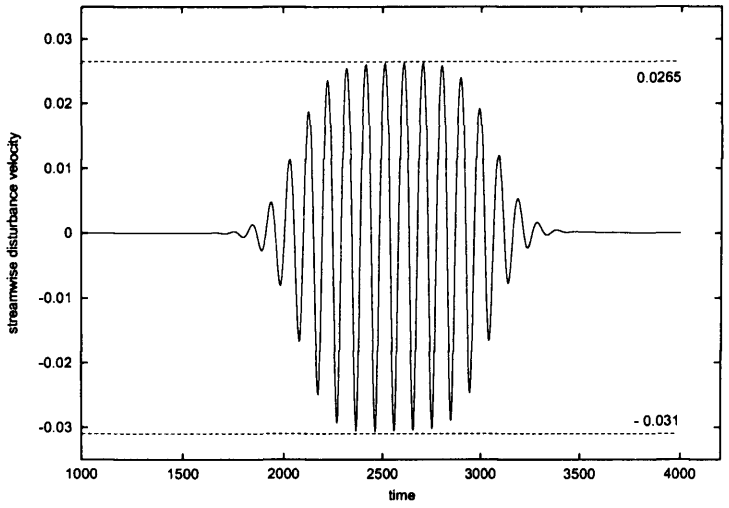

Figure 5.1: A typical asymmetric wavepacket from the simulation results, where Blasius flow was perturbed by a wavepacket disturbance. This time history data was taken at about a distance of $600\delta^*$ downstream of the forcing location. The Reynolds number was $R = 2240$.

produces an envelope that oscillates. For example, were this method used to calculate the envelope of a wavepacket that is asymmetric about the x-axis, then the envelope would oscillate. Once differentiated, it is hard to distinguish the maximum gradient and the minimum gradient as a result of the underlying oscillation in the envelope. In order to overcome this, modifications are made to the wavepacket to ensure that the resulting envelope does not oscillate. This is highly desirable for two reasons:

- a non-oscillating envelope conforms to our intuitive idea of an envelope as a slow-varying outline of an oscillation;
- the gradient of the envelope plays a vital role in identifying wave-envelope steepening. If the envelope oscillates its gradient will oscillate and the underlying behaviour of the gradient is obscured.

5.1.1 Calculating the Hilbert Transform of a function

In this section, there are real variables ω, s, t, and τ; real-valued functions e, f, h and k; and the discrete Fourier Transform and its inverse are represented by $\mathcal{F}[\cdot]$ and $\mathcal{F}^{-1}[\cdot]$

respectively.

The Hilbert Transform $h(t)$ of a function $f(t)$ is defined as

$$h(t) = \mathcal{H}[f(t)] = \frac{1}{\pi} \int_{-\infty}^{\infty} \frac{-f(s)}{t-s}\, ds \ , \tag{5.1}$$

where the Cauchy principal value of the integral is assumed. By taking $k(t-s) = \frac{-1}{\pi\,(t-s)}$, it becomes clear that the Hilbert Transform is a convolution:

$$\begin{aligned} h(t) &= \int_{-\infty}^{\infty} f(s)\, k(t-s)\, ds \\ &= (f * k)(t) \ . \end{aligned}$$

From the convolution theorem we have

$$\mathcal{F}[(f * k)] = \mathcal{F}[f]\, \mathcal{F}[k] \ ,$$

where $\mathcal{F}[f]$ represents the Fourier transform of f, that is,

$$\mathcal{F}[f] = \int_{-\infty}^{\infty} f(\tau) \exp(-i\omega\tau)\, d\tau \ .$$

So, by using the convolution theorem, the Hilbert Transform of the function f can be rewritten as

$$h(t) = \mathcal{F}^{-1}\Big[\mathcal{F}[f]\, \mathcal{F}[k]\Big]\,(t) \ . \tag{5.2}$$

The term $\mathcal{F}[k]$ can be evaluated:

$$\begin{aligned} \mathcal{F}[k] &= -\int_{-\infty}^{\infty} k(\tau) \exp(-i\omega\tau)\, d\tau \\ &= \frac{i}{\pi} \int_{-\infty}^{\infty} \frac{\sin(\omega\tau)}{\tau}\, d\tau \\ &= \frac{i}{\pi}\ \mathrm{sgn}\,(\omega) \int_{-\infty}^{\infty} \frac{\sin(t)}{t}\, dt \qquad \text{(where } \ t = \omega\tau) \\ &= i\ \mathrm{sgn}\,(\omega) \ . \end{aligned}$$

Substituting for $\mathcal{F}[k]$ into equation (5.2) gives

$$h(t) = \mathcal{F}^{-1}\Big[i\,\mathrm{sgn}\,(\omega)\;\mathcal{F}[f]\Big](t)\;. \tag{5.3}$$

This form of the Hilbert Transform is much more conducive to implementation in a computational code than that shown in equation (5.1), because Fourier transforms can be implemented extremely efficiently by using the routines in the NAG library for example.

5.1.2 A Simple example of calculating the Hilbert Transform

Several types of function have analytic Hilbert transforms. In section 5.1.4 we shall use the fact that

$$\mathcal{H}\,[\sin(t)\,] = \cos(t)\;.$$

The Hilbert transform of the Sinc function is also known:

$$\mathcal{H}\left[\frac{\sin(t)}{t}\right] = \frac{\cos(t)-1}{t}\;.$$

(See mathworld.wolfram.com/HilbertTransform.html for other examples.) Below we demonstrate the numerical routine used to calculate the Hilbert Transform of a set of data. The function to be tested is

$$\frac{\sin(t-500)}{t-500}\;. \tag{5.4}$$

Figure 5.2 shows a graph of the numerical Hilbert Transform of this function calculated with the method described in section 5.1.1. Also shown in this graph is the exact Hilbert Transform of equation (5.4) which is

$$\frac{\cos(t-500)-1}{t-500}\;.$$

The absolute error is shown beneath.

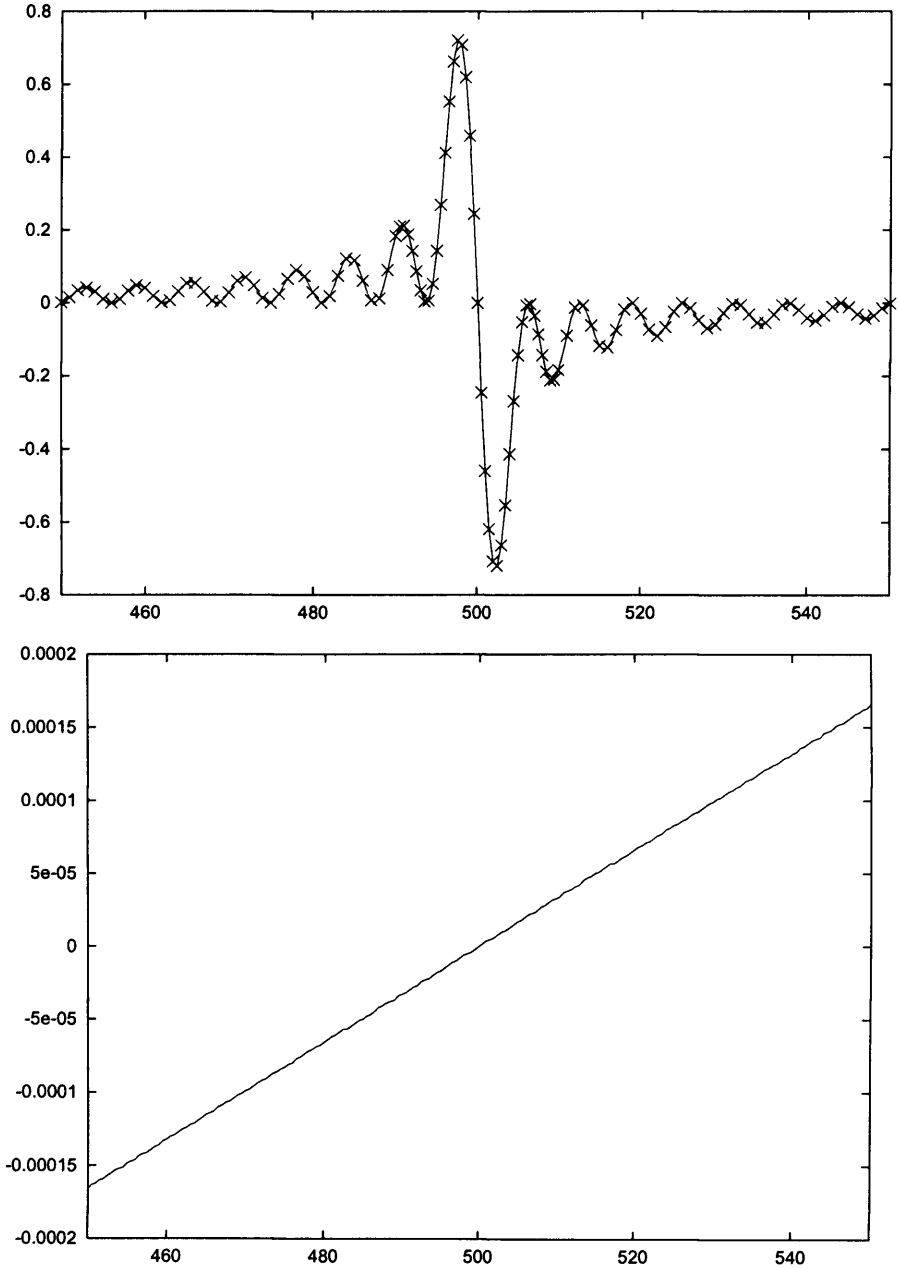

Figure 5.2: Above: the Hilbert Transform of equation (5.4) (crosses) and the exact Hilbert Transform (solid line). Below: the absolute error.

5.1.3 Calculating the envelope of a wavepacket

Consider a real-valued function $f(t)$. It can be associated with a complex-valued function $z(t)$, which is known as the analytic signal and is defined in the following way:

$$z(t) = f(t) + ih(t) \; ; \qquad \text{for } f, h, t \in \mathbb{R} \; ,$$

where $h(t)$ is in fact the Hilbert Transform of $f(t)$. The envelope $e(t)$ of the function $f(t)$ can then be defined as

$$e(t) = \sqrt{f^2(t) + h^2(t)} \; . \tag{5.5}$$

This method of calculating a wave envelope has been implemented numerically using equation (5.3) and (5.5), and has given good results. Shown below is a typical wavepacket and its envelope.

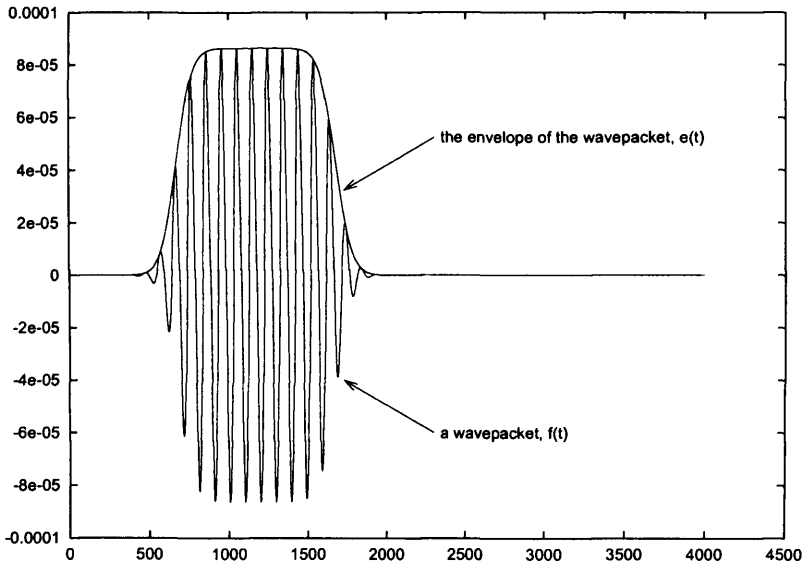

Figure 5.3: A wavepacket $f(t)$ and its envelope $e(t)$. This time history data is taken from the same simulation as figure 5.1, just $100\delta^*$ downstream of the forcing location.

The success of the method is due to the fact that the Hilbert transform h is such that the envelope function, $\sqrt{f^2 + h^2}$, varies over a long time-scale in comparison to the oscillation,

which is entirely contained in the term $\exp[i(\tan^{-1}(h/f))]$. In other words, the wave has been decomposed into an oscillating part and a slowly-varying envelope:

$$z(t) = f(t) + ih(t) \equiv (\sqrt{f^2 + h^2})\ (\exp[i(\tan^{-1}(h/f))])\ .$$

5.1.4 Calculating the envelope of an asymmetric wavepacket

Applying the same method for calculating the envelope of a wavepacket that is asymmetric about the x-axis is not so successful. In any case, it is not clear what envelope would best represent an asymmetric wave such as that seen in figure 5.1 because the positive and negative values of the wave seem to require different envelopes.

To try and understand the result of applying this method to asymmetric wavepackets, it is instructive to consider two simple analytic functions first. For example, consider the function $f_1(t) = a\cos t$ where a is a constant. The Hilbert transform of f_1 is $h_1(t) = a\sin t$, and the envelope, according to equation (5.5), is

$$\begin{aligned} e_1(t) &= \sqrt{a^2\cos^2 t + a^2\sin^2 t} \\ &= a\ . \end{aligned}$$

Now consider an asymmetric function $f_2(t) = a\cos t + b$ where b is a constant. The Hilbert transform of this function is $h_2(t) = a\sin t$, and its envelope is

$$e_2(t) = \sqrt{a^2 + b^2 + 2ab\cos t}\ .$$

Clearly this envelope will oscillate over a time-scale comparable with the original function f_2 unless $b = 0$, in which case, f_2 is reduced to the symmetric wave f_1.

The following examples are shown in figure 5.4 with the parameters $a = 1.0$ and $b = 0.1$.

symmetric wave	asymmetric wave
$f_1(t) = \cos t$	$f_2(t) = \cos t + 0.1$
$h_1(t) = \sin t$	$h_2(t) = \sin t$
$e_1(t) = 1$	$e_2(t) = \sqrt{1.01 + 0.2\cos t}$

The envelope of the symmetric wave does not oscillate, whereas that of the asymmetric

wave oscillates between two values, determined by a minimum envelope (corresponding to the positive values) and a maximum envelope (corresponding to the negative values).

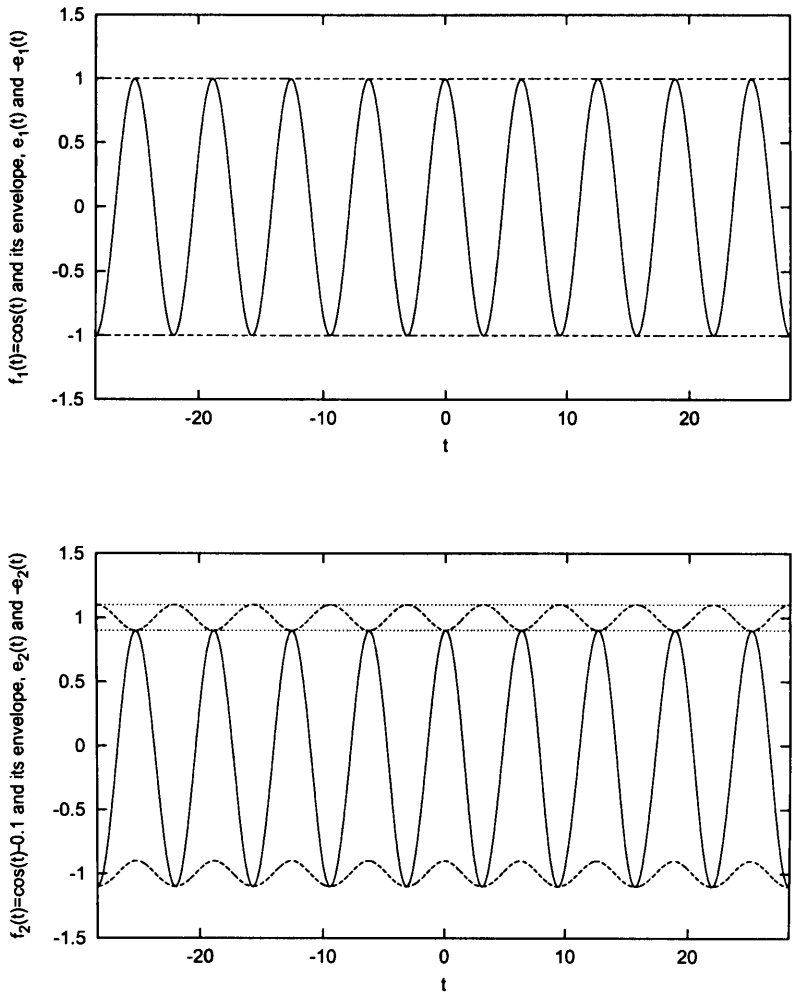

Figure 5.4: A symmetric wave, f_1 (—), and its envelope $\pm e_1$ (---) (above);
and an asymmetric wave, f_2 (—), its envelope $\pm e_2$ (---), and $y = 0.9$ and 1.1 (···) (below).

If we now take the wavepacket shown in figure 5.1, and try to calculate its envelope we see similar behaviour. The envelope oscillates on a scale comparable to that of the wave. We can also see that the envelope oscillates inbetween what could be thought of as an envelope which fits the positive velocities and one which fits the negative velocities.

So, for the asymmetric wavepacket, the term $\sqrt{f^2 + h^2}$ varies on a time-scale comparable with the oscillation. The method does not successfully decompose the original wave into a slowly-varying amplitude function and an oscillating part.

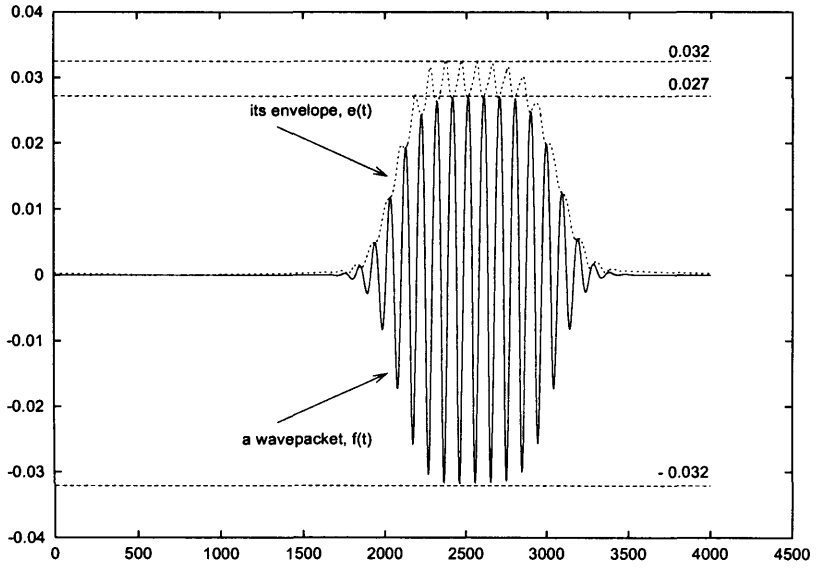

Figure 5.5: An asymmetric wave and its oscillating envelope. The data has been taken from a similar numerical experiment to that shown in figure 5.1, only a coarser grid was used.

As previously stated, to obtain clear and instructive information from the gradient of the envelope, the envelope itself must not oscillate. Clearly, from figure 5.5, the envelope is oscillating. To resolve this problem, first consider the spectrum of this wave, which is shown in figure 5.6. There are several bands of frequency where the power is non-zero. The first non-zero band corresponds to a mean (non-oscillatory) flow, the second corresponds to a band centred around a fundamental frequency f_0 (this actually corresponds to the frequency of the Tollmien–Schlichting mode). Other higher-frequency bands can be seen

centred around integer multiples of the fundamental frequency. The mean flow and these higher frequency components cause the wavepacket to be asymmetric about the x-axis. Therefore, if the wavepacket is passed through a filter that preserves only the coefficients of the band centred about the fundamental, then we will have a symmetric wavepacket. The envelope of this filtered wavepacket can now be determined using the method set out above and, as can be seen from figure 5.7, results in a smooth envelope. Figure 5.8 shows the original wave with the envelope calculated from the modified wave; this highlights the difference between the original wave and the modified wave.

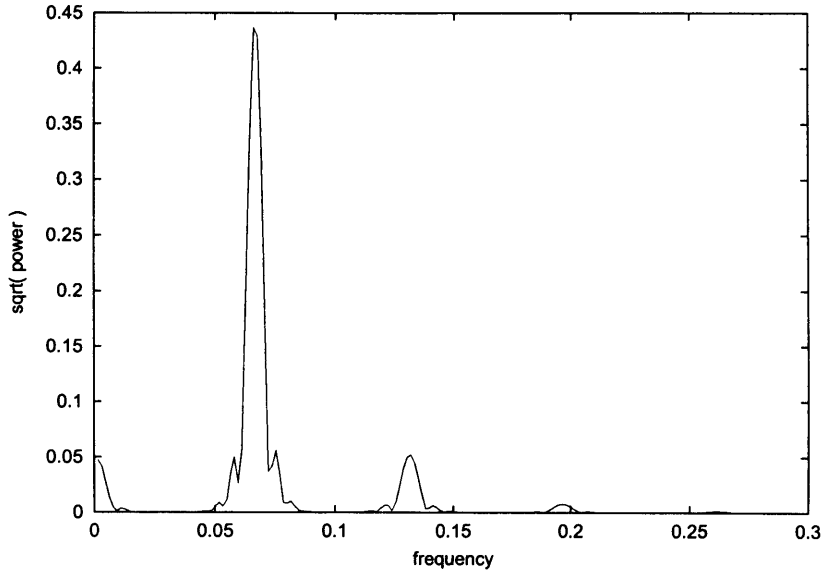

Figure 5.6: The spectrum of the wave shown in figure 5.5.

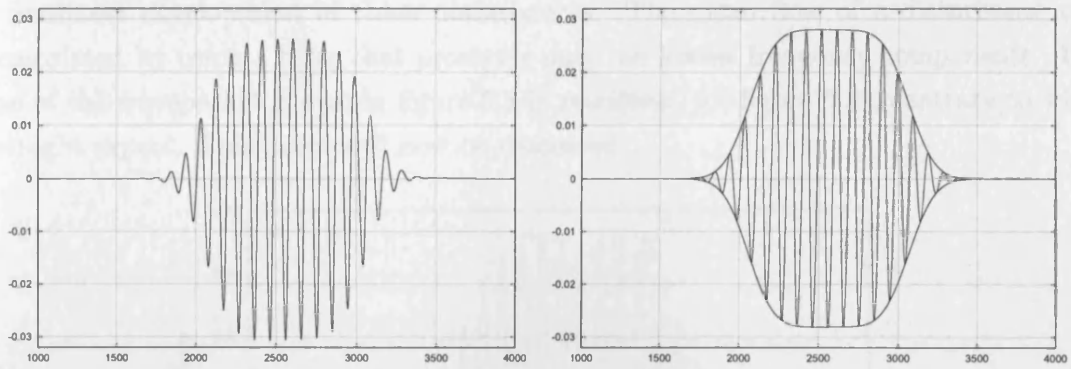

Figure 5.7: Left, an asymmetric wave, (from the same numerical results as figure 5.1) and right, this wave after filtering with its envelope ($\pm e$).

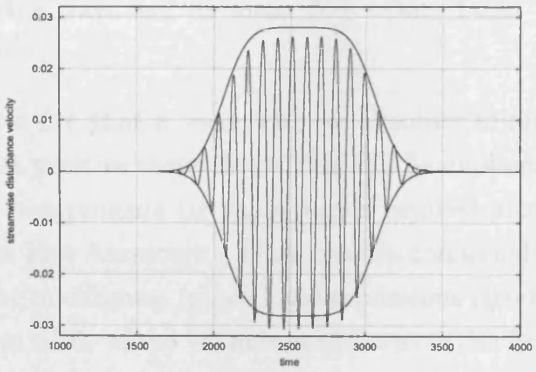

Figure 5.8: The original wave, before modification, with the envelope.

5.1.5 Mean flow

The mean (non-oscillatory) part of the velocity is thought to play an important role in the nonlinear development of these disturbances. The mean flow of a disturbance can be calculated by using a filter that preserves only the lowest frequency components. The mean of the wavepacket shown in figure 5.5 is ***positive*** (see figure 5.9), contrary to what one might expect. This point will now be discussed.

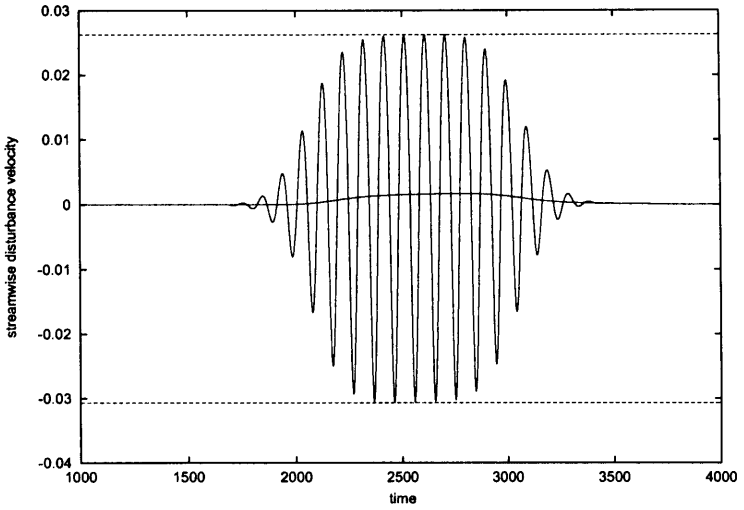

Figure 5.9: An asymmetric wave and its mean flow. Data taken from the same numerical experiment as for figure 5.1.

It may seem counter-intuitive that a wave with an absolute minimum value greater than it's maximum value has a positive mean flow. This can be explained considering the effect of the higher frequency components (ie those bands centred around $2f_0$, $3f_0$, $4f_0$, etc.). Consider a wave and its first harmonic. They can be combined in such a way that the harmonic lessens both the maximums (peaks) and minimums (troughs) of the fundamental. This can be seen in figure 5.10, where we have a sine wave (the fundamental) and it's first harmonic ($\pi/2$ out of phase with the fundamental) combined in the following way:

$$\sin(t) + 0.2\cos(2t) \ .$$

A non-zero mean can be incorporated by simply adding a constant:

$$\sin(t) + 0.2\cos(2t) + 0.15 \ .$$

This is plotted in figure 5.11. Here, the absolute minimum value of the wave is greater than the maximum value, yet the wave has a positive mean flow. This also demonstrates the broadening of the wave above the x-axis and its thinning below the axis that is typical of wave disturbances in a boundary layer.

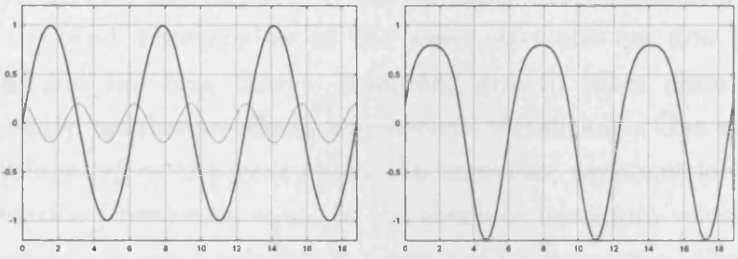

Figure 5.10: left: $\sin(t)$ and $0.2\cos(2t)$; right: $\sin(t) + 0.2\cos(2t)$

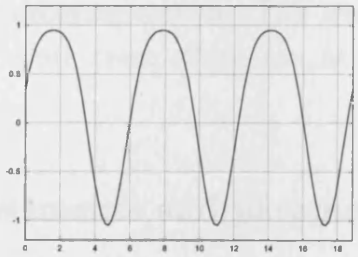

Figure 5.11: $\sin(t) + 0.2\cos(2t) + 0.15$

In this section we have seen how the envelope of a wavepacket may be calculated by means of a Hilbert Transform. For waves that develop asymmetrically we have seen that, by filtering out high and low frequencies, leaving a band of non-zero modes centred around the fundamental frequency, we can obtain a non-oscillating envelope of the wavepacket. A non-oscillating envelope is required in order to determine whether or not wave-envelope steepening is occurring.

5.2 What is wave-envelope steepening?

Healey (2000) uses the term wave-envelope steepening to describe one particular aspect of the nonlinear, asymmetric development of modulated waves propagating in a transitional boundary layer.

As we know from linear theory (see §4.2), if a two-dimensional parallel flow over a flat plate is disturbed by a wave, then the wave will either grow or decay exponentially with respect to the streamwise coordinate. Which of these two possibilities occurs depends upon the frequency and wavenumber of the wave, and also on flow parameters (the Reynolds number and the base flow). Assuming growth takes place, once the wave has grown sufficiently, nonlinear effects will become significant. One such effect is the 'asymmetric' development of the wave about the time-axis; asymmetric in the sense that the maximum velocity (previously equal to the absolute minimum velocity) will become less than the absolute minimum velocity as a result of nonlinearities. This effect has been explored theoretically by Smith (1979). If the disturbance is a wavepacket, then as well as developing asymmetrically in time, the wavepacket will develop asymmetrically about a vertical line through its centre. In other words, the growing section of the wavepacket will develop differently to the decaying section. This was referred to as wave-envelope steepening by Healey (2000). Both these effects can be seen clearly in the simulation results that follow.

5.2.1 Numerical experiments and parameters

A similar computational domain is used to generate the numerical results in this chapter and the two following chapters. Flow parameters need to be specified. First a Reynolds number R is chosen. A streamwise pressure gradient can be introduced through a non-zero choice for the Falkner–Skan parameter m, which will be discussed in more detail in chapter 6. Boundary conditions are described in §2.1.4, and the disturbance (introduced through a boundary condition on the wall) requires setting the forcing location, x_f, a parameter related to the streamwise length over which the disturbance is introduced, L_{slot}, an amplitude, A, and a frequency, ω_{ts}. The forcing location should be chosen far enough downstream so that any modes travelling upstream will have decayed sufficiently

by the time they reach the inflow. The frequency will be taken to correspond to that of the most unstable mode for the specified Reynolds number.[1] A wavenumber also must be specified for the outflow condition (see page 22). Experience shows that the success of the simulation is not too dependent on this choice. The wavenumber chosen is that which is consistent with the specified Reynolds number and frequency.

Discretization parameters must also be specified. Time and streamwise step-lengths, dt and dx, are required along with the total time of the simulation and the streamwise length of the domain, T_{end} and X_{end}. For stability of the numerical scheme, $dt \lesssim \frac{dx}{2}$. The wall-normal discretization is determined by the number of Chebyshev polynomials used, N_z. For efficient use of Fast Fourier algorithms, N_z should be some power of 2. For efficiency, the total streamwise length, X_{end}, should be $(2^n - 2)\,dx$ for an integer n, because of the sine transform used to solve the Poisson equation. The number of iterations for the first time step must be specified, N_{its}, and finally, the mapping parameter for the wall-normal transformation to a finite domain, ℓ.

The simulation starts from the parallel flow $U(z)$, which is calculated as part of the simulation. The wavepacket disturbance is introduced to the flow and the disturbance propagates downstream according to the (discretization of the) governing equations. Points of measurement are located at regular streamwise intervals at the wall-normal collocation point which corresponds most closely to the inner maximum of the Tollmien–Schlichting wave. At these streamwise points (denoted by x_s) the time history of the streamwise velocity is recorded for post-processing.

Most of the simulations were run on the Welsh e-Science computers, in particular their 8 processor SGI-IRIX Origin 300 machines. Initial work was carried out on a UNIX Compaq

[1] With the forcing function of equation (2.11), the most prominent frequency is ω_0. When ω_0 is taken to be the most unstable mode at the chosen Reynolds number, since this mode has the highest spatial growth rate it will dominate as time progresses. If ω_0 corresponds to a mode which grows at a lower rate than the most unstable mode, then, as before, ω_0 will dominate initially. However, this forcing function excites all frequencies, so the most unstable mode will be weakly excited. After a sufficient time it will compete with ω_0 and eventually dominate. These two modes travel at different phase speeds and the resulting linear, dispersive effects will complicate the simulations, making it difficult to distinguish the wave-envelope steepening effect from these other effects. This is why ω_0 is always set as the most unstable mode for the chosen Reynolds number.

Flow parameters	R	2240	varied in chapter 7
	m	0.0	varied in chapter 6
	A	0.000 010	varied in this chapter
	x_f	100.0	not varied
	L_{slot}	8.0	not varied
	ω_{ts}	0.065	set according to R
	α_{ts}	(0.2, 0)	set according to R and ω_{ts}
Discretization parameters	dx	0.5	varied
	dt	0.25	varied
	X_{end}	1023.0	varied
	T_{end}	4000.0	varied
	N_z	64	varied
	N_{its}	5	not varied
	ℓ	2.0	not varied

Table 5.1: Parameters used in the numerical simulations

DEC Alpha machine.

5.2.2 Numerical results

Figures 5.12 to 5.14

Figure 5.12 shows the instantaneous wall-normal profile of a wavepacket at a certain streamwise location (x=690, t=2000). The upper plot uses the mapped variable $\zeta = \frac{\ell}{\ell + z}$. The lower plot uses the physical variable z, and only one third of the computational domain is shown in this case. For $N_z = 64$, ζ maps onto the domain $z \in [0, 65]$. Had the entire domain been plotted the graph is unclear as the z-variation appears very steep. Figure 5.13 shows the streamwise disturbance velocity at $t = 2000$ against x and ζ. The mapped variable was chosen for clarity. Figure 5.14 shows the instantaneous vorticity against x and ζ. As expected from linear theory, values of the vorticity are larger than those of the the streamwise velocity, and the vorticity decays faster in ζ than the streamwise velocity.

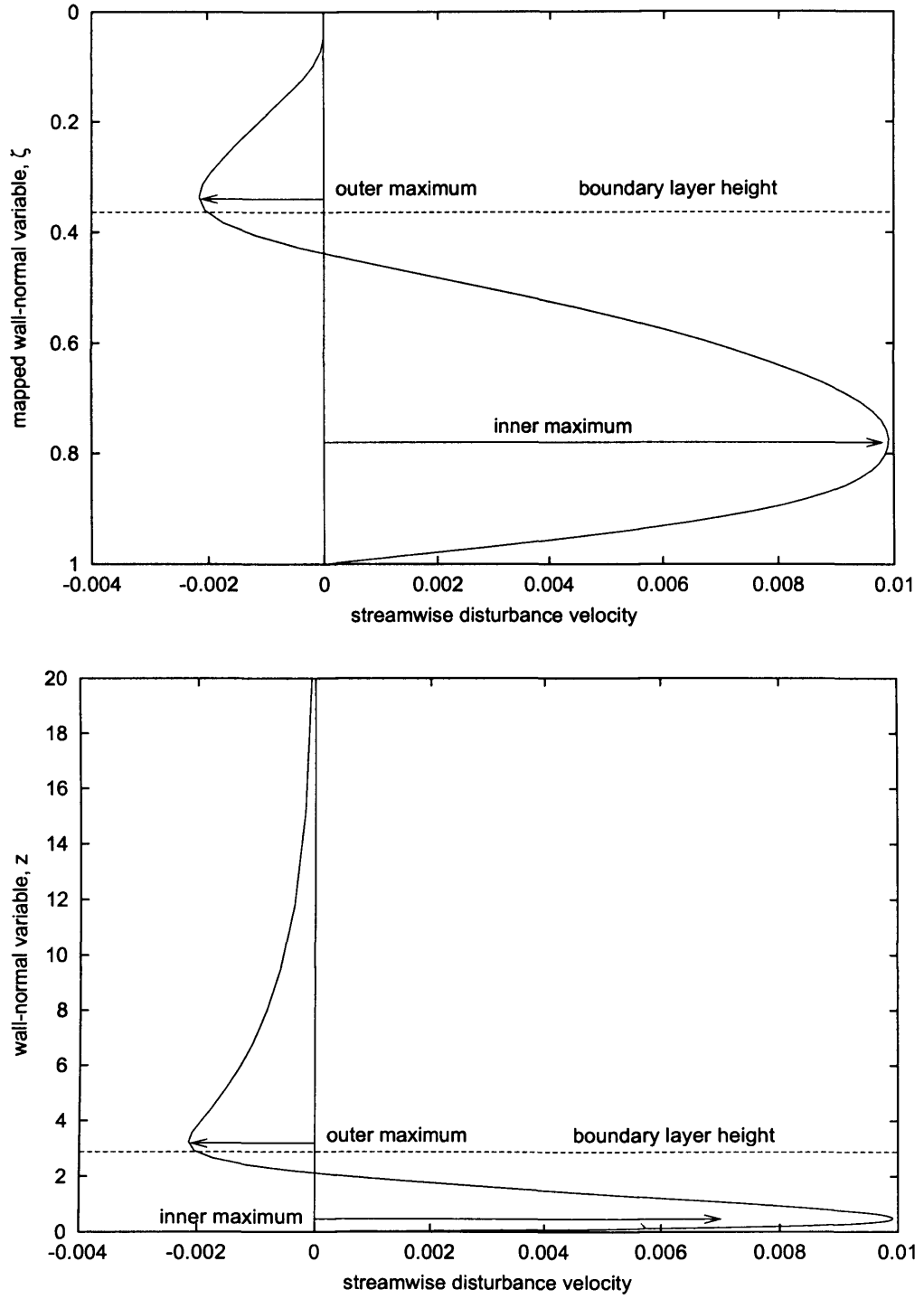

Figure 5.12: Two plots at $t = 2000$ and $x = 690$, of the streamwise velocity against ζ (upper plot) and against z (lower plot). In each case the surface is located along the x-axis. In the upper plot the entire domain is shown ($\zeta \in (0, 1]$), whereas in the lower plot only about $1/3$ of the domain is shown (as $z \in [0, 65]$ for $N_z = 64$). The surface corresponds to $\zeta = 1$ (or $z = 0$).

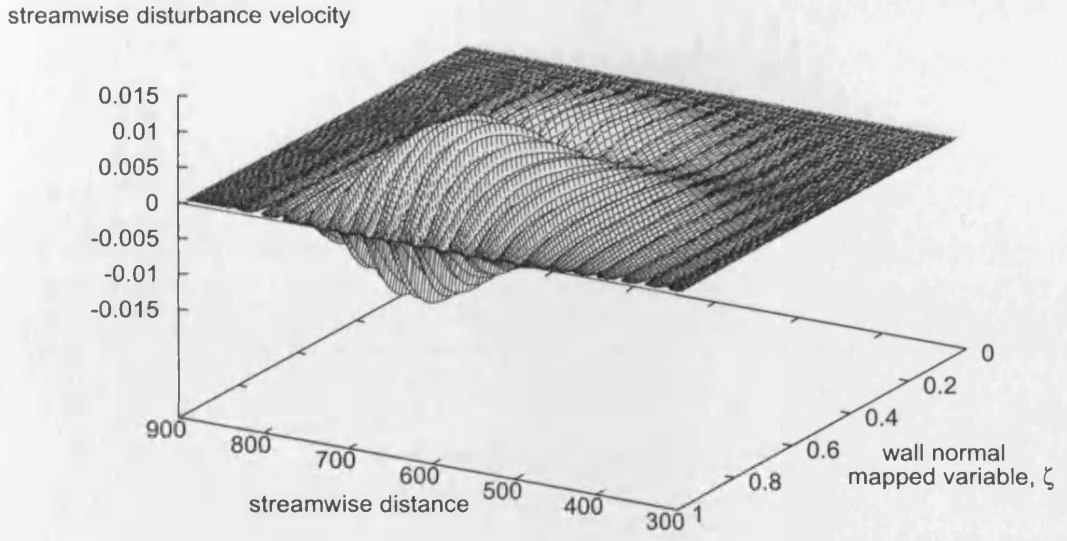

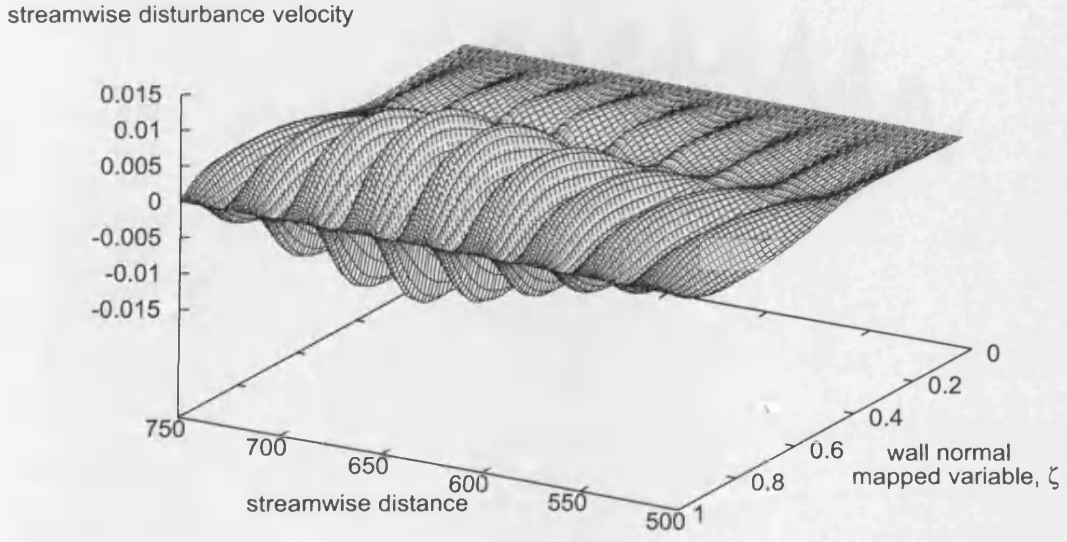

Figure 5.13: Streamwise velocity at $t = 2000$. The solid boundary to the flow occurs at $\zeta = 1$. Both plots show the same result, but a smaller range of the streamwise coordinate is displayed in the lower plot

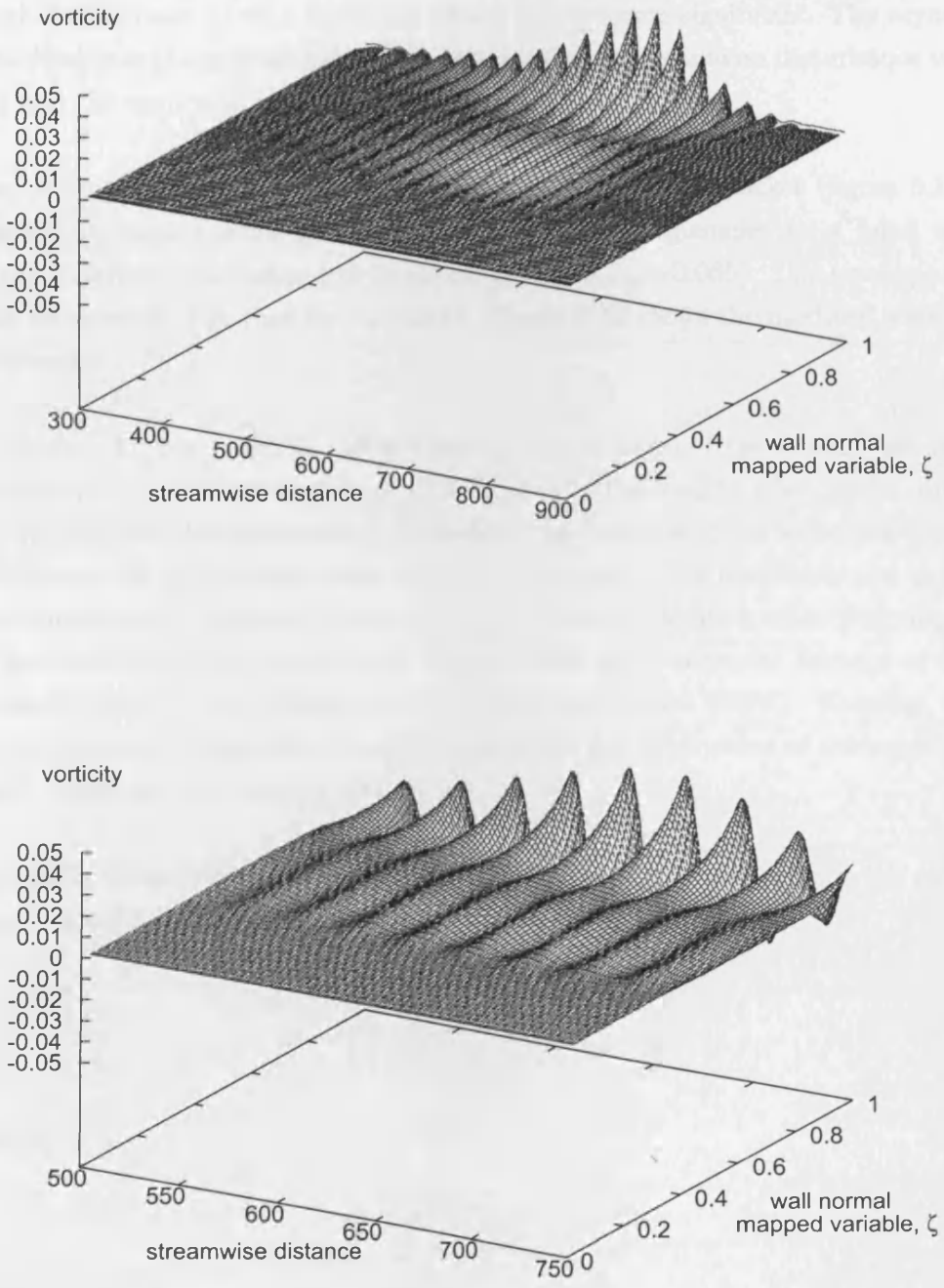

Figure 5.14: Vorticity at $t = 2000$. The solid boundary to the flow occurs at $\zeta = 1$. Both plots show the same result, but a smaller range of the streamwise coordinate is displayed in the lower plot

Figures 5.15–5.17

Shown in figure 5.15 is the time history of a wavepacket measured at a streamwise position far enough downstream so that nonlinear effects have become significant. The asymmetry about the time-axis is apparent here, where the maximum streamwise disturbance velocity is 0.0265 and the minimum is -0.031.

Following the method set out in section 5.1.4, the original wavepacket (figure 5.15) has been passed through a filter which retains only those frequencies in a band centred around the Tollmien Schlichting frequency (in this case $\omega_{ts} \approx 0.065$). The envelope of this 'modified wavepacket' can then be calculated. Figure 5.16 shows the modified wavepacket and its envelope.

Finally, figure 5.17 is a graph of the gradient of the envelope of the streamwise velocity. The gradient reaches a maximum value of 0.0000345 at the leading edge, and a minimum value of -0.000033 at the trailing edge. Therefore, the envelope of the wavepacket is found to be steeper at the leading edge than at the trailing edge. (The maximum and minimum gradients correspond to inflexion points in the disturbance velocity profile occurring at the leading and trailing edges respectively.) These results agree with the findings of Houten et al. (2000), Healey (2000), Houton et al. (2001) and Houten (2004). However, Healey (2000) also investigated this effect in experiments and the implication of the experimental data will be discussed in the next section.

The inspection of the gradient of the envelope of the modified wavepacket is the means by which wave-envelope steepening is detected in fact.

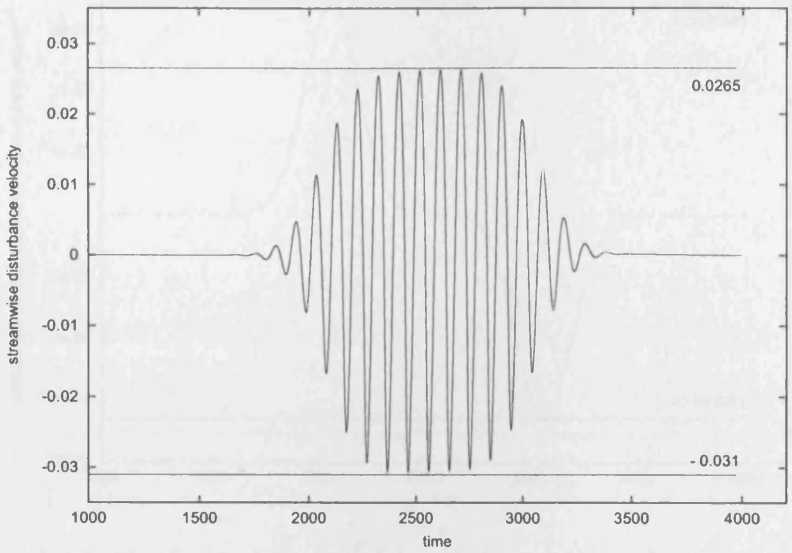

Figure 5.15: Time history of the streamwise disturbance velocity at $x_s = 62$.

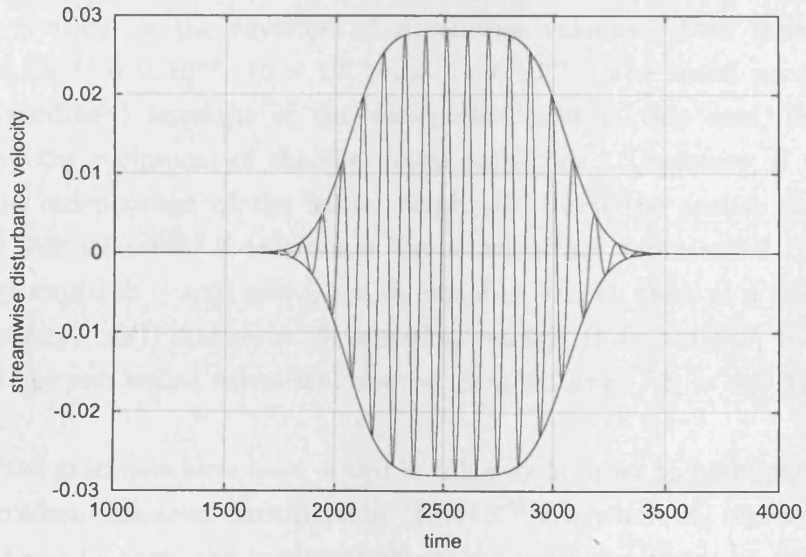

Figure 5.16: Modified wavepacket and its envelope.

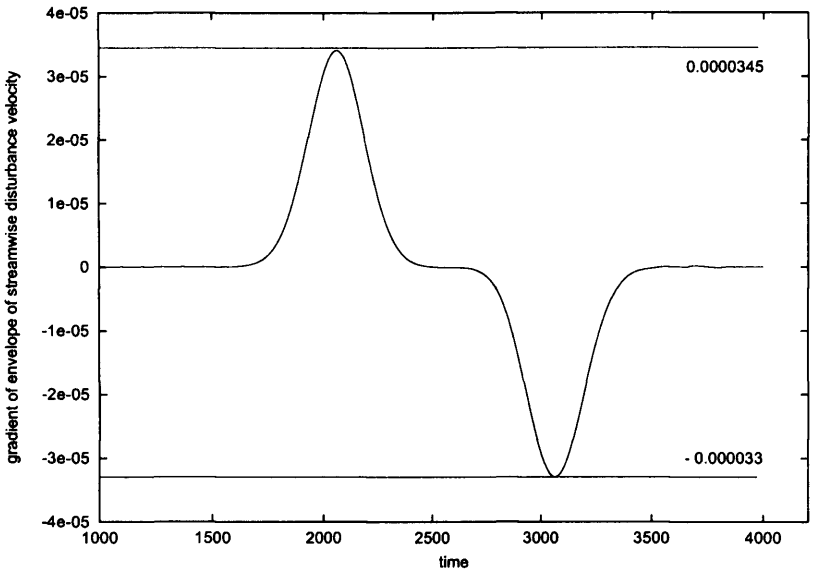

Figure 5.17: Gradient of the envelope of streamwise velocity at $x_s = 62$.

Figure 5.18

Using different initial amplitudes we can look at how the nonlinearities manifest themselves in the gradient of the envelope of streamwise velocity. Four initial amplitudes are used: 2×10^{-6}, 6×10^{-6}, 10×10^{-6} and 14×10^{-6}. The usual procedure is used to find the (modified) envelope of the wavepacket, and in this case, the gradient is then scaled by the reciprocal of the the initial amplitude. Therefore, if the behaviour were linear (ie independent of the initial amplitude) then the scaled gradients would be identical. For example, if two linear disturbances are represented by w_1 and w_2, where $w_1 = A_1 \exp(i(kx - \omega t))$ and $w_2 = A_2 \exp(i(kx - \omega t))$, then at a certain point x_0, $w_1 = A_1 \exp(i(kx_0 - \omega t))$ and $w_2 = A_2 \exp(i(kx_0 - \omega t))$. If we scale w_1 by $1/A_1$ and w_2 by $1/A_2$, then the two scaled waves will now be identical as $w_1/A_1 = w_2/A_2$.

In figure 5.18 the gradients have been scaled in this way in order to highlight the nonlinear effects: each gradient has been multiplied by $(10 \times 10^{-6})/A_0$ where A_0 represents the initial amplitude. As can be seen, the nonlinear effects are most significant at the trailing edge and their effect is to lessen the steepness of the gradient, thereby causing the gradient at the leading edge to become steeper than the gradient at the trailing edge.

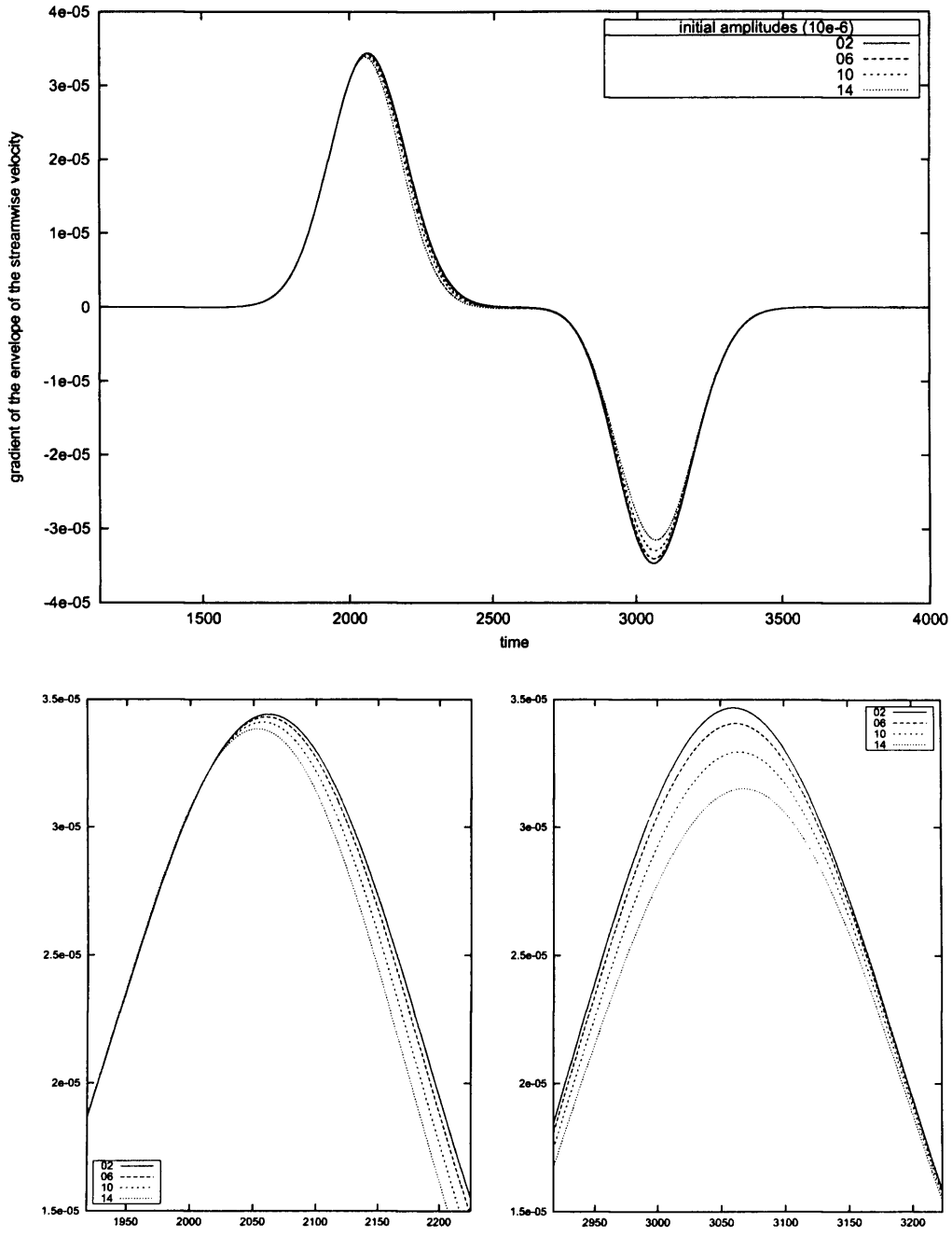

Figure 5.18: 'Scaled' gradient of the envelope of streamwise velocity at $x_s = 62$ for initial amplitudes of 2×10^{-6}, 6×10^{-6}, 10×10^{-6} and 14×10^{-6}, and below, close-ups of the leading and trailing edges (left and right respectively). Note that the scale on the y-axis is the same for both plots, and the the absolute value of the gradient is plotted. Results for $R = 2240$ taken at a height corresponding to the inner maximum of the Tollmien–Schlichting wave.

Figure 5.19

The previous time histories have been measured at one streamwise location. The procedure of calculating a 'modified' wavepacket and envelope was repeated at many streamwise positions, enabling a picture to be built up of how the maximum and absolute minimum values of the streamwise velocity evolve in the streamwise direction. The maximum and absolute minimum values of the gradient of the envelope of streamwise velocity can also be tracked as a function of streamwise position, see figure 5.19. This shows clearly that early on in the wavepacket's development, the absolute value of the gradient of the envelope is the same at the leading and the trailing edges. As the wave propagates downstream the maximum and absolute minimum values of the gradient begin to differ; this difference increases progressively as the downstream distance increases and we can see that wave-envelope steepening is occurring.

By inspection of figure 5.19 it would seem reasonable to conclude that once wave-envelope steepening occurs, the gradient at the leading edge becomes progressively steeper than the gradient at the trailing edge as we move downstream. This is the correct conclusion for the most part, however, on closer inspection a slight variation to this behaviour is found. Tables 5.2 and 5.3 below highlight this variation. For two streamwise positions ($x_s = 52$ and $x_s = 62$ respectively), the columns show the initial amplitude, the maximum streamwise disturbance velocity (u_{max}), the absolute value of the minimum velocity ($|\, u_{min}|$), the maximum gradient (g_{max}), the absolute minimum gradient ($|\, g_{min}|$) and a quantity Σ, defined as

$$\Sigma = 1 + \frac{\min\{g(t) : t \in (0, T_{end})\}}{\max\{g(t) : t \in (0, T_{end})\}}\ , \tag{5.6}$$

where $g(t)$ represents the gradient of the envelope of the streamwise disturbance velocity at time t and T_{end} represents the final time of the simulation, so Σ is a dimensionless measure of the difference between maximum and absolute minimum gradients. For time histories, the maximum gradient occurs at the leading edge and is positive, and the minimum gradient occurs at the trailing edge and is negative. Therefore, if the gradient becomes steeper at the leading edge Σ will be positive, if the gradient becomès steeper at the trailing edge Σ will be negative, and if the absolute maximum and minimum values of the gradient are equal then Σ will be zero. The previous results show that the leading edge becomes steeper

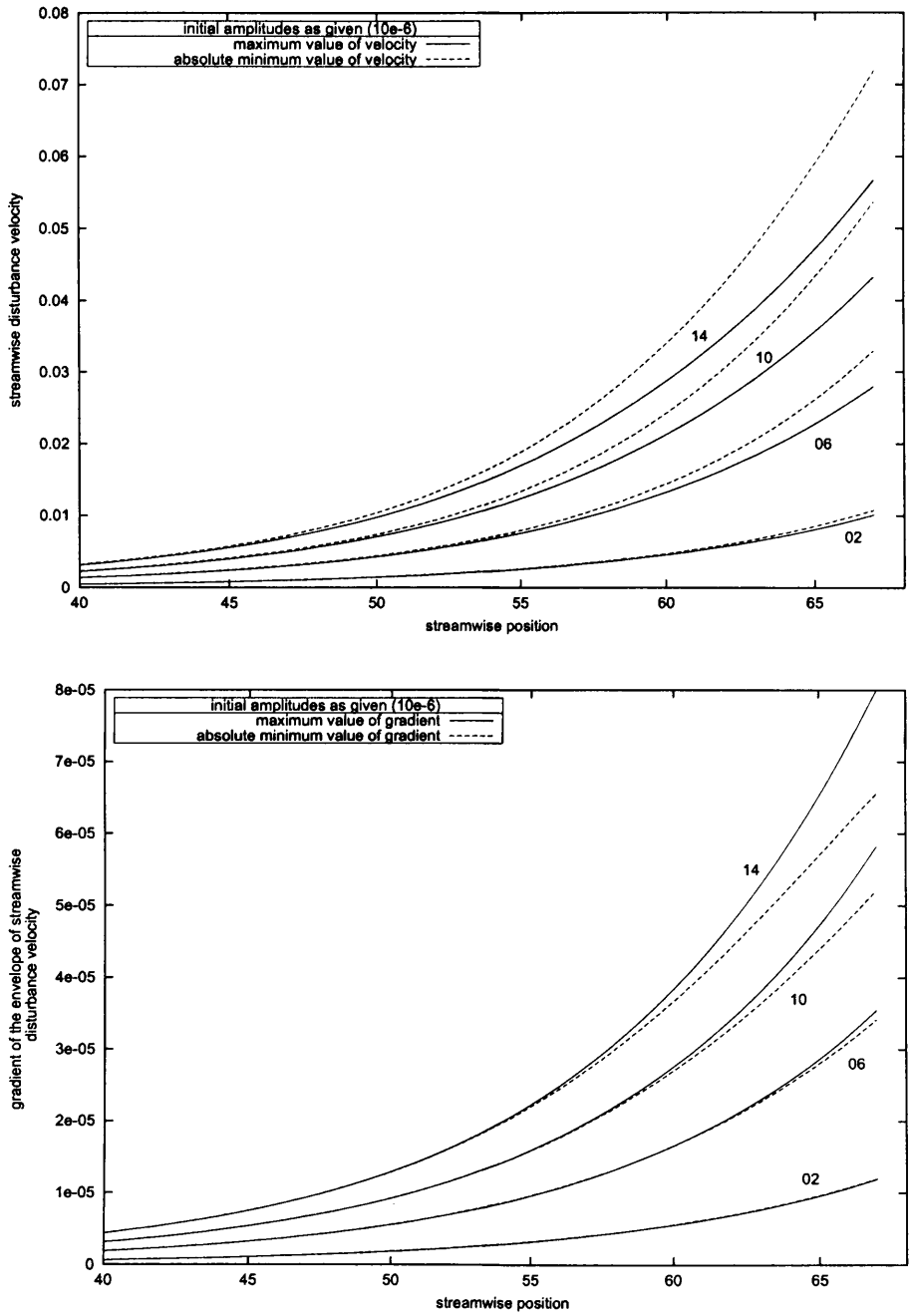

Figure 5.19: Above: the maximum and absolute minimum values of the streamwise velocity against streamwise position. Below: the maximum and absolute minimum values of the gradient of the envelope of streamwise velocity against streamwise position. Four different initial amplitudes were used: 2×10^{-6}, 6×10^{-6}, 10×10^{-6} and 14×10^{-6}.

than the trailing edge, so we would expect to see positive values of Σ. As you can see from the tables, Σ is negative for lower amplitudes, becoming positive for larger amplitudes and for readings taken further downstream.

initial amplitude	u_{max}	$\lvert u_{min}\rvert$	g_{max} (10^{-6})	$\lvert g_{min}\rvert$ (10^{-6})	Σ
0.000002	0.001810	0.001830	2.2966	2.3075	-0.004771
0.000006	0.005354	0.005547	6.8872	6.9101	-0.003325
0.000010	0.008826	0.009330	11.4716	11.4759	-0.000380
0.000014	0.012193	0.013162	16.0471	15.9832	0.003983

Table 5.2: Data for the streamwise position represented by $x_s = 52$.

initial amplitude	u_{max}	$\lvert u_{min}\rvert$	g_{max} (10^{-6})	$\lvert g_{min}\rvert$ (10^{-6})	Σ
0.000002	0.005733	0.001830	6.8844	6.9353	-0.007393
0.000006	0.016469	0.018254	20.5893	20.4371	0.007392
0.000010	0.026225	0.030664	34.1141	32.9506	0.034103
0.000014	0.035136	0.042615	47.3866	44.1218	0.068897

Table 5.3: Data for the streamwise position represented by $x_s = 62$.

Figures 5.20 and 5.21

Figure 5.20 illustrates this over a larger range of streamwise positions by plotting the quantity Σ.

At a streamwise position of $x_s = 42$, for an initial amplitude of 10^{-5} the value of $|u_{max}|$ is 0.003. This could indicate that linear effects are responsible for an initial positive value of Σ. After this, as the streamwise distance increases Σ becomes negative (for all but the highest initial amplitude) before nonlinear effects become significant, where Σ is positive once again.

Finally we shall see these quantities plotted against amplitude rather than streamwise position in figure 5.21.

These results are similar to those obtained by Walker (2005), who investigated the evolution of wavepackets governed by amplitude equations with a linear model and a nonlinear model. Based on weakly nonlinear theory, Healey (1995a) derived amplitude equations for a two-mode system; a fundamental (ω_{ts}) and a first harmonic($2\omega_{ts}$). According to Walker (2005), Healey and a co-worker extended the model to N modes. Walker used 20 modes locating the mode unstable mode at the 10th mode. The wavepacket evolves in time and found that the linear model did yield a small, but positive value of Σ. This will be caused by different effects from those which cause wave-envelope steepening. The nonlinear model gave a positive value of Σ initially, then, a while later, a negative value, and finally, at a later time, Σ became positive, indicating steepening at the trailing edge.

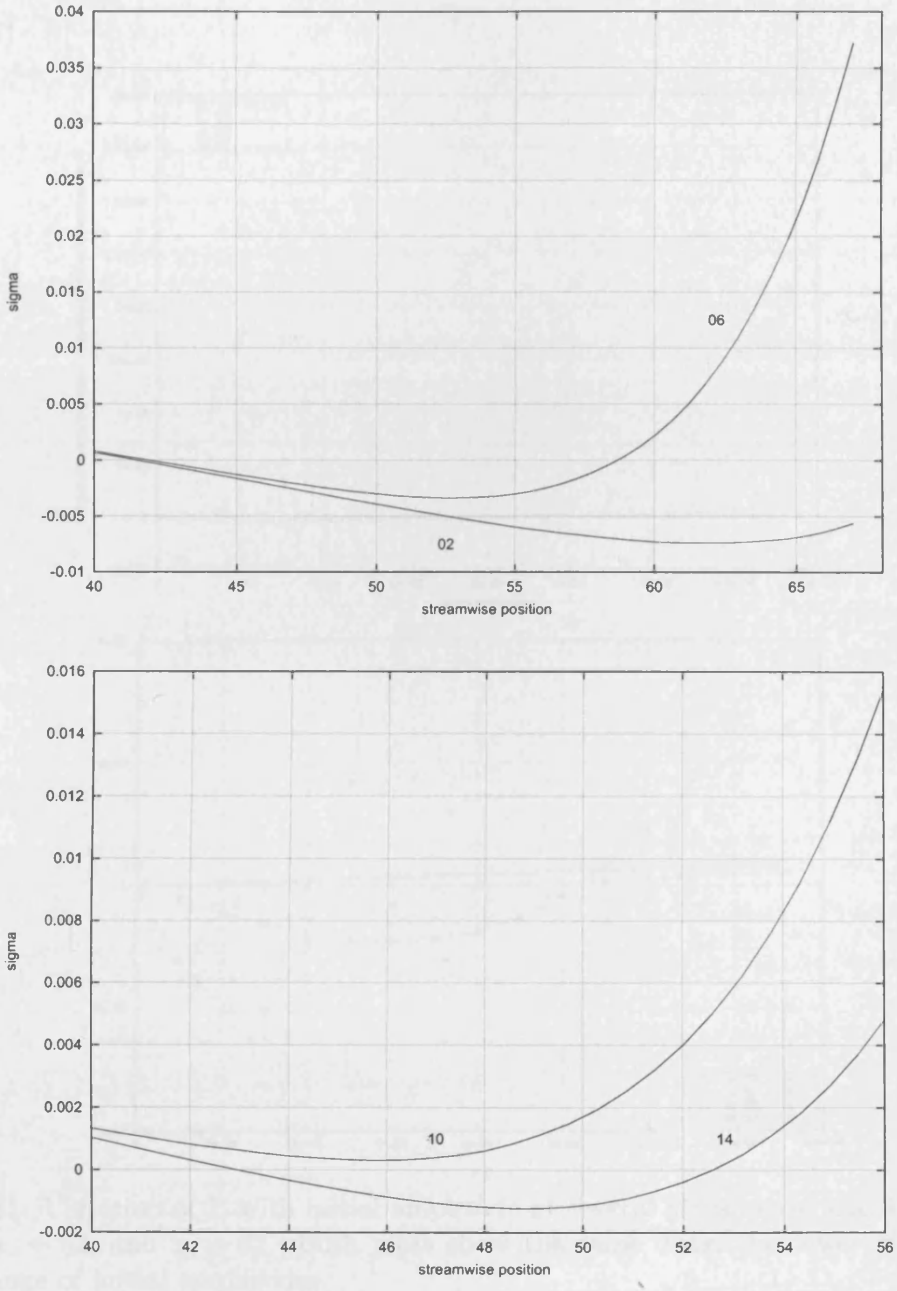

Figure 5.20: Variation of Σ with streamwise position for four different initial amplitudes: 2×10^{-6}, 6×10^{-6}, 10×10^{-6} and 14×10^{-6}..

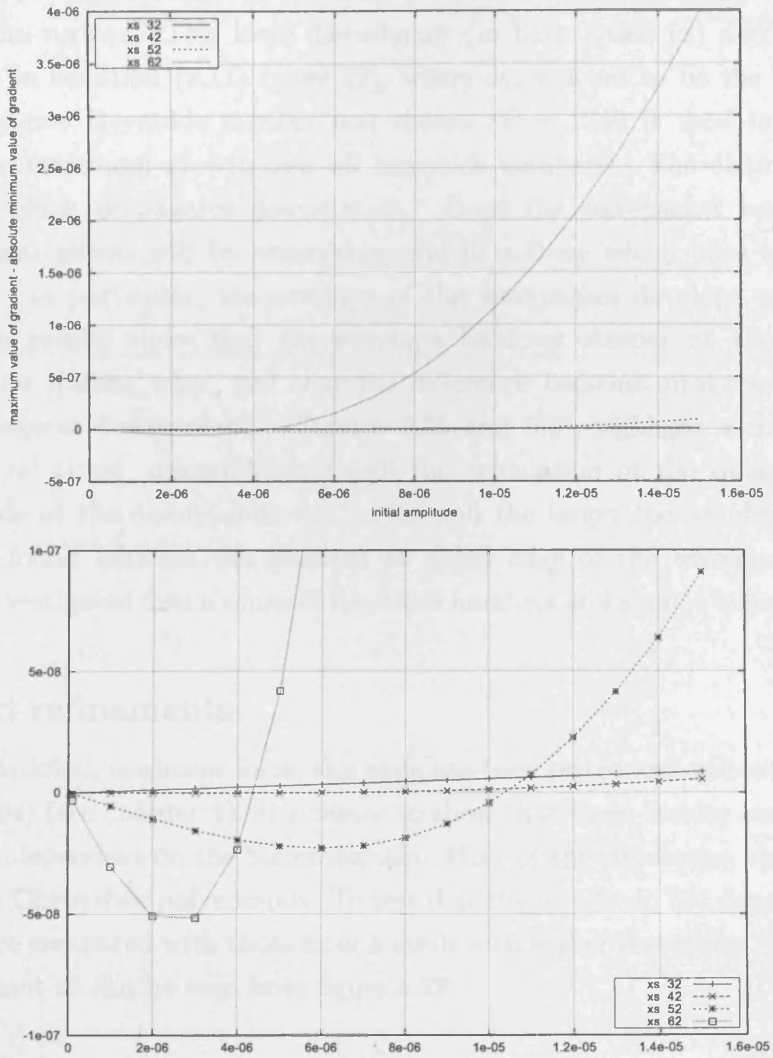

Figure 5.21: Variation of Σ with initial amplitude at several streamwise locations $x_s = 32$, $x_s = 42$, $x_s = 52$, and $x_s = 62$. Both plots show the same data, the lower plot covers a smaller range of initial amplitudes.

In this section we have seen numerical results from simulations of a wavepacket propagating in a transitional boundary layer. The parallel Blasius profile has been used as a basic state. A disturbance was fed into the boundary layer through the boundary condition on the surface. This local disturbance (in both space (x) and time), was of the form given in equation (2.11) (page 19), where ω_{ts} was set to be the most unstable mode for whichever Reynolds number was chosen ($R = 2240$ is used in this chapter, which gives the maximum growth over all Reynolds numbers). The disturbance excites a wavepacket which propagates downstream. Once the wavepacket has grown large enough, nonlinear effects will be observable, and it is these which have been presented in this section. In particular, the envelope of the wavepacket develops asymmetrically. Our simulation results show that the envelope becomes steeper at the leading edge than it is at the trailing edge, and that the difference becomes progressively larger as the wave propagates downstream. (Figures 5.20 and 5.21 highlight a minor deviation from this general trend, discernible through the calculation of the quantity Σ.) The initial amplitude of the disturbance was varied and the larger the amplitude, the more difference was found between the gradient at either edge of the wavepacket. This effect has been investigated over a range of Reynolds numbers and similar behaviour is found.

5.2.3 Grid refinements

In its two-dimensional, nonlinear form, this code has been tested and validated extensively by Houten (2004) (see chapter 4). It remains to show that these results are neither 'grid-dependent' nor dependent on the buffer domain. Most of the simulation results use the a resolution of 64 Chebyshev polynomials. To test that the results do not depend on the grid size, results were compared with those from a mesh with higher resolution. The results are in good agreement as can be seen from figure 5.22.

Resolution:	normal	higher
Number of Chebyshevs, N_z	64	96
Spatial increment, dx	0.5	0.25
Time step, dt:	0.25	0.125

To test that results are not affected by the buffer domain, the downstream boundary was

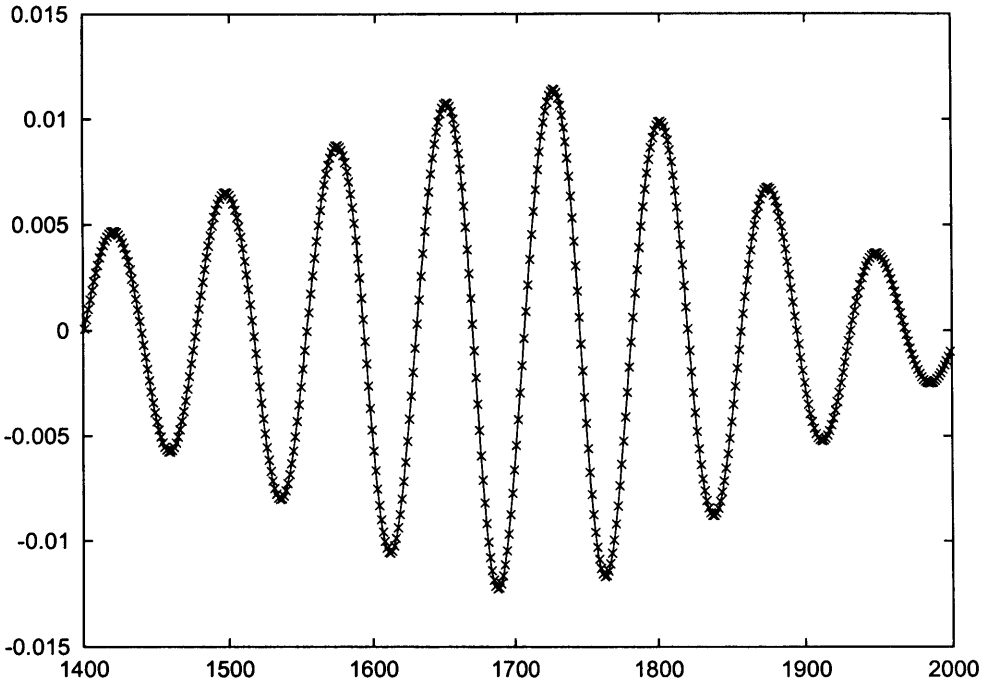

Figure 5.22: Streamwise velocity against streamwise distance at 2000 time units; normal resolution (× × ×), higher resolution (—).

extended and the buffer domain, still of length 200, moved downstream. See figure 5.23. Figure 5.24 shows results for both these computational domains. Results for the shorter domain are valid up to $x = 823$ as indicated. Results for the larger domain are valid up to $x = 1437$. The results are clearly in agreement, so we can conclude that the presence of a buffer domain has not affected the results.

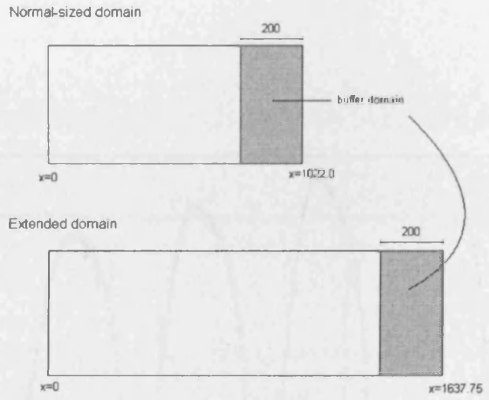

Figure 5.23: The two domains used to determine whether or not the buffer domain affects the results. (x non-dimensionalized with δ.)

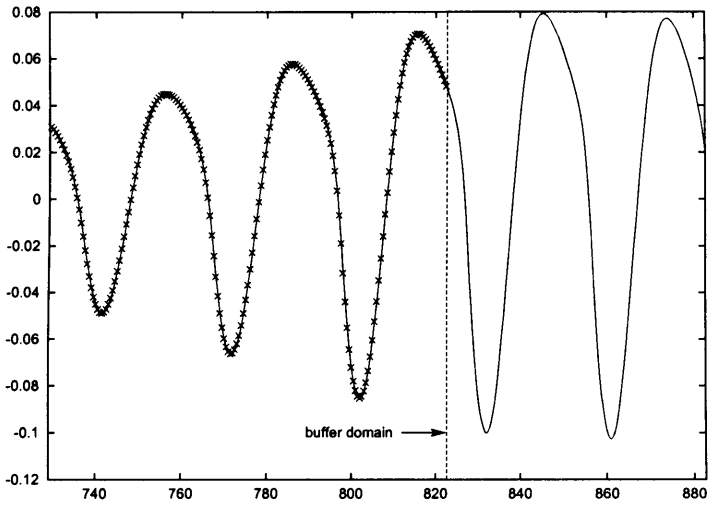

Figure 5.24: Streamwise velocity against x (at time $t = 2500$) for the smaller domain ($\times\times\times$); and for the larger domain (—). The buffer domain shown is that associated with the smaller domain.

Chapter 6

Pressure Gradients and their effect on wave-envelope steepening

Wave-envelope steepening has been found to develop in wavepackets that propagate in a transitional boundary layer. Results from chapter 5 show that, for a zero streamwise pressure gradient, the envelope of the wavepacket becomes steeper at the leading edge than it is at the trailing edge. In the earlier, linear stages of development, the absolute value of the gradient of the envelope at the leading edge is very close to that at the trailing edge.

However, results from experiments (Healey, 2000) show that the envelope becomes steeper at the trailing edge. One possible explanation for this inconsistency between the numerical and experimental results is that there may have been a non-zero pressure gradient present in the experiment. This might have caused the steeper envelope to occur not at the leading edge, but at the trailing edge. In order to test this hypothesis, numerical simulations were carried out as before (chapter 5), only now, the streamwise pressure gradient is non-zero.

This chapter first explains how streamwise pressure gradients can be modelled. Second, the computed velocity profiles of several flows driven by pressure gradients were validated. The third section presents results showing the nonlinear development of a modulated, two-dimensional Tollmien–Schlichting wave, in particular, examining how this wavepacket develops at the leading and trailing edges.

6.1 Modelling streamwise pressure gradients

6.1.1 Falkner–Skan flows

In 1931 Falkner and Skan discovered independently that, if the external flow is proportional to some power of x^*, then the boundary layer equations can be written as an ordinary differential equation and there exists a family of similarity solutions. Hartree calculated some of these profiles numerically in 1937. A brief outline of the derivation of this ordinary differential equation follows.

Consider the two-dimensional Navier Stokes equations and the continuity equation,

$$\begin{aligned}
\frac{\partial u^*}{\partial t^*} + u^*\frac{\partial u^*}{\partial x^*} + w^*\frac{\partial u^*}{\partial z^*} &= -\frac{1}{\rho}\frac{\partial p^*}{\partial x^*} + \nu\left(\frac{\partial^2 u^*}{\partial x^{*2}} + \frac{\partial^2 u^*}{\partial z^{*2}}\right) \\
\frac{\partial w^*}{\partial t^*} + u^*\frac{\partial w^*}{\partial x^*} + w^*\frac{\partial w^*}{\partial z^*} &= -\frac{1}{\rho}\frac{\partial p^*}{\partial z^*} + \nu\left(\frac{\partial^2 w^*}{\partial x^{*2}} + \frac{\partial^2 w^*}{\partial z^{*2}}\right) \\
\frac{\partial u^*}{\partial x^*} + \frac{\partial w^*}{\partial z^*} &= 0\,,
\end{aligned}$$

with the boundary conditions

$$\begin{aligned}
u^* = 0 \quad \text{and} \quad w^* = 0 \qquad & \text{for} \quad z^* = 0\,, \\
u^* \to U^*(x^*) \qquad & \text{as} \quad z^* \to \infty\,.
\end{aligned}$$

In a boundary layer the variation is much greater in the wall-normal direction than in the streamwise direction. By considering the order of magnitude of the terms in the light of this assertion, it can be shown that the steady solution will satisfy the following simplified system,

$$\begin{aligned}
u^*\frac{\partial u^*}{\partial x^*} + w^*\frac{\partial u^*}{\partial z^*} &= -\frac{1}{\rho}\frac{\partial p^*}{\partial x^*} + \nu\frac{\partial^2 u^*}{\partial z^{*2}} \qquad (6.1) \\
\frac{\partial p^*}{\partial z^*} &= 0 \\
\frac{\partial u^*}{\partial x^*} + \frac{\partial w^*}{\partial z^*} &= 0\,.
\end{aligned}$$

These equations are known as the boundary layer equations. In this approximation the

pressure depends solely on the streamwise coordinate, so the pressure in the boundary layer will be equal to the pressure in the freestream. Hence, we can replace dp^*/dx^* by $-\rho U^* dU^*/dx^*$. To obtain the so-called Falkner–Skan similarity solutions we next assume that the external flow is of the form $U^* = U^*_\infty (x^*/l^*)^m$ where m is a real number. Instead of solving for u^*, we rewrite the equations in terms of the variable $\eta = z^*\sqrt{(U^*/\nu x^*)}$ and the streamfunction $\psi = \sqrt{U^* \nu x^*} f(\eta)$, and solve for $f(\eta)$. From the streamfunction we can see that $f(\eta)$ is related to u^* by $df/d\eta = u^*/U^*$. Substituting these new variables into the system of equations (6.1) reduces the boundary layer equations to an ordinary differential equation:

$$f''' + \left(\frac{m+1}{2}\right) f'' f + m(1 - (f')^2) = 0 \ ,$$

$$f(0) = 0 = f'(0), \qquad f'(\infty) = 1 \ .$$

The parameter m characterizes the pressure gradient:

- $m > 0$ corresponds to a negative (or favourable) pressure gradient, where the external flow is accelerating;
- $m < 0$ corresponds to a positive (or adverse) pressure gradient where the external flow is decelerating;
- and $m = 0$ corresponds to a zero pressure gradient where the flow travels at a constant speed.

Another parameter is sometimes used to describe the pressure gradient, and that is the Hartree parameter β. It is related to m by

$$\beta = \frac{2m}{m+1} \ .$$

For the zero pressure-gradient case ($m = 0$), the velocity profile has a point of inflection at $z = 0$. For positive pressure gradients ($m < 0$), the point of inflection occurs above the plate in the boundary layer. According to Rayleigh's criterion (see page 323, Acheson, 1990), an inflectional velocity profile is inviscidly unstable. As inviscid instabilities are usually much stronger than viscous instabilities, positive pressure gradients are destabilizing whereas negative pressure gradients are stabilizing. (This can be seen in the plot of the growth rates for different pressure gradients in figure 6.5.) Positive pressure

gradients are also known as 'adverse' pressure gradients because they provide a force which acts to oppose the flow. Likewise, negative pressure gradients are also referred to as 'favourable' pressure gradients.

For $m > 0$ a unique solution of the Falkner–Skan ordinary differential equation exists. However, if $-0.0904 < m < 0$, then two solutions exist: one physical solution in which u^* (or $f'(\eta)$) increases monotonically with height, and one solution that corresponds to a region of reverse flow at the wall. The boundary layer equations are of questionable validity when reverse flow occurs, and it turns out that the second solution is not physically valid. In the computational code, the Falkner–Skan ordinary differential equation is solved with a NAG routine. The condition $f' > 0$ is imposed, in order to ensure that the solution does not have a region reverse flow at the wall. The nonlinearity is handled iteratively.

The Falkner–Skan profiles describe flow over a wedge, but as can be seen from the diagram below, they can also describe flow over a flat plate ($x \geqslant 0$) with a streamwise pressure gradient imposed at $x = 0$.

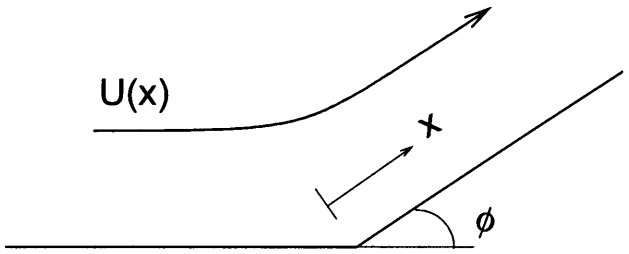

Figure 6.1: Flow over a wedge of half angle $\phi = \pi m/m + 1$.

6.2 Falkner–Skan Profiles

6.2.1 Verification

Falkner–Skan profiles have been generated with NAG routines designed to solve ordinary differential equations. Some profiles are plotted in figure 6.2. The validation of these profiles is undertaken, by comparing the second derivative of streamwise velocity with

respect to similarity variable η with the results of Woodley and Peake (1997).

Figure 6.3 shows the second derivative of streamwise velocity against η for three pressure gradients, corresponding to $m = 0.0, -0.05$, and -0.09. It can be seen that as the pressure gradient becomes larger, the inflection point in the velocity profile occurs higher above the plate (corresponding to higher values of η), and therefore the flow becomes more unstable.

Also, by recalling that f satisfies the following equation and boundary conditions, we can calculate the value of $\frac{d^2u}{d\eta^2}$ at the wall.

$$f''' + \left(\frac{m+1}{2}\right) f''f + m(1 - (f')^2) = 0 \ , \tag{6.2}$$

$$f(0) = 0 = f'(0), \qquad f'(\infty) = 1 \ . \tag{6.3}$$

As $\frac{d^2u}{d\eta^2} = f'''$ we have the following from equation (6.2):

$$\frac{d^2u}{d\eta^2} = -\left(\frac{m+1}{2}\right) f''f - m(1 - (f')^2) \ .$$

Using the boundary conditions from (6.3) gives

$$\left.\frac{d^2u}{d\eta^2}\right|_{\eta=0} = -m \ .$$

Indeed, as can be seen in figure 6.3, the second derivative does take the value $-m$ at the wall. Figure 6.3 also shows excellent agreement with the results of Woodley and Peake (1997).

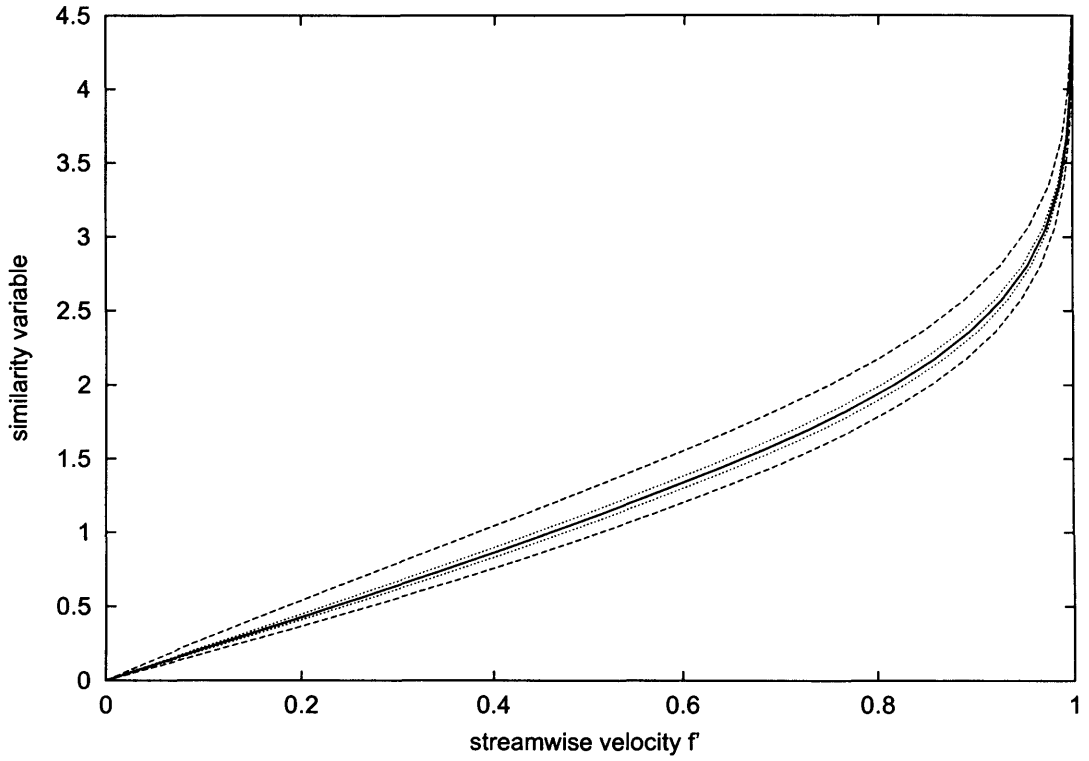

Figure 6.2: Falkner–Skan profiles for pressure gradients corresponding to $m = -0.04$ (– – –), $m = -0.01$ ($\cdots$), $m = 0.0$ (—), $m = 0.01$ ($\cdots$), and $m = 0.04$ (– – –).

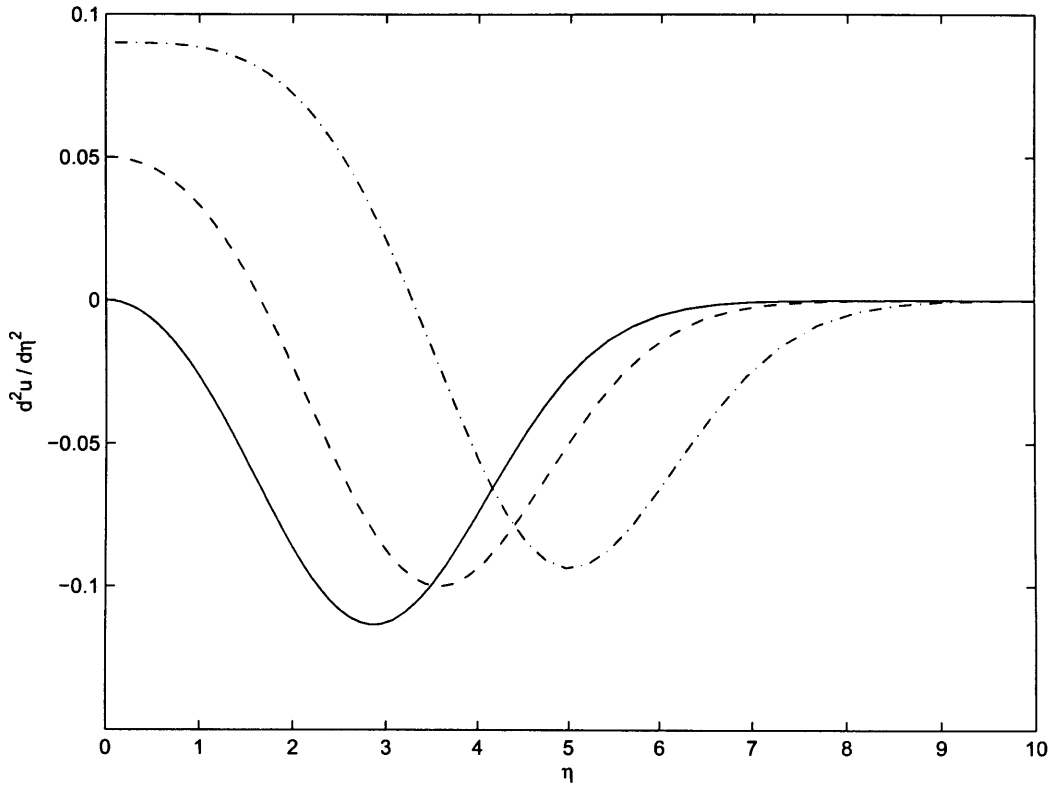

Figure 6.3: The second derivative of streamwise velocity against η for three Falkner–Skan profiles. ($m = 0.00$ —— , $m = -0.05$ − − − , and $m = -0.09$ − · − · −)

Cooper and Carpenter (1997) present a plot of the growth rate against frequency for a Reynolds number of 5000 and a pressure gradient corresponding to $m = -0.0698$. An eigenvalue solver (written by Davies) was used to solve the Orr–Sommerfeld equation for Falkner–Skan profiles in order to determine eigenvalues corresponding to the wavenumber and growth rate of the linear stability problem (frequency, Reynolds number both given). The results from the eigenvalue solver shown here in figure 6.4 agree well with those of Cooper and Carpenter.

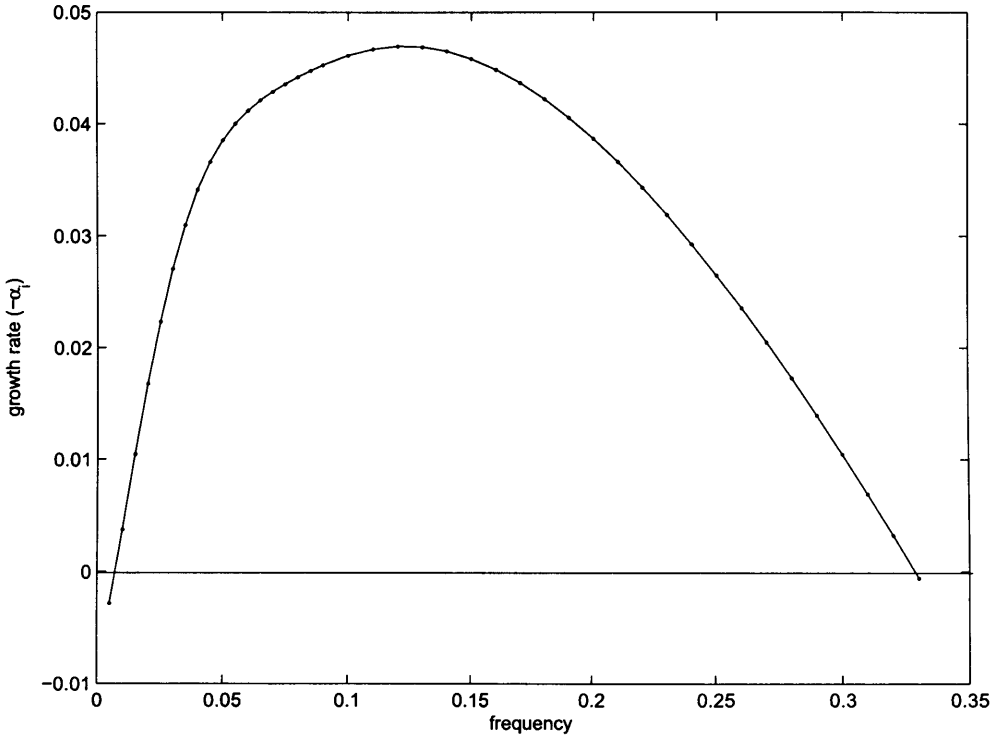

Figure 6.4: Linear growth rate against frequency for the Falkner–Skan profile determined by $m = -0.0698$ at a Reynolds number $R=5000$

6.2.2 Parameters used

In the simulations presented in the following section, six streamwise pressure gradients are employed, corresponding to values of $m = \pm 0.04$, $m = \pm 0.02$ and $m = \pm 0.01$. Shown in figure 6.2 is a graph of some of the streamwise velocity profiles for these particular pressure gradients.

Figure 6.5 shows how growth rate varies with frequency at $R = 2240$ for each of the flows given in figure 6.2. Again, these results were generated with the eigenvalue solver of Davies that was used to generate the results shown in the previous subsection (section 6.2.1).

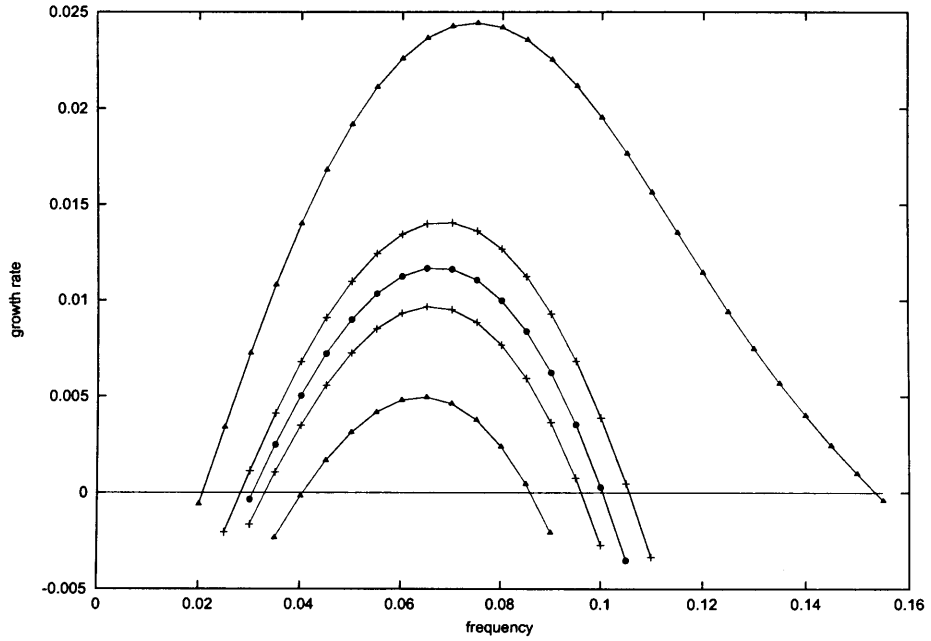

Figure 6.5: Growth rate dependence upon frequency for several pressure gradients, from top to bottom, m= -0.04 (▲▲▲), m= -0.01 (+++), m=0.0 (•••), m=0.01 (+++), and m=0.04 (▲▲▲).

Table 6.1 summarizes the parameters for Falkner–Skan flows at a Reynolds number of $R = 2240$. At this Reynolds number for $m = 0$, the mode with the maximum growth rate was found, as this is the mode in the numerical simulations which we want to excite most strongly (see section 5.2.1).

m	α_r	α_i	ω	displacement thickness (δ)	momentum thickness (θ)
0.04	0.215032	-0.004953	0.065	1.107271	0.439095
0.02	0.214642	-0.007892	0.065	1.156597	0.451924
0.01	0.214439	-0.009654	0.065	1.185084	0.459419
0.0	0.21424	-0.011665	0.065	1.216781	0.466929
-0.01	0.227733	-0.014040	0.070	1.252370	0.475418
-0.02	0.227413	-0.016879	0.070	1.292782	0.484166
-0.04	0.239904	-0.024441	0.075	1.393896	0.503029

Table 6.1: Parameters of the Falkner–Skan flows used in the following numerical simulations.

6.3 Results

Numerical simulations were carried out as before (chapter 5). The flow at the input is a Falkner–Skan flow which has an associated pressure gradient. As before, this flow is disturbed by a wavepacket. The disturbance propagates downstream and measurements of the time history of the disturbance are taken at suitable streamwise points.

Six different pressure gradients were tested, three negative (favourable) pressure gradients and three positive (adverse) ones corresponding to; $m = \pm 0.01$, $m = \pm 0.02$ and $m = \pm 0.04$. In each simulation the forcing amplitude A (see equation (2.11)) was chosen so that the amplitude of the streamwise disturbance velocity would exceed $O(10^{-2})$ before the buffer domain. This ensures that nonlinear effects occur in the domain.

Each of the following figures from 6.6 to 6.11 consists of two graphs: the first shows the gradient of the envelope of the streamwise disturbance velocity at one streamwise position and the second shows the maximum and absolute minimum values of the gradient over a range of streamwise positions. These maximum and minimum values occur at the leading and trailing edges respectively.

In each case, the first graph shows that the envelope at the leading edge has become steeper than at the trailing edge, and the second graph shows that the envelope at the

leading edge becomes progressively steeper than the envelope at the trailing edge as the disturbance moves downstream.

The results are summarized in the following table.

m	pressure gradient	envelope is steeper at which edge?	does the difference in gradient at leading and trailing edges increase as the wavepacket moves downstream?
0.04	} favourable	leading	✓
0.02		leading	✓
0.01		leading	✓
0.0	no pressure gradient	leading	✓
-0.01	} adverse	leading	✓
-0.02		leading	✓
-0.04		leading	✓

In conclusion, the code has been used to solve the governing equations for fluid flowing over a flat plate in the presence of a streamwise pressure gradient. When there is no pressure gradient, a wavepacket disturbance becomes steeper at its leading edge than at its trailing edge. From the results shown in this chapter it is clear that, in the presence of both adverse and favourable pressure gradients, the wavepacket still becomes steeper at the leading edge in each case. From these results it can be concluded that the presence of a streamwise pressure gradient does not affect the location of the steepest part of the envelope, at least for the range of m considered. There is no evidence of any trends that could lead to reversal of the behaviour if stronger pressure gradients were considered.

Favourable pressure gradient m=0.04

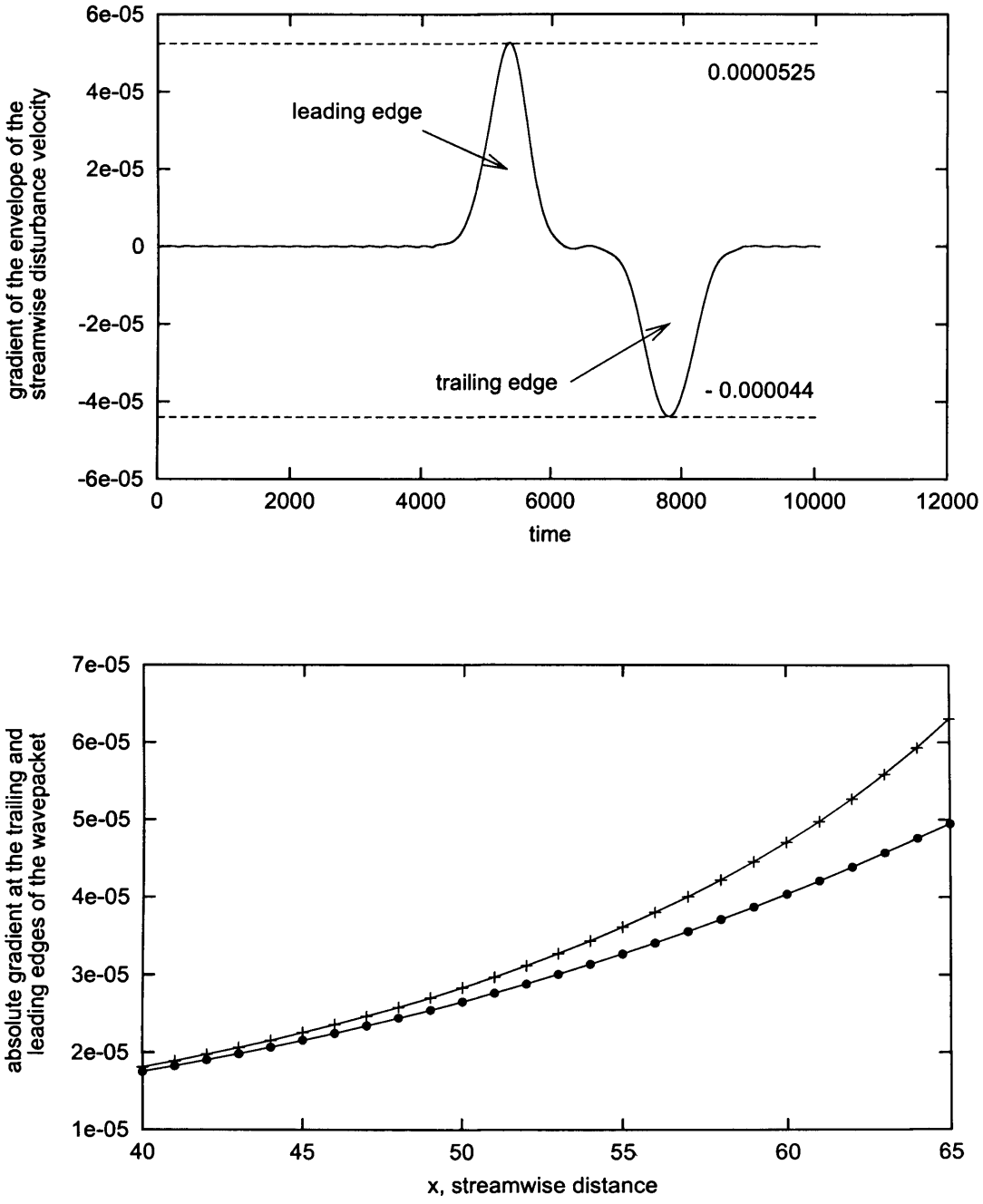

Figure 6.6: Above: gradient of the envelope of the streamwise disturbance velocity at $x_s = 62$,
and below: absolute value of the gradient at the leading (+ + +) and trailing edges (• • •)) over a range of streamwise distance ($x = x_s$)

Favourable pressure gradient m=0.02

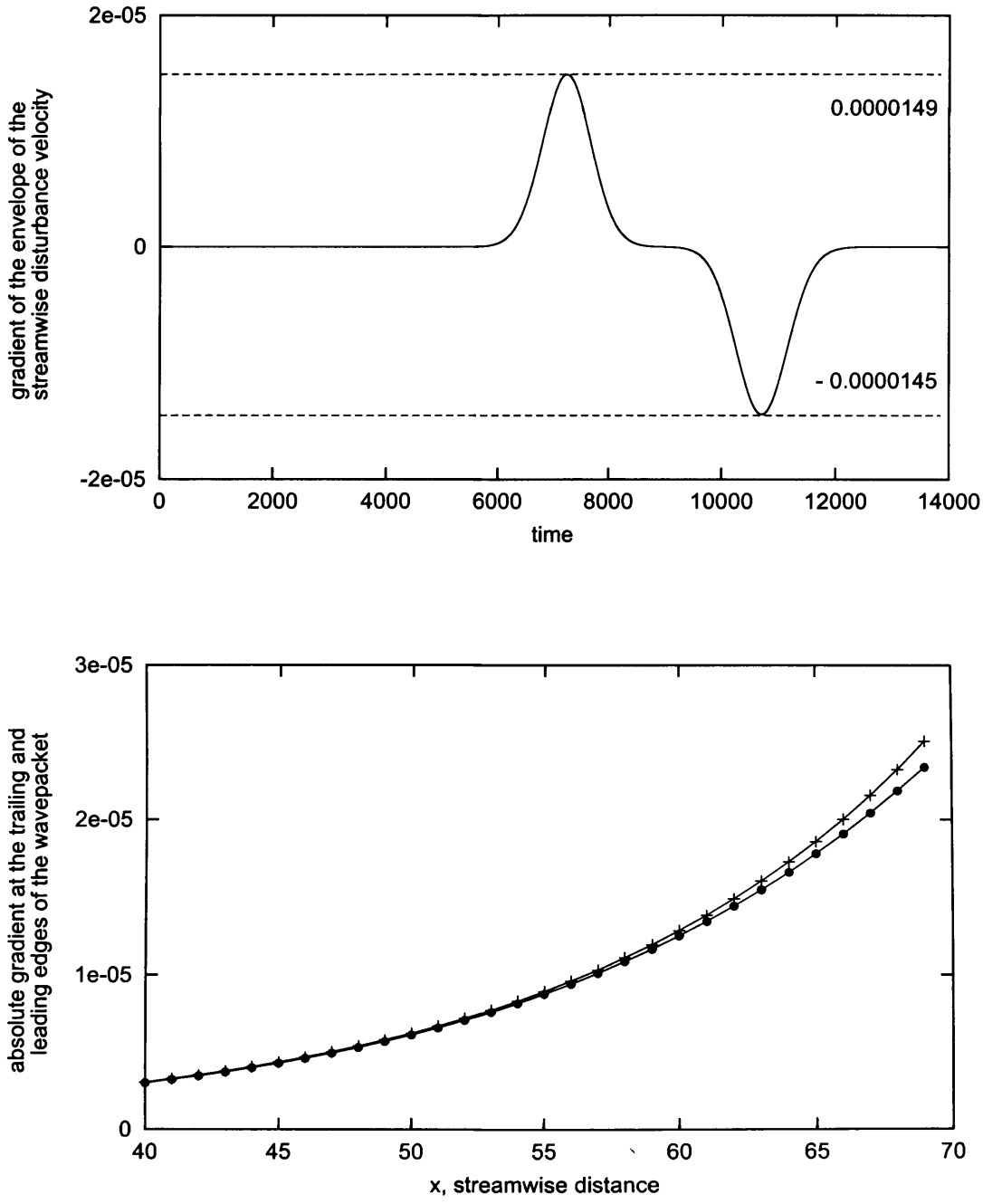

Figure 6.7: Above: gradient of the envelope of the streamwise disturbance velocity at $x_s = 62$,
and below: absolute value of the gradient at the leading (+ + +) and trailing edges (• • •)) over a range of streamwise distance ($x = x_s$)

Favourable pressure gradient m=0.01

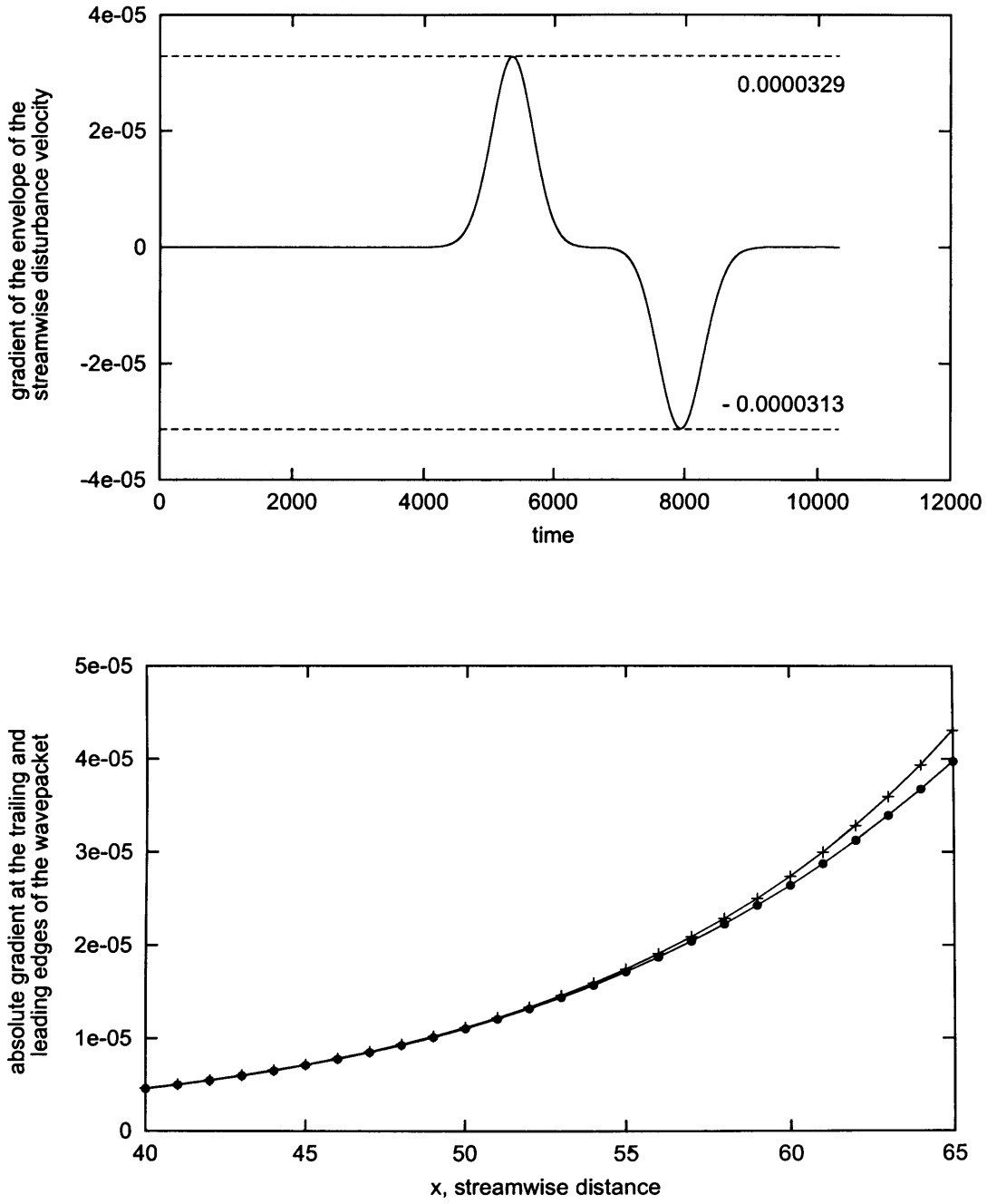

Figure 6.8: Above: gradient of the envelope of the streamwise disturbance velocity at $x_s = 62$,
and below: absolute value of the gradient at the leading (+ + +) and trailing edges (• • •)) over a range of streamwise distance ($x = x_s$)

Adverse pressure gradient m=-0.01

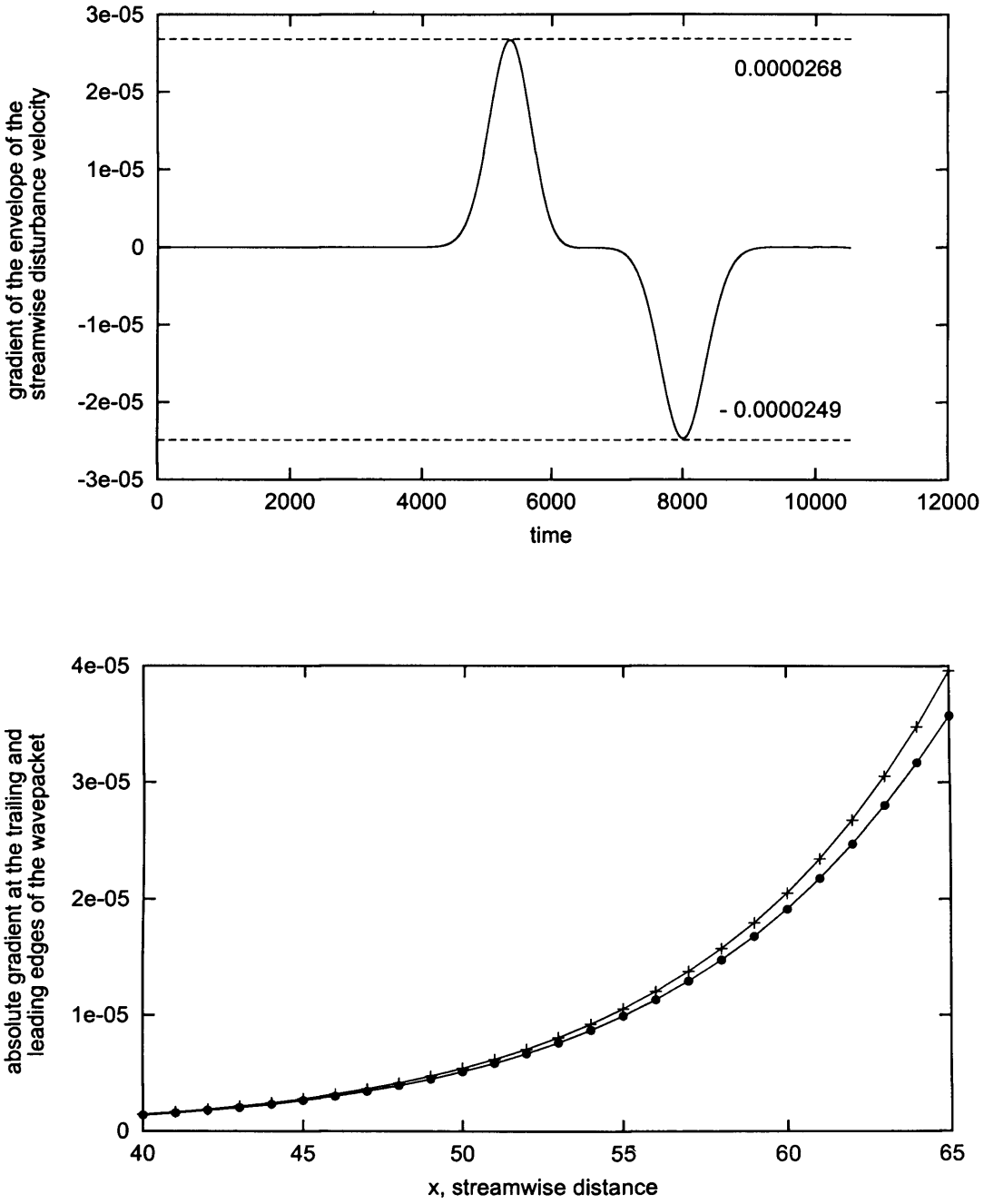

Figure 6.9: Above: gradient of the envelope of the streamwise disturbance velocity at $x_s = 62$,
and below: absolute value of the gradient at the leading (+ + +) and trailing edges (• • •)) over a range of streamwise distance ($x = x_s$)

Adverse pressure gradient m=-0.02

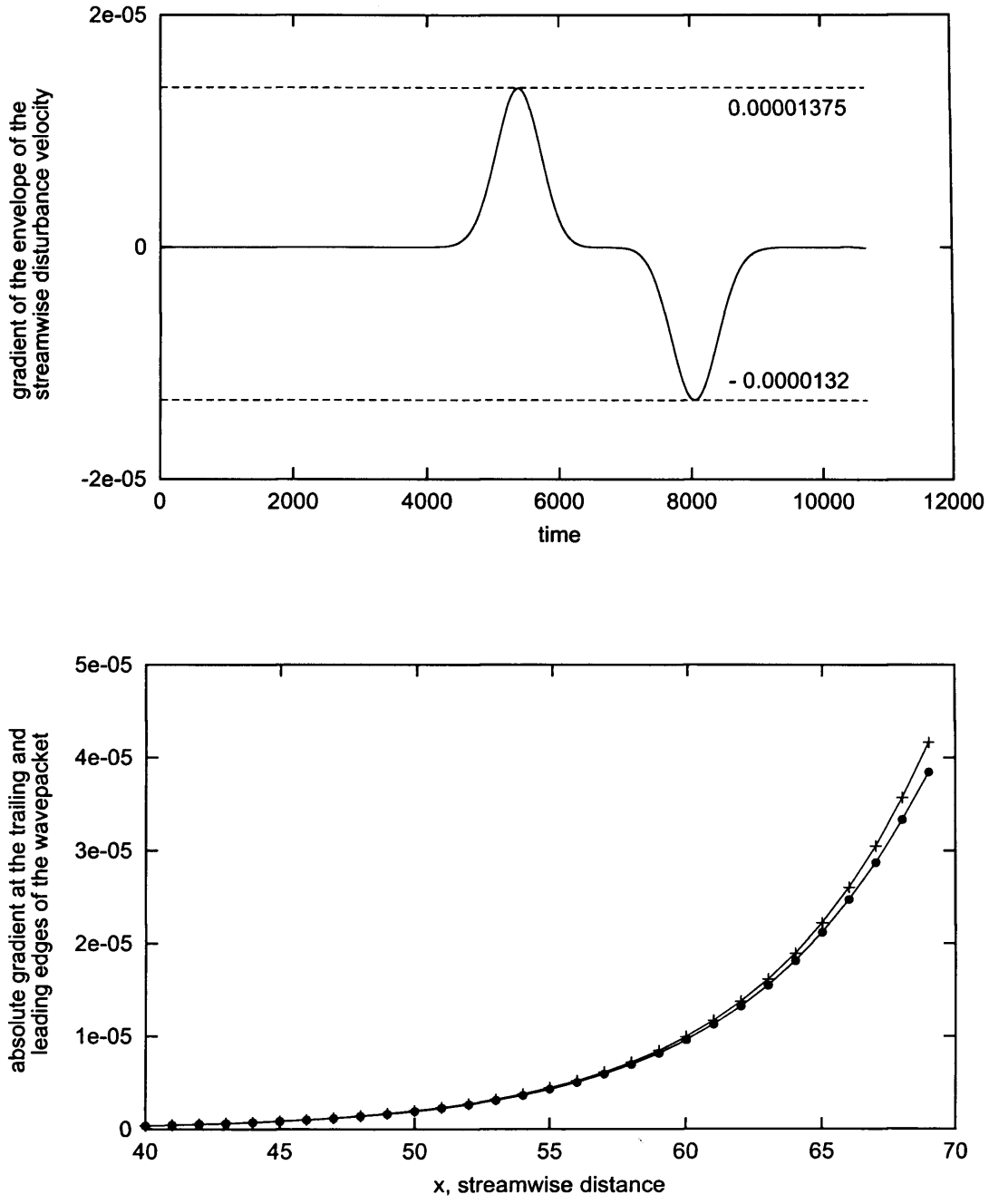

Figure 6.10: Above: gradient of the envelope of the streamwise disturbance velocity at $x_s = 62$,
and below: absolute value of the gradient at the leading (+ + +) and trailing edges (• • •)) over a range of streamwise distance ($x = x_s$)

Adverse pressure gradient m=-0.04

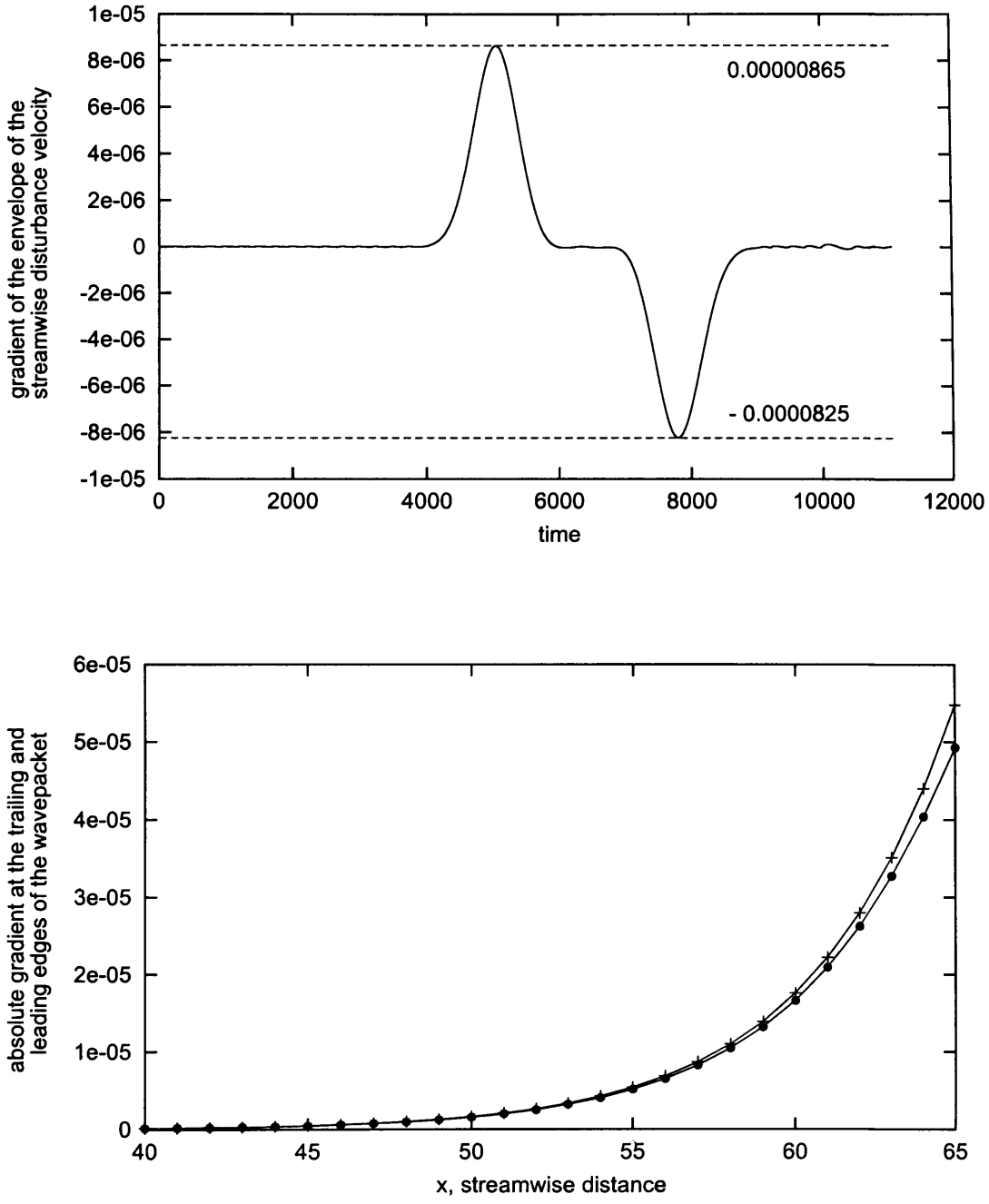

Figure 6.11: Above: gradient of the envelope of the streamwise disturbance velocity at $x_s = 57$),
and below: absolute value of the gradient at the leading (+ + +) and trailing edges (• • •)) over a range of streamwise distance ($x = x_s$)

Chapter 7

Random Forcing

In chapter 5 wave-envelope steepening was studied by comparing the behaviour of leading and trailing edges of a wavepacket. Two-dimensional simulations predict that after a period of linear, and symmetric development[1], the wave envelope becomes steeper at the leading edge than it is at the trailing edge, resulting in an asymmetric wave envelope. This is caused by a weak nonlinear effect that depends on the sign of the gradient of the envelope; this is different at the leading and trailing edges, hence the asymmetry.

Shaikh and Gaster (1994) and Healey (2000) have undertaken experiments which investigate the evolution of a randomly-modulated three-dimensional wavepacket. In this chapter results are presented which aim to model such a randomly-modulated wavepacket. A relatively long wave will possess many occurrences of increasing and decreasing envelope. For disturbances which are large enough to develop nonlinearly, wave-envelope steepening should occur. From the previous numerical results (see chapter 5) we expect negative gradients to become less steep than positive gradients, so overall there is a skewness in the gradient towards positive values. The skewness will be calculated to see if this is the case.

7.1 How to generate a random signal

Previously we have disturbed the boundary layer with a Tollmien–Schlichting wave localized in space and short in time. In addition, we wish to impose a slowly-varying random

[1]The development could be slightly asymmetric due to dispersive effects, however this is small in comparison with the asymmetry seen that is caused by the wave-envelope steepening effect.

envelope upon this wave. A set of complex Fourier coefficients are determined by choosing a random phase and amplitude. Fourier coefficients of high frequency terms are set to zero. The inverse Fourier Transform is then taken, and the temporal perturbation that occurs at the wall has the form $g(t)$,

$$g(t)\sin(\omega_{ts}t) = 0.5\mathcal{F}^{-1}[\hat{f}_k]\left(\tanh\left(\frac{\omega_{ts}(t-t_a)}{t_0}\right)+\tanh\left(\frac{\omega_{ts}(t_b-t)}{t_0}\right)\right)\sin(\omega_{ts}t)\ , \quad (7.1)$$

where $\hat{f}_k$ are the Fourier coefficients. This is similar to the forcing which has been used before, see (2.13) on page 19, except for the inclusion of the Fourier coefficients. As previously described, ω_0 is taken to be the frequency corresponding to the most unstable mode at the chosen Reynolds number, $t_0 = 5$, $t_a = 400$, and $t_b = 6000$. This value for t_b is substantially larger than before because we want to ensure that there are many occurrences of decaying and growing parts of the envelope, and also we would wish to excite a wavepacket with a skewness that is as close to zero as possible.

As the randomly-modulated wave envelope should be real, our Fourier coefficients will be Hermitian in form, and will satisfy

$$\hat{f}_k = \hat{f}^*_{N-k} \quad (7.2)$$

where the asterisk denotes the complex conjugate. This means we need chose only $N/2$ Fourier coefficients, the remaining half can be calculated using this relationship (7.2). Random numbers $A_k \in (0,1]$ and $\theta_k \in (0,2\pi]$ are generated. From these the Fourier coefficients are calculated as follows:

$$\Re\{\hat{f}_k\} = A_k\cos\theta_k \quad (7.3)$$

$$\Im\{\hat{f}_k\} = A_k\sin\theta_k \quad (7.4)$$

To ensure that the envelope is slowly-varying we can restrict the number of modes that have a non-zero amplitude. For example, if we wish to allow non-zero modes up to one fifth of the frequency of the Tollmien–Schlichting wave we set

$$A_k = 0 \qquad \text{for} \quad k > 0.2k_{ts}\ , \quad (7.5)$$

where k_{ts} is corresponds to the index of the discrete representation of the Tollmien–Schlichting frequency:

$$k_{ts} = \left\lceil \frac{\omega_{ts} N\, dt}{2\pi} \right\rceil . \tag{7.6}$$

In general the discrete frequency is given by

$$w_k = \frac{2\pi k}{N dt} , \qquad k = 1, \ldots, N . \tag{7.7}$$

7.2 How to measure asymmetry

The asymmetry arises in the gradient of the envelope of the streamwise velocity. We look at the skewness of this quantity therefore. The skewness (referred to as normalized skewness) is defined as follows:

$$\gamma_n = \frac{\sum_{j=1}^{N}(g_j - \bar{g})^3}{\sigma^3 N} \tag{7.8}$$

where g_j is the gradient at time t_j, $\bar{g}$ is the average gradient and σ is the standard deviation of the gradient given by

$$\sigma = \sqrt{\frac{\sum_{j=1}^{N}(g_j - \bar{g})^2}{N}} . \tag{7.9}$$

An alternate definition has been used by Healey (2000) and Houten (2004),

$$\gamma = \sqrt[3]{\frac{\sum_{j=1}^{N}(g_j - \bar{g})^3}{N}} . \tag{7.10}$$

This definition is referred to as non-normalized skewness.

We now consider the interpretation of these definitions. If we have two sets of results from identical simulations both showing linear behaviour, where set one had an initial amplitude of 1.0 and the other an initial amplitude of A, then if the mean value of set one is given by $\bar{g}$ then the mean value of set two will be $A\bar{g}$. Similarly, if the standard deviation of set one is given by σ then the standard deviation of set two will be $A\sigma$. Using the definition of normalized skewness given in (7.8), then if set one has a skewness of γ_n then set two will also have this skewness. Using the definition of non-normalized skewness given in (7.10) if set one has skewness γ then set two will have a skewness of $A\gamma$. When examining the

results then, if using the normalized definition of skewness it should be constant for linear behaviour and then should deviate from this when nonlinear effects become significant. If using the non-normalized definition of skewness it should be proportional to (initial) amplitude for linear behaviour and then should deviate from this when nonlinear effects become significant. From chapter 4 we expect the wave-envelope steepening effect to be amplitude dependent (ie wave-envelope steepening will be more prominent, the larger the amplitude). So, if using the normalized definition, we expect the skewness to deviate from a constant once nonlinear terms become significant. When using the non-normalized definition, we expect the skewness to deviate from linear behaviour once nonlinear terms become significant.

7.3 Results

7.3.1 R=1300

A Reynolds number of R=1300 and a total simulation time of 12000 were used to generate the following results. A cut-off frequency of $0.2\omega_{ts}$ has been used throughout this chapter. Other values were used, for example, $0.15\omega_{ts}$, $0.25\omega_{ts}$, $0.3\omega_{ts}$, $0.35\omega_{ts}$, $0.4\omega_{ts}$, $0.6\omega_{ts}$ and $0.8\omega_{ts}$. All the results were similar to those which will be shown, however $0.2\omega_{ts}$ does seem to illustrate the wave-envelope steepening effect most strongly. The initial amplitude varied from 100×10^{-9} to 30×10^{-6} and the wavepacket was longer than that used previously. This was to increase the number of growing and decaying portions in the wavepacket due to the random variation.

The random forcing signal used is shown in figure 7.1. This forcing creates a disturbance in the form of a wavepacket which then propagates downstream. The time histories of the wavepacket and its envelope at the location $x_s = 52$ for an initial amplitude of 10×10^{-6} are shown in the top plot of figure 7.2. There are almost no nonlinear effects appearing at this stage, although, at a time of 2000 the velocity is slightly more negative than the envelope (of the modified velocity, see section 5.1.4 on page 114). If we use a higher initial amplitude (200×10^{-6}), then at the same streamwise location we can see that nonlinearities are strongly evident by looking at the middle plot of figure 7.2. Here we can see that the maximum streamwise velocity is much less than the absolute value of the minimum velocity. The final plot of figure 7.2 shows the modified streamwise velocity and

envelope.

It should be noted that as the modulation is confined to low frequency modes ($< 0.2\omega_{ts}$), that the signal processing involved in finding the modified wavepacket and its envelope will filter out these modes.

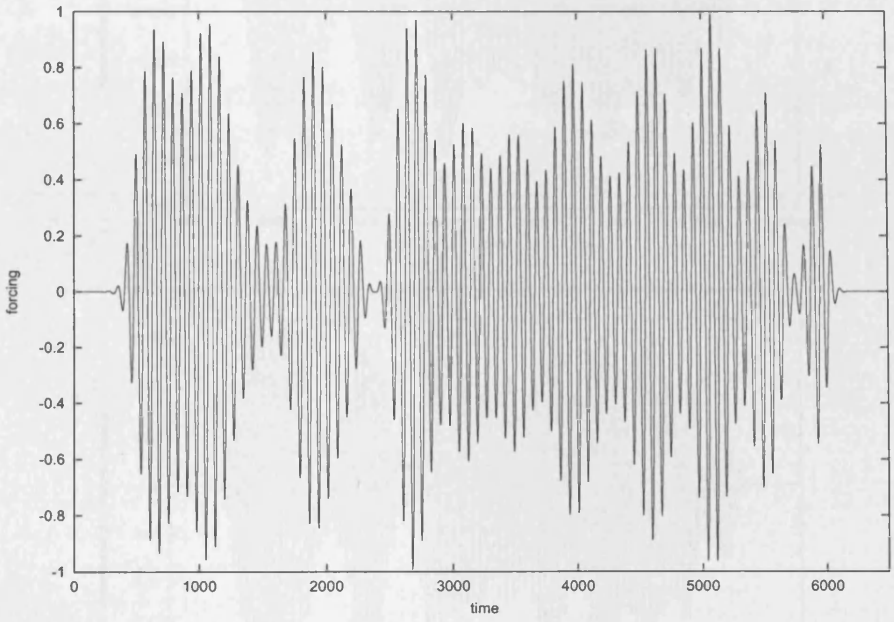

Figure 7.1: The temporal forcing function $g(t)\sin(\omega_{ts}t)$ as given by (7.1).

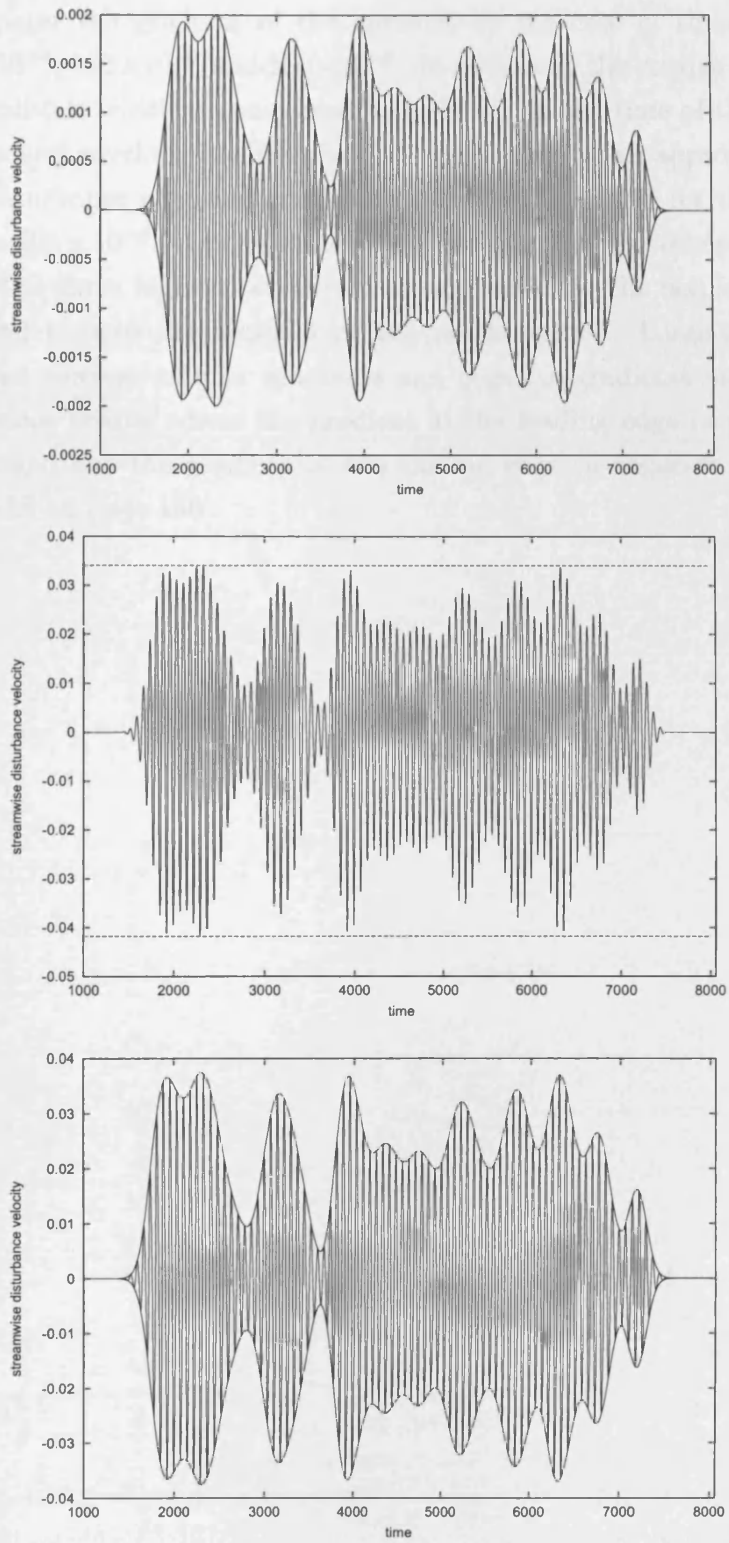

Figure 7.2: Streamwise velocity and envelopes at $x_s = 52$ for an amplitude of 10×10^{-6} (top plot) and 200×10^{-6} (lower two plots). There are no discernible nonlinear effects in the top plot, but for the larger amplitude, the middle plot shows that the velocity is exhibiting signs of nonlinearity ($u_{max} \neq u_{min}$).

Figure 7.3 compares the gradient of the envelope in the case of three different initial amplitudes: 1×10^{-6}, 160×10^{-6} and 260×10^{-6}. In each case, the comparison is made with the smallest amplitude which is considered to be linear in the time of the simulation. In each case this second envelope has been scaled by dividing by an appropriate value, that is 160 for the disturbance of initial amplitude 160×10^{-6} and 260 for the disturbance of initial amplitude 260×10^{-6}. If both simulations had no nonlinear effects then these plots would overlap. The three highest peaks remain unaffected by the nonlinearities, however smaller peaks and troughs are lessened by the nonlinearities. Large positive gradients remain unchanged whereas smaller gradients and negative gradients are lessened, which agrees with previous results where the gradient at the leading edge (a positive gradient) remained unchanged and the gradient at the trailing edge (a negative gradient) became less, see figure 5.18 on page 130.

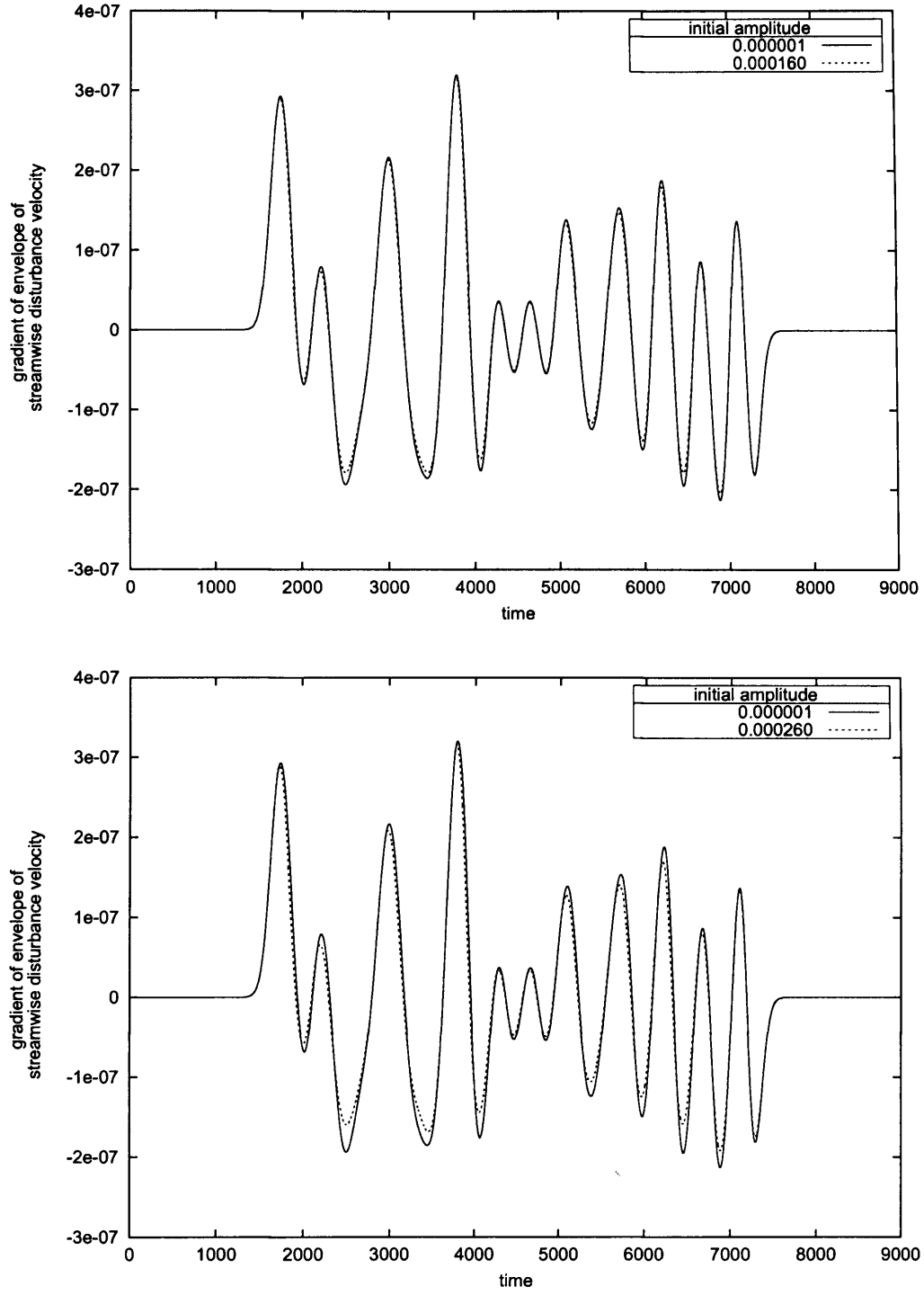

Figure 7.3: Scaled gradient of envelope of the streamwise disturbance velocity at $x_s = 52$ for two different initial amplitudes (top: 1×10^{-6} and 160×10^{-6}, bottom: 1×10^{-6} and 260×10^{-6}).

The skewness has been calculated using the normalized formula (7.8). A linear, quadratic and cubic fit are shown in figure 7.4, the cubic fit is the closest. As argued in section 7.2, if the normalized skewness deviates from a constant then the initial amplitude does affect the skewness, and the higher the amplitude, the more positive the skewness is.

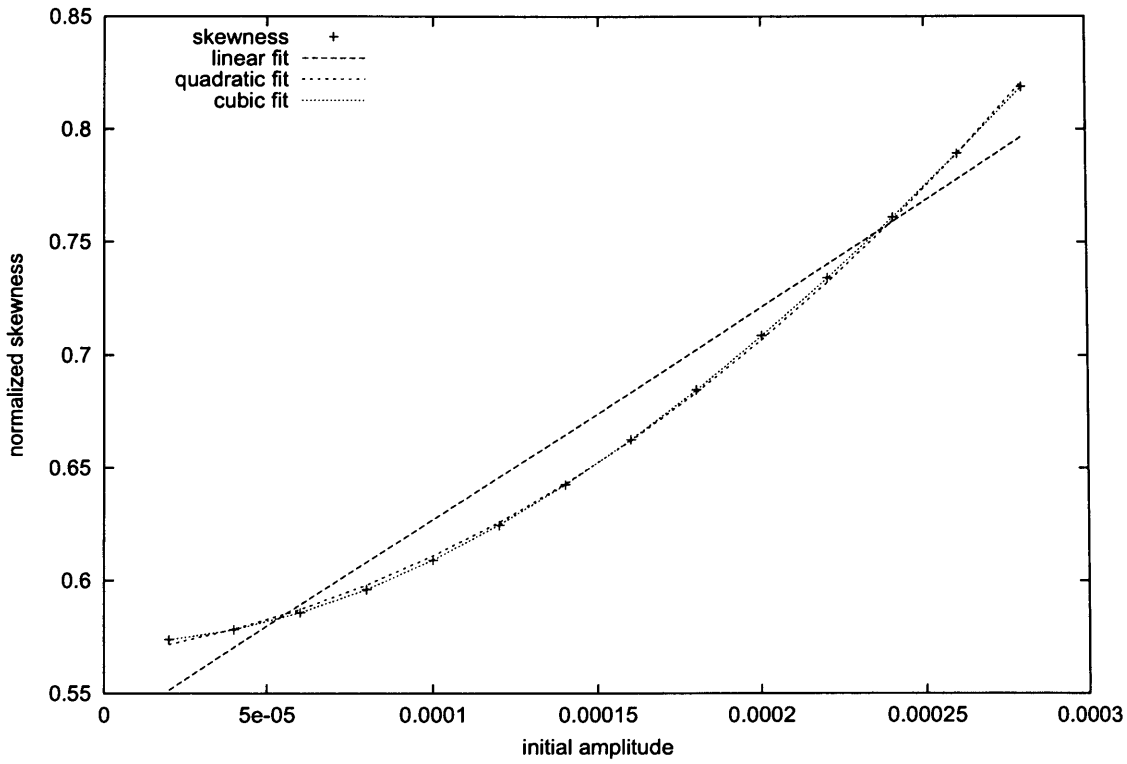

Figure 7.4: Normalized skewness of the gradient for $R = 1300$ over a range of amplitudes.

Now the skewness has been calculated using Houten and Healey's non-normalized definition and given in (7.10).

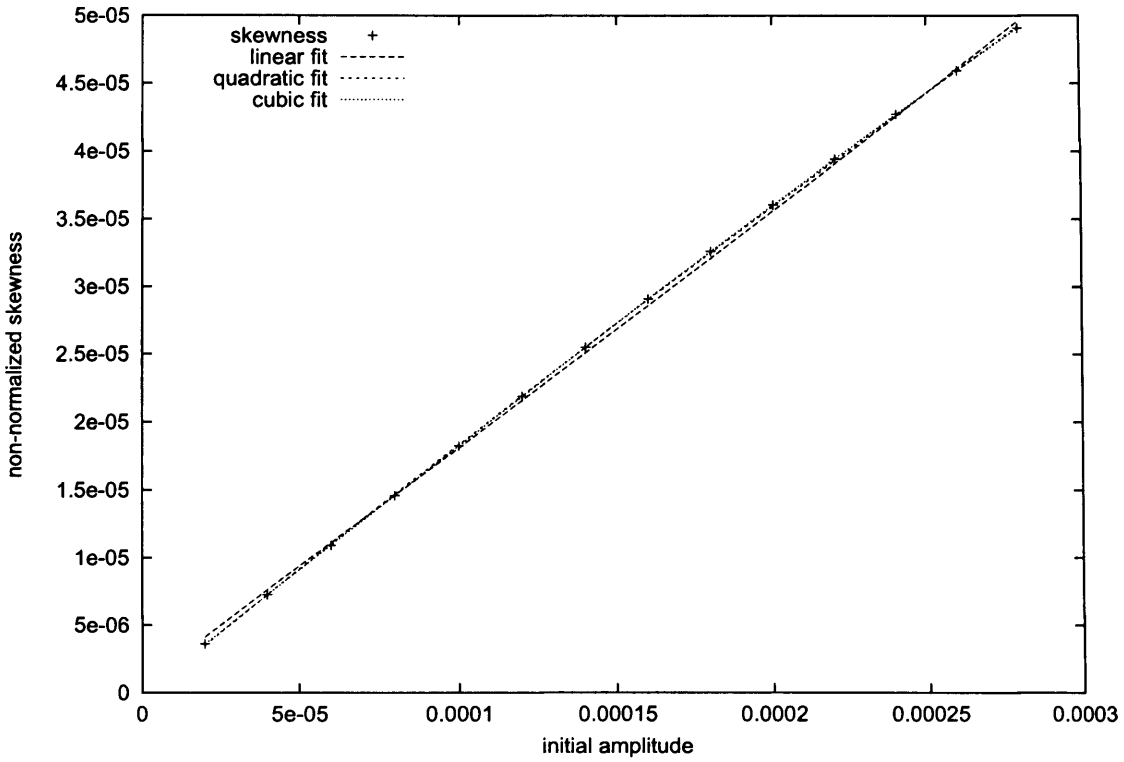

Figure 7.5: Non-normalized skewness of the gradient for $R = 1300$ over a range of amplitudes.

This varies slightly from being linear, and therefore we could say that the amplitude has a very slight effect on the results.

These two definitions of the skewness result in very different graphs. As said before, the normalized definition is more sensitive as it does not involve the cubic root. It is possible that at such low Reynolds numbers, the skewness is low compared with that found by Healey (2000) in his experiments (conducted at approximately R=2000).

Possibly skewness is not the best measure of wave-envelope steepening. In chapters 5 and 6

the quantity Σ was used to detect wave-envelope steepening. Recall that Σ is defined as

$$\Sigma = 1 + \frac{\min\{g(t) : t \in (0, T_{end})\}}{\max\{g(t) : t \in (0, T_{end})\}} \text{ (from page 131).}$$

Shown below in 7.6 is a graph of Σ at calculated at four different streamwise locations. From the definition of Σ, if it is zero, no wave-envelope steepening is occurring, otherwise wave-envelope steepening does occur: if Σ is positive, the leading edge is steeper than trailing edge, if Σ is negative then the trailing edge is steeper than the leading edge. The results shown below clearly indicate that the leading edge is becoming steeper. However, this data just concerns the leading edge and the trailing edge. It does not take into account all the other growing and decaying portions of the wavepacket. If Σ could be calculated for the entire wavepacket this might prove to be a better way of detecting wave-envelope steepening.

Another similar feature of the graphs of skewness and sigma is the fact that these quantities both seem to tend to a non-zero constant for small values of initial amplitude. This is not expected, since for small initial amplitudes the simulations will develop linearly and there should be no nonlinear effects and therefore no wave-envelope steepening. This could indicate that the randomly-modulated wavepacket has a skewness towards positive values (which looks reasonable by examining figure 7.1). If the wavepacket could be extended further in space, this effect could perhaps be negated. Although, from a numerical point of view, a longer wavepacket means that the simulations will be more unstable as the waves will reach higher amplitudes at the end of the domain.

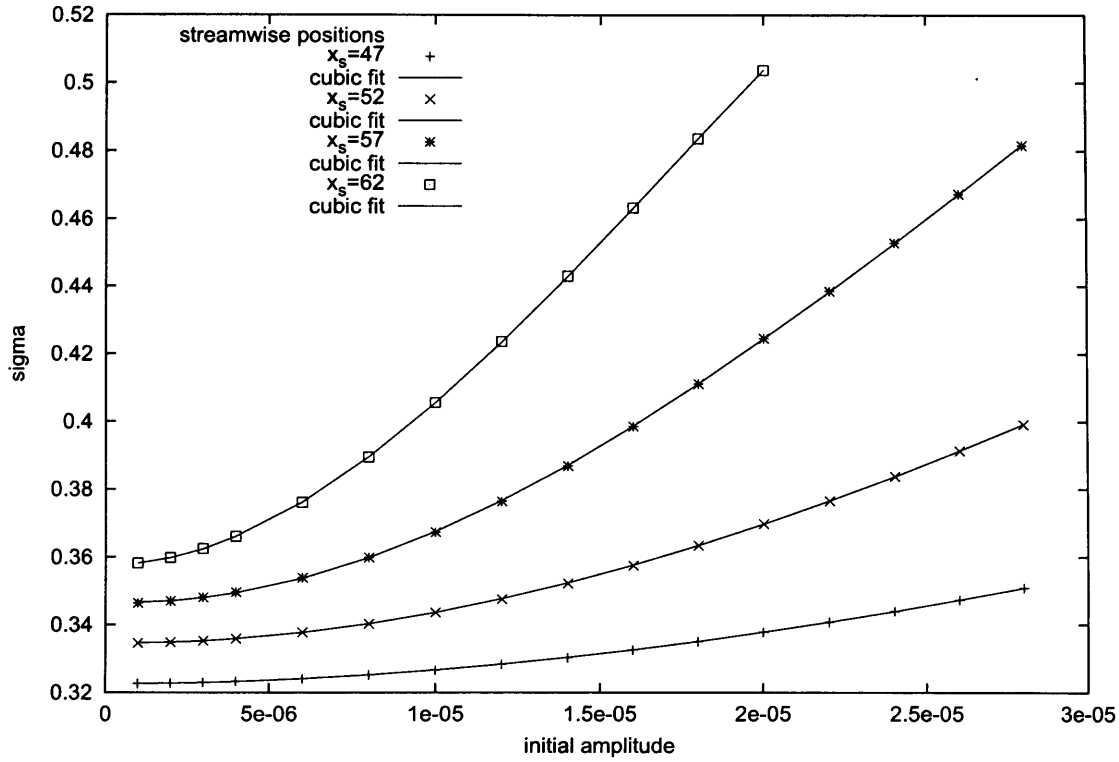

Figure 7.6: Σ at streamwise locations $x_s = 47, 52, 57, 62$ in ascending order with $x_s = 47$ being the lowest curve and $x_s = 67$ the highest at $R = 1300$.

7.3.2 R=1500

The random forcing signal used is the same as before, see figure 7.1. The time history of the wavepacket and its envelope at the location $x_s = 52$ are shown for an initial amplitude of 10×10^{-6} in figure 7.7. No obvious nonlinear effects can be seen in this plot. In figure 7.8 the initial amplitude was higher, 120×10^{-6}, and so nonlinear effects have influenced the development of the wavepacket. Figure 7.9 illustrates the nonlinear development which has taken place. This is very similar to the behaviour reported for $R = 1300$.

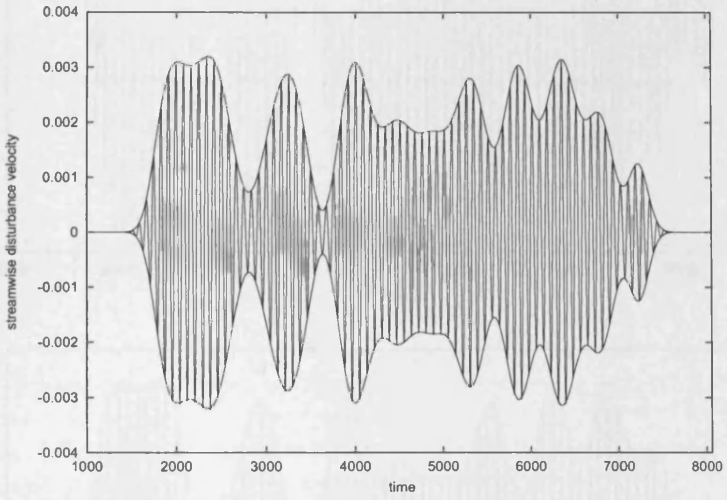

Figure 7.7: Streamwise velocity and envelope at $x_s = 52$ for an initial amplitude of 10×10^{-6}.

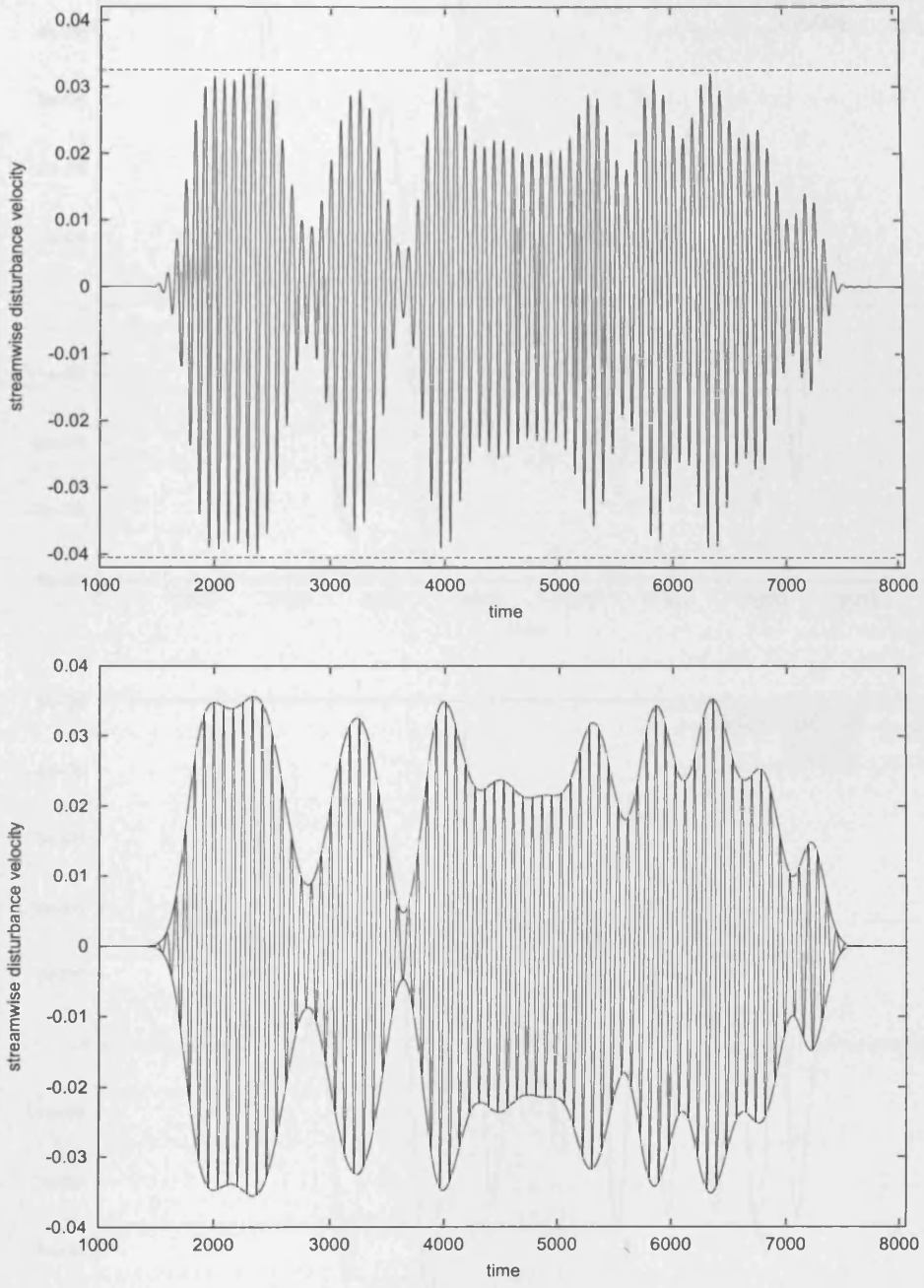

Figure 7.8: Above: streamwise velocity at $x_s = 52$ an initial amplitude of 120×10^{-6}. Below: the modified wavepacket and envelope at $x_s = 52$ for the same initial amplitude.

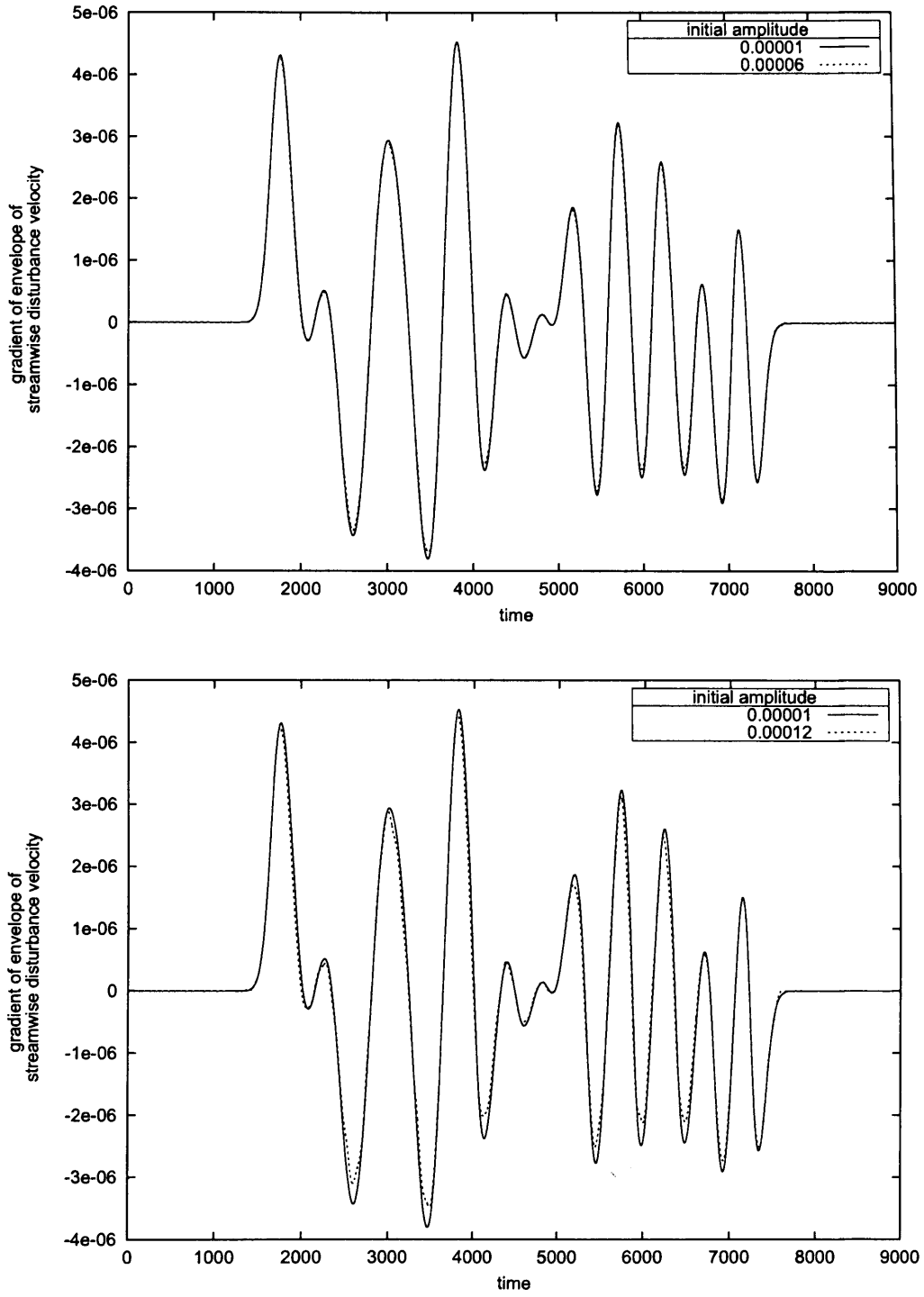

Figure 7.9: Scaled gradient of envelope of the streamwise disturbance velocity at $x_s = 52$ for two different initial amplitudes (top: 10×10^{-6} and 60×10^{-6}, bottom: 10×10^{-6} and 120×10^{-6}).

In summary, the results here do show that wave-envelope steepening occurs for a randomly-modulated disturbance. The effect is not as strong as we might have expected however, and when calculating skewness according to Houten and Healey's non-normalized definition (7.10), we do not find a quadratic dependence on the amplitude, instead behaviour which weakly deviates from linear. Three possible explanations for why only a weak effect occurrs are, first on inspection of the form of the wavepacket, there are not many growing and decaying parts of comparable magnitude to the leading and trailing edges of the wavepackets. Introducing more changes in envelope on this scale might increase wave-envelope steepening and increase the variation in the skewness. Also, if the wavepacket were longer this would have two advantages: first, more growing and decaying sections would occur in the wavepacket which would increase the skewness, if the wave-envelope steepening effect was occurring; and second, for small initial amplitudes the skewness would be closer to zero, rather than the case here, where the wavepacket already has a non-zero skew. As increasing the length of the wavepacket has been found to test the code, perhaps a temporal model should be implemented, instead of the spatial model used throughout.

Second, the random modulation is introduced through low frequencies ($< 0.2\omega_{ts}$). If the amplitude is low enough these modes will decay according to linear theory and so will have a limited influence on the flow. Finally, in Healey's experiments a higher Reynolds number was used. Here the highest Reynolds number reached was $R = 1800$ (as above this the computer code crashed), so the wave-envelope steepening effect would not be as strong. As these simulations used a longer wavepacket, the code was more susceptible to crash than for larger Reynolds numbers but shorter wavepackets. For shorter wavepackets interesting results can be gained before the main part of the wavepacket reaches the buffer domain. For longer wavepackets this is not the case. Increasing the length of the wavepacket would decrease the Reynolds number for which results would be attainable. However, possibly key to the success of these simulations is recreating a wavepacket disturbance that has more instances of steeper growing and decaying sections. Perhaps the forcing that Healey (2000) used in his experiments could serve as a model.

Chapter 8

Conclusions and further work

In flat-plate boundary layers wave-envelope steepening has been observed both in experiments and in numerical simulations. This effect is weakly nonlinear and refers to the process whereby a symmetrical wavepacket disturbance becomes asymmetrical as it propagates downstream. This asymmetry manifests itself in two ways. Initially the maximum amplitude of the wavepacket is equal to its absolute minimum value, and the gradient at the leading edge of the envelope of the wavepacket is equal to the absolute gradient at the trailing edge. The nonlinearities cause the maximum value of the amplitude of the wavepacket to be less than the absolute minimum value of the amplitude. The nonlinearities also cause the gradient of the envelope of the wavepacket at the leading edge to differ from the absolute gradient at the trailing edge as can be seen in plots of the time histories of the wavepacket. This latter effect is referred to as wave-envelope steepening.

The steepest part of the envelope is found to develop at the trailing edge in three-dimensional experiments but at the leading edge in two-dimensional nonlinear numerical simulations. Two explanations for this difference have been put forward for investigation: first that a non-zero streamwise pressure gradient in the experiment may have affected results. To test this premiss the input profile to the simulation can be changed from the Blasius flow (zero pressure gradient) to a Falkner–Skan flow, which has an associated streamwise pressure gradient. Second, wave-envelope steepening could be a three-dimensional effect and therefore would not be adequately modelled in two dimensions. This could be tested by developing a three-dimensional nonlinear version of the code.

Work done so far and reported in this thesis includes:

- the development an appropriate method of finding a non-oscillatory envelope of a wavepacket, especially for when the maximum amplitude of the wavepacket is not equal to the minimum value (see chapter 5).
- an investigation of the Ginzburg–Landau equation for a parallel flow (often used to model weakly nonlinear fluid flow even in the case of nearly-parallel flows). This was found to predict the occurrence of wave-envelope steepening only when the higher-order terms were included (see chapter 4).
- the use of Falkner–Skan profiles in order to investigate the effect of positive and negative streamwise pressure gradients. The steepest part of the envelope was found to occur at the leading edge, as previously reported for flows with no streamwise pressure gradient (see chapter 6).
- imposing a randomly-modulated envelope on the disturbance to investigate how wave-envelope steepening manifests itself when there are more instances of decaying and growing sections of the wave envelope present in a disturbance (see chapter 7).
- developing and giving a full account of a three-dimensional Poisson solver which can be used as part of a three-dimensional nonlinear code (see chapter 3).

During these investigations the mean flow of the disturbance was calculated. Once nonlinear effects come into play the disturbance no longer has a zero mean; the mean-flow distortion becomes positive. This could perhaps induce local pressure gradients at the leading and trailing edges. Were this true, the numerical results presented here suggest we should expect a local adverse pressure gradient to develop at the leading edge which would further destabilize the flow. At the trailing edge we would expect a local favourable streamwise pressure gradient to develop which would act to lessen the instability of the flow. The effect of these local pressure gradients could explain why the absolute gradient of the envelope is greater at the leading edge than it is at the trailing edge. Results from experiments carried out by Medeiros show that for a three-dimensional flow the mean disturbance flow is negative. The local pressure gradients which develop in this case will act to destabilize the flow at the trailing

edge, resulting in a larger gradient at the trailing edge than the leading edge. It is thus conjectured that the non-zero mean disturbance structure is a key ingredient in the wave-envelope steepening effect and may explain why this effect differs in two and three dimensions. Further work will be suggested in regard to testing this hypothesis[1].

Suggestions for further pieces of work that would naturally supplement the findings of this thesis are now discussed. First, the sign of the mean-flow distortion could be artificially changed. The non-oscillating early transitional flow is made up of two parts, the base flow, U^B, and a mean-flow distortion, $\langle u \rangle$, from nonlinear terms. Starting a simulation with the non-oscillatory part given by $U^B - \langle u \rangle$ instead of $U^B + \langle u \rangle$ might reverse the stability of the leading and trailing edges. The derivative $\frac{\partial \langle u \rangle}{\partial x}$ at the leading and trailing edges may affect wave-envelope steepening. Therefore, simulations could be run, aimed at increasing or decreasing the magnitude of this term.

Second, the development of an efficient three-dimensional nonlinear code could be undertaken. The code would then need to be validated, before the wealth of features of transition, such as secondary instabilities, could then be investigated. Bearing in mind the focus of this thesis, of particular interest would be to attempt to use this code to replicate the results of Medeiros' experiments (2004b), especially with regard to the negative mean-flow distortion. We could also discover whether a three-dimensional code would predict a steeper envelope at the trailing edge, in agreement with the experimental results.

Third, the real part of the higher-order complex Ginzburg–Landau equation was used to model the evolution of the amplitude of the wavepacket (equation (4.60), page 96). In this case the diffusion term was neglected and the method of characteristics was used to solve the equation. This work could be repeated, with the diffusion term included. Standard numerical schemes could be used to solve the equation.

Finally, a Ginzburg–Landau type equation for the non-parallel Blasius flow could be developed and tested to see whether it will predict wave-envelope steepening.

[1]It should be noted, however, that in three dimensions the leading and trailing edges are not so obviously defined as for two dimensions. Also, which particular spanwise position is used to take the flow measurements could affect the mean-flow distortion.

Bibliography

Acheson, D. J. (1990). *Elementary Fluid Dynamics.* Oxford Applied Mathematics and Computing Science Series. Oxford University Press.

Ali, R. (2003). *Receptivity and transition in boundary layers over rigid and compliant surfaces.* PhD thesis, University of Warwick, School of Engineering.

Anderson, J. D. (2005). Ludwig Prandtl's boundary layer. *Physics Today*, 58(12):42–48.

Bake, S., Fernholz, H. H., and Kachanov, Y. S. (2000). Resemblance of K- and N-regimes of boundary-layer transition at late stages. *European Journal of Mechanics: B - Fluids*, 19:1–22.

Benjamin, T. B. (1960). The development of three-dimensional disturbances in an unstable film of liquid flowing down an inclined plane. *Journal of Fluid Mechanics*, 10(3):401–419.

Bowles, R. I. (2000). Transition to turbulent flow in aerodynamics. *Philosophic Transactions of the Royal Society of London (Series A)*, 358:245–260.

Bowles, R. I., Davies, C., and Smith, F. T. (2003). On the spiking stages in deep transition and unsteady separation. *Journal of Engineering Mathematics*, 45:227–245.

Breuer, K. S., Cohen, J., and Haritonidis, J. H. (1997). The late stages of transition induced by a low-amplitude wavepacket in a laminar boundary-layer. *Journal of Fluid Mechanics*, 340:395–411.

Bridges, T. J. and Morris, P. J. (1984). Differential eigenvalue problems in which the parameter appears nonlinearly. *Journal of Computational Physics*, 55:437–460.

Canuto, C., Hussaini, M., Quarteroni, A., and Zang, T. (1988). *Spectral methods in fluid dynamics.* Springer.

Carpenter, M. H., Gottlieb, D., and Abarbanel, S. (1993). Stable and accurate boundary treatments for compact, high-order finite-difference schemes. *Applied Numerical Mathematics*, 12:55–87.

Carpenter, P. W., Davies, C., and Lucey, A. D. (2000). Hydrodynamics and compliant walls: Does the dolphin have a secret? *Current Science*, 79(6):758–765.

Carpenter, P. W., Lockerby, D. A., and Davies, C. (2002). Numerical simulation of the interaction of of microactuators and boundary layers. *American Institute of Aeronautics and Astronautics Journal*, 40:67–73.

Cohen, J., Breuer, K. S., and Haritonidis, J. H. (1991). On the evolution of a wavepacket in a laminar boundary-layer. *Journal of Fluid Mechanics*, 225:575–606.

Cooper, A. J. and Carpenter, P. W. (1997). The effect of wall compliance on inflexion point instability in boundary layers. *Physics of Fluids*, 9(2):468–470.

Corbett, P. and Bottaro, A. (2000). Optimal perturbations for boundary layers subject to streamwise pressure gradient. *Physics of Fluids*, 12(1):120–130.

Corke, T. C. and Gruber, S. (1996). Resonant growth of three-dimensional modes in Falkner–Skan boundary layers with adverse pressure gradients. *Journal of Fluid Mechanics*, 320:211–233.

Cowley, S. J. and Wu, X. (1993). Asymptotic approaches to transition modelling. Technical report, AGARD Report 793.

Craik, A. D. D. (1971). Non-linear resonant instability in boundary layers. *Journal of Fluid Mechanics*, 50(2):393–413.

Craik, A. D. D. (2001). A model for subharmonic resonance within wavepackets in unstable boundary layers. *Journal of Fluid Mechanics*, 432:409–418.

Criminale, W. O., Jackson, T. L., and Joslin, R. D. (2003). *Theory and Computation of Hydrodynamic Stability.* Cambridge University Press.

Davies, C. (1995). *Evolution of Tollmien-Schlichting waves over a compliant panel.* PhD thesis, University of Warwick.

Davies, C. (2003). Convective and absolute instabilities of flow over compliant walls. In *Flow past highly compliant boundaries and in collapsible tubes (editors P W Carpenter and T J Pedley)*, pages 69–93. Kluwer Academic Publishers.

Davies, C. (2005). Numerical simulation of boundary-layer disturbance evolution. *Philosophical Transactions of the Royal Society (A)*, 363(1830):1109–1118.

Davies, C. (2006). Computational studies of boundary-layer disturbance development. In *One hundred years of boundary layer research*, pages 325–334. IUTAM Symposium, Göttingham, Springer.

Davies, C. and Carpenter, P. W. (1997a). Instabilities in a plane channel flow between compliant walls. *Journal of Fluid Mechanics*, 352:205–243.

Davies, C. and Carpenter, P. W. (1997b). Numerical simulation of the evolution of Tollmien–Schlichting waves over finite compliant panels. *Journal of Fluid Mechanics*, 335:361–392.

Davies, C. and Carpenter, P. W. (2001). A novel velocity-vorticity formulation of the Navier–Stokes equations with applications to boundary layer disturbance evolution. *Journal of Computational Physics*, 172:119–165.

Davies, C. and Carpenter, P. W. (2003). Global behaviour corresponding to the absolute instability of the rotating-disc boundary layer. *Journal of Fluid Mechanics*, 486:287–329.

Davies, C., Carpenter, P. W., and Lockerby, D. A. (2001). A novel velocity-vorticity method with applications to flow control. In *ECCOMAS Computational Fluid Dynamics Conference.*

Davies, C., Thomas, C., and Carpenter, P. W. (2007). Global stability of the rotating-disk boundary layer. *Journal of Engineering Mathematics*, 57:219–236.

Delbende, I. and Chomaz, J.-M. (1998). Nonlinear convective / absolute instabilities in parallel two-dimensional wakes. *Physics of Fluids*, 10(11):2724–2736.

Drazin, P. (2000). Fluid mechanics in the twenty-first century. *Mathematics Today*, 36:135–139.

Fasel, H. (1976). Investigation of the stability of boundary layers by a finite-difference model of the Navier–Stokes equations. *Journal of Fluid Mechanics*, 78:355–383.

Fasel, H. (1980). Recent developments in the numerical solution of the Navier–Stokes equations and hydrodynamic stability problems. In *Computational Fluid Dynamics.* Hemisphere.

Fasel, H. (1984). Numerical simulation of nonlinear growth of wave packets in a boundary layer. In *Turbulence and chaotic phenomena in fluids; proceedings of the international symposium (editor T Tatsumi)*, Kyoto, Japan. Elsevier Science Publishers.

Fasel, H. and Konzelmann, U. (1990). Non-parallel stability of a flat-plate boundary layer using the complete Navier–Stokes equations. *Journal of Fluid Mechanics*, 221:311–347.

Fasel, H., Rist, U., and Konzelmann, U. (1990). Numerical investigation of the three-dimensional development in boundary-layer transition. *American Institute of Aeronautics and Astronautics Journal*, 28(1):29–37.

Fasel, H. F. (2002). Numerical investigation of the interaction of the Klebanoff-mode with a Tollmien–Schlichting wave. *Journal of Fluid Mechanics*, 450:1–33.

Fletcher, C. A. J. (2003). *Computational Techniques for fluid dynamics:* Fundamental and General Techniques (Volume 1). Springer, second edition.

Gaster, M. (1962). A note on the relation between temporally-increasing and spatially-increasing disturbances in hydrodynamic stability. *Journal of Fluid Mechanics*, 14:222–224.

Gaster, M. (1975). A theoretical model of a wave packet in the boundary layer on a flate plate. *Proceedings of the Royal Society of London Series A Mathematics, Physics and Engineering Sciences*, 347:271–289.

Gaster, M. (1979). The physical processes causing breakdown to turbulence. In *Twelfth Naval Hydrodynamics Symposium (Washington DC, 1978)*. National Academy of Sciences.

Gaster, M. and Grant, I. (1975). An experimental investigation of the formation and development of a wave packet in a laminar boundary layer. *Proceedings of the Royal Society of London Series A Mathematics, Physics and Engineering Sciences*, 347:253–269.

Gatski, T. B. (1991). Review of incompressible fluid flow computations using the vorticity-velocity formulation. *Applied Numerical Mathematics*, 7:227–239.

Gibbon, J. D. and McGuinness, M. J. (1981). Amplitude equations at the critical points of unstable dispersive physical systems. *Proceedings of the Royal Society of London Series A Mathematics, Physics and Engineering Sciences*, 377:185–219.

Goldstein, M. E. and Durbin, P. A. (1986). Nonlinear critical layers eliminate the upper branch of spatially growing Tollmien–Schlichting waves. *Physics of Fluids*, 29:2344–2345.

Grosch, C. E. and Orszag, S. A. (1977). Numerical solution of problems in unbounded regions: coordinate transforms. *Journal of Computational Physics*, 25:273–295.

Hall, P. and Smith, F. T. (1984). On the effects of nonparallelism, three-dimensionality, and mode interaction in nonlinear boundary-layer stability. *Studies in Applied Mathematics*, 70:91–120.

Healey, J. J. (1995a). A new boundary layer resonance enhanced by wave modulation: theory and experiment. *Journal of Fluid Mechanics*, 304:231–262.

Healey, J. J. (1995b). On the neutral curve of the flate-plate boundary layer: comparison between experiment, Orr–Sommerfeld theory and asymptotic theory. *Journal of Fluid Mechanics*, 288:59–73.

Healey, J. J. (2000). Wave-envelope steepening in the Blasius boundary-layer. *European Journal of Mechanics Part B - Fluids*, 19:871–888.

Herbert, T. (1988). Secondary instability of boundary layers. *Annual Review of Fluid Mechanics*, 20:487–526.

Hinch, E. J. (1991). *Perturbation Methods.* Cambridge University Press.

Houten, S. (2004). *Evolution of finite amplitude disturbances in the Blasius boundary layer.* PhD thesis, Keele University.

Houten, S., Healey, J. J., and Davies, C. (2000). Nonlinear evolution of Tollmien–Schlichting waves at finite Reynolds numbers. In *Symposium Laminar-Turbulent Transition (editors H Fasel and W S Saric)*, Arizona. Springer-Verlag.

Houton, S., Healey, J. J., and Davies, C. (2001). Evidence for a higher order Ginzburg–Landau equation for waves in Blasius flow. A poster presentation for the British Applied Mathematics Colloquium, University of Reading.

Ikeda, M. (1977). Non-linearity and non-periodicity of a two-dimensional disturbance in plane Poiseuille flow. *Journal of the Physical Society of Japan*, 42(5):1764–1771.

Jennings, M., Stewart, P., and Cowley, S. (1999). When is the weakly nonlinear evolution of a localized disturbance governed by the Ginzburg–Landau equation? *Proceedings of the Royal Society of London Series A Mathematics, Physics and Engineering Sciences*, 455:1521–1560.

Jordinson, R. (1970). The flat plate boundary layer. Part 1: numerical integration of the Orr–Sommerfeld equation. *Journal of Fluid Mechanics*, 43(4):801–811.

Joslin, R. D., Streett, C. L., and Chang, C.-L. (1991). Validation of three-dimensional incompressible spatial direct numerical simulation code: a comparison with linear stability and parabolic stability equation theories for boundary-layer transition on a flat plate. Technical Report NASA TP-3205, NASA Langley Research Center.

Joslin, R. D., Streett, C. L., and Chang, C.-L. (1993). Spatial direct numerical simulations of boundary-layer transition mechanisms: validation of PSE theory. *Theoretical and Computational Fluid Dynamics*, 4:271–288.

Kachanov, Y. S. (1994). Physical mechanisms of laminar-boundary-layer transition. *Annual Review of Fluid Mechanics*, 26:411–482.

Klebanoff, P., Tidstrom, K., and Sargent, L. (1962). The three-dimensional nature of boundary-layer instability. *Journal of Fluid Mechanics*, 12:1–34.

Klingmann, B. G. B., Boiko, A. V., Westin, K. J. A., Kozlov, V. V., and Alfredsson, P. H. (1993). Experiments on the stability of Tollmien–Schichting waves. *European Journal of Mechanics Part B - Fluids*, 12:493–514.

Kloker, M., Konzelmann, U., and Fasel, H. (1993). Outflow boundary conditions for spatial Navier–Stokes simulations of transition boundary layers. *American Institute of Aeronautics and Astronautics Journal*, 31:620–628.

Kudar, K. (2004). *Flow control using pulsed jets.* PhD thesis, School of Engineering, University of Warwick.

Laurien, E. and Kleiser, L. (1986). Numerical simulation of transition control in boundary layers. In *Numerical Methods in Fluid Mechanics (editors D Ruen and W Kordell)*, pages 225–232.

Laurien, E. and Kleiser, L. (1989). Numerical simulation of boundary-layer transition and transition control. *Journal of Fluid Mechanics*, 199:403–440.

Lele, S. K. (1990). Compact finite difference schemes with spectral-like resolution. Technical report, Center for Turbulence Research, NASA-Ames Research Center.

Liu, C. and Liu, Z. (1993). High order finite difference and multigrid methods for spatially evolving instability in a planar channel. *Journal of Computational Physics*, 106:92–100.

Lockerby, D. A., Carpenter, P. W., and Davies, C. (2002). Numerical simulation of the interaction of microactuators and boundary layers. *AIAA Journal*, 36(1):67–73.

Medeiros, M. A. F. (2004a). The nonlinear evolution of a wavetrain emanating from a point source in a boundary layer. *Journal of Fluid Mechanics*, 508:287–317.

Medeiros, M. A. F. (2004b). Nonlinear wavepackets in boundary layers. In *Sixth IUTAM Symposium on laminar-turbulent transition (editor R. Govindarajan)*, Bangalore. Springer.

Medeiros, M. A. F. and Gaster, M. (1999a). The influence of phase on the nonlinear evolution of wavepackets in boundary layers. *Journal of Fluid Mechanics*, 397:259–283.

Medeiros, M. A. F. and Gaster, M. (1999b). The production of subharmonic waves in the nonlinear evolution of wavepackets in boundary layers. *Journal of Fluid Mechanics*, 399:301–318.

Meitz, H. L. and Fasel, H. F. (2000). A compact-difference scheme for the Navier–Stokes equations in vorticity-velocity formulation. *Journal of Computational Physics*, 157:371–403.

Peyret, R. (2002). *Spectral Methods for Incompressible Viscous Flow.* Springer.

Press, W. H., Flannery, B. P., Teukolsky, S. A., and Vetterling, W. T. (1989). *Numerical Recipes: The Art of Scientific Computing (FORTRAN Version).* Cambridge University Press.

Reshotko, E. (1976). Boundary layer stability and transition. *Annual Review of Fluid Mechanics*, 8:311–349.

Rist, U. and Fasel, H. (1995). Direct numerical simulation of controlled transition in a flat-plate boundary layer. *Journal of Fluid Mechanics*, 298:211–248.

Saric, W. S., Reed, H. L., and Kerschen, E. J. (2002). Boundary-layer receptivity to freesteam disturbances. *Annual Review of Fluid Mechanics*, 34:291–319.

Schlichting, H. (2000). *Boundary Layer Theory.* Springer, eighth edition.

Schmid, P. J. and Henningson, D. S. (2001). *Stability and transition in Shear flows.* Springer.

Schubauer, G. B. and Skramstad, H. K. (1948). Laminar-boundary-oscillations and transition on a flat plate. Technical report, NACA TR 909. (This was first published in the annual report NACA ACR 34 (1943), pp 327-357).

Sen, P. K. and Vashist, T. K. (1989). On the nonlinear stability of boundary-layer flow over a flat plate. *Proceedings of the Royal Society of London Series A Mathematics, Physics and Engineering Sciences*, 424:81–92.

Shaikh, F. N. and Gaster, M. (1994). The nonlinear evolution of modulated waves in a boundary. *Journal of Engineering Mathematics*, 28:55–71.

Smith, F. T. (1979). Nonlinear stability of boundary layers for disturbances of various sizes. *Procedings of the Royal Society London Series A*, 368:573–589.

Smith, F. T. and Burggraf, O. R. (1985). On the development of large-sized short-scaled disturbances in boundary layers. *Proceedings of the Royal Society of London Series A Mathematics, Physics and Engineering Sciences*, 399(1816):25–55.

Souza, L. F., Mendonca, M. T., and Medeiros, M. A. F. (2005). The advantages of using high-order finite differences schemes in laminar-turbulent transition studies. *International Journal for Numerical Methods in Fluids*, 48:565–582.

Squire, H. B. (1933). On the stability for three-dimensional disturbances of viscous fluid flow between parallel walls. *Proceedings of the Royal Society of London Series A Mathematics, Physics and Engineering Sciences*, 142:621–628.

Stewartson, K. and Stuart, J. T. (1971). A non-linear instability theory for a wave system in plane Poiseuille flow. *Journal of Fluid Mechanics*, 48(3):529–545.

Stuart, J. T. (1960). On the non-linear mechanics of wave disturbances in stable and unstable parallel flows. Part 1: the basic behaviour in plane Poiseuille flow. *Journal of Fluid Mechanics*, 9:353–370.

Stuart, J. T. (1965). Hydrodynamic stability. *Applied Mechanics Reviews*, 18(7):523–531.

Tritton, D. J. (1988). *Physical Fluid Dynamics.* Oxford University Press, second edition.

Walker, P. (2005). A new model for wave packet evolution in a boundary layer. *Unpublished work: a project undertaken at Keele University.*

Watson, J. (1960). On the nonlinear mechanics of wave disturbances in stable and unstable parallel flows. Part 2. the development of a solution for plane Poiseuille flow and for plane Couette flow. *Journal of Fluid Mechanics*, 9:371–389.

Watson, J. (1962). On spatially-growing finite disturbances in plane poiseuille flow. *Journal of Fluid Mechanics*, 14(2):211–221.

Weinstein, M. (1981). Nonlinear instability in plane Poiseuille flow: a quantative comparison between the methods of amplitude expansions and the method of multiple scales. *Proceedings of the Royal Society of London Series A Mathematics, Physics and Engineering Sciences*, 375:155–167.

Woodley, B. and Peake, N. (1997). Global linear stability analysis of thin aerofoil wakes. *Journal of Fluid Mechanics*, 339:239–260.